Delft University of Technology

Hover and fast flight of minimum-mass mission-capable flying robots

de Wagter, C.

Important note
To cite this publication, please use the final published version (if applicable).
Please check the document version above.

HOVER AND FAST FLIGHT

OF MINIMUM-MASS MISSION-CAPABLE

FLYING ROBOTS

$$\Delta w_{ij}^* = \alpha \cdot \frac{\partial E}{\partial w_{ij}} + \gamma \cdot \Delta w_{ij}^{t-1}$$

$$- k \cdot x - c_v \cdot \dot{x} + f(t) = m \cdot \ddot{x}$$

$$x_{i,j}^l = \sum_m \sum_l w_{m,n}^l \; o_{i+m,j+n}^{l-1} + b_{i,j}$$

$$o_{i,j}^l = f(x_{i,j}^l)$$
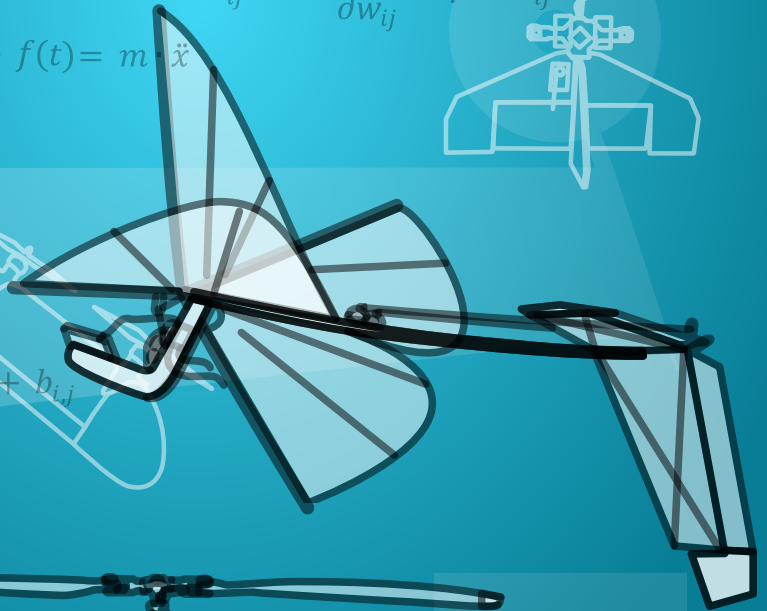
$$a_A = a_B + \alpha \times r + \omega \times (\omega \times r) + 2\omega \times v_{rel} + a_{rel}$$

Christophe De Wagter

Hover and fast flight of minimum-mass mission-capable flying robots

Hover and fast flight of minimum-mass mission-capable flying robots

Dissertation

for the purpose of obtaining the degree of doctor
at Delft University of Technology,
by the authority of the Rector Magnificus, prof. dr. ir. T.H.J.J. van der Hagen,
chair of the Board for Doctorates,
to be defended publicly on Tuesday 5, July 2022 at 15:00 o'clock

by

Christophe DE WAGTER

Master of Science in Aerospace Engineering,
Delft University of Technology, the Netherlands,
born in Eeklo, België.

This dissertation has been approved by the promotors.

Composition of the doctoral committee:

Rector Magnificus,	chairman
prof. dr. ir. J.M. Hoekstra,	Delft University of Technology, promotor
prof. dr. G.C.H.E. de Croon,	Delft University of Technology, promotor

Independent members:

prof. dr. ir. E. Johnson	Penn State University, USA
prof. dr. ir. P. Campoy	Universidad Politécnica de Madrid, Spain
prof. dr. ing. J-M. Moschetta	Institut Supérieur de l'Aéronautique et de l'Espace, France
prof. dr. ir. M. Wisse	Delft University of Technology
prof. dr. ir. R. Benedictus	Delft University of Technology

*TU*Delft
Delft
University of
Technology

An electronic version of this dissertation is available at:
http://repository.tudelft.nl/.

Contents

Summary

Highly automated Unmanned Aerial Vehicles (UAVs) or "flying robots" are rapidly becoming an important asset to society. The last decade has seen the advent of an impressive number of new UAV types and applications. For many applications, the UAVs need to be safe, highly automated, and versatile. Safety is a prerequisite to allowing their use in society. While flight safety comprises many aspects, one important safety factor is the total system mass. The common thread through this research is therefore to minimize the system mass while maintaining mission capabilities to increase safety. Flight automation is required to reach many applications' full potential by addressing operational labor costs and scalability. But despite great advances in ground-based robotics, the weight and power constraints of flying robots still constitute important challenges. Last but not least, many applications also require versatile aircraft that combine the ability to hover and fly fast efficiently. Hover is required for precision take-off & landing in confined areas at a growing number of locations and for the close-up inspection of assets. Fast and efficient flight is needed to reach distant locations, perform large surveys, cope with high headwind conditions, or simply reach destinations quickly. Unfortunately, the requirements for hover and fast flight are conflicting, and this drives the search for solutions to "combine hover with fast flight in mission-capable flying robots while cost-effectively minimizing their size and maximizing their safety."

To investigate the minimal feasible mass of mission-capable robots, in this thesis, a novel 20 g tailed flapping-wing robot called DelFly Explorer is presented that can autonomously explore unknown unprepared rooms. It was equipped with a 4 g micro stereo-vision system which necessitated algorithms that were optimized for tiny microcontrollers with low memory. Combined with a navigation strategy that keeps the area in front of the robot free of obstacles, a 0.9 g autopilot, and DelFly's novel stable slow hovering flight regime, this led to the lightest flying indoor exploration robot that could navigate in unknown environments. But to combine passive dynamic longitudinal stability at slow hover and fast flight in tailed ornithopters, a shift in the center of gravity location was shown to be needed. Moreover, the aerodynamically stabilizing tail also causes sensitivity to turbulence. Therefore, by using four pairs of flapping wings, a new tail-less flapping-wing concept called Quadthopter was created which can hover precisely and transition to fast forward flight. The cranked-rocker-based mechanism contains no expensive parts and by re-using the main propulsion motors for attitude control, powerful control moments can be created which are very important in disturbance rejection. This design represents one of the first tailless flapping wing designs that was sufficiently light and agile for performing real missions while featuring a mechanism simple enough to permit large-scale production.

Versatility of flight is also an asset for outdoor flight. Theory predicts that the

most efficient hover is achieved by using a single large rotor while the most efficient forward flight is performed by using high aspect ratio fixed wings to generate lift. The combination of both has led to a novel helicopter-with-wings concept called DelftaCopter. The control of this platform yields unique challenges such as the inertia of the large fixed-wing interferes with the dynamics of the helicopter rotor. A controller was derived, and the dynamics were identified in hover and forward flight. The real-world performance of this flying robot is presented by analyzing the results of its participation in the *outback medical challenge*, showing that large single-rotor-equipped fixed-wing aircraft combine powerful attitude control, efficient hover, and efficient forward flight.

Since efficiency in forward flight is not sufficient to achieve a very long endurance in electrically powered flying robots, a novel platform was developed around a hydrogen pressure cylinder and a fuel cell. The concept focuses on versatility, minimal weight, good control, and redundancy. A 12-motor tail-sitter is presented that re-uses all its motors for attitude control, hover, and forward flight and uses the wing structure to carry the propulsion. A dual automotive CAN-bus control network and dual flight modes remove the most critical single points of failure. The platform is called the Nederdrone and is shown to fly 3h38 in a test departing from a moving ship at sea in 5 Beaufort wind conditions.

While reaching fast flight in large free blocks of air is mainly a challenge for the design of the airframe and its energy source, as soon as obstacles are introduced, new bottlenecks appear and the weight and power consumption of sensing and processing become driving design considerations. Increasing the flight speed of flying robots in obstacle-packed or GPS-denied environments highlights the need for very lightweight fast but intelligent systems, as the processing weight and power not only reduce the flight times but also reduce the maneuvering capabilities and the maximum speed. Therefore, in this work, an extreme example is studied in the context of autonomous drone racing. A computationally light Artificial Intelligence (AI) based monocular navigation system is presented for indoor flight through obstacles. It enabled the flying robot to fly at higher speeds than what was possible with state-of-the-art visual-inertial odometry solutions.

Overall, aerospace platforms require extreme optimization as every gram kept in the air requires constant energy. The consequence is that different missions will require vastly different platforms, while traditionally a lot of flying robot applications are still performed by multicopters. This thesis contributes to the design of intelligent flying robots that can both hover and fly fast, by solving several fundamental problems in novel concepts optimized around the five key requirements of mass, agility, efficiency, range, and speed-near-obstacles. These concepts are expected to contribute to the improvement of the mission capabilities of minimal-size flying robots to address the needs of society.

Samenvatting

Sterk geautomatiseerde onbemande luchtvaartuigen of "vliegende robots' zijn een belangrijke aanwinst aan het worden voor de maatschappij. De laatste decennia zijn tal van nieuwe onbemande vliegtuigtypes en bijbehorende toepassingen ontstaan. Veel van die toepassingen vereisen dat de vliegende robots veilig, sterk geautomatiseerd maar ook veelzijdig zijn. Veiligheid is noodzakelijk voordat enige vlucht in de burgerluchtvaart kan worden gemaakt. Terwijl veiligheid veel aspecten kent, speelt de massa van het luchtvaartuig hierin een erg belangrijke rol. De rode draad door dit onderzoek is daarom de stelling dat "het uitvoeren van eenzelfde missie met een lichter platform in belangrijke mate kan bijdragen aan de veiligheid." Een sterke mate van automatisering is nodig om tot schaalbare en kost-effectieve toepassingen te komen, maar ondanks de grote vooruitgang in de automatisering van statische en rijdende robots zijn er bij vliegende robots strikte gewichts- en energiebeperkingen, die een grote nieuwe uitdaging vormen. Tot slot vereisen veel toepassingen ook veelzijdige luchtvaartuigen, die zowel stationair kunnen blijven hangen als snel kunnen vliegen. Het stilhangen is nodig voor het opstijgen en landen zonder landingsbaan of voor inspectiedoeleinden. Een efficiënte snelle vlucht is nodig om grote afstanden af te leggen, tijdsgevoelige vracht te vervoeren of simpelweg te kunnen vliegen bij meer wind. Helaas zijn de vereisten voor stationaire en snelle vlucht tegenstrijdig. Samen vragen deze vereisten om onderzoek naar oplossingen die stationaire vlucht en snelle vlucht optimaal combineren in vliegende robots die een missie kunnen uitvoeren terwijl hun massa vanwege de veiligheid wordt geminimaliseerd.

De combinatie van een stationaire en snelle vlucht in een zo licht mogelijke robot heeft in dit onderzoek geleid tot de DelFly Explorer. Deze vliegende robot met flappende vleugels van 20 g is in staat om zelfstanding een onbekende en onaangepaste ruimte te verkennen. Daartoe is hij uitgerust met een 4 g micro stereocamera met algoritmes, die zijn aangepast om te draaien op diens kleine microprocessor. Samen met zijn 1 g autopiloot, navigatiestrategie en vernieuwende stabiele langzame stationaire vlucht heeft dit geleid tot de lichtste vliegende robot, die onbekende binnenruimtes kan verkennen. Om deze passieve stabiliteit te behouden in snelle voorwaartse vlucht is echter een verplaatsing van het zwaartepunt nodig dat in het volgende hoofdstuk is uitgewerkt. Bovendien heeft het stabiliserende staartvlak als nadeel dat de robot gevoelig wordt voor turbulentie. Daarom is een nieuw staartloos concept geïntroduceerd dat bestaat uit 4 paar afzonderlijk aangedreven flappende vleugels. Deze zogenaamde Quad-thopter kan stilhangen en snel vliegen terwijl het gebruik van zijn hoofdvoortstuwing voor de standbesturing hem in staat stellen om turbulentie krachtig tegen te sturen. Het ontwerp vormt één van de eerste vliegende robots met flappende vleugels zonder staart, die licht en wendbaar genoeg was om met een nuttige lading missies te vliegen, terwijl het eenvoudige mechanisme zich

goed leent voor massaproductie.

Ook bij grotere buiten-robots is veelzijdigheid van belang. De theorie voorspelt dat de efficiëntste manier om stationair stil te hangen wordt verkregen met een enkele grote rotor terwijl efficiënte voorwaartse vlucht met slanke vleugels wordt verkregen. De combinatie van beiden is uitgewerkt tot een nieuw concept: de gevleugelde helikopter DelftaCopter. De besturing van dit concept levert echter unieke uitdagingen door de interactie van de vleugel op de rotordynamica. Er is een controller uitgewerkt en de dynamica van de DelftaCopter is geïdentificeerd in stationaire en snelle voorwaartse vlucht. De prestaties van de DelftaCopter zijn getest tijdens de *outback medical challenge* en tonen de gecombineerde, krachtige standsturing, efficiënte stationaire vlucht en efficiënte voorwaarste vlucht van de gevleugelde helikopter aan.

Omdat enkel een verhoogde efficiëntie niet voldoende is om de vluchtduur significant te vergroten is vervolgens een nieuw platform uitgewerkt rondom een waterstof drukvat en brandstofcel. Dit concept is gebaseerd op veelzijdigheid, minimaal gewicht, krachtige stand besturing en redundantie. Het 12-motorige toestel hergebruikt zowel de vleugelstructuur om de motoren te dragen en de motoren voor de stand sturing, stationaire vlucht en snelle vlucht. De aansturing via een dubbele CAN-bus en de dubbele vliegmodus helpen de meeste single-point-of-failure fouten te overwinnen. Een testvlucht van deze Nederdrone gedurende 3 uur en 38 minuten vanaf een bewegend schip op zee in 5 Beaufort wind illustreert de prestaties in operationele omstandigheden.

Terwijl snel vliegen in grote stukken luchtruim vooral te maken heeft met de efficiëntie en energie van het platform, leidt een snelle vlucht in de nabijheid van obstakels vooral tot knelpunten op het gebied van sensoren en rekenkracht. Een hele snelle vlucht dichtbij tal van obstakels en zonder GPS vraagt om snelle, lichte energiezuinige intelligentie, aangezien gewicht niet alleen de vluchtduur maar ook de wendbaarheid en maximale snelheid beinvloedt. In dit werk is een extreem voorbeeld bestudeerd in de context van autonoom drone-racen. Daartoe is een licht, artificiële intelligentie-gedreven camera-navigatiesysteem ontwikkeld dat een vliegende robot in staat stelt sneller te vliegen dan mogelijk met traditionele visueel-inertiële navigatie in een binnenomgeving zonder GPS en met obstakels.

Samenvattend vragen luchtvaartuigen om een extreme optimalisatie, omdat elke gram, die in de lucht gehouden moet worden, constant energie vraagt. Het gevolg is dat verschillende missies ook om erg verschillende platformen vragen en de populaire multicopters niet overal de beste oplossing voor vormen. Alles bij elkaar draagt dit onderzoek bij aan de combinatie van stationaire en snelle vlucht van vliegende robots door meerdere fundamentele problemen op te lossen in vliegende robot concepten die zijn geoptimaliseerd voor gewicht, wendbaarheid, efficiëntie, bereik en snelheid rondom obstakels. Deze oplossingen dragen bij aan het verbeteren van de prestaties en het vliegbereik van vliegende robots met minimale massa wat bijdraagt aan de veiligheid en mogelijkheden van vernieuwende maatschappelijke toepassingen.

Acronyms

ADR Autonomous Drone Racing
AED Automated External Defibrillator
AGL Above Ground Level
AI Artificial Intelligence
AIRR Artificial Intelligence Robotic Racing
API Application Programming Interface
BLDC Brush-Less Direct Current
BVLOS Beyond Visual Line of Sight
CAN Controller Area Network
CASA Civil Aviation Safety Authority
CD Cylinder Dynamics
CMOS Complementary Metal-Oxide Semiconductor
CNG Compressed Natural Gas
CNN Convolutional Neural Network
CoMC Coefficient of Multiple Correlation
CPLD Complex Programmable Logic Device
CPU Central Processing Unit
CTS Composite Technical Systems
CURVACE Curved Artificial Compound Eye
DC Direct Current
DCMI Digital Camera Media Interface
DNN Deep Neural Network
DOF Degree of Freedom
DSP Digital Signal Processor
EA Evolutionary Algorithm
EMD Elementary Motion Detector
EPP Expanded Polypropylene
ESC Electronic Speed Controller
FOV Field Of View
FPV First Person View
FWMAV Flapping Wing Micro Air Vehicle
GCS Ground Control Station
GPS Global Positioning System
GPU Graphics Processing Unit

HDR High Dynamic Range

HSV Hue Saturation Value

IMU Inertial Measurement Unit

INDI Incremental Nonlinear Dynamic Inversion

IR Infrared

IoU Intersection over Union

LED Light Emitting Diode

LEV Leading Edge Vortex

LHV Lower Heating Value

LQR Linear Quadratic Regulator

MAV Micro Air Vehicle

MHE Moving Horizon Estimator

MEMS Microelectromechanical systems

NTC Negative Temperature Coefficient

OJF Open Jet Facility

PCB Printed Circuit Board

PCP Pre-Charged Pneumatic

PEM Polymer Electrolyte Membrane

PET Polyethylene Terephthalate

PIV Particle Image Velocimetry

PnP Perspective-n-Point

RANSAC Random Sample Consensus

RPM Rotations Per Minute

SGBM Semi-Global Block Matching

SLAM Simultaneous Localization and Mapping

SSD Single Shot MultiBox Detector

SWaP Size, Weight, and Power

TPED Transportable Pressure Equipment Directive

TPP Tip-Path Plane

UAV Unmanned Air Vehicle

VHDL Very High Speed Integrated Circuit Hardware Description Language

VIO Visual-Inertial Odometry

VTOL Vertical Take-Off and Landing

1

Introduction

Science is the best tool ever devised,
for understanding how the world works.

Michael Shermer

Flying robots are rapidly becoming an important asset to society as scientific and technological advances have translated into their pervasive use for civilian use-cases [1, 2]. The last decade has seen the advent of a broad variety of new types of flying robots and corresponding applications in a wide range of domains [3, 4]. The applications of flying robots range from passive remote sensing [5] to actively delivering packages [6] or interacting with the world individually [7, 8] and collectively [9]. Sectors range from inspection of infrastructure [10] to smart farming, which promises to improve our crops through precision agriculture [11, 12], reduce the use of pesticides through frequent mapping with precision spraying [13] and reduce risks of malnutrition and infestations through regular crop monitoring, both outdoors and indoors [14]. In the energy sector, the costs of windmill, gas pipe, or power-line inspections [15] can be reduced. Flying robots have a role in surveillance [16], emergency response [17, 18], and autonomous flight in warehouses promises unprecedented verification of the stock [19]. Flying robot applications have even been developed to go underwater [20] and fly on other planets [21].

But most Unmanned Air Vehicle (UAV) (also known as 'drone') applications will only reach their full potential if they meet some important characteristics. They should be highly *automated* and become flying robots to save on labor costs. They should be *versatile* to take-off and land in situ while flying either fast, far, or long. Finally, flying robots need to be sufficiently *safe* to allow their widespread use in an increasingly populated world [22, 23]. One important contributor to UAV safety is the total mass of the platform [24]. So if the same mission can be performed with a much lighter platform, this can substantially contribute to increasing safety.

1

1

This is reflected in regulations and has for instance driven research towards smaller flying robots like the sub-250 gram DJI-mini series[1]. One of the main requirements for most envisaged applications is flight versatility and in particular, the combined ability to hover and fly forward fast and efficiently. Hover is required for precision landing in confined areas and for close-up inspection of assets, while an efficient fast flight is needed to reach distant locations, perform large surveys, cope with high wind conditions, or reach destinations quickly. Unfortunately, the requirements for hover and fast flight are conflicting. The result is that most aerial vehicles are either optimized for hovering while sacrificing speed and range or are optimized to be fast efficient platforms but then need runways or infrastructure like catapults to take-off and nets to land. The ability to combine both not only improves the applicability of UAS but can also contribute to their safety by removing runway requirements and offering a backup flight mode in case of failure.

This drives the search for solutions to *combine hover with fast flight* in *mission-capable flying robots* while *minimizing their mass* to maximize their safety. But depending on additional requirements or optimization criteria, the combination of hover and fast flight can take significantly different forms and constitute different technological challenges. The following sections will investigate the combined ability to hover and fly fast along several sub-objectives.

1.1. Minimal-mass hover and fast flight

Miniaturization of flying robots brings several fundamental challenges. The first challenge is related to the size constraints of the aircraft. When scaling down aircraft, their dynamics become faster [25], their mass has to scale quadratically with the size to maintain lift [26], while the viscous properties of air get worse with decreasing Reynolds number, which decreases with vehicle size, airspeed and density [27]. Their onboard energy scales down linearly with mass. This heavily influences the total flight time and affects the ability to be able to perform a useful mission. And last but not least, the energy used for their onboard robotic computations should also scale down with battery size while the robots instead have faster dynamics than larger robots and their smaller sensors are noisier than their larger counterparts. Worse even, the perturbations like wind gusts or headwinds that these platforms need to cope with, appear much larger to tiny light aircraft than they are felt by massive big aerial vehicles. This results in the two fundamental challenges for tiny flying robots: achieving controllability and efficient flight over a wide range of airspeeds—from hover to fast forward flight—while computationally performing autonomous flight with minimal amounts of power.

Given that these challenges have been successfully solved by nature, it is not surprising that insects and birds have inspired flying robots for a long time [28–31]. While flying insects may seem ordinary, they have successfully addressed all the former problems for 350 million years [32]. Their flapping wings cope well with reducing Reynolds numbers [33, 34] while the many degrees of freedom of their

---

[1]The importance of mass in UAV safety combined with the scientifically interesting challenges involved in making smaller flying robots were the driving reason to name the UAV research laboratory of the TUDelft: the Micro Air Vehicle Lab, or MAVLab.

1

wings' flapping motion [35] gives them excellent control [36]. Evolution shaped a variety of solutions like tiny halteres to function as stabilizing gyroscopes [37–39], power-efficient optical flow sensing for flight stability [40], landing [41–43], odometry & navigation [44], avoidance & evading predators [45], and for stabilizing head motions to improve visual inputs [46]. Natural solutions include Leading Edge Vortex (LEV) to increase the lift on animal wings [47–49], stability increasing vibrations [50], up to morphing wings to adapt flight-performance in-flight [51]. Also in the area of computation and control nature has inspired robotics. The Elementary Motion Detector (EMD) to compute optic flow has shown to help with both low-level flight control as navigation and obstacle avoidance [52, 53]. And while deep neural networks are inspired by principles seen in animal brains [31, 54, 55], the spiking neural networks appear to enable particularly power-efficient implementations that spend computational energy only where signals are needed [56–59].

(a) RoboBee [60] (b) Solar Robobee[61] (c) Microglider [62] (d) Microbat [63]

(e) MC2 microflyer [64] (f) Nano hummingbird [65] (g) Co-axial helicopter (h) DelFly Explorer [66]
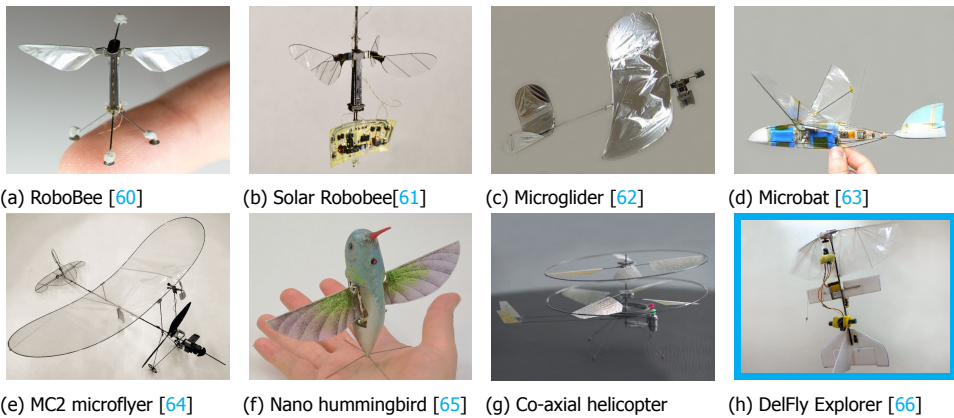
Figure 1.1: Minimal-mass flying robots. The robot in the blue box is proposed in this research.

The state of the art in micro and nano robotic flight reached capabilities that separately approach what is seen in nature, but not combined in a single system [67]. The research into the miniaturization of flight is roughly split into two classes. The top-down approach strived to always keep a mission-capable platform while minimizing the size. The bottom-up approach develops technologies [68, 69] needed for the smallest sizes until a flying system is achieved. In terms of weight, the bottom-up approach yielded flying pico air vehicles or sub-gram flying machines like the RoboBee [60] (Figure 1.1a). These tiny robots can hover and are expected to be able to perform fast flight as well. But although flights were made with on-board sensors [70–72], these systems still rely on external sensors for autonomous navigation and avoidance. And while untethered flights powered by laser light [73] or solar power [61] have been performed (Figure 1.1b), energy is still an important bottleneck. Finally, despite the technology evolving fast, no flights carrying any camera have been performed yet.

In the top-down approach, the lightest platforms carrying their own energy are faster fixed-wing aircraft like the 1.5 g microglider [62] which is able to perform
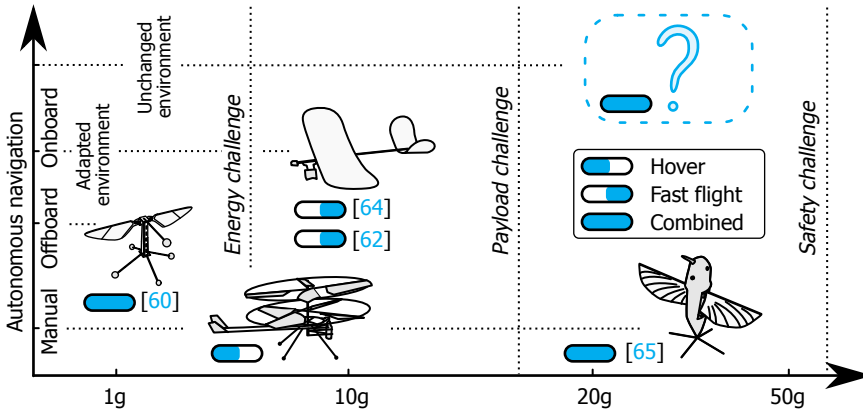
Figure 1.2: Combining hover and fast flight in minimum-mass flying robots at various autonomous navigation levels. This research proposes flapping-wing indoor exploration robots with onboard navigation to explore unchanged environments. Solutions are proposed to embed the required sensing and processing, combine hover and fast flight, and maximize the agility to cope with real-world mission conditions.

phototaxis (Figure 1.1c) and microbat [63] (Figure 1.1d). Zufferey *et al.* [64] even managed to add optical flow sensors and processing to achieve robotic flight of their micro flier at a mere 10 g (Figure 1.1e). To allow automatic flight with minimal processing, the room they flew in had to be prepared with special textures, and the tiny fixed-wing Micro Air Vehicle (MAV) did not carry a payload. Overall, the fixed-wing aircraft aerodynamic performance drops steeply with Reynolds numbers, making fixed-wings not ideal for miniaturization combined with slow flight [74]. Keennon *et al.* [65] developed an impressive flapping-wing aircraft of 19 g resembling a hummingbird (Figure 1.1f) which was able to hover and fly forward under manual control. A patent describes many variations of the high-tech micromachined flapping mechanism [75]. The smallest helicopters included the work from Petter Mürren (Figure 1.1g), and while the initial co-axial indoor helicopters were not able to fly at high speed nor fly automatically, it paved the way to an impressive outdoor micro helicopter[2]. To overcome the size-related limitations of tiny platforms, 'collaboration between robots' has been proposed. Research on swarming and flocking started decades ago [76] and yielded a lot of promising ideas such as unpredictable surveillance, resilient exploration, and inspiring entertainment, but typically did not yet address the onboard sensing and navigation problems [77].

Overall, developing low-mass, mission-capable, autonomously flying robots that combine hover and fast flight with all processing onboard while being able to navigate in unchanged environments remains a challenge (See Figure 1.2). The smaller flying robots get, the more important it becomes that their operational range of speeds and agility remains large enough to compensate for the shorter mission times and relatively larger turbulence levels. Finally, at small sizes, reducing the computational cost of their automation becomes extremely challenging. This research proposes a series of mass-minimized novel autonomous indoor exploration

---

[2]http://www.proxdynamics.com

robot concepts called DelFly (Figure 1.1h). Solutions are proposed to embed the required sensing and processing, to combine hover and fast flight, and to maximize agility to cope with real-world mission conditions.

1.2. Efficiency-optimized hover and fast flight

When the size and mass constraints are relaxed, for instance when flying robots do not have to fly inside buildings nor fit through doors, the next parameter to optimize is the efficiency. A higher flight efficiency will allow the use of smaller flying robots for a given mission requirement. Particularly when flying in an increasingly densely populated world closer to populated areas, the need for safety and redundancy becomes ever more important. On top of that, flying longer and faster while being able to take off and land from any tiny patch of ground or even a box can also help in reducing the operational costs in a variety of mission types. Therefore, finding mission-capable minimum-mass redundant combinations of hovering capabilities with efficient fast flight capabilities in flying robots could boost the success of many mini-UAV applications. The possible applications of flying robots with combined fast efficient long-range flight and hovering capabilities—further called *hybrid UAV*—are numerous. Typical examples range from operations departing from ships or in vast forests to long-distance package delivery in densely built-up areas [2].

Unfortunately, requirements for fast and slow or even hovering flight are conflicting [78]. Hovering flight is ideally done with a single large rotor [79] while fast forward flight calls for small propellers on a very aerodynamic vehicle with an optimal wing loading depending on cruise speed [80]. Finding an optimal combination of efficient hover and efficient forward flight thereby often comes as a compromise. Therefore a lot of different concepts have been proposed.

Hybrid aircraft have existed for a long time [81]. The first hybrid aircraft had to carry a human pilot, and this created additional constraints. Early manned designs often included complex and heavy mechanisms to tilt the wing, the motors, or even the pilot during the transition from hover to forward flight [82], such that the pilot could remain vertical and see the surroundings. Mechanically simpler platforms like the tailsitter (e.g. Convair XF-Y1 in Figure 1.3a) proved to be very hard to control and impractical for the pilot [83], which reduced their success. But the advent of unmanned aircraft revived the interest in hybrid platforms as several problems like pilot comfort and pilot training were no longer applicable.

Current hybrid UAVs can be divided into four categories depending on the orientation of the lifting devices in hover (typically rotors) and forward flight (typically wings). The first category contains vehicles where both lift generating devices are fixed in the same plane [84, 94–96] (Figure 1.3b). The biggest disadvantage is that components of one flight regime are not reused in the other. For instance, the hover propulsion system only creates drag and weight in forward flight. On top of that, an extra structure is needed to hold the hover propellors away from the wing and create their down-wash on the wing. Maximizing the speed or flight endurance in this category means that the hover system is kept as small as possible and this reduces the resilience to perturbations in hover. The second category reconfigures the aircraft by either tilting the motors [97, 98][85] (Figure 1.3c), tilting the entire

(a) Convair-XFY-1 [83]   (b) Quadplane [84]   (c) Songbird [85]   (d) DHL Parcelcopter 3 [86]

(e) VertiKUL [87]   (f) Quadshot [88]   (g) ATMOS [89]   (h) Cyclone [90, 91]

(i) Pacflyer S100 [92]   (j) Amazon Prime Air [93]   (k) DelftaCopter   (l) Nederdrone

Figure 1.3: Hybrid aircraft and UAVs that can take-off and land vertically while using fixed wings to increase flight efficiency during fast forward flight. Robots in the blue boxes are proposed in this research.

wing [86, 99] (Figure 1.3d) or even tilting multiple wings [100]. This has the advantage to re-use the propulsion in both flight modes but comes at the cost of heavy tilting mechanisms and a varying control morphology. The third group contains the so-called tail-sitters. These aircraft typically re-use the main hover propulsion in forward flight but pitch the whole vehicle down 90° to reorient the thrust forward [87] (Figure 1.3e). The remaining concepts fall in the final category of special concepts. This includes spinning mono-copters [101, 102], spinning fuselage UAVs [103, 104], or other types of hybrid, transformable, or fast Vertical Take-Off and Landing (VTOL) UAVs. The spinning fuselage UAVs combine hover and fast flight by spinning their wings like a rotor in hover to generate lift. But this requires complex mechanisms to rotate both wings in opposing directions and faces interesting control challenges during the transition.

To optimize flight efficiency, hybrid tail-sitters have several special advantages. They allow to re-use of the propulsion systems in both flight regimes, do not require mass for tilting mechanisms, and they can often re-use wing structures to bear loads of the hovering propulsion instead of needing additional structures. Reducing the mass plays a role in role in both efficiency and safety.

The first tail-sitter UAVs were combinations of fixed-pitch quad-copters and a flying wing. This led to concepts such as the Quadshot [88, 105, 106] (Figure 1.3f). These platforms had four propellers and typically two aerodynamic actuators for forward flight. A lot of structural variations have been tried [105]. While being technically simple, their single-size fixed-pitch propellers make it theoretically im-

possible to be very efficient in both hovering and forward flight. To address this problem, some platforms used two sets of propellers with different properties with large low pitch propellers for hover and small high pitch propellers optimized for the fast forward flight [89] (Figure 1.3g). The large main hovering propellers fold during fast flight. A downside is that using two types of propellers makes the yaw control by torque variation impossible [107]. Yaw control then has to be done by aerodynamic actuators on the wing which have very low effectiveness during hover, or by rotating the tip motors at the cost of added structural weight.

To reduce the number of moving parts and actuators and hereby decrease the complexity and the system weight, several researchers have investigated a tail-sitter concept with only two motors and two aerodynamic actuators (e.g. Cyclone [91] shown in Figure 1.3h). Aerodynamically efficient delta-wings were also converted to tail-sitters by adding 2 motors [108]. They showed that while being efficient in forward flight, the hover had lower control authority and disturbance rejection than quadrotor-based tail-sitters. At the other end of the spectrum, Verling *et al.* [92] have designed a platform with relatively larger motors and a minimalistic wing, which increases the control authority in hover at the expense of forward flight efficiency (Figure 1.3i). But good controllability and efficiency in both hover and fast flight could not be achieved simultaneously. Instead of using a reflexed stable airfoil or delta wings, Ke *et al.* [109] proposed a concept with a vertical and horizontal stabilizer to have more freedom in the selection of the main wing airfoils. While this can improve flight performance during fast flight, it comes at the cost of ground stability after landing and increased gust sensitivity in pitch during hover. Although lighter, simpler, and theoretically more efficient than the four motor hybrid concepts, the two motor concepts still suffer from the fact that fixed pitch propellers cannot be efficient during both hover and fast flight. To address this, variable pitch propellers were used in twin-motor tailsitter UAVs [110]. This makes it possible to improve fast flight efficiency but comes at the expense of two extra actuators to control the pitch and adds the weight and fragility of the mechanisms. All versions of the dual-motor tail-sitter use aerodynamic actuators for pitch and yaw. These actuators have a control effectiveness that is highly dependent on the amount of air that passes over the aerodynamic surfaces. In hover, only the down-wash from the propellers passes over these control surfaces. This creates relatively small moments compared to the moments induced by turbulence on the entire wing. Meanwhile, during fast forward flight, the aerodynamic surfaces become very effective from all the air that passes over them. This requires the controller to use a good model or have a wide range of gains that depend on airspeed. In the case of fast descent from a hover with air flowing in the reverse direction over the wing, there is even a point where the platform becomes un-controllable when this reversed flow from the descend cancels out the downward flow of the propellers [111].

Further reducing the number of propellers to only one creates the need for at least three aerodynamic actuators to maintain full attitude control. Knoebel and McLain [112] use a delta-wing and Matsumoto *et al.* [113] a conventional fixed-wing with a single fixed-pitch propeller upfront and have shown successful hover. But, the single propeller creates a torque that must be compensated with aerody-

1

namic actuators. This reduces the maximum perturbation they can handle. To solve the torque problem, Escareno *et al.* [114] proposed to use a coaxial dual propeller system. Canceling each other's torque also results in slightly higher aerodynamic propulsion efficiency at the cost of an extra motor and coaxial system [115]. These concepts still suffer from the effects linked to their fixed-pitch propellers and aerodynamic control surfaces. This limits their ability to handle strong turbulence while hovering and reduces their flight efficiency during either hover or fast flight.

Therefore this research will investigate the design of a single rotor (theoretic optimum for propulsion) tailsitter (minimum-mass) with not only variable pitch to maintain efficiency in hover and forward flight, but also cyclic blade control like conventional helicopters to create rapid large attitude control moments to improve the hover control in real-world conditions: the DelftaCopter (Figure 1.3k).

1.3. Hover and fast flight with hydrogen

Even with very efficient aircraft, energy remains a bottleneck. While battery technology is being pushed further every year [116], the gap between battery-powered UAVs and biological fliers remains very large [117]. For long-distance applications of minimum-mass flying robots, novel energy sources are required [118]. Possible solutions include refueling, energy harvesting in the broadest sense of the word [119–122], or beaming energy to UAVs with microwave [123] or lasers [73]. The drone delivery market would for instance benefit from hovering flight combined with longer ranges to deliver their goods (e.g. Amazon Prime Air Figure 1.3j). This led to patents protecting their energy solutions [93]. And while solar energy can be very promising in some niche applications like high altitude long endurance flight, many applications still require the UAV to carry all their energy upon take-off.

One promising fuel to drive electrically driven flying robots is hydrogen thanks to its availability, power density, and potential for environmental friendliness [124]. Hydrogen is abundant, can be created off-grid using solar energy [125], and, given a certain size threshold, has a higher energy density than any available battery technology [126]. But while hydrogen-powered hovering platforms have been tested [127], the vast majority of hydrogen-powered UAVs consists of fixed-wings which can not hover [128–134]. Very few aircraft that can hover and fly long-endurance missions have been able to use hydrogen as fuel. Hydrogen brings a new set of shape, power, system, and safety requirements, which influence the design of the flying robot using it. This research proposes a solution that maximizes safety and controllability while minimizing mass and demonstrating the mission capabilities (The Nederdrone concept is shown in Figure 1.3l).

1.4. GPS-denied hover and fast flight near obstacles

Whenever combined hover and fast flight is required closer to obstacles or in GPS-denied environments, the paradigm shifts from an efficiency or energy problem to a navigation, situation awareness, and path-planning problem. The mainstream autonomous GPS-denied sensing and navigation is done with larger multicopters carrying 2D scanning lasers [135, 143] (Figure 1.4a), stereo vision [144] or monoc-

(a) Pelican [135, 136]   (b) Pelican with Kinect [137]   (c) Pixhawk Cheetah [138]   (d) KMel Nano+ [139]

(e) Asctec [140]   (f) Indoor fixedwing [141]   (g) Je-vois trashcan [142]   (h) Racer-AI
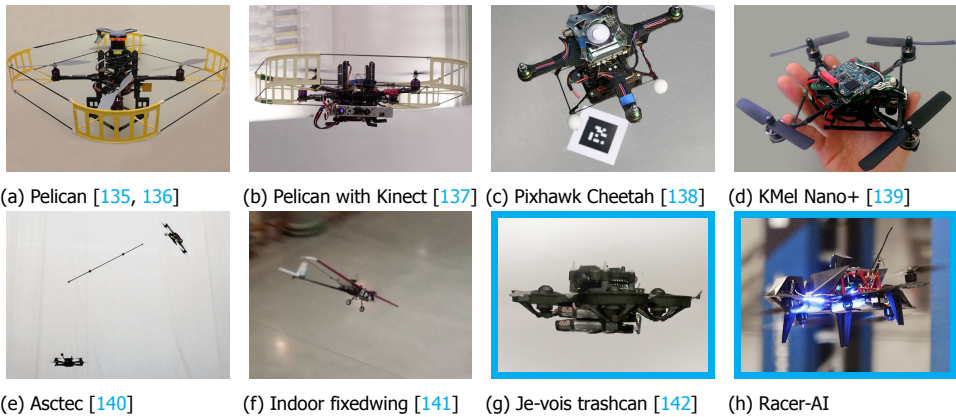
Figure 1.4: Examples of research on GPS-denied navigation close to obstacles. The flying robot in the blue box is proposed in this research.

ular depth map estimation hardware [145]. Other researchers used a depth camera like the Microsoft Kinect [137] (Figure 1.4b) or external aids like ArUco markers detected by a single camera [138] (Figure 1.4c). While camera-based stable flight has been demonstrated on smaller platforms [139] (Figure 1.4d), the state-of-the-art indoor navigation and obstacle avoidance solutions were performed on larger quadcopters with reduced maneuverability and important safety considerations when operating close to people. At higher speeds, Bry *et al.* [141] demonstrated navigation and avoidance of their fixed-wing in a large Global Positioning System (GPS) denied environment (Figure 1.4f). But fixed-wing aircraft require a large room to fly and can't hover to explore small indoor spaces or perform inspections.
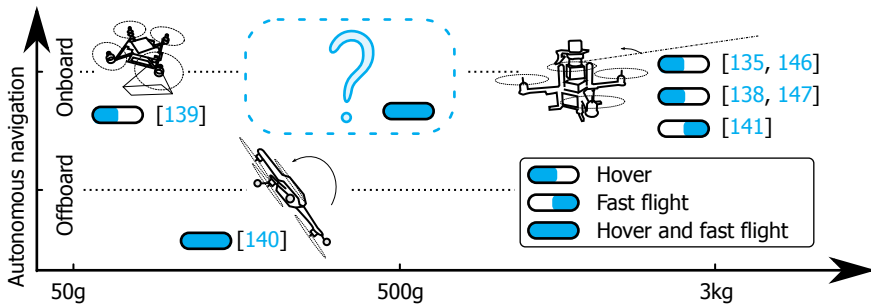
Figure 1.5: Fast GPS-denied navigation of flying robots near obstacles based on light onboard processing remains a challenge.

When the processing is done off-board, quadcopters have been shown to combine hover and fast flight with amazing maneuverability like flying through narrow vertical gaps [148] or even juggling with poles [140] (Figure 1.4e). Although this demonstrates the future promises of flying robots, the offboard processing and absence of payload limit their current use as mission-capable flying robots in unknown

1

environments.

Overall, developing minimum-mass, mission-capable flying robots with onboard autonomous navigation that combine hover and very fast flight near obstacles in GPS-denied environments remains a challenge (See Figure 1.5). Not only does fast flight near obstacles require state-of-the-art navigation capabilities, but to increase the speed, the sensing and processing must become faster and lighter. To address this, this research proposes a novel high-speed but computationally minimalistic monocular Artificial-Intelligence (AI) based navigation solution to fly near known obstacles in a GPS-denied environment. The solution extends previous own work of a 72-gram indoor racing drone [142] (Figure 1.4g) and describes the solution that won the 2019 autonomous drone racing world championship season (Figure 1.4h).

1.5. Problem statement and research questions

In an increasing number of applications, UAVs must be highly automated to improve scalability and cost-effectiveness. Moreover, these *flying robots* need both hovering and fast flight capabilities to perform inspections or deliveries while traveling large distances or reaching destinations quickly. The requirements for both are conflicting, and performing this trade-off from several perspectives forms the main thread through this thesis.

Additionally, to allow the flying robots to fly closer to humans and in populated areas, it is crucial to reduce the risks to acceptably low levels [149]. While aviation safety is a particularly complex topic especially in a quickly evolving world [150], three main approaches can be followed to reduce risks.
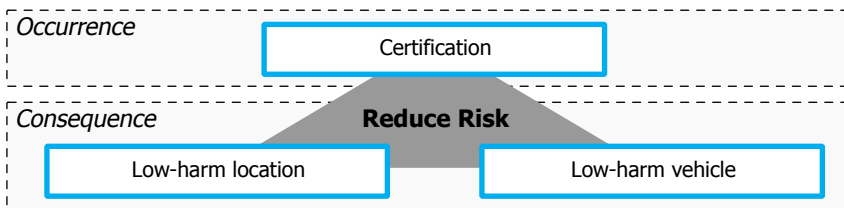
Figure 1.6: Three directions to reduce risk.

Traditionally in aviation, a lot of effort is put into certification with the intent to reduce occurrences of failures (Figure 1.6 top). In the case of UAVs where damage to the platform does not necessarily have the same life-threatening effects, new options can arise. Model remote-controlled aircraft regulations, for instance, focus on selecting remote locations far from people (Figure 1.6 bottom left). A third direction consists of making low-harm vehicles in which, given a fixed mission, one of the principal components that scale the consequences of a mishap is the total mass (Figure 1.6 bottom right). This leads to the secondary objectives through this research: reducing the mass of flying robots while maintaining the mission capabilities. Reducing the mass of mission-capable flying robots brings stringent additional challenges. One particular challenge is that, as aircraft become smaller, the same mission profile appears larger with regards to the size of the vehicle. This

reinforces the need to fly at high speed, which reinforces the primary objective. Overall it leads to the following problem statement:

Problem Statement

How can minimum-mass, mission-capable flying robots combine hover and fast flight?

The problem statement can be approached from several perspectives. The first approach is to investigate the limits of mass-minimization while maintaining autonomous flight capabilities. Several applications, and in particular indoor applications (Figure 1.1), envision flight close to humans and would benefit from the creation of very low-harm flying robots through the minimization of mass. This leads to the first research question:

Research Question 1

How light can minimum-mass flying robots be created that combine hover and fast flight for autonomous exploration missions?

This research question led to the development of very lightweight stable flapping wing robots. However, these robots are affected by turbulence, drafts, and wind. To perform real-world missions, very light flying robots need to maximize their gust response and their fast flight capabilities while maintaining the hover capabilities needed to perform up-close inspections and spot landings. This leads to the second research question:

Research Question 2

How can sensitivity to gusts be reduced and controllability increased in light flapping-wing robots?

When the flight endurance or maximum speed become bottlenecks for a given mission, the minimal mass of a flying robot is obtained by maximizing its efficiency [80]. Although highly promising especially at low Reynolds numbers [151], at larger sizes and speeds, flapping-wing robots do not yet reach the same efficiencies as rotors and wings. Classical propulsion theory dictates that the most efficient propulsion is achieved by a single large rotor while efficient forward flight is best achieved with high aspect ratio wings [78]. Combining both leads to the third research question:

Research Question 3

How can an efficient hover and an efficient forward flight be combined using a single rotor and high aspect ratio wings?

1

To further increase the range and endurance of flying robots, only maximizing efficiency does not suffice. The weight of the required energy remains the largest bottleneck and drives the search for concepts that safely fly with higher density energy sources. Hydrogen was identified as a promising energy source for electric flying robots. But creating a hydrogen-powered flying robot capable of hover and fast flight brings novel challenges and has led to the fourth research question:

> **Research Question 4**
>
> How can electrically powered flying robots capable of hover and fast flight be designed to use pressurized hydrogen as their energy source?

While endurance and maximum flight speed in large blocks of segregated airspace are mainly efficiency and energy challenges, in the presence of obstacles, the maximum speed at which a robot can fly mainly becomes a sensing, processing, and control challenge. The applications include quickly bringing an Automated External Defibrillator (AED) device to a person in need while avoiding all encountered obstacles [152]. One extreme example that is pushing the speed of drones near obstacles is found in autonomous indoor drone racing where flying robots need to traverse an obstacle course as rapidly as possible [153]. The maximum speed is typically not yet determined by aerodynamic limits but mainly by the performance of the situation awareness and control. By developing fast and robust but light and computationally efficient solutions, the robot size can be kept to a minimum to benefit safety. This has driven the final research question:

> **Research Question 5**
>
> How can very fast forward flight through gates be achieved in a GPS denied environment with minimal processing and training time?

1.6. Scope and Limitations

To focus on the different perspectives of the problem statement given by the research questions, several limitations are in place. A top-down approach to miniaturization is followed keeping in mind to always obtain a real-world mission capable platform. For the scope of this thesis, a mission is defined as being able to perform visual observation tasks and a UAV becomes a robot when it can automatically navigate and interact with the world using cameras. Practical constraints like opening doors, flying in total darkness, loss of communication links while exploring buildings, manufacturability, and cost are not (or only partially) taken into account. In all flying robots, the scope is limited to heavier than air machines with propulsion by electric motors. No explicit weight limitations are imposed but the desire to achieve a minimal mass is always kept in mind. All robots are tested either in competition environments or in demonstration missions for third parties to realistically assess their potential.
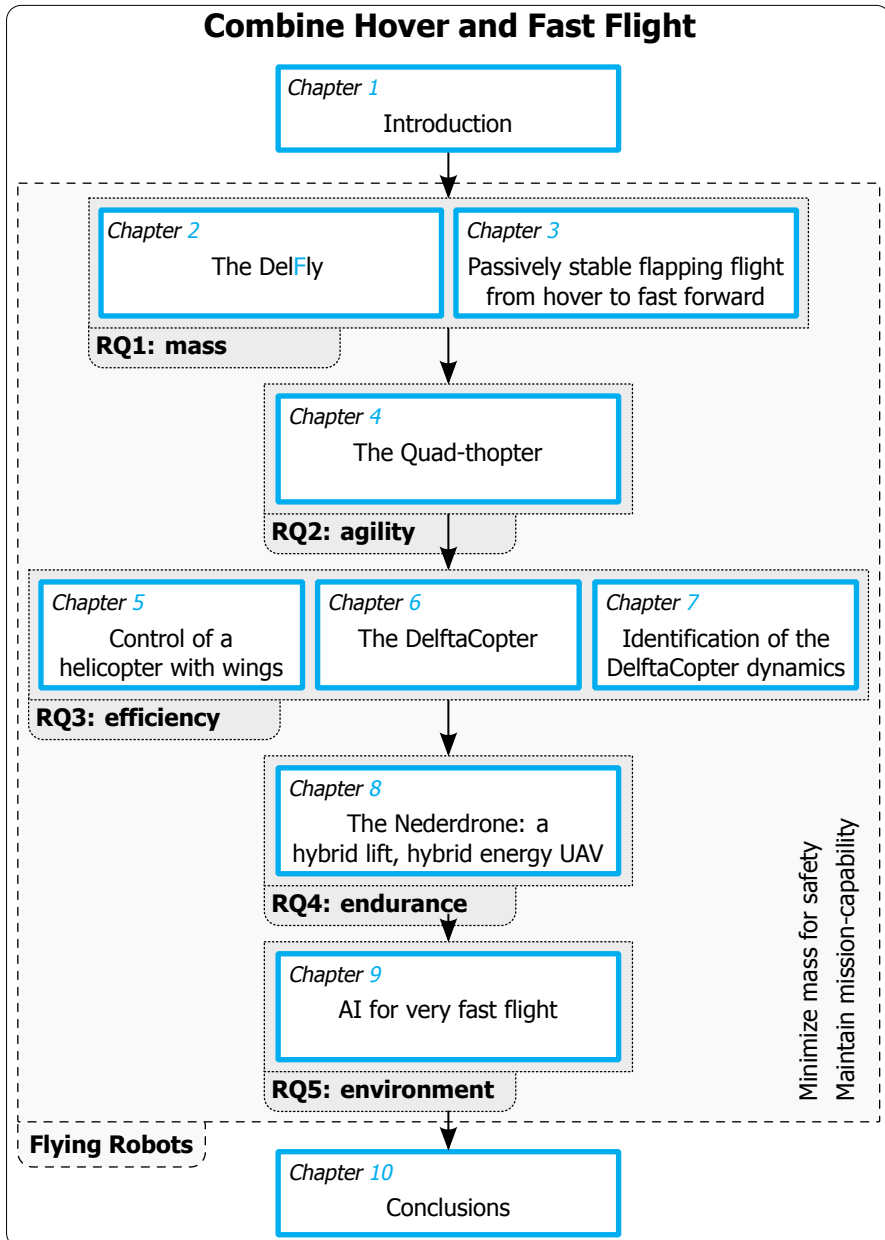
1

Figure 1.7: Outline of the thesis focusing on different aspects (mass, agility, efficiency, endurance, and environment) of real-world mission-capable flying robots while stretching their flight envelope from hover to fast forward flight.

1.7. Outline

The following chapters answer these five research questions as illustrated in Figure 1.7. Chapter 2 presents the development of a passively stable 20 g indoor reconnaissance robot, which became the lightest autonomous indoor exploration robot able to fly in non-prepared rooms based on onboard sensors. The chapter identifies the capabilities and shortcomings of the platform. Then Chapter 3 offers a solution to the conflicting stability requirements of combining stable slow hovering flight and fast flight in flapping wing vehicles. Together they address **RQ1**. To increase controllability and sensitivity to gusts requirements of **RQ2** while maintaining simple construction principles, a new flapping-wing concept called "quad-thopter" is proposed in Chapter 4. To maximize propulsion and forward flight efficiency from **RQ3**, a helicopter rotor is equipped with wings to in Chapter 5. The chapter investigates the uncommon control properties of this novel type of tailsitter UAV in simulation and proposes a control strategy for the inner-loop. To verify the real-world performance, this so-called DelftaCopter is tested in a competition in Chapter 6. Finally, Chapter 7 proposes a strategy to identify the unstable DelftaCopter's dynamics from flight data. To achieve very long endurance flights from a ship, a novel platform is developed around a hydrogen pressure cylinder with fuel-cell and tested in Chapter 8 to address **RQ4**. Finally, increasing forward flight speed in a constrained, obstacle-packed, and GPS-denied environments is linked to lightweight Artificial Intelligence (AI) in Chapter 9, which is proposing an answer to **RQ5**.

References

[1] D. Floreano and R. J. Wood, *Science, technology and the future of small autonomous drones,* Nature **521**, 460 (2015).

[2] W. W. Greenwood, J. P. Lynch, and D. Zekkos, *Applications of UAVs in civil infrastructure,* Journal of Infrastructure Systems **25**, 04019002 (2019).

[3] M. Hassanalian and A. Abdelkefi, *Classifications, applications, and design challenges of drones: A review,* Progress in Aerospace Sciences **91**, 99 (2017).

[4] M. Freeman, M. Kashani, and P. Vardanega, *Aerial robotic technologies for civil engineering: established and emerging practice,* Journal of Unmanned Vehicle Systems **9**, 75 (2021).

[5] G. Pajares, *Overview and current status of remote sensing applications based on unmanned aerial vehicles (UAVs),* Photogrammetric Engineering & Remote Sensing **81**, 281 (2015).

[6] R. D'Andrea, *Guest editorial can drones deliver?* IEEE Transactions on Automation Science and Engineering **11**, 647 (2014).

[7] S. Kim, S. Choi, and H. J. Kim, *Aerial manipulation using a quadrotor with a two dof robotic arm,* in *2013 IEEE/RSJ International Conference on Intelligent Robots and Systems* (IEEE, 2013) pp. 4990–4995.

[8] S. Hamaza, I. Georgilas, M. Fernandez, P. Sanchez, T. Richardson, G. Heredia, and A. Ollero, *Sensor installation and retrieval operations using an unmanned aerial manipulator,* IEEE Robotics and Automation Letters **4**, 2793 (2019).

[9] D. Mellinger, M. Shomin, N. Michael, and V. Kumar, *Cooperative grasping and transport using multiple quadrotors,* in *Distributed autonomous robotic systems* (Springer, Berlin, Heidelberg, 2013) pp. 545–558.

[10] T. Rakha and A. Gorodetsky, *Review of unmanned aerial system (UAS) applications in the built environment: Towards automated building inspection procedures using drones,* Automation in Construction **93**, 252 (2018).

[11] P. Lottes, R. Khanna, J. Pfeifer, R. Siegwart, and C. Stachniss, *Uav-based crop and weed classification for smart farming,* in *2017 IEEE International Conference on Robotics and Automation (ICRA)* (IEEE, Singapore, 2017) pp. 3024–3031.

[12] U. R. Mogili and B. Deepak, *Review on application of drone systems in precision agriculture,* Procedia Computer Science **133**, 502 (2018).

[13] A. Barrientos, J. Colorado, J. d. Cerro, A. Martinez, C. Rossi, D. Sanz, and J. Valente, *Aerial remote sensing in agriculture: A practical approach to area coverage and path planning for fleets of mini aerial robots,* Journal of Field Robotics **28**, 667 (2011).

[14] A. L. Virk, M. A. Noor, S. Fiaz, S. Hussain, H. A. Hussain, M. Rehman, M. Ahsan, and W. Ma, *Smart farming: An overview,* in *Smart Village Technology* (Springer International Publishing, 2020) pp. 191–201.

[15] G. Zhou, J. Yuan, I.-L. Yen, and F. Bastani, *Robust real-time uav based power line detection and tracking,* in *2016 IEEE International Conference on Image Processing (ICIP)* (IEEE, 2016) pp. 744–748.

[16] A. Singh, D. Patil, and S. Omkar, *Eye in the sky: Real-time drone surveillance system (dss) for violent individuals identification using scatternet hybrid deep learning network,* in *Proceedings of the IEEE Conference on Computer Vision and Pattern Recognition (CVPR) Workshops* (IEEE, Salt Lake City, UT, USA, 2018) pp. 1710–1718.

[17] J. J. Boutilier, S. C. Brooks, A. Janmohamed, A. Byers, J. E. Buick, C. Zhan, A. P. Schoellig, S. Cheskes, L. J. Morrison, and T. C. Y. Chan, *Optimizing a drone network to deliver automated external defibrillators,* Circulation **135**, 2454 (2017).

[18] B. M. Bogle, W. D. Rosamond, K. T. Snyder, and J. K. Zègre-Hemsey, *The case for drone-assisted emergency response to cardiac arrest,* North Carolina Medical Journal **80**, 204 (2019).

1

[19] M. Beul, D. Droeschel, M. Nieuwenhuisen, J. Quenzel, S. Houben, and S. Behnke, *Fast autonomous flight in warehouses for inventory applications,* IEEE Robotics and Automation Letters **3**, 3121 (2018).

[20] R. Siddall and M. Kovač, *Launching the AquaMAV: bioinspired design for aerial–aquatic robotic platforms,* Bioinspiration & Biomimetics **9**, 031001 (2014).

[21] M. Radotich, S. Withrow-Maser, Z. deSouza, S. Gelhar, and H. Gallagher, *A study of past, present, and future mars rotorcraft,* in *9th Biennial Autonomous VTOL Technical Meeting* (2021).

[22] R. A. Clothier, B. P. Williams, and N. L. Fulton, *Structuring the safety case for unmanned aircraft system operations in non-segregated airspace,* Safety science **79**, 213 (2015).

[23] E. Vattapparamban, I. Guvenc, A. I. Yurekli, K. Akkaya, and S. Uluagac, *Drones for smart cities: Issues in cybersecurity, privacy, and public safety,* in *2016 International Wireless Communications and Mobile Computing Conference (IWCMC)* (IEEE, 2016).

[24] B. Rattanagraikanakorn, D. I. Gransden, M. Schuurman, C. De Wagter, R. Happee, A. Sharpanskykh, and H. A. P. Blom, *Multibody system modelling of unmanned aircraft system collisions with the human head,* International Journal of Crashworthiness **25**, 689 (2019).

[25] R. Wood, B. Finio, M. Karpelson, K. Ma, N. Pérez-Arancibia, P. Sreetharan, H. Tanaka, and J. Whitney, *Progress on 'pico' air vehicles,* The International Journal of Robotics Research **31**, 1292 (2012).

[26] V. Kumar and N. Michael, *Opportunities and challenges with autonomous micro aerial vehicles,* The International Journal of Robotics Research **31**, 1279 (2012).

[27] A. Santhanakrishnan and J. Jacob, *Effect of regular surface perturbations on flow over an airfoil,* in *35th AIAA Fluid Dynamics Conference and Exhibit* (American Institute of Aeronautics and Astronautics, 2005) pp. 1–17.

[28] F. Ruffier, S. Viollet, S. Amic, and N. Franceschini, *Bio-inspired optical flow circuits for the visual guidance of micro air vehicles,* in *Proceedings of the 2003 International Symposium on Circuits and Systems, 2003. ISCAS 03.* (IEEE, 2003).

[29] R. Wootton, *From insects to microvehicles,* Nature **403**, 144 (2000).

[30] D. Floreano, J.-C. Zufferey, M. V. Srinivasan, and C. Ellington, eds., *Flying Insects and Robots* (Springer Berlin Heidelberg, 2010).

[31] Y. LeCun, Y. Bengio, and G. Hinton, *Deep learning,* Nature **521**, 436 (2015).

[32] R. J. Wootton, *Palaeozoic insects,* Annual Review of Entomology **26**, 319 (1981).

[33] J. M. Birch, *Force production and flow structure of the leading edge vortex on flapping wings at high and low reynolds numbers,* Journal of Experimental Biology **207**, 1063 (2004).

[34] D. D. Chin and D. Lentink, *Flapping wing aerodynamics: from insects to vertebrates,* The Journal of Experimental Biology **219**, 920 (2016).

[35] A. Ramezani, S.-J. Chung, and S. Hutchinson, *A biomimetic robotic platform to study flight specializations of bats,* Science Robotics **2**, eaal2505 (2017).

[36] M. H. Dickinson and F. T. Muijres, *The aerodynamics and control of free flight manoeuvres in drosophila,* Philosophical Transactions of the Royal Society B: Biological Sciences **371**, 20150388 (2016).

[37] G. Nalbach, *The halteres of the blowfly calliphora,* Journal of Comparative Physiology A **173**, 293 (1993).

[38] R. Hengstenberg, *Controlling the fly's gyroscopes,* Nature **392**, 757 (1998).

[39] W. Wu, R. Wood, and R. Fearing, *Halteres for the micromechanical flying insect,* in *Proceedings 2002 IEEE International Conference on Robotics and Automation (Cat. No.02CH37292)* (IEEE, Washington, DC, USA, 2002) pp. 60–65.

[40] G. K. Taylor and H. G. Krapp, *Sensory systems and flight stability: What do insects measure and why?* in *Advances in Insect Physiology* (Elsevier, 2007) pp. 231–316.

[41] H. Wagner, *Flow-field variables trigger landing in flies,* Nature **297**, 147 (1982).

[42] C. Evangelista, P. Kraft, M. Dacke, J. Reinhard, and M. V. Srinivasan, *The moment before touchdown: landing manoeuvres of the honeybee apis mellifera,* Journal of Experimental Biology **213**, 262 (2009).

[43] J. S. Chahl, M. V. Srinivasan, and S. W. Zhang, *Landing strategies in honeybees and applications to uninhabited airborne vehicles,* The International Journal of Robotics Research **23**, 101 (2004).

[44] M. Srinivasan, S. Zhang, M. Lehrer, and T. Collett, *Honeybee navigation en route to the goal: visual flight control and odometry,* Journal of Experimental Biology **199**, 237 (1996), https://jeb.biologists.org/content/199/1/237.full.pdf .

[45] F. T. Muijres, M. J. Elzinga, J. M. Melis, and M. H. Dickinson, *Flies evade looming targets by executing rapid visually directed banked turns,* Science **344**, 172 (2014).

1

[46] C. Schilstra and J. H. van Hateren, *Stabilizing gaze in flying blowflies,* Nature **395**, 654 (1998).

[47] C. P. Ellington, C. van den Berg, A. P. Willmott, and A. L. R. Thomas, *Leading-edge vortices in insect flight,* Nature **384**, 626 (1996).

[48] M. H. Dickinson, *Wing rotation and the aerodynamic basis of insect flight,* Science **284**, 1954 (1999).

[49] F. T. Muijres, L. C. Johansson, R. Barfield, M. Wolf, G. R. Spedding, and A. Hedenstrom, *Leading-edge vortex improves lift in slow-flying bats,* Science **319**, 1250 (2008).

[50] M. Karásek, *Good vibrations for flapping-wing flyers,* Science Robotics **5**, eabe4544 (2020).

[51] D. Lentink, U. K. Müller, E. J. Stamhuis, R. de Kat, W. van Gestel, L. L. M. Veld-huis, P. Henningsson, A. Hedenström, J. J. Videler, and J. L. van Leeuwen, *How swifts control their glide performance with morphing wings,* Nature **446**, 1082 (2007).

[52] N. Franceschini, S. Viollet, F. Ruffier, and J. Serres, *Neuromimetic robots inspired by insect vision,* Advances in Science and Technology **58**, 127 (2008).

[53] H. Eichner, M. Joesch, B. Schnell, D. F. Reiff, and A. Borst, *Internal structure of the fly elementary motion detector,* Neuron **70**, 1155 (2011).

[54] D. Silver, A. Huang, C. J. Maddison, A. Guez, L. Sifre, G. Van Den Driessche, J. Schrittwieser, I. Antonoglou, V. Panneershelvam, M. Lanctot, and Others, *Mastering the game of Go with deep neural networks and tree search,* Nature **529**, 484 (2016).

[55] B. Illing, W. Gerstner, and J. Brea, *Biologically plausible deep learning – but how far can we go with shallow networks?* Neural Networks **118**, 90 (2019), 1905.04101 .

[56] P. A. Merolla, J. V. Arthur, R. Alvarez-Icaza, A. S. Cassidy, J. Sawada, F. Akopyan, B. L. Jackson, N. Imam, C. Guo, Y. Nakamura, B. Brezzo, I. Vo, S. K. Esser, R. Appuswamy, B. Taba, A. Amir, M. D. Flickner, W. P. Risk, R. Manohar, and D. S. Modha, *A million spiking-neuron integrated circuit with a scalable communication network and interface,* Science **345**, 668 (2014).

[57] K. Bai, J. Li, K. Hamedani, and Y. Yi, *Enabling an new era of brain-inspired computing: Energy-efficient spiking neural network with ring topology,* in *2018 55th ACM/ESDA/IEEE Design Automation Conference (DAC)* (IEEE, 2018).

[58] S. Kim, S. Park, B. Na, and S. Yoon, *Spiking-YOLO: Spiking neural network for energy-efficient object detection,* Proceedings of the AAAI Conference on Artificial Intelligence **34**, 11270 (2020).

[59] S. S. Radhakrishnan, A. Sebastian, A. Oberoi, S. Das, and S. Das, *A biomimetic neural encoder for spiking neural network,* Nature Communications **12** (2021), 10.1038/s41467-021-22332-8.

[60] K. Ma, P. Chirarattananon, S. Fuller, and R. Wood, *Controlled flight of a biologically inspired, insect-scale robot.* Science **340**, 603 (2013).

[61] N. T. Jafferis, E. F. Helbling, M. Karpelson, and R. J. Wood, *Untethered flight of an insect-sized flapping-wing microscale aerial vehicle,* Nature **570**, 491 (2019).

[62] M. Kovac, A. Guignard, J.-D. Nicoud, J.-C. Zufferey, and D. Floreano, *A 1.5g SMA-actuated microglider looking for the light,* in *Proceedings 2007 IEEE International Conference on Robotics and Automation* (IEEE, 2007).

[63] M. Keennon and J. Grasmeyer, *Development of two MAVs and vision of the future of MAV design,* in *AIAA International Air and Space Symposium and Exposition: The Next 100 Years* (American Institute of Aeronautics and Astronautics, 2003).

[64] J.-C. Zufferey, A. Klaptocz, A. Beyeler, J.-D. Nicoud, and D. Floreano, *A 10-gram vision-based flying robot,* Advanced Robotics **21**, 1671 (2007).

[65] M. Keennon, K. Klingebiel, H. Won, and A. Andriukov, *Development of the nano hummingbird: A tailless flapping wing micro air vehicle,* in *50th AIAA Aerospace Sciences Meeting including the New Horizons Forum and Aerospace Exposition* (American Institute of Aeronautics and Astronautics, 2012) pp. 1–24.

[66] C. De Wagter, S. Tijmons, B. D. W. Remes, and G. C. H. E. de Croon, *Autonomous flight of a 20-gram flapping wing mav with a 4-gram onboard stereo vision system,* in *Robotics and Automation (ICRA), 2014 IEEE International Conference on* (IEEE, Hong Kong, China, 2014) pp. 4982–4987.

[67] L. Petricca, P. Ohlckers, and C. Grinde, *Micro- and nano-air vehicles: State of the art,* International Journal of Aerospace Engineering **2011**, 1 (2011).

[68] J. A. Roll, B. Cheng, and X. Deng, *Design, fabrication, and experiments of an electromagnetic actuator for flapping wing micro air vehicles,* in *2013 IEEE International Conference on Robotics and Automation* (IEEE, 2013).

[69] S. Felton, M. Tolley, E. Demaine, D. Rus, and R. Wood, *A method for building self-folding machines,* Science **345**, 644 (2014).

[70] S. B. Fuller, M. Karpelson, A. Censi, K. Y. Ma, and R. J. Wood, *Controlling free flight of a robotic fly using an onboard vision sensor inspired by insect ocelli,* Journal of The Royal Society Interface **11**, 20140281 (2014).

1

[71] S. Fuller, E. Helbling, P. Chirarattananon, and R. Wood, *Using a gyroscope to stabilize the attitude of a fly-sized hovering robot,* in *International Micro Air Vechicle Competition and Conference 2014* (Delft, The Netherlands, 2014) pp. 102–109.

[72] E. F. Helbling, S. B. Fuller, and R. J. Wood, *Pitch and yaw control of a robotic insect using an onboard magnetometer,* in *2014 IEEE International Conference on Robotics and Automation (ICRA)* (IEEE, Hong Kong, China, 2014) pp. 5516–5522.

[73] J. James, V. Iyer, Y. Chukewad, S. Gollakota, and S. B. Fuller, *Liftoff of a 190 mg laser-powered aerial vehicle: The lightest wireless robot to fly,* in *2018 IEEE International Conference on Robotics and Automation (ICRA)* (IEEE, Brisbane, QLD, Australia, 2018) pp. 3587–3594.

[74] T. J. Mueller and J. D. DeLaurier, *Aerodynamics of small vehicles,* Annual Review of Fluid Mechanics **35**, 89 (2003).

[75] M. T. Keennon, A. Andryukov, K. R. Klingebiel, and H. T. Won, *Air vehicle flight mechanism and control method for non-sinusoidal wing flapping,* (2012).

[76] C. W. Reynolds, *Flocks, herds and schools: A distributed behavioral model,* in *Proceedings of the 14th annual conference on Computer graphics and interactive techniques - SIGGRAPH '87* (ACM Press, 1987).

[77] C. Virágh, G. Vásárhelyi, N. Tarcai, T. Szörényi, G. Somorjai, T. Nepusz, and T. Vicsek, *Flocking algorithm for autonomous flying robots,* Bioinspiration & Biomimetics **9**, 025012 (2014).

[78] J. D. Anderson, *Aircraft Performance & Design*, 1st ed., edited by K. T. Kane (WCB McGraw-Hill Education, 1998).

[79] H. Glauert, *Airplane propellers,* in *Aerodynamic theory* (Springer, Berlin, Heidelberg, Berlin, Heidelberg, 1935) pp. 169–360.

[80] J. Roskam and C.-T. E. Lan, *Airplane aerodynamics and performance* (DARcorporation, 1997).

[81] S. B. Anderson, *Historical overview of V/STOL aircraft technology*, techreport 19810010574 (NASA Ames Reseach Center, Moffett Field, CA, United States, 1981).

[82] H. Rosenstein and R. Clark, *Aerodynamic development of the v-22 tilt rotor,* in *Twelfth European Rotorcraft Forum*, 14 (AIAA, Philadelphia, PA, USA, 1986).

[83] P. M. Lovell Jr, R. H. Kibry, and C. C. Smith Jr, *Flight Investigation of the Stability and Control Characteristics of a 0.13-Scale Model of the Convair XFY-1 Vertically Rising Airplane During Constant-Altitude Transitions*, techreport 20050029472 (TED No. NACA DE 368, Langley Field, VA, 1953).

[84] J. K. Gunarathna and R. Munasinghe, *Development of a quad-rotor fixed-wing hybrid unmanned aerial vehicle,* in *2018 Moratuwa Engineering Research Conference (MERCon)* (IEEE, Moratuwa, Sri Lanka, 2018) pp. 72–77.

[85] F.-P. Thamm, N. Brieger, K.-P. Neitzke, M. Meyer, R. Jansen, and M. Mönninghof, *Songbird - an innovative uas combining the advantages of fixed wing and multi rotor uas,* ISPRS - International Archives of the Photogrammetry, Remote Sensing and Spatial Information Sciences **XL-1/W4**, 345 (2015).

[86] P. Hartmann, M. Schütt, and D. Moormann, *Control of departure and approach maneuvers of tiltwing VTOL aircraft,* in *AIAA Guidance, Navigation, and Control Conference* (American Institute of Aeronautics and Astronautics, 2017) pp. 1–18.

[87] M. Hochstenbach, C. Notteboom, B. Theys, and J. De Schutter, *Design and Control of an Unmanned Aerial Vehicle for Autonomous Parcel Delivery with Transition from Vertical Take-off to Forward Flight -VertiKUL, a Quadcopter Tailsitter,* International Journal of Micro Air Vehicles **7**, 395 (2015).

[88] P. Sinha, P. Esden-Tempski, C. Forrette, J. Gibboney, and G. Horn, *Versatile, modular, extensible vtol aerial platform with autonomous flight mode transitions,* in *IEEE Aerospace Conference* (IEEE, Big Sky, MT, USA, 2012) pp. 1–17, 3-10 March 2012.

[89] S. Hulsman, J. De Groot, and D. Dokter, *Atmos uav; high-tech startup with game-changing ideas,* Leonardo Times **18** (2014).

[90] M. Bronz, E. Smeur, and H. de Marina, *Development of A Fixed-Wing mini UAV with Transitioning Flight Capability,* in *35th AIAA Applied Aerodynamics Conference* (Denver, Colorado, 2017).

[91] E. J. Smeur, M. Bronz, and G. C. de Croon, *Incremental control and guidance of hybrid aircraft applied to a tailsitter unmanned air vehicle,* Journal of Guidance, Control, and Dynamics , 1 (2019).

[92] S. Verling, B. Weibel, M. Boosfeld, K. Alexis, M. Burri, and R. Siegwart, *Full attitude control of a VTOL tailsitter UAV,* in *Robotics and Automation (ICRA), 2016 IEEE International Conference on*, IEEE (IEEE, Stockholm, Sweden, 2016) pp. 3006–3012.

[93] B. C. Beckman, A. Navot, D. Buchmueller, G. Kimchi, F. Hensel, S. A. Green, B. W. Porter, and S. S. J.-M. Rault, *Electricity generation in automated aerial vehicles,* (2017), uS Patent 9,550,577.

[94] G. Flores and R. Lozano, *Lyapunov-based controller using singular perturbation theory: An application on a mini-uav,* in *2013 American Control Conference* (IEEE, Washington, DC, USA, 2013) pp. 1596–1601.

1

1

[95] D. Orbea, J. Moposita, W. G. Aguilar, M. Paredes, R. P. Reyes, and L. Montoya, *Vertical take off and landing with fixed rotor,* in *2017 CHILEAN Conference on Electrical, Electronics Engineering, Information and Communication Technologies (CHILECON)* (IEEE, Pucon, Chile, 2017) pp. 1–6.

[96] J. Zhang, Z. Guo, and L. Wu, *Research on control scheme of vertical take-off and landing fixed-wing UAV,* in *2017 2nd Asia-Pacific Conference on Intelligent Robot Systems (ACIRS)* (IEEE, Wuhan, China, 2017) pp. 200–204.

[97] G. R. Flores, J. Escareño, R. Lozano, and S. Salazar, *Quad-tilting rotor convertible MAV: Modeling and real-time hover flight control,* Journal of Intelligent & Robotic Systems **65**, 457 (2011).

[98] L. Yu, D. Zhang, and J. Zhang, *Transition flight modeling and control of a novel tilt tri-rotor UAV,* in *2017 IEEE International Conference on Information and Automation (ICIA)* (IEEE, 2017).

[99] M. Schütt, P. Hartmann, and D. Moormann, *Fullscale windtunnel investigation of actuator effectiveness during stationary flight within the entire flight envelope of a tiltwing mav,* in *International Micro Air Vechicle Competition and Conference 2014*, edited by G. de Croon, E. van Kampen, C. D. Wagter, and C. de Visser (Delft, The Netherlands, 2014) pp. 77–83.

[100] E. Çetinsoy, S. Dikyar, C. Hançer, K. Oner, E. Sirimoglu, M. Unel, and M. Aksit, *Design and construction of a novel quad tilt-wing uav,* Mechatronics **22**, 723 (2012).

[101] E. R. Ulrich, D. J. Pines, and J. S. Humbert, *From falling to flying: the path to powered flight of a robotic samara nano air vehicle,* Bioinspiration & Biomimetics **5**, 045009 (2010).

[102] K. Fregene and C. L. Bolden, *Dynamics and control of a biomimetic single-wing nano air vehicle,* in *Proceedings of the 2010 American Control Conference* (IEEE, Baltimore, MD, USA, 2010) pp. 51–56.

[103] J. E. Low, L. T. S. Win, D. S. B. Shaiful, C. H. Tan, G. S. Soh, and S. Foong, *Design and dynamic analysis of a transformable hovering rotorcraft (THOR),* in *2017 IEEE International Conference on Robotics and Automation (ICRA)* (IEEE, Singapore, 2017) pp. 6389–6396.

[104] D. S. B. Shaiful, L. T. S. Win, J. E. Low, S. K. H. Win, G. S. Soh, and S. Foong, *Optimized transition path of a transformable HOvering rotorcraft (THOR),* in *2018 IEEE/ASME International Conference on Advanced Intelligent Mechatronics (AIM)* (IEEE, Auckland, New Zealand, 2018) pp. 460–465.

[105] A. Oosedo, S. Abiko, A. Konno, T. Koizumi, T. Furui, and M. Uchiyama, *Development of a quad rotor tail-sitter VTOL UAV without control surfaces and experimental verification,* in *2013 IEEE International Conference on Robotics and Automation* (IEEE, 2013) pp. 317–322.

[106] E. J. J. Smeur, Q. P. Chu, G. C. H. E. de Croon, B. Remes, C. De Wagter, and E. van der Horst, *Modelling of a hybrid uav using test flight data,* in *International Micro Air Vehicle Competition and Conference 2014*, edited by G. de Croon, E. J. van Kampen, C. De Wagter, and C. C. de Visser (IMAV, Delft, the Netherlands, 2014) pp. 196–203.

[107] C. De Wagter, D. Dokter, G. C. H. E. de Croon, and B. Remes, *Multi-lifting-device uav autonomous flight at any transition percentage,* in *Proceedings of the EuroGNC 2013, 2nd CEAS Specialist Conference*, edited by J. A. Mulder, D. Choukroun, E. J. van Kampen, C. C. de Visser, and G. J. Looye (Springer Verlag, Delft, the Netherlands, 2013) pp. 1190–1204.

[108] R. Bapst, R. Ritz, L. Meier, and M. Pollefeys, *Design and implementation of an unmanned tail-sitter,* in *Intelligent Robots and Systems (IROS), 2015 IEEE/RSJ International Conference on* (IEEE, 2015) pp. 1885–1890.

[109] Y. Ke, K. Wang, and B. M. Chen, *A preliminary modeling and control framework for a hybrid uav j-lion,* in *International Micro Air Vechicle Competition and Conference 2016*, edited by P. Z. PENG and D. F. LIN (IMAV, Beijing, PR of China, 2016) pp. 28–34.

[110] K. Wong, J. Alfredo Guerrero, D. Lara, and R. Lozano, *Attitude Stabilization in Hover Flight of a Mini Tail-Sitter UAV with Variable Pitch Propeller,* IEEERSJ International Conference on Intelligent Robots and Systems (2007).

[111] M. Itasse, J.-M. Moschetta, Y. Ameho, and R. Carr, *Equilibrium transition study for a hybrid mav,* International Journal of Micro Air Vehicles **3**, 229 (2011).

[112] N. B. Knoebel and T. W. McLain, *Adaptive quaternion control of a miniature tailsitter uav,* in *American Control Conference, 2008*, IEEE (IEEE, Seattle, WA, USA, 2008) pp. 2340–2345.

[113] T. Matsumoto, K. Kita, R. Suzuki, A. Oosedo, K. Go, Y. Hoshino, A. Konno, and M. Uchiyama, *A hovering control strategy for a tail-sitter vtol uav that increases stability against large disturbance,* in *Robotics and Automation (ICRA), 2010 IEEE International Conference on*, IEEE (IEEE, Anchorage, AK, USA, 2010) pp. 54–59.

[114] J. Escareno, R. Stone, A. Sanchez, and R. Lozano, *Modeling and control strategy for the transition of a convertible tail-sitter uav,* in *Proceedings of the European Control Conference 2007*, WeC08.1, IEEE (IEEE, Kos, Greece, 2007) pp. 3385–3390.

[115] J. Escareño, A. Sanchez, O. Garcia, and R. Lozano, *Modeling and global control of the longitudinal dynamics of a coaxial convertible mini-UAV in hover mode,* Journal of Intelligent and Robotic Systems **54**, 261 (2008).

1

[116] Q. Cai, D. Brett, D. Browning, and N. Brandon, *A sizing-design methodology for hybrid fuel cell power systems and its application to an unmanned underwater vehicle,* Journal of Power Sources **195**, 6559 (2010).

[117] A. Hedenström, *Extreme endurance migration: what is the limit to non-stop flight?* PLoS Biol **8**, e1000362 (2010).

[118] M. N. Boukoberine, Z. Zhou, and M. Benbouzid, *A critical review on unmanned aerial vehicles power supply and energy management: Solutions, strategies, and prospects,* Applied Energy **255**, 113823 (2019).

[119] M. Allen, *Autonomous soaring for improved endurance of a small uninhabitated air vehicle,* in *43rd AIAA Aerospace Sciences Meeting and Exhibit* (American Institute of Aeronautics and Astronautics, 2005).

[120] C. White, S. Watkins, E. W. Lim, and K. Massey, *The soaring potential of a micro air vehicle in an urban environment,* International Journal of Micro Air Vehicles **4**, 1 (2012).

[121] V. Bonnin, E. Benard, J.-M. Moschetta, and C. A. Toomer, *Energy-harvesting mechanisms for UAV flight by dynamic soaring,* International Journal of Micro Air Vehicles **7**, 213 (2015).

[122] A. Fisher, M. Marino, R. Clothier, S. Watkins, L. Peters, and J. L. Palmer, *Emulating avian orographic soaring with a small autonomous glider,* Bioinspiration & Biomimetics **11**, 016002 (2015).

[123] B. Strassner and K. Chang, *Microwave power transmission: Historical milestones and system components,* Proceedings of the IEEE **101**, 1379 (2013).

[124] C. Tarhan and M. A. Çil, *A study on hydrogen, the clean energy of the future: Hydrogen storage methods,* Journal of Energy Storage **40**, 102676 (2021).

[125] E. Troncoso, N. Lapeña-Rey, and O. Valero, *Off-grid test results of a solar-powered hydrogen refuelling station for fuel cell powered unmanned aerial vehicles,* International Journal of Hydrogen Energy **39**, 11267 (2014).

[126] Z. Pan, L. An, and C. Wen, *Recent advances in fuel cells based propulsion systems for unmanned aerial vehicles,* Applied Energy **240**, 473 (2019).

[127] M. N. Boukoberine, M. F. Zia, M. Benbouzid, Z. Zhou, and T. Donateo, *Hybrid fuel cell powered drones energy management strategy improvement and hydrogen saving using real flight test data,* Energy Conversion and Management **236**, 113987 (2021).

[128] C. Herwerth, C. Chiang, A. Ko, S. Matsuyama, S. B. Choi, M. Mirmirani, D. Gamble, R. Paul, V. Sanchez, A. Arena, A. Koschany, G. Gu, T. Wankewycz, and P. Jin, *Development of a small long endurance hybrid PEM fuel cell powered UAV,* in *SAE Technical Paper Series* (SAE International, 2007) pp. 1–8.

[129] T. Bradley, B. Moffitt, D. Parekh, and D. Mavris, *Flight test results for a fuel cell unmanned aerial vehicle,* in *45th AIAA Aerospace Sciences Meeting and Exhibit* (American Institute of Aeronautics and Astronautics, 2007) pp. 1–8.

[130] M. K. Furrutter and J. Meyer, *Small fuel cell powering an unmanned aerial vehicle,* in *AFRICON 2009* (IEEE, 2009) pp. 1–6.

[131] T. Kim and S. Kwon, *Design and development of a fuel cell-powered small unmanned aircraft,* International Journal of Hydrogen Energy **37**, 615 (2012).

[132] N. Lapeña-Rey, J. Blanco, E. Ferreyra, J. Lemus, S. Pereira, and E. Serrot, *A fuel cell powered unmanned aerial vehicle for low altitude surveillance missions,* International Journal of Hydrogen Energy **42**, 6926 (2017).

[133] N. Gavrilovic, D. Vincekovic, and J.-M. Moschetta, *A long range fuel cell/soaring uav system for crossing the atlantic ocean,* in *11th International Micro Air Vehicle Competition and Conference*, edited by P. Campoy (IMAV, Madrid, Spain, 2019) pp. 121–131, iMAV2019-16.

[134] E. Özbek, G. Yalin, S. Ekici, and T. H. Karakoc, *Evaluation of design methodology, limitations, and iterations of a hydrogen fuelled hybrid fuel cell mini UAV,* Energy **213**, 118757 (2020).

[135] T. Tomic, K. Schmid, P. Lutz, A. Domel, M. Kassecker, E. Mair, I. Grixa, F. Ruess, M. Suppa, and D. Burschka, *Toward a fully autonomous UAV: Research platform for indoor and outdoor urban search and rescue,* IEEE Robotics & Automation Magazine **19**, 46 (2012).

[136] I. Dryanovski, R. G. Valenti, and J. Xiao, *An open-source navigation system for micro aerial vehicles,* Autonomous Robots **34**, 177 (2013).

[137] W. N. Greene, K. Ok, P. Lommel, and N. Roy, *Multi-level mapping: Real-time dense monocular SLAM,* in *2016 IEEE International Conference on Robotics and Automation (ICRA)* (IEEE, Stockholm, Sweden, 2016) pp. 833–840.

[138] L. Meier, P. Tanskanen, L. Heng, G. H. Lee, F. Fraundorfer, and M. Pollefeys, *PIXHAWK: A micro aerial vehicle design for autonomous flight using onboard computer vision,* Autonomous Robots **33**, 21 (2012).

[139] C. Forster, M. Pizzoli, and D. Scaramuzza, *SVO: Fast semi-direct monocular visual odometry,* in *2014 IEEE International Conference on Robotics and Automation (ICRA)* (IEEE, 2014).

[140] D. Brescianini, M. Hehn, and R. D'Andrea, *Quadrocopter pole acrobatics,* in *2013 IEEE/RSJ International Conference on Intelligent Robots and Systems* (IEEE, 2013).

[141] A. Bry, A. Bachrach, and N. Roy, *State estimation for aggressive flight in GPS-denied environments using onboard sensing,* in *2012 IEEE International Conference on Robotics and Automation* (IEEE, 2012).

1

1

[142] S. Li, E. van der Horst, P. Duernay, C. De Wagter, and G. C. H. E. de Croon, *Visual model-predictive localization for computationally efficient autonomous racing of a 72-gram drone,* Journal of Field Robotics **37**, 667 (2020).

[143] S. Grzonka, G. Grisetti, and W. Burgard, *Towards a navigation system for autonomous indoor flying,* in *2009 IEEE International Conference on Robotics and Automation* (IEEE, 2009).

[144] K. Schmid, P. Lutz, T. Tomić, E. Mair, and H. Hirschmüller, *Autonomous vision-based micro air vehicle for indoor and outdoor navigation,* Journal of Field Robotics **31**, 537 (2014).

[145] K. Ok, D. Gamage, T. Drummond, F. Dellaert, and N. Roy, *Monocular image space tracking on a computationally limited MAV,* in *2015 IEEE International Conference on Robotics and Automation (ICRA)* (IEEE, 2015).

[146] A. Bachrach, R. He, and N. Roy, *Autonomous flight in unknown indoor environments,* International Journal of Micro Air Vehicles **1**, 217 (2009).

[147] S. Jung, S. Cho, D. Lee, H. Lee, and D. H. Shim, *A direct visual servoing-based framework for the 2016 IROS autonomous drone racing challenge,* Journal of Field Robotics **35**, 146 (2017).

[148] D. Mellinger, N. Michael, and V. Kumar, *Trajectory generation and control for precise aggressive maneuvers with quadrotors,* The International Journal of Robotics Research **31**, 664 (2012).

[149] B. Aydin, *Public acceptance of drones: Knowledge, attitudes, and practice,* Technology in Society **59**, 101180 (2019).

[150] E. A. Lofquist, *The art of measuring nothing: The paradox of measuring safety in a changing civil aviation industry using traditional safety metrics,* Safety Science **48**, 1520 (2010).

[151] L. Zheng, T. Hedrick, and R. Mittal, *A comparative study of the hovering efficiency of flapping and revolving wings,* Bioinspiration & Biomimetics **8**, 036001 (2013).

[152] P. V. de Voorde, S. Gautama, A. Momont, C. Ionescu, P. D. Paepe, and N. Fraeyman, *The drone ambulance [a-UAS]: golden bullet or just a blank?* Resuscitation **116**, 46 (2017).

[153] H. Moon, J. Martinez-Carranza, T. Cieslewski, M. Faessler, D. Falanga, A. Simovic, D. Scaramuzza, S. Li, M. Ozo, C. De Wagter, G. C. H. E. de Croon, S. Hwang, S. Jung, H. Shim, H. Kim, M. Park, T.-C. Au, and S. J. Kim, *Challenges and implemented technologies used in autonomous drone racing,* Intelligent Service Robotics **12**, 137 (2019).

2

The DelFly

__Uncertainty__ is an uncomfortable position,
but certainty is an absurd position.

Voltaire

Autonomous indoor flying robots form a promise to reach places that are too small or too dangerous for humans to enter and observe our world from new perspectives. Operating flying robots close to humans also poses hard requirements on mass and risks. These stringent mass and size restrictions limit the available onboard processing, and makes any autonomous flight in indoor environements challenging. In this chapter, we propose a stable slowly hovering flapping-wing robot called the DelFly. DelFly is a flying robot system including a camera that can perform real-world missions. The main system characteristics and limitations of the platform are discussed, and the chapter shows how autonomous indoor navigation is achieved within the stringent weight limitations.

2.1. Introduction

The long term goal of research on MAV is to arrive at fly-sized vehicles [11] that can perform a mission autonomously in complex environments. Such MAVs form a promise for observation tasks in places that are too small or too dangerous for humans to enter. Their small size would allow the MAVs to enter and navigate in narrow spaces, while autonomous flight would allow the MAV to operate at a large distance from its user.

Figure 2.1: DelFly I flying outdoors in Garmish-Partkirchen at EMAV2005.

The requirements for this type of MAV are legion [12]. For one, it needs to be as light as possible for endurance, while having enough onboard sensors and processing to navigate autonomously. Moreover, it needs to be sufficiently slow to perform its inspection task and navigate in confined areas. At the same time, it needs to travel sufficiently large distances to perform a useful mission.

Flying insects provide a lot of inspiration for solving the engineering problems encountered in the creation of tiny MAVs [13, 14]. One of the key properties of systems inspired by flying insects is that they use flapping wing propulsion [11, 15–20]. Especially at smaller sizes, due to the decreasing Reynolds number, this propulsion method produces more lift than fixed-wing configurations [21–24]. Flapping wings have been shown to scale well to lower Reynolds numbers [25, 26]. At the size of fruit flies, flapping wings are believed to even yield longer flying times [27, 28].

Some researchers have focussed on developing the technology that will allow the creation of tiny fly-sized flying robots [11]. While these so-called "bottom-up" approaches to insect-sized MAVs give an insight into the future possibilities [29], this chapter will focus on a top-down approach where a fully functional robot is down-sized, but at all times remains capable of performing an observation mission.

2.2. Design of the DelFly

The main aim of the original DelFly design (See Figure 2.1) was to achieve an airborne camera platform with stable slow flight characteristics. While helicopters offer the great advantage of hovering flight, this comes at the cost of the need for active stabilization. While for larger UAVs this problem has been solved [30], for the tiniest insect size platforms this is not obvious at all. Fixed-wing aircraft offer stability and range advantages over rotorcraft but do not fit well in small indoor environments due to their high forward speed. Moreover, they do not scale well to very small sizes due to the decreasing Reynolds number [17]. Tailed ornithopters on the other hand can combine the advantages of both by offering dynamically stable slow hovering flight, while not required the active stabilization needed by tail-less flappers [31].

In [1], three flapping-wing concepts were compared. The first concept was a simple monoplane with one set of wings. The second was a biplane where two sets of wings were place above each other. These wings move in counter phase on a common rotational axle. The third concept involved a tandem configuration, where the wings were placed behind one another.

To compare the concepts, balsa wood models were built and tested. The results are shown in Table 2.1. For a given weight and size, the biplane was found to use the smallest amount of energy while not having excessive rocking of the fuselage and camera.
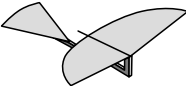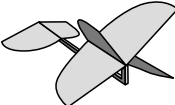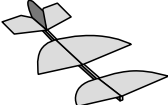
	Monoplane	Biplane	Tandem
Average flight speed	2.35 m/s	1.40 m/s	1.36 m/s
Power consumption	0.75 W	0.69 W	1.00 W
Rocking amplitude	≈ 80 mm	≈ 0 mm	≈ 0 mm

Table 2.1: Concepts of flapping wing MAV with comparative measurements.

The shape of the wing was found to be an important factor to determine the lift and efficiency [25]. The two wings on top of each other clap against one another and fling or peel apart. This was found to help a lot in the generation of thrust [32, 33]. The complex nature of non-steady flow around flexible flapping wings sparked a wide range of new research [8]. This for instance led to the first flow visualization around DelFly in hover [34, 35], forward flight [35] and even in free flight [36] once precise control was achieved [37]. The unsteady lift was enhanced [38] and flapping-wing kinematic [39] and quasi-steady aerodynamic models were derived [40]. The flow around flapping wings was studied in simulation [41] and the complex wing-fluid-wing interactions were analyzed [42]. The resulting slow hovering platform, capable of stable slow flight at about 0.8 m/s, but also capable of performing fast forward flight, provides an interesting basis for a flying indoor

reconnaissance robot. The platform was called "DelFly" and weighed only 16 g.

2.3. Autonomous Vision-based Control

To attain autonomous behavior, the physical properties of the robot determine its capabilities to a wide extent [4, 43–45]. DelFly was initially equipped with a small monocular CMOS camera as shown in Figure 2.2.
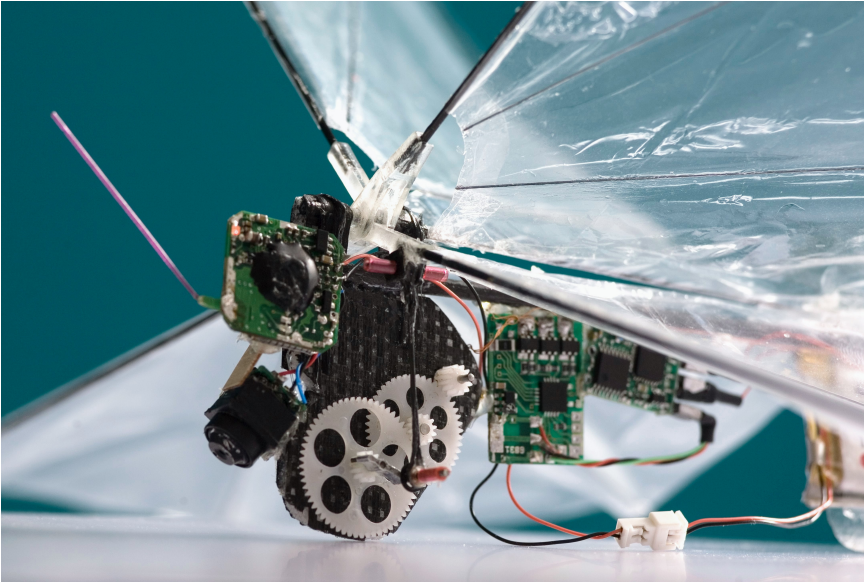
Figure 2.2: Close-Up of the DelFly II with its analog camera.

Images were streamed to a computer where they could be analyzed via a 2.4 GHz analog video link.

Figure 2.3: Two subsequent DelFly II images with image distortion [4].

But the video noise due to the analog transmission combined with the rolling shutter camera images with high distortion due to the flapping wing platform (See

Figure 2.3), limit the available computer vision methods that can be applied. On top of that, man-made indoor environments often contain large texture-less areas. This causes well-known approaches like Simultaneous Localization and Mapping (SLAM) [46] or even optic-flow [47–50] methods to not give good results.

Neuro-morphic sensing with a higher time resolution [51], tiny low-power global shutter cameras, or digital video links may solve many of the latter problems but were too heavy for micro flying robots. However, inspired by nature where amazing control performance is often achieved even in the presence of distorted, noisy, or blurred sensory input, novel approaches were sought to achieve autonomous indoor flight of this very light platform [52–54].

2.3.1. Appearance

One method that is resilient to vibration and distortion is the extraction of appearance features. Flies are for instance known to stay away from small flying objects as they risk being predators. But they fly towards tall or ultra-violet objects, which form likely feeding places [55]. They do so by recognizing "appearance".

Inspired by this complex behavior based on simple appearance classification, height control of the DelFly was achieved by learning to classify the appearance of the surroundings as being seen from a low, medium, or high altitude [2, 56]. Appearance can also be used in outdoor collision avoidance by performing sky segmentation and finding obstacles protruding above the horizon [5, 57]. Finally, appearance variation—the variation in texture—was found to be a cue for indoor obstacle proximity in man-made indoor environments, as the variation in the appearance of many different objects in view is larger than that of the detailed texture of one object alone [3, 58] (See Figure 2.4). By computing the Shannon entropy [59] of the texton probability distribution [60] of a dictionary of random textons clustered by a Kohonen network [61], a cue was created to successfully control the DelFly II. Appearance-based methods could benefit from "random sub-sampling" to speed up computer vision and thereby enhance the flight control [62].
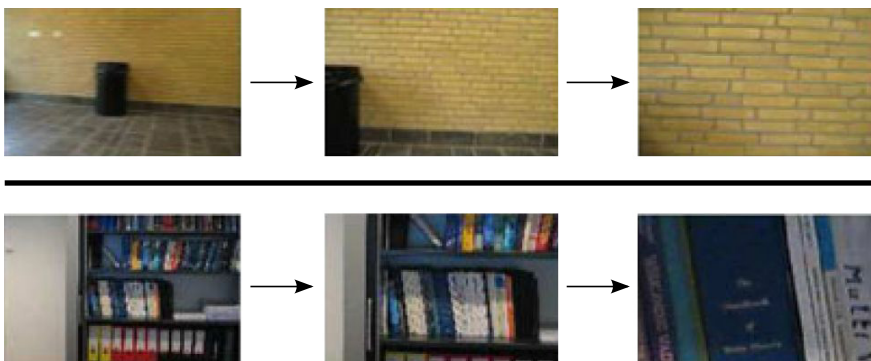

Figure 2.4: Reduction of appearance variation when approaching indoor obstacles [58].

2.3.2. Visual Servoing

To guide DelFly more precisely, another category of algorithms was applied to the tiny indoor flying robot. Visual servoing is also known as vision-based robot control and refers to the process of controlling a robot using feedback information directly from a vision sensor [63, 64]. One approach is to use offboard cameras and offboard processing while tracking the flying vehicle, for instance by equipping the robot with Light Emitting Diode (LED)s for better visibility [65]. This was used to control the DelFly height in [1]. Another approach is to process the wireless images coming from the vehicle on an offboard computer. This enabled the first fully autonomous micro air vehicle flight at the Micro Air Vehicle competition 2008.
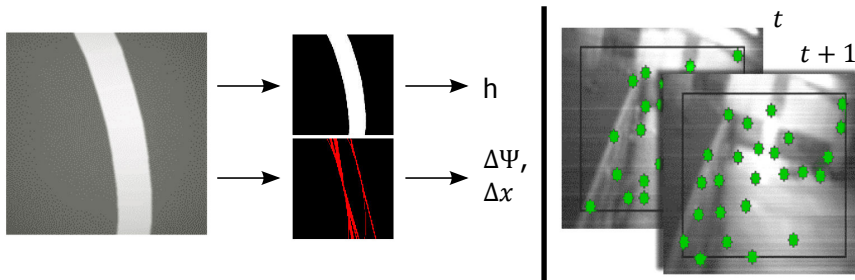
Figure 2.5: Illustration of the image processing for the DelFly path-tracking algorithm. On the left, a down-looking input image looking at a white line is thresholded and a hough line detector is used to parametrize the Canny edges. On the right, forward-looking optical flow is used to extract the yaw rate.

To achieve this, a path tracking algorithm was designed in which the visually distinct line on the ground was used to obtain fully autonomous flight (Left part in Figure 2.5). First, a thresholding algorithm was employed to segment the path in the down-looking onboard camera image. Using a combination of Gaussian blur, dilation, and erosion, the effects of analog transmission noise were minimized.

A sample image is shown in Figure 2.5. After segmentation, the percentage of path pixels p_{path} was used as cue to estimate the height h based on the assumption that the path will run from top to bottom using $h = p_{path} * w_{path}/v$, where v is the Field Of View (FOV) and w_{path} is the estimated actual path width in meters. Using a Hough detector[1] on top of a Canny edge detector, the edges of the path were reconstructed. The average orientation of the vertical edges was then used as an estimate for the heading error $\Delta\Psi$ and their lateral position in the image was used to estimate the lateral position Δx of the DelFly. Finally, the yaw rate r was found from the lateral optic flow of the front-facing camera using a Lucas Kanade detector [66] on 128x128 pixel images (Right part in Figure 2.5). The system won the prize for best automatic indoor MAV at the 2008 International Micro Air Vehicle Conference and Competition.

By using specialized integrated circuits, like the Wii-mote IR-tracker, visual servoing can be entirely performed onboard tiny flying robots in tasks like precision landing [67] or homing [68]. Similarly, DelFly was equipped with a sub-gram autopi-

---

[1]http://sourceforge.net/projects/opencvlibrary/
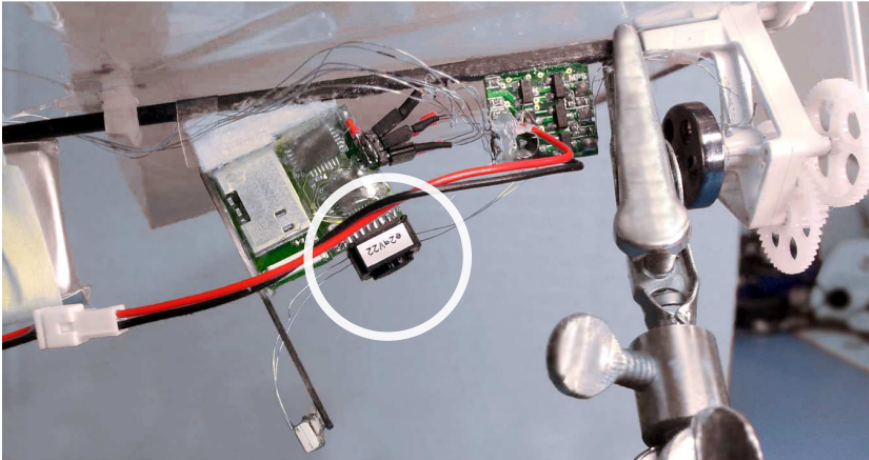
Figure 2.6: DelFly II with miniature autopilot using Wii-mote IR-tracker [6].

lot containing the Wii-mote camera with processing and Bluetooth module shown in Figure 2.6. This allowed the DelFly to perform closed-loop position hold flights in the open-jet wind tunnel of the TUDelft [6], using traditional control onboard an 8-bit microcontroller to fly towards an Infrared (IR) marker in the tunnel.

2.4. Autonomous Indoor Exploration

Specific integrated circuits have been used to create the smallest indoor flying robots. This includes using the sub-gram Wii-mote sensor flying in front of IR LEDs [6], the minimalistic 1D camera on a 10-gram fixed-wing flying in a room prepared with maximum contrast patterns [69, 70], and super-tiny visual orientation sensors [71]. While this allows the creation of very light robots, it does come with stringent constraints and limited applicability and the design of novel system-on-chip systems is a very expensive complex time-consuming task. Other sensors like the very fast bio-inspired Curved Artificial Compound Eye (CURVACE) compound eye [72, 73] or event cameras [74], overcome the speed limitation of traditional Complementary Metal-Oxide Semiconductor (CMOS) cameras but are heavier and do not include the visual processing.

Nevertheless, to perform more flexible higher-level autonomous missions like the indoor exploration of a random room or building, the intelligence of the DelFly needed to be increased by adding onboard sensors and processing [43, 45]. Larger drones have achieved autonomous indoor exploration using for instance laser-scanner-based 2D SLAM [75, 76]. Other researchers used large onboard computers and high resolution cameras to perform SLAM [46, 77] or Visual-Inertial Odometry (VIO) [78–82]. Some even used dual stereo-vision systems onboard to better estimate the height and distance to obstacles [83]. When the weight budget allows this, the best results are obtained onboard even larger helicopters by merging several methods like stereo-vision and optic flow on high-resolution images [84].
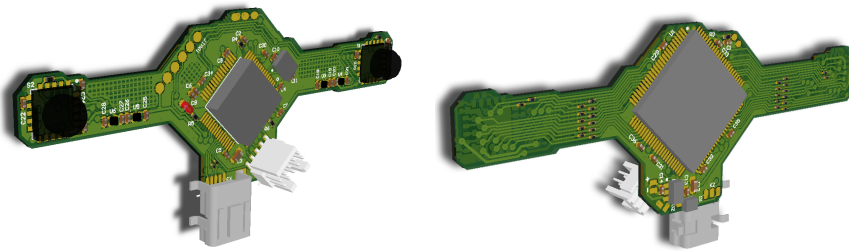
(a) Front side with dual TCM8230MD and STM32F4   (b) Back side with MAX II CPLD

Figure 2.7: The 4 g stereo-camera with onboard processing of DelFly Explorer [7].

But onboard an MAV like the DelFly—which can lift not much more than 20 g—most available options are simply too heavy. To nevertheless allow DelFly to autonomously explore, new very light stereo vision systems were developed. Initial stereo-based avoidance tests were performed by combining two analog CMOS cameras through an analog switch that switched every video line using the H-Sync output of cameras [85]. While the stereo merging and avoidance were very promising, the wireless transmission added a lot of noise. This reduced the reliability and limited the distance that the robot could move away from the base station [86].
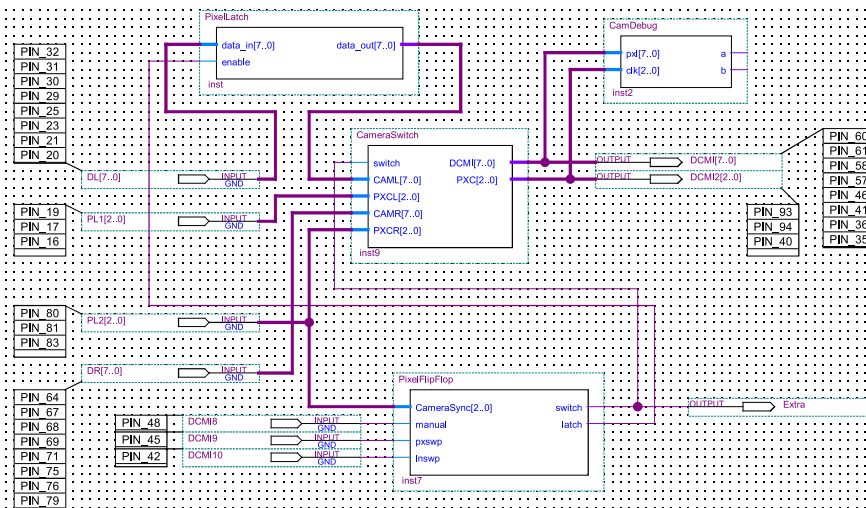
Figure 2.8: VHDL logic inside the stereo camera CPLD [7].

Therefore a new fully digital 4 g stereo vision system was created with onboard processing. Two small TCM8230MD CMOS cameras were connected to an STM32F405 microcontroller (See Figure 2.7a) by merging the two camera streams using a MAX II Complex Programmable Logic Device (CPLD) (See Figure 2.7b) running Very High Speed Integrated Circuit Hardware Description Language (VHDL) [7] (See Figure 2.8).
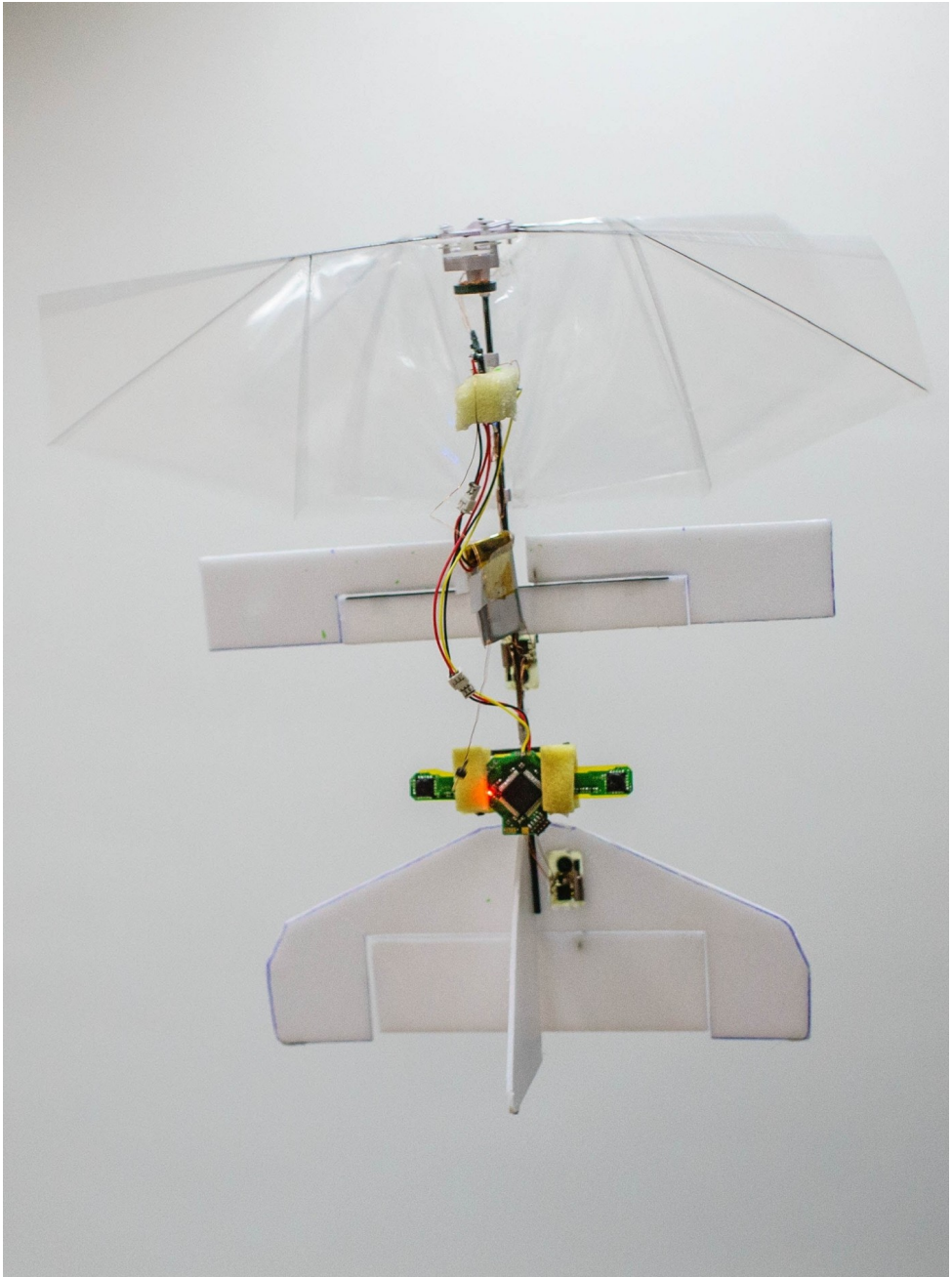
Figure 2.9: The 20-gram DelFly Explorer flapping-wing robot with a 4-gram stereo camera with onboard processing for autonomous indoor exploration [7].

By replacing the color bytes in the YUV422 image stream of the left camera with intensity bytes from the same pixel of the hardware synchronized right camera, a single stream is obtained that contains both images. This is done by feeding the same oscillator clock to both cameras and resetting them at the exact same time. Furthermore, the 8-bit data bus of the right camera is delayed exactly one pixel-clock through a buffer, and a digital switch outputs the data bus of the left camera on uneven pixel clock cycles and the right bus on the even cycles. The single-bus stream is then fed to the single Digital Camera Media Interface (DCMI) of the small Digital Signal Processor (DSP). The baseline between the cameras is 6 cm and the total weight is below 4 g with wires and connectors. A picture of the stereocam onboard DelFly Explorer is shown in Figure 2.9 and a close-up of the camera can be seen in Figure 2.10.
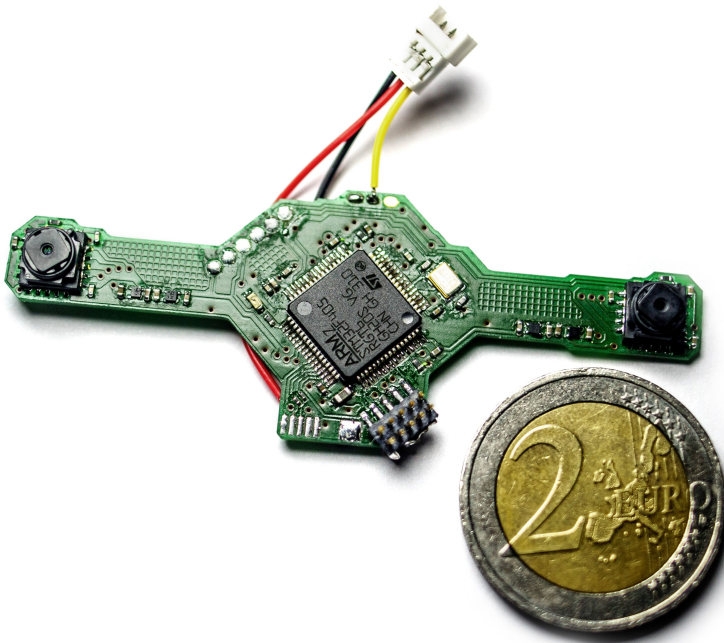
Figure 2.10: The less than 4 gram DelFly Explorer stereo camera with dual TCM8230MD, a CPLD camera stream merging and onboard STM32 DSP processing running at 168 MHz [7].

The depth reconstruction is done by processing the images in the 196 kb of memory of the 168 MHz 32-bit DSP at a resolution of $128x96$ pixels. Among the large number of stereo vision algorithms, we could not find a single algorithm that suited these specific requirements. The algorithms that perform global optimization are too heavy while the local matching algorithms do not deal well with the little texture found in low-resolution images of indoor environments. Inspired by semi-global optimization algorithms like the fast 1-dimensional dynamic programming [87] and semi-global matching [88], a dedicated new algorithm was developed [7].

(a) Left camera image   (b) Right camera image   (c) Disparity image

Figure 2.11: Sample disparity image if the 4 g stereo vision system on $128x96$ pixels processed on a 168 MHz 32-bit DSP with a single camera port and only 196 kb of memory. In areas of low contrast, the algorithm propagates the disparity of the closest edge. While the disparity image is not state-of-the-art in terms of accuracy, in terms of memory and computational power, it nevertheless enables the 20 g robot to safely navigate.

The algorithm is named LongSeq, because it favors long sequences with a constant disparity in an image line to overcome areas with low texture. A sample stereo pair and resulting disparity image is shown in Figure 2.11. Since the DelFly Explorer always had to keep flying forward, the stereo algorithm was combined with an avoidance strategy named Droplet, that keeps the droplet-shaped area in front of the robot clear of obstacles to always have an escape route. Onboard a novel version of DelFly with enlarged ailerons for better directional control, reliable indoor onboard collision avoidance was obtained [89]. The resulting Flapping Wing Micro Air Vehicle (FWMAV) was called: DelFly Explorer and a timelapse of a testflight is shown in Figure 2.12.

Video

Figure 2.12: Time lapse of the DelFly Explorer autonomously exploring a room [7, 89].

Figure 2.13: Multi-room exploration flight of DelFly Explorer [9].

This allowed the autonomous flying robot to perform room exploration and corridor traversal [10]. By adding a computationally light "door detector" based on the extremely light Snake-Gate algorithm [90], robust multi-room exploration was achieved with a 20 g flying robot [9].

2.5. Discussion and Conclusions

The main challenges for achieving small-sized autonomous indoor flying robots lie in reducing the weight of all its components. Namely, it is easier to reduce the size than to reduce its weight. A reduction of the size of factor two causes a reduction in wing area of a factor four and would require a reduction in weight of a factor of at least four to keep a comparable flight speed. This is made even worse by the reduction in Reynolds number which causes aerodynamic performance reductions as well.

At smaller sizes, the dynamics of the platform are also faster [91]. Sensors should not only be lighter but also measure higher turn rates and faster changes in rotational speed. In practice, the performance of components degrades with size and the options for vibration damping reduce with reductions in mass.

Smaller motors have more loss, smaller batteries have worse energy density and much lighter sensors have more noise. This limits the minimum size at which fully autonomous flying robots can still be made that still have sufficient flight time and payload to perform useful missions in the real world.

By exploiting passive aerodynamic longitudinal pitch stability with low-speed capable flapping wings, a stable slow indoor flying platform was created. This Flapping

Wing Micro Air Vehicle (FWMAV) called DelFly Explorer was found to fly at a stable 0.8 m/s slow hovering flight with only slow drift in heading and altitude. This enabled a tiny 1 g autopilot and 4 g 30 fps stereo-vision board operating at low resolution to guide the flying robot in man-made indoor environments like offices and corridors at a total weight of 20 g. The result is the lightest flying robot able to autonomously explore non-prepared indoor environments.

References

[1] G. C. H. E. de Croon, K. M. E. De Clercq, R. Ruijsink, B. Remes, and C. De Wagter, *Design, aerodynamics, and vision-based control of the delfly,* International Journal of Micro Air Vehicles **1**, 71 (2009).

[2] G. C. H. E. de Croon, C. De Wagter, B. D. W. Remes, and R. Ruijsink, *Random sampling for indoor flight,* in *International Micro Air Vehicle Conference and Flight Competition 2010*, edited by D. G. für Ortung und Navigation e.V. (DGON) (IMAV, Braunschweig, Germany, 2010) pp. 94–102.

[3] G. C. H. E. de Croon, E. De Weerdt, C. De Wagter, B. D. W. Remes, and R. Ruijsink, *The appearance variation cue for obstacle avoidance,* in *Robotics and Biomimetics (ROBIO), 2010 IEEE International Conference on* (IEEE, Tianjin, China, 2010) pp. 1606–1611.

[4] G. C. H. E. de Croon, B. W. van Oudheusden, B. D. W. Remes, C. De Wagter, and R. Ruijsink, *Aerodynamics and autonomy of the delfly,* in *International Workshop on BioInspired Robotics* (Nantes, France, 2011).

[5] G. C. H. E. de Croon, C. De Wagter, B. D. W. Remes, and R. Ruijsink, *Sky segmentation approach to obstacle avoidance,* in *Aerospace Conference, 2011 IEEE* (IEEE, Big Sky, MT, USA, 2011) pp. 1–16.

[6] C. De Wagter, A. Koopmans, G. C. H. E. de Croon, B. Remes, and R. Ruijsink, *Autonomous wind tunnel free-flight of a flapping wing mav,* in *Proceedings of the EuroGNC 2013, 2nd CEAS Specialist Conference*, edited by J. A. Mulder, D. Choukroun, E. J. van Kampen, C. C. de Visser, and G. J. Looye (Springer Verlag, Delft, the Netherlands, 2013) pp. 17–35.

[7] C. De Wagter, S. Tijmons, B. D. W. Remes, and G. C. H. E. de Croon, *Autonomous flight of a 20-gram flapping wing mav with a 4-gram onboard stereo vision system,* in *Robotics and Automation (ICRA), 2014 IEEE International Conference on* (IEEE, Hong Kong, China, 2014) pp. 4982–4987.

[8] G. C. H. E. de Croon, M. Perçin, B. D. W. Remes, R. Ruijsink, and C. De Wagter, *The DelFly: Design, Aerodynamics, and Artificial Intelligence of a Flapping Wing Robot*, 1st ed. (Springer Netherlands, 2016).

[9] K. Y. Scheper, M. Karásek, C. De Wagter, B. D. W. Remes, and G. C. H. E. de Croon, *First autonomous multi-room exploration with an insect-inspired*

flapping wing vehicle, in *ICRA 2018: 2018 IEEE International Conference on Robotics and Automation* (IEEE, Brisbane, Australia, 2018) pp. 5546–5552.

[10] S. Tijmons, C. De Wagter, B. Remes, and G. C. H. E. de Croon, *Autonomous door and corridor traversal with a 20-gram flapping wing mav by onboard stereo vision,* Aerospace – Open Access Aeronautics and Astronautics Journal **5** (2018), 10.3390/aerospace5030069.

[11] R. Wood, *The first takeoff of a biologically-inspired at-scale robotic insect,* IEEE Transactions on Robotics **24**, 341 (2008).

[12] D. J. Pines and F. Bohorquez, *Challenges facing future micro-air-vehicle development,* Journal of Aircraft **43**, 290 (2006).

[13] R. Wootton, *From insects to microvehicles,* Nature **403**, 144 (2000).

[14] D. Floreano, J.-C. Zufferey, M. V. Srinivasan, and C. Ellington, eds., *Flying Insects and Robots* (Springer Berlin Heidelberg, 2010).

[15] T. Pornsin-Sirirak, S. Lee, H. Nassef, J. Grasmeyer, Y. Tai, C. Ho, and M. Keennon, *MEMS wing technology for a battery-powered ornithopter,* in *Proceedings IEEE Thirteenth Annual International Conference on Micro Electro Mechanical Systems (Cat. No.00CH36308)* (IEEE, 2000).

[16] M. Keennon and J. Grasmeyer, *Development of two MAVs and vision of the future of MAV design,* in *AIAA International Air and Space Symposium and Exposition: The Next 100 Years* (American Institute of Aeronautics and Astronautics, 2003).

[17] T. J. Mueller and J. D. DeLaurier, *Aerodynamics of small vehicles,* Annual Review of Fluid Mechanics **35**, 89 (2003).

[18] F. Boria, R. Bachmann, P. Ifju, R. Quinn, R. Vaidyanathan, C. Perry, and J. Wagener, *A sensor platform capable of aerial and terrestrial locomotion,* in *2005 IEEE/RSJ International Conference on Intelligent Robots and Systems* (IEEE, 2005).

[19] R. C. Michelson, *Test and evaluation for fully autonomous micro air vehicles,* The ITEA Journal **29**, 367 (2008).

[20] F. van Breugel, Z. E. Teoh, and H. Lipson, *A passively stable hovering flapping micro-air vehicle,* in *Flying Insects and Robots* (Springer Berlin Heidelberg, 2009) pp. 171–184.

[21] C. P. Ellington, C. van den Berg, A. P. Willmott, and A. L. R. Thomas, *Leading-edge vortices in insect flight,* Nature **384**, 626 (1996).

[22] M. H. Dickinson, *Wing rotation and the aerodynamic basis of insect flight,* Science **284**, 1954 (1999).

[23] V. Malolan, M. Dineshkumar, and V. Baskar, *Design and development of flapping wing micro air vehicle,* in *42nd AIAA Aerospace Sciences Meeting and Exhibit* (American Institute of Aeronautics and Astronautics, 2004).

[24] S. Ansari, R. Żbikowski, and K. Knowles, *Aerodynamic modelling of insect-like flapping flight for micro air vehicles,* Progress in Aerospace Sciences **42**, 129 (2006).

[25] N. Bradshaw and D. Lentink, *Aerodynamic and structural dynamic identification of a flapping wing micro air vehicle,* in *26th AIAA Applied Aerodynamics Conference* (American Institute of Aeronautics and Astronautics, 2008).

[26] W. Shyy, H. Aono, C. kwon Kang, and H. Liu, *An Introduction to Flapping Wing Aerodynamics* (Cambridge University Press, 2013).

[27] Z. Liu and J.-M. Moschetta, *Rotary vs. flapping-wing nano air vehicles: Comparing performances,* in *European Micro Air Vehicle Conference and Flight Competition 2009* (IMAV, Delft, the Netherlands, 2009) pp. 114–120.

[28] E. W. Hawkes and D. Lentink, *Fruit fly scale robots can hover longer with flapping wings than with spinning wings,* Journal of The Royal Society Interface **13**, 20160730 (2016).

[29] K. Ma, P. Chirarattananon, S. Fuller, and R. Wood, *Controlled flight of a biologically inspired, insect-scale robot.* Science **340**, 603 (2013).

[30] E. Johnson and S. Kannan, *Adaptive flight control for an autonomous unmanned helicopter,* in *AIAA Guidance, Navigation, and Control Conference and Exhibit* (American Institute of Aeronautics and Astronautics, 2002).

[31] R. Hengstenberg, *Controlling the fly's gyroscopes,* Nature **392**, 757 (1998).

[32] F.-O. Lehmann, *The aerodynamic effects of wing-wing interaction in flapping insect wings,* Journal of Experimental Biology **208**, 3075 (2005).

[33] S. S. Jadhav, K. B. Lua, and W. B. Tay, *Effect of clap-and-fling mechanism on force generation in flapping wing micro aerial vehicles,* Bioinspiration & Biomimetics **14**, 036006 (2019).

[34] K. D. Clercq, R. de Kat, B. Remes, B. van Oudheusden, and H. Bijl, *Flow visualization and force measurements on a hovering flapping-wing MAV DelFly II,* in *39th AIAA Fluid Dynamics Conference* (American Institute of Aeronautics and Astronautics, 2009).

[35] M. Perçin, H. Eisma, B. van Oudheusden, B. Remes, R. Ruijsink, and C. De Wagter, *Flow visualization in the wake of the flapping-wing mav 'delfly ii' in forward flight,* in *30th AIAA Applied Aerodynamics Conference*, 2664, AIAA (American Institute of Aeronautics and Astronautics (AIAA), New Orleans, Louisiana, USA, 2012) pp. 1–12.

[36] A. del Estal Herrero, M. Percin, M. Karasek, and B. van Oudheusden, *Flow visualization around a flapping-wing micro air vehicle in free flight using large-scale PIV,* Aerospace **5**, 99 (2018).

[37] M. Karásek, M. Perçin, T. Cunis, B. W. Oudheusden, C. De Wagter, B. D. W. Remes, , and d. G. C. H. E., *Accurate position control of a flapping-wing robot enabling free-flight flow visualisation in a wind tunnel,* International Journal of Micro Air Vehicles **11**, 175682931983368 (2019).

[38] K. M. D. Clercq, R. de Kat, B. Remes, B. W. van Oudheusden, and H. Bijl, *Aerodynamic experiments on DelFly II: Unsteady lift enhancement,* International Journal of Micro Air Vehicles **1**, 255 (2009).

[39] J. V. Caetano, M. B. Weehuizen, C. C. de Visser, G. C. H. E. de Croon, and M. Mulder, *Rigid-body kinematics versus flapping kinematics of a flapping wing micro air vehicle,* Journal of Guidance, Control, and Dynamics **38**, 2257 (2015).

[40] S. F. Armanini, J. V. Caetano, G. C. H. E. de Croon, C. C. de Visser, and M. Mulder, *Quasi-steady aerodynamic model of clap-and-fling flapping MAV and validation using free-flight data,* Bioinspiration & Biomimetics **11**, 046002 (2016).

[41] W. Tay, B. van Oudheusden, and H. Bijl, *Numerical simulation of a flapping four-wing micro-aerial vehicle,* Journal of Fluids and Structures **55**, 237 (2015).

[42] M. Percin, B. W. van Oudheusden, G. C. H. E. de Croon, and B. Remes, *Force generation and wing deformation characteristics of a flapping-wing micro air vehicle 'DelFly II' in hovering flight,* Bioinspiration & Biomimetics **11**, 036014 (2016).

[43] R. A. Brooks, *Elephants don't play chess,* Robotics and Autonomous Systems **6**, 3 (1990).

[44] M. Egelhaaf and A. Borst, *A look into the cockpit of the fly: visual orientation, algorithms, and identified neurons,* The Journal of Neuroscience **13**, 4563 (1993).

[45] R. Pfeifer and C. Scheier, *Understanding intelligence* (The MIT Press, Cambridge, Massachusetts, 1999).

[46] J. Fuentes-Pacheco, J. Ruiz-Ascencio, and J. M. Rendón-Mancha, *Visual simultaneous localization and mapping: a survey,* Artificial Intelligence Review **43**, 55 (2012).

[47] F. Ruffier, S. Viollet, S. Amic, and N. Franceschini, *Bio-inspired optical flow circuits for the visual guidance of micro air vehicles,* in *Proceedings of the 2003 International Symposium on Circuits and Systems, 2003. ISCAS 03.* (IEEE, 2003).

[48] F. Ruffier and N. Franceschini, *Optic flow regulation: the key to aircraft automatic guidance,* Robotics and Autonomous Systems **50**, 177 (2005).

[49] J. Serres, D. Dray, F. Ruffier, and N. Franceschini, *A vision-based autopilot for a miniature air vehicle: joint speed control and lateral obstacle avoidance,* Autonomous Robots **25**, 103 (2007).

[50] F. Ruffier and N. Franceschini, *Optic flow regulation in unsteady environments: A tethered MAV achieves terrain following and targeted landing over a moving platform,* Journal of Intelligent & Robotic Systems **79**, 275 (2014).

[51] N. Franceschini, S. Viollet, F. Ruffier, and J. Serres, *Neuromimetic robots inspired by insect vision,* Advances in Science and Technology **58**, 127 (2008).

[52] H. Wagner, *Flow-field variables trigger landing in flies,* Nature **297**, 147 (1982).

[53] J. S. Chahl, M. V. Srinivasan, and S. W. Zhang, *Landing strategies in honeybees and applications to uninhabited airborne vehicles,* The International Journal of Robotics Research **23**, 101 (2004).

[54] D. Clarke, H. Whitney, G. Sutton, and D. Robert, *Detection and learning of floral electric fields by bumblebees,* Science **340**, 66 (2013).

[55] G. Maimon, A. D. Straw, and M. H. Dickinson, *A simple vision-based algorithm for decision making in flying drosophila,* Current Biology **18**, 464 (2008).

[56] G. C. H. E. de Croon, C. De Wagter, B. D. W. Remes, and H. M. Ruijsink, *Local sampling for indoor flight,* in *BNAIC 2009: 21st Benelux Conference on Artificial Intelligence, Eindhoven, The Netherlands, 29-30 October 2009* (Eindhoven, The Netherlands, 2009).

[57] T. McGee, R. Sengupta, and K. Hedrick, *Obstacle detection for small autonomous aircraft using sky segmentation,* in *Proceedings of the 2005 IEEE International Conference on Robotics and Automation* (IEEE, 2005).

[58] G. C. H. E. de Croon, E. De Weerdt, C. De Wagter, B. D. W. Remes, and R. Ruijsink, *The appearance variation cue for obstacle avoidance,* IEEE Transactions on Robotics **28**, 529 (2012).

[59] C. E. Shannon, *A mathematical theory of communication,* Bell System Technical Journal **27**, 379 (1948).

[60] M. Varma and A. Zisserman, *Texture classification: are filter banks necessary?* in *2003 IEEE Computer Society Conference on Computer Vision and Pattern Recognition, 2003. Proceedings.* (IEEE Comput. Soc, 2003).

[61] P. H. Mähönen and P. J. Hakala, *Automated source classification using a kohonen network,* The Astrophysical Journal **452** (1995), 10.1086/309697.

[62] G. C. H. E. de Croon, C. De Wagter, B. D. W. Remes, and R. Ruijsink, *Sub-sampling: Real-time vision for micro air vehicles,* Robotics and Autonomous Systems **60**, 167 (2012).

[63] P. Rudol, M. Wzorek, G. Conte, and P. Doherty, *Micro unmanned aerial vehicle visual servoing for cooperative indoor exploration,* in *2008 IEEE Aerospace Conference* (IEEE, 2008).

[64] S. Ryu, U. Kwon, and H. J. Kim, *Autonomous flight and vision-based target tracking for a flapping-wing MAV,* in *2016 IEEE/RSJ International Conference on Intelligent Robots and Systems (IROS)* (IEEE, 2016).

[65] L. C. Mak, M. Whitty, and T. Furukawa, *A localisation system for an indoor rotary-wing MAV using blade mounted LEDs,* Sensor Review **28**, 125 (2008).

[66] J. Bouguet, *Pyramidal implementation of the lucas kanade feature tracker description,* Technical Report for Intel Corporation Microsoft Research Lab: Santa Clara, CA, USA (2000).

[67] K. E. Wenzel, P. Rosset, and A. Zell, *Low-cost visual tracking of a landing place and hovering flight control with a microcontroller,* Journal of Intelligent and Robotic Systems **57**, 297 (2009).

[68] S. S. Baek, F. L. G. Bermudez, and R. S. Fearing, *Flight control for target seeking by 13 gram ornithopter,* in *2011 IEEE/RSJ International Conference on Intelligent Robots and Systems* (IEEE, 2011).

[69] J. christophe Zufferey, A. Klaptocz, A. Beyeler, J. daniel Nicoud, and D. Floreano, *A 10-gram microflyer for vision-based indoor navigation,* in *2006 IEEE/RSJ International Conference on Intelligent Robots and Systems* (IEEE, 2006).

[70] J.-C. Zufferey, A. Klaptocz, A. Beyeler, J.-D. Nicoud, and D. Floreano, *A 10-gram vision-based flying robot,* Advanced Robotics **21**, 1671 (2007).

[71] S. B. Fuller, M. Karpelson, A. Censi, K. Y. Ma, and R. J. Wood, *Controlling free flight of a robotic fly using an onboard vision sensor inspired by insect ocelli,* Journal of The Royal Society Interface **11**, 20140281 (2014).

[72] R. Pericet-Camara, M. Dobrzynski, G. L'Eplattenier, J.-C. Zufferey, F. Expert, R. Juston, F. Ruffier, N. Franceschini, S. Viollet, M. Menouni, S. Godiot, A. Brückner, W. Buss, R. Leitel, F. Recktenwald, C. Yuan, H. Mallot, and D. Floreano, *CURVACE – CURVed artificial compound eyes,* Procedia Computer Science **7**, 308 (2011).

[73] D. Floreano, R. Pericet-Camara, S. Viollet, F. Ruffier, A. Brückner, R. Leitel, W. Buss, M. Menouni, F. Expert, R. Juston, M. K. Dobrzynski, G. L'Eplattenier, F. Recktenwald, H. A. Mallot, and N. Franceschini, *Miniature curved artificial compound eyes,* Proceedings of the National Academy of Sciences **110**, 9267 (2013).

[74] C. Brandli, R. Berner, M. Yang, S.-C. Liu, and T. Delbruck, *A 240 × 180 130 dB 3 μs latency global shutter spatiotemporal vision sensor,* IEEE Journal of Solid-State Circuits **49**, 2333 (2014).

[75] S. Grzonka, G. Grisetti, and W. Burgard, *Towards a navigation system for autonomous indoor flying,* in *2009 IEEE International Conference on Robotics and Automation* (IEEE, 2009).

[76] A. Bachrach, R. He, and N. Roy, *Autonomous flight in unknown indoor environments,* International Journal of Micro Air Vehicles **1**, 217 (2009).

[77] A. Davison and D. Murray, *Simultaneous localization and map-building using active vision,* IEEE Transactions on Pattern Analysis and Machine Intelligence **24**, 865 (2002).

[78] M. Li and A. I. Mourikis, *High-precision, consistent EKF-based visual-inertial odometry,* The International Journal of Robotics Research **32**, 690 (2013).

[79] C. Forster, M. Pizzoli, and D. Scaramuzza, *SVO: Fast semi-direct monocular visual odometry,* in *2014 IEEE International Conference on Robotics and Automation (ICRA)* (IEEE, 2014).

[80] D. Scaramuzza, M. C. Achtelik, L. Doitsidis, F. Friedrich, E. Kosmatopoulos, A. Martinelli, M. W. Achtelik, M. Chli, S. Chatzichristofis, L. Kneip, D. Gurdan, L. Heng, G. H. Lee, S. Lynen, M. Pollefeys, A. Renzaglia, R. Siegwart, J. C. Stumpf, P. Tanskanen, C. Troiani, S. Weiss, and L. Meier, *Vision-controlled micro flying robots: From system design to autonomous navigation and mapping in GPS-denied environments,* IEEE Robotics & Automation Magazine **21**, 26 (2014).

[81] V. Usenko, J. Engel, J. Stuckler, and D. Cremers, *Direct visual-inertial odometry with stereo cameras,* in *2016 IEEE International Conference on Robotics and Automation (ICRA)* (IEEE, 2016).

[82] D. Abeywardena, S. Huang, B. Barnes, G. Dissanayake, and S. Kodagoda, *Fast, on-board, model-aided visual-inertial odometry system for quadrotor micro aerial vehicles,* in *2016 IEEE International Conference on Robotics and Automation (ICRA)* (IEEE, 2016).

[83] K. Schauwecker and A. Zell, *On-board dual-stereo-vision for the navigation of an autonomous MAV,* Journal of Intelligent & Robotic Systems **74**, 1 (2013).

[84] S. Hrabar, G. Sukhatme, P. Corke, K. Usher, and J. Roberts, *Combined optic-flow and stereo-based navigation of urban canyons for a UAV,* in *2005 IEEE/RSJ International Conference on Intelligent Robots and Systems* (IEEE, 2005).

[85] S. Tijmons, G. C. H. E. de Croon, B. Remes, C. De Wagter, R. Ruijsink, E.-J. van Kampen, and Q. Chu, *Stereo vision based obstacle avoidance on flapping wing mavs,* in *Advances in Aerospace Guidance, Navigation and Control* (Springer, Berlin, Heidelberg, Berlin, Heidelberg, 2013) pp. 463–482.

2

2

[86] S. Tijmons, G. C. H. E. de Croon, B. Remes, C. De Wagter, R. Ruijsink, E.-J. van Kampen, and Q. Chu, *Stereo vision based obstacle avoidance on flapping wing mavs,* in *Proceedings of the EuroGNC 2013, 2nd CEAS Specialist Conference,* edited by J. A. Mulder, D. Choukroun, E. J. van Kampen, C. C. de Visser, and G. J. Looye (Springer Verlag, Delft, the Netherlands, 2013) pp. 1225–1244.

[87] S. Forstmann, Y. Kanou, J. Ohya, S. Thuering, and A. Schmitt, *Real-time stereo by using dynamic programming,* in *2004 Conference on Computer Vision and Pattern Recognition Workshop* (IEEE, 2004).

[88] H. Hirschmuller, *Accurate and efficient stereo processing by semi-global matching and mutual information,* in *2005 IEEE Computer Society Conference on Computer Vision and Pattern Recognition (CVPR'05)* (IEEE, 2005).

[89] S. Tijmons, G. C. H. E. de Croon, B. D. W. Remes, C. De Wagter, and M. Mulder, *Obstacle avoidance strategy using onboard stereo vision on a flapping wing mav,* IEEE Transactions on Robotics **33**, 858 (2017).

[90] S. Li, M. M. Ozo, C. De Wagter, and G. C. H. E. de Croon, *Autonomous drone race: A computationally efficient vision-based navigation and control strategy,* arXiv , 1 (2018), 1809.05958 .

[91] D. Floreano and R. J. Wood, *Science, technology and the future of small autonomous drones,* Nature **521**, 460 (2015).

3

Passively Stable Flapping Flight from Hover to Fast Forward

Once we delimit what can be satirized, we are no longer living in a free society.

Gad Saad

Combining slow hovering flight and fast flight in Flapping Wing Micro Air Vehicle (FWMAV) is required for many real-world applications. Although static longitudinal stability can be obtained using a conventional horizontal tailplane, this requires different center of gravity locations in both regimes. Inspired by nature, it is proposed to achieve this by shifting the wings forward and backward using a lightweight mechanism. The DelFly II FWMAV is equipped with such a mechanism, tested, and shown to obtain passive static stability from a slow hovering flight (~ 0.8 m/s, pitch attitude of $55°$) to fast forward flight (~ 6 m/s, pitch attitude of $10°$) and back. The proposed mechanism paves the way for performing long-range FWMAV missions without compromising slow up-close observation capabilities.

Parts of this chapter have been published in the International Journal of Micro Air Vehicles **7**, 4 (2015) [1], were presented as [2], and use data from the International Journal of MAV **5**, 273 (2013) [3] & the DelFly book [4]. Specifically, I proposed the idea of obtaining passively stable flight in both hover and forward flight, analyzed the stability, and was the main author of the manuscript. The idea to not move a heavy component but move the wing instead to obtain a larger effective shift in the center of gravity was proposed by A. Koopmans. The construction was made by S. Tijmons.

47

3.1. Introduction

Many real-world missions for MAVs require a large flight envelope. In observation or search-and-rescue missions, for instance, the MAV might have to cover large distances to reach the point of interest. Upon arrival, the small aircraft is subsequently required to hover close to the target to obtain close-up images [5]. Rotorcraft such as quadrotors can combine fast forward and hovering flight. But quadrotors are not range-efficient, and at smaller scales, this is even worse [6]. They also require constant active stabilization, and their propellers must be shielded against even minor collisions during indoor exploration. In this respect, FWMAVs are an interesting alternative. They hold the potential for both fast forward and hovering flight, while the lift generated by the wings makes them energy efficient in forward flight. Moreover, they can obtain static longitudinal stability passively [7], and their wings can bounce off obstacles without appreciable damage upon low-speed collision. While some of these feats are common in nature—hummingbirds can for instance migrate over large distances while also maneuvering close to a flower upon arrival [8]—they remain a challenge for robotic MAVs. To combine fast forward flight and slow hovering flight, the FWMAV must exhibit stability in both flight modes. In this respect, two classes of FWMAVs can be discerned.

The first class is "tailless" and passively unstable in both flight modes [9–13]. They require active onboard sensing, actuation, and control to achieve stable flight. A significant obstacle is the design of sufficiently light, fast, and powerful actuation mechanisms [9, 11, 14], as the three requirements are conflicting. Moreover, this class of FWMAVs has mostly been designed for use around hover, and so far only little attention is paid to the fast flight regime.

The second class of FWMAVs has aerodynamic longitudinal and lateral-directional stabilizers—further called vertical and horizontal stabilizers or "tail"—and can obtain static longitudinal and lateral stability without the need for closed-loop control [15]. This is further called passive stability. The tail dampens rotation rates and also creates moments to correct attitude perturbations aerodynamically. Tailed FWMAVs are typically controlled using aerodynamic surfaces on the tail, such as a rudder and elevator. The flight speed at which the attitude of the tailed FWMAV is stable depends on the overall geometry and the location of the center of mass.

Existing tailed FWMAVs are often either designed for fast forward outdoor flight [7, 16–18] or for slow indoor flight [3, 19, 20], but not both combined. Active onboard stabilization of unstable tailed MAVs requires fast and strong actuators and is further complicated by the significant changes in the effectiveness of the aerodynamic control surfaces in various conditions, requiring precise airspeed measurements. This change in effectiveness also adds a resolution requirement to the actuation, as large deflections are needed in slow flight while precise small deflections are required in fast flight.

It would therefore be highly beneficial to achieve passive stability in all flight regimes [21]. Flying animals such as insects and birds extensively change the morphology of their body in different flight regimes [22]. For instance, dragonflies move their wings front and aft to displace the center of lift with respect to the center of gravity to maintain equilibrium and stability [23].

In this chapter, an FWMAV morphing mechanism is presented that displaces the relative position of the wings with respect to the center of gravity. We demonstrate that this mechanism allows the FWMAV to fly with passive stability in both fast forward and slow hovering flight. The remainder of the chapter is structured as follows. In Section 3.2, we compare the stability requirements of a tailed FWMAV in hover and forward flight. In Section 3.3, we present the DelFly flapping-wing platform and its morphing mechanism. Then, in Section 3.4 we discuss the experimental setup and show the results. Conclusions are drawn in Section 3.5 and recommendations are given in Section 3.6.

3.2. Passively Stable Flight

Passive aerodynamic stability of flapping-wing MAVs can be obtained by using horizontal and vertical aerodynamic stabilizers, also referred to as "tail" or "empennage" [7, 24]. However, stable flight is only obtained when the center of gravity (cg) lies within bounds called the stability margin. From experiments, it was seen that in FWMAV such as the DelFly, the stability bounds differ in the case of slow hovering flight and fast forward flight. The following sections will look at the differences in stability requirements in both regimes.

3.2.1. Model
To analyze the stability of the DelFly, a longitudinal model is introduced in Figure 3.1.

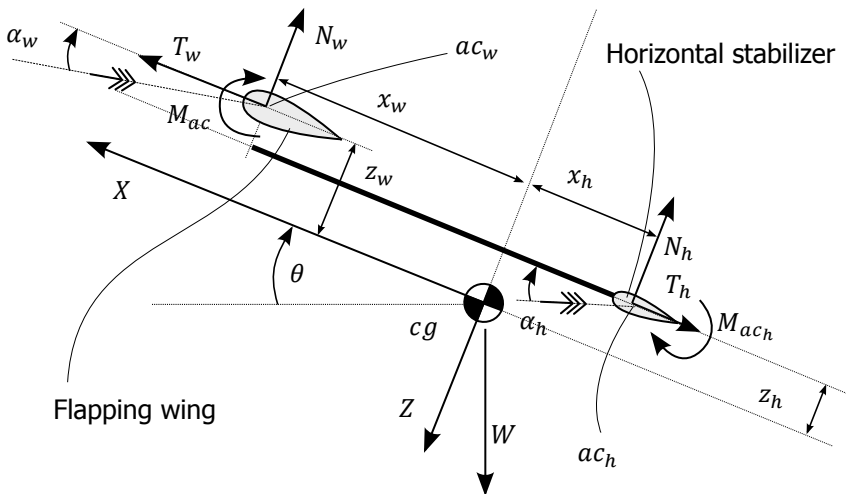Figure 3.1: Longitudinal dynamic model of the DelFly flapping wing.

The main wing has a normal aerodynamic force N_w and a tangential force T_w. Note that in the case of flapping-wing MAV, the tangential force points forward and provides thrust. The aerodynamic center ac_w is the point where the aerodynamic moment of the wing does not change with changes in angle of attack α_w. The

aerodynamic moment of the wing is M_{ac}. The horizontal stabilizer has normal force N_h, tangential force T_h, moment M_{ac_h} and an angle of attack α_h. In equilibrium, the vector sum of all aerodynamic forces and flapping wing thrust precisely balances out the weight W, and the total moment M around the center of gravity cg is zero:

$$M = M_{ac} + N_w \cdot x_w - T_w \cdot z_w + M_{ac_h} - N_h \cdot x_h + T_h \cdot z_h \qquad (3.1)$$

In non-dimensional form, the total pitching moment is defined as $C_m = M/(q \cdot S)$ where q is the free stream aerodynamic pressure $0.5 \cdot \rho V^2$ and S is the wing surface.

3.2.2. Conflicting stability requirements

Static longitudinal aerodynamic stability of DelFly refers to the principle that a perturbation in attitude $d\theta$ will lead to a correcting total aerodynamic pitch moment increment dC_m that counters the initial perturbation. In other words, the derivative of Equation (3.1) for θ should be negative. This applies to both hover and fast flight. To compute this derivative, the effect of attitude changes $d\theta$ on the normal and tangential forces N and T must be investigated. Aerodynamics theory shows that, for a given wing, lift and drag are influenced by the dynamic pressure q and the lift and drag coefficients, which themselves are a function of angle of attack α [25]. And for a given fluid, the dynamic pressure q is only dependent on the fluid velocity over the wing. What does differ in both flight phases is the effect that a change in pitch has on the change in angle of attack α and total speed $\vec{V}$ of airflow over the wings.
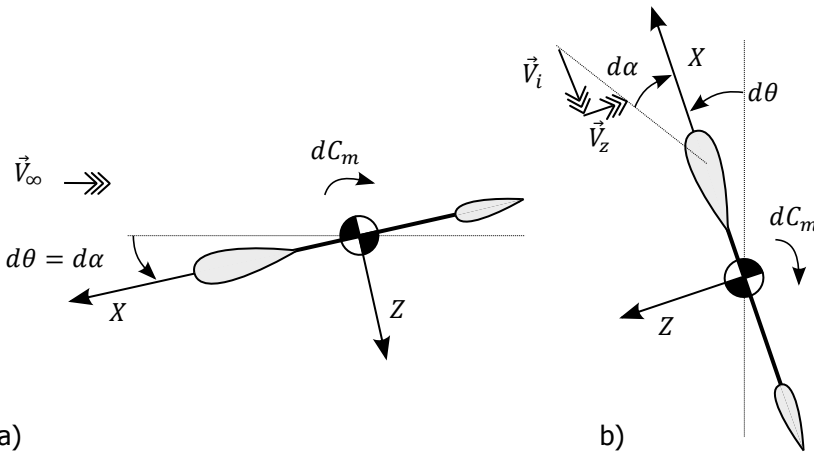
Figure 3.2: Static stability in hover and forward flight both require a positive moment C_m upon a negative perturbation $d\theta$. In forward flight, however, the negative change in pitch directly causes a negative change in angle of attack $d\alpha$ while in hover the same negative change in pitch indirectly induces a positive change in angle of attack. The free-stream velocity in forward flight is $\vec{V}_\infty$, the induced velocity from the flapping wings in hover is $\vec{V}_i$ and the lateral body velocity in hover is $\vec{V}_z$.

In fast forward flight, the so-called fixed-stick static longitudinal stability theory of fixed-wing aircraft [26] states that in stationary flight, a negative pitch perturba-

tion $d\theta$ of the aircraft in an airflow with free-stream velocity $\vec{V}_\infty$, directly leads to a decrease in angle of attack $d\alpha$ which needs to be corrected by a positive nose-up pitch moment dC_m to return towards the equilibrium state as shown in Figure 3.2a. The effect that a change in pitch directly has on the airflow $\vec{V}_\infty$ is neglectable. The condition for stability is written as

$$\frac{dC_m}{d\theta} < 0 \implies \frac{dC_m}{d\alpha} < 0 \tag{3.2}$$

and is analyzed at the point where $C_m = 0$, which in equilibrium for a DelFly corresponds to the location of its center of gravity.

In hover, on the other hand, the increment $d\theta$ does not directly lead to a different angle of attack since the DelFly does not move and there is no free-stream velocity $\vec{V}_\infty$. Instead, there is only an induced flow over the flapping wings $\vec{V}_i$ as shown in Figure 3.3, which for DelFly II was measured to be on average about 2 to 3 m/s. This induced flow remains largely aligned with the fuselage and thus tilts with the pitch angle θ and does not directly generate any attitude correcting pitch moment.
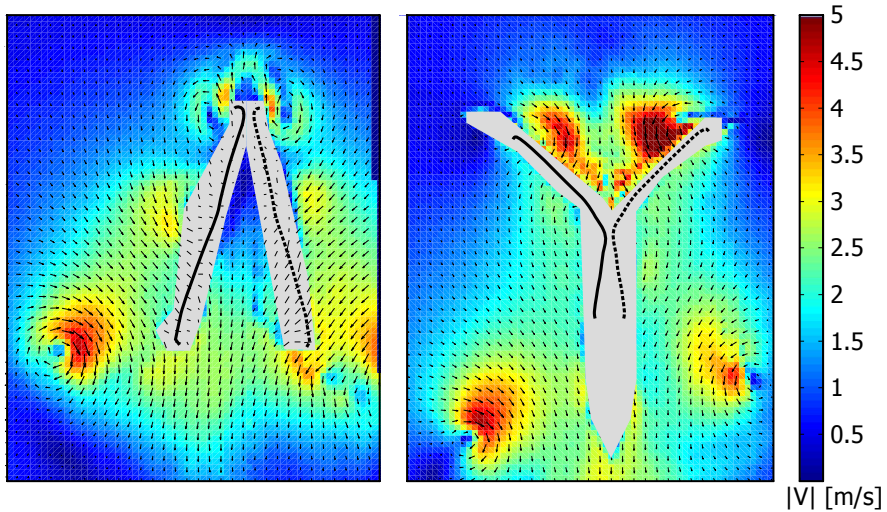
Figure 3.3: Cross-section of the induced flow over the wings of the DelFly as measured from Particle Image Velocimetry (PIV) [4] and showing the non-steady aerodynamics and time-varying induced down-flow $\vec{V}_i$ containing leading and trailing edge vortices.

The tilted fuselage, however, also tilts the thrust vector and this integrates into a lateral velocity $\vec{V}_z$. Combined with the induced flow velocity $\vec{V}_i$ from the flapping wings, the total airflow $\vec{V}_i + \vec{V}_z$ is seen by the DelFly as a positive change in angle of attack $d\alpha$ as shown in Figure 3.2b. To correct this perturbed state, a positive pitch-up moment C_m is required from this increased angle of attack. This can be expressed as

$$\frac{dC_m}{d\theta} < 0 \implies \frac{dC_m}{d\alpha} > 0 \tag{3.3}$$

As seen from Equation (3.2) and Equation (3.3), the requirement for stability in hover and forward flight are the exact opposites of each other in both regimes.

The point where the $dC_m/d\alpha = 0$ is called the neutral point. While the exact computation of the location of the neutral point in DelFly is challenging due to the unsteady aerodynamic flow which changes local angles of attack in function of time (See Figure 3.3), what is known is that the cg must be in front of the neutral point in fast forward flight (Equation (3.2)) and behind it for hover (Equation (3.3)).

Experimental attempts to find a center of gravity enabling both flight regimes confirmed that only a single regime could be made longitudinally stable [3]. Forward flight with an aft center of gravity causes unstable diving as soon as a critical forward speed is reached, and slow hovering flight with a forward center of gravity instantly falls back to fast forward flight. Combining aerodynamic stability in both regimes requires an inflight change in $dC_m/d\alpha$.

3.3. Morphing mechanism

To obtain longitudinally stable flight from slow hovering flight to fast forward flight, the location of the center of gravity (cg) has to be moved from one side of the neutral point to the other. This can be accomplished in several ways. One obvious way is to move a heavy component and thereby the center of gravity. Another way is to move of the entire wing and thereby also move the neutral point.
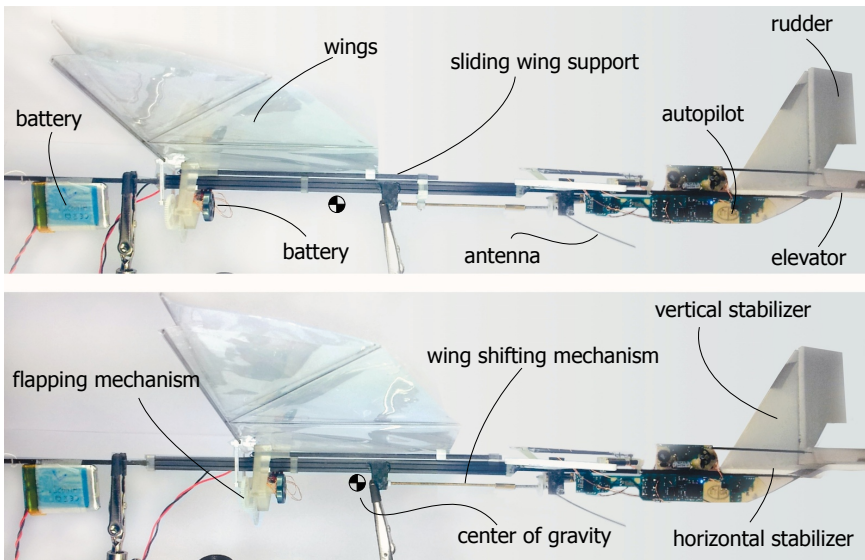

Figure 3.4: Side view of DelFly LiMo showing the wing forward for slow forward flight (top) and aft for fast forward flight (bottom) with a positive stability margin.
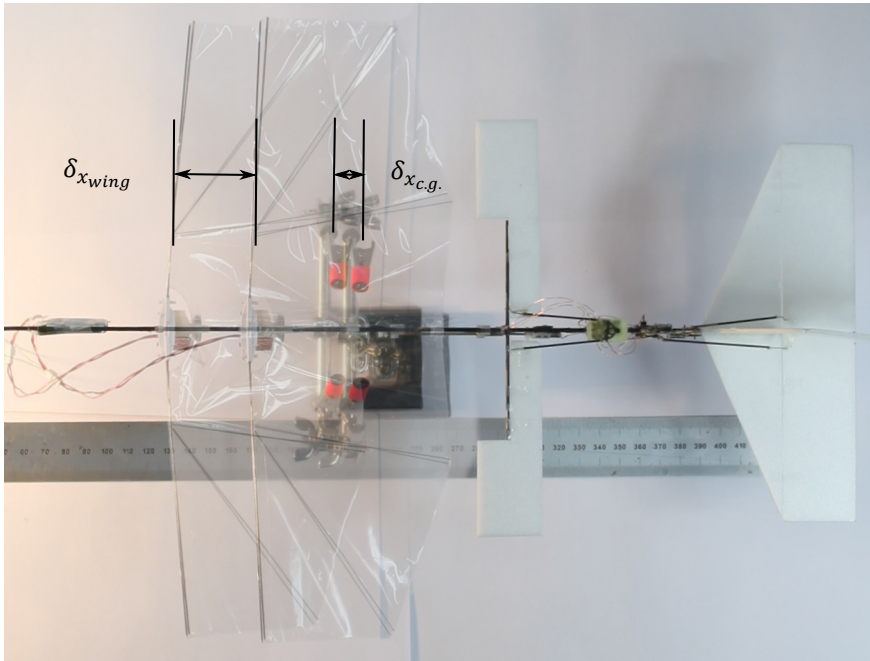
Figure 3.5: Photos of the wing configurations for hover and fast flight superimposed on each other. The DelFly LiMo is balanced on red supports under each wing to show the longitudinal location of the center of gravity. When the wing is shifted forward, the cg also shifts forward with $\delta_{x_{cg}}$. The change in position of the main wing $\delta_{x_{wing}}$ is visible by the difference in location of the wing leading edges.

3.3.1. DelFly Limo

It was empirically established that a shift of 3 cm in the relative position of the wing and cg was needed to obtain favorable flight characteristics of the DelFly II in both flight regimes [3]. While shifting the battery—which is the heaviest component—seems the simplest way of achieving this, the battery weighs only 4 g compared to the 16 g of the total platform. It would therefore have to shift 12 cm, which presents considerable challenges considering the total length is only 28 cm.

Instead, moving the wing together with the attached motor, motor housing, gears and Electronic Speed Controller (ESC) requires much smaller motions to obtain the same result. Because the wing and motor make up about one-quarter of the total mass, this shift also moves the location of the cg as illustrated in Figure 3.5. When the wing is shifted forward 4.2 cm ($\delta_{x_{wing}}$), the cg moves forward 1.0 cm ($\delta_{x_{cg}}$). The net effect is a change of 3.2 cm in the position of the cg relative to the aerodynamic center. In slow hovering flight with the wing extended forward, the cg lies at ∼ 85 % chord length. In fast forward flight, the cg lies at ∼ 55 % chord length when the wing is moved back.

A DelFly II was modified and called DelFly LiMo and equipped with a linear sliding motion system that moves the main wing along the fuselage, shown in Figure 3.4.

Figure 3.6: Two hard plastic injection molded sliders (white/left) clamp two round carbon rods (middle), over which the complete wing, motor house, mo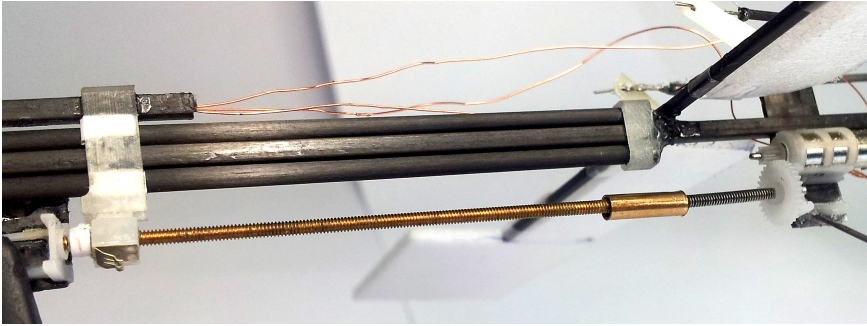tor, and Electronic Speed Controller (ESC) moves. The lead nut is attached to the main wing (bottom left). The lead screw runs via gearing to a small brushed motor (right)

Using a threaded rod driven by gears from a 1.6-gram micro servo, a slow but powerful and light actuator was created (See Figure 3.6). The wing is moved 42 mm in about 1 s when transitioning to hover and a bit more in the opposite direction due to the load of the wing pulling on the mechanism.

To obtain low friction, the main wing was equipped with two sliders made of hard injection-molded plastic that slide over two rounded carbon rods attached to the main body. The dual rod construction prevents the main wing from rotating along the longitudinal axis and is shown in Figure 3.6. The total system makes the DelFly LiMo 4 g heavier than the regular DelFly II, leading to a total of 20 g.

3.4. Flight testing

Flight tests in both regimes were performed to assess the stability, as well as the transitions from slow to fast forward flight and vice versa. The DelFly LiMo was first flown in the TUDelft "Cyberzoo," which is equipped with an OptiTrack motion capture system to measure DelFly's position and attitude.

Figure 3.7 shows transitions from forward center of gravity to hovering center of gravity in the left column. The pitch angle θ cannot be kept in a hovering attitude but drops after takeoff until the mechanism transitions to hover at the red line. Then the DelFly automatically slows down again to slow hovering flight. The right column shows measurements that start in a slow hovering flight. The DelFly LiMo is passively stable and is easily flown hands-off when properly trimmed in this regime. It flies at a speed of 0.8 m/s at a pitch angle of 55°. After switching to forward flight at the red line, the DelFly LiMo pitches forward and picks up speed. No significant elevator control input was given during the hand-flown maneuver. Once the forward flight speed is reached, the DelFly remains stable and flies much like a fixed-wing aircraft. The DelFly LiMo was also flown outdoors in fast flight to illustrate its stability. Flight speed is estimated to be around 5 to 7 m/s. Transitions in both directions were successfully performed and resulted in good flight characteristics in both regimes.

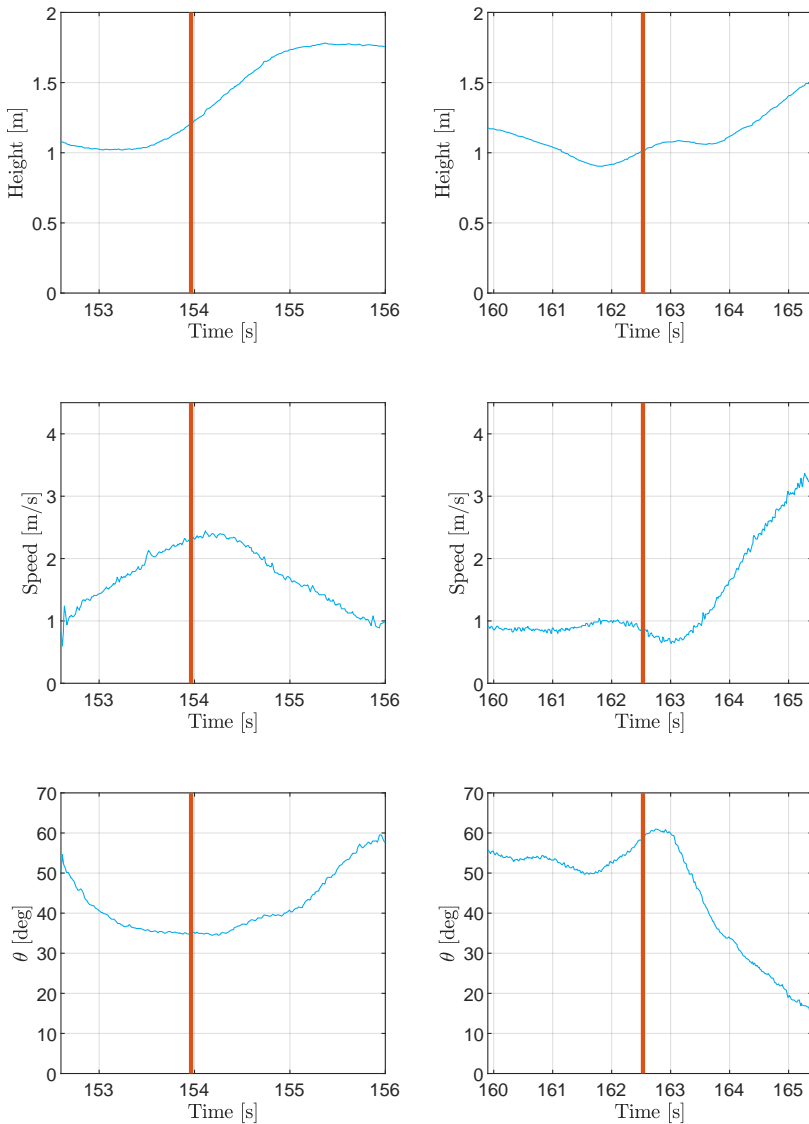Figure 3.7: Height, speed, and pitch angle θ during the acceleration to forward flight and subsequent transition to hover (left) and transition from slow hovering flight to fast forward flight (right) during tests in the CyberZoo. The time at which the main wing shifts starts is indicated with a red vertical line. Due to the limited size of the test area, the DelFly LiMo can not reach its top speed of around 5 to 7 m/s.

3.5. Conclusion

The analysis of the stability of slow hovering flight and fast forward flight of the DelFly flapping-wing MAV showed different requirements for the location of the center of gravity in both flight regimes. Therefore a morphing wing mechanism was developed to enlarge its passively stable flight envelope. A lightweight system was presented capable of generating a large enough force to move the main wing over the required 4 cm. The proof of concept was successfully tested indoors and outdoors. With this system, the so-called "DelFly LiMo" is capable of adapting its flight dynamics to achieve passively stable flight in both slow hovering and fast forward flight.

3.6. Recommendations

Although the presented analysis captures simplified essential properties of the stability of the DelFly, our understanding of the unsteady aerodynamics and flight dynamics is still very limited. Better knowledge of the flapping wing aerodynamics will give insight into the many non-linear effects that could explain in greater detail how the DelFly flies. While the presented actuator is light and under 1.6 g, the total added weight of the mechanism of 4 g might allow other solutions to be implemented. Any solution resulting in fast, light, and powerful (reliable) actuators will have a very important beneficial effect on the flight performance of MAV.

References

[1] J. A. Koopmans, S. Tijmons, C. De Wagter, and G. C. H. E. de Croon, *Passively stable flapping flight from hover to fast forward through shift in wing position,* International Journal of Micro Air Vehicles **7**, 407 (2015).

[2] J. A. Koopmans, S. Tijmons, C. De Wagter, and G. C. H. E. de Croon, *Passively stable flapping flight from hover to fast forward through shift in wing position,* in *International Micro Air Vehicles Conference and Flight Competition IMAV 2015* (IMAV, Aachen, Germany, 2015).

[3] J. V. Caetano, C. C. de Visser, G. C. H. E. de Croon, B. Remes, C. De Wagter, J. Verboom, and M. Mulder, *Linear aerodynamic model identification of a flapping wing mav based on flight test data,* International Journal of Micro Air Vehicles **5**, 273 (2013).

[4] G. C. H. E. de Croon, M. Perçin, B. D. W. Remes, R. Ruijsink, and C. De Wagter, *The DelFly: Design, Aerodynamics, and Artificial Intelligence of a Flapping Wing Robot*, 1st ed. (Springer Netherlands, 2016).

[5] T. Tomic, K. Schmid, P. Lutz, A. Domel, M. Kassecker, E. Mair, I. Grixa, F. Ruess, M. Suppa, and D. Burschka, *Toward a fully autonomous UAV: Research platform for indoor and outdoor urban search and rescue,* IEEE Robotics & Automation Magazine **19**, 46 (2012).

[6] S. Bouabdallah, P. Murrieri, and R. Siegwart, *Design and control of an indoor micro quadrotor,* in *IEEE International Conference on Robotics and Automation, 2004. Proceedings. ICRA '04. 2004* (IEEE, 2004).

[7] J. M. Dietl and E. Garcia, *Stability in ornithopter longitudinal flight dynamics,* Journal of Guidance, Control, and Dynamics **31**, 1157 (2008).

[8] P. Chai and R. Dudley, *Maximum flight performance of hummingbirds: Capacities, constraints, and trade-offs,* The American Naturalist **153**, 398 (1999).

[9] M. Keennon, K. Klingebiel, H. Won, and A. Andriukov, *Development of the nano hummingbird: A tailless flapping wing micro air vehicle,* in *50th AIAA Aerospace Sciences Meeting including the New Horizons Forum and Aerospace Exposition* (American Institute of Aeronautics and Astronautics, 2012) pp. 1–24.

[10] K. Ma, P. Chirarattananon, S. Fuller, and R. Wood, *Controlled flight of a biologically inspired, insect-scale robot.* Science **340**, 603 (2013).

[11] R. Wood, *The first takeoff of a biologically-inspired at-scale robotic insect,* IEEE Transactions on Robotics **24**, 341 (2008).

[12] S. Fuller, E. Helbling, P. Chirarattananon, and R. Wood, *Using a gyroscope to stabilize the attitude of a fly-sized hovering robot,* in *International Micro Air Vechicle Competition and Conference 2014* (Delft, The Netherlands, 2014) pp. 102–109.

[13] N. Gaissert, R. Mugrauer, G. Mugrauer, A. Jebens, K. Jebens, and E. M. Knubben, *Inventing a micro aerial vehicle inspired by the mechanics of dragonfly flight,* in *Towards Autonomous Robotic Systems* (Springer, 2014) pp. 90–100.

[14] M. T. Keennon, A. Andryukov, K. R. Klingebiel, and H. T. Won, *Air vehicle flight mechanism and control method for non-sinusoidal wing flapping,* (2012).

[15] J. V. Caetano, J. Verboom, C. C. de Visser, G. C. H. E. de Croon, B. D. W. Remes, C. De Wagter, and M. Mulder, *Near-hover flapping wing mav aerodynamic modelling - a linear model approach,* in *Proceedings of the International Micro Air Vehicle Conference and Flight Competition IMAV 2013* (IMAV, Toulouse, France, 2013) pp. 79–88.

[16] J. Gerdes, S. Gupta, and S. Wilkerson, *A review of bird-inspired flapping wing miniature air vehicle designs,* Journal of Mechanism and Robotics **4** (2012), 10.1115/1.4005525.

[17] J. Gerdes, A. Holness, A. Perez-Rosado, L. Roberts, E. Barnett, A. Greisinger, J. Kempny, D. Lingam, C.-H. Yeh, H. Bruck, *et al., Design, manufacturing, and testing of robo raven,* Digital Repository at the University of Maryland (2014).

3

[18] J. Grauer, E. Ulrich, J. E. Hubbard, D. Pines, and J. S. Humbert, *Testing and system identification of an ornithopter in longitudinal flight,* Journal of Aircraft **48**, 660 (2011).

[19] S. Baek and R. Fearing, *Flight forces and altitude regulation of 12 gram i-bird,* in *IEEE RAS and EMBS International Conference on Biomedical Robotics and Biomechatronics (BioRob)* (2010) pp. 454–460.

[20] G. C. H. E. de Croon, M. A. Groen, C. De Wagter, B. Remes, R. Ruijsink, and B. W. van Oudheusden, *Design, aerodynamics and autonomy of the delfly,* Bioinspiration & Biomimetics **7**, 1 (2012).

[21] S. Barbarino, O. Bilgen, R. M. Ajaj, M. I. Friswell, and D. J. Inman, *A review of morphing aircraft,* Journal of Intelligent Material Systems and Structures **22**, 823 (2011).

[22] R. J. Wootton, *The mechanical design of insect wings,* Scientific American **263**, 114 (1990).

[23] A. Azuma and T. Watanabe, *Flight performance of a dragonfly,* Journal of Experimental Biology **137**, 221 (1988).

[24] H. E. Taha, M. R. Hajj, and A. H. Nayfeh, *Flight dynamics and control of flapping-wing mavs: a review,* Nonlinear Dynamics **70**, 907 (2012).

[25] S. F. Armanini, J. V. Caetano, G. C. H. E. de Croon, C. C. de Visser, and M. Mulder, *Quasi-steady aerodynamic model of clap-and-fling flapping MAV and validation using free-flight data,* Bioinspiration & Biomimetics **11**, 046002 (2016).

[26] A. Filippone, *Static longitudinal stability,* in *Encyclopedia of Aerospace Engineering* (John Wiley & Sons, Ltd, 2010).

4

Quad-thopter

Discovery is seeing what everybody else has seen, and thinking what nobody else has thought.

dr. Abert Szent-Gyorgyi

We present a novel design of a tailless FWMAV, which uses four independently driven pairs of flapping wings to fly and perform agile maneuvers. The wing pairs are arranged such that differential thrust generates the desired roll and pitch moments, similar to a quadrotor. Moreover, two pairs of wings are tilted clockwise and two pairs of wings anti-clockwise. This allows the MAV to generate a yaw moment. We have constructed the design and performed multiple flight tests with it, both indoors and outdoors. These tests have shown the vehicle to be capable of agile maneuvers, and able to cope with wind gusts. The main advantage is that the proposed design is relatively simple to produce, and yet has the capabilities expected of tailless flapping wing MAVs.
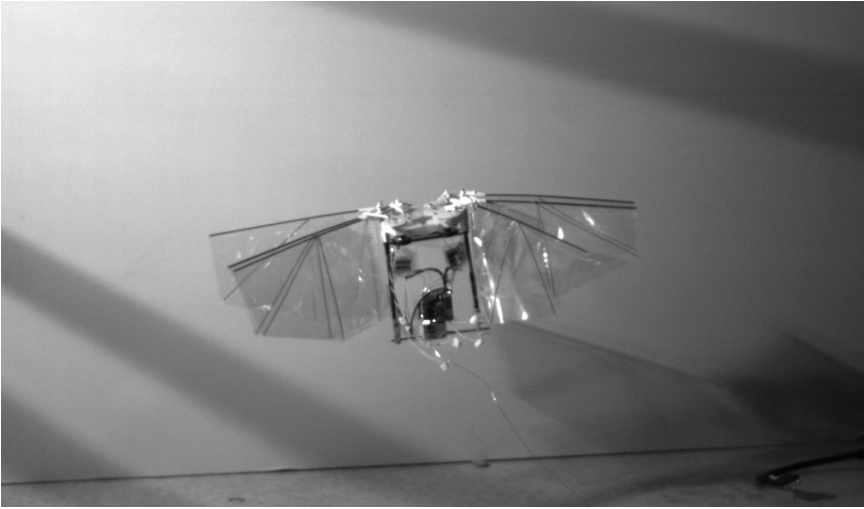
Figure 4.1: High speed camera recording of a quad-thopter

4.1. Introduction

Flying animals remain unrivaled when it comes to their flying skills and flight characteristics. Hummingbirds can hover and maneuver in narrow spaces to feed and then subsequently fly hundreds of kilometers when migrating [5]. Besides the energy and sensory processing aspects, a great deal of the advantages of flying animals over current Micro Air Vehicle (MAV)s is attributed to their way of propulsion. Flapping wings are predicted to achieve higher lift coefficients than conventional MAV designs, especially when scaled further down towards insect scales. In addition, they are expected to have a higher energy efficiency when flying at higher speeds, extending the range and duration of the flight [6].

Despite considerable efforts—and successes [7, 8]—in the last few decades, the dominating MAV types are still rotorcraft, fixed wings, or recently combinations of both [9, 10]. An important reason for this is the difficulty of producing a flapping wing MAV that fulfills some of the promises of animal flight.

On the one hand, there is a large class of "tailed" flapping-wing MAVs, which goes back to rubber-band flapping wing vehicles designed in the 19th century [11]. Flapping wing MAVs such as "small bird" [12], "big bird" [13], or the "DelFly" [14], have single degree of freedom motor-driven flapping wings for generating thrust. The control moments are generated by actuated control surfaces on the tail. Since the tail is relatively large, it dampens the body dynamics sufficiently to make this type of MAV passively stable [15].

The tail actuation typically consists of a rudder and an elevator and can be used for changing the MAV's direction, height, or velocity. However, the aerodynamically stabilizing tail section also makes the vehicle particularly sensitive to external perturbations [14]. The forces and moments generated by the tail actuators are in general insufficient to compensate perturbations in 'gusty' environments, with even

air-conditioning causing considerable problems to these light wing loading MAVs [16]. Finally, elevator and rudder effectiveness vary orders of magnitude based on the incoming airflow and can even reverse when descending in hover. This makes tuning autopilot control loops dependent on more sensors and creates uncontrollable areas in the flight envelope.

On the other hand, there is a growing class of "tailless" flapping-wing MAVs, which use the wings themselves for control. The idea is that the wings can generate much larger forces and moments in shorter amounts of time than tailed actuators. In combination with the absence of a tail and its damping effect, this leads to higher maneuverability. The first successful design of this class was the "Nano Hummingbird" [7]. It featured an ingenious but complex mechanism to generate all three moments required for full attitude control. Recently, other MAVs of similar size have been designed, which aim for simpler designs, but which have not yet shown the same maneuverability as the Nano Hummingbird and, at the same time, suffer from very limited flight endurance of several tens of seconds at best [17–20]. The smallest type of flapping-wing MAV of this class is the well-known 'Robobee' [21], which for now requires the energy source to be off-board.

Although current tailless flapping wing MAVs are closing in on the ideal set by nature, none of them are yet able to perform real flight missions and are at the same time relatively easy to construct.

To broaden the field of application of flapping-wing MAVs, a light and simple wing actuation mechanism would be needed that can quickly create large attitude control moments in all three axes. Based on this idea, we present in this paper a new tailless flapping wing MAV design, referred to as a "quad-thopter". The design is similar to a quadrotor, in the sense that it uses the thrust of four wing-pairs to do thrust vectoring (Figure 4.1). It is also reminiscent of the very early "Mentor" design [22], which also had four wing pairs for flying. However, that design used a single main actuator driving the 4 wings at the same flapping frequency. The control relied upon control surfaces interacting with the wake of the flapping wings, which reduces their effectiveness and limits the controllability of the system. Instead, the "quad-thopter" can drive all wings independently from zero to maximal thrust, which can generate significant roll and pitch moments, and the flapping planes of diagonally opposing wing-pairs are tilted with respect to each other for yaw controllability.

The quad-thopter design proposed in this paper represents a close-to-optimal choice in the design space consisting of the magnitude of the generated control moments, the control bandwidth, and the weight, size, and energy requirements of the actuators. In addition, the quad-thopter is relatively easy to construct with widely available current-day technology, and has a flight time of 9 minutes or more, depending on the flight regime. Hence, it is suitable for real-world missions.

In Section 4.2, we discuss current flapping-wing designs and actuators in more detail, to get a better understanding of the difficulties involved in tailless flapping wing MAV design. Then, in Section 4.3, we present the new design. We study the body's vibrations in Section 4.4 and the less evident yaw moment generation in Section 4.5. We describe the flight characteristics in Section 4.6, showing pictures of the flapping wing MAV in flight and providing links to flight footage. Finally,

we discuss possible variations of the design in Section 4.7 and draw conclusions in Section 4.8.

4.2. Tailless flapping wing

Most ornithopter designs use a tail, which provides passive aerodynamic stabilization and typically carries also conventional actuated control surfaces. When the tail is removed, active stabilization becomes necessary and some mechanism is required to create the 3 moments needed to orient and stabilize the platform.

Many solutions have been proposed. Some add propeller thrusters besides the flapping wing [23]. But the vast majority of researchers, inspired by biological fliers, search for new degrees of freedom to incorporate in the main flapping wings to vary their aerodynamic force over the flapping cycle [7, 8, 17, 20, 21, 24, 25]. To use these degrees of freedom in closed-loop control, they must be actuated with sufficient speed and force.

4.2.1. Hovering without tail

The minimal requirement for controllable hovering of an aircraft is being able to control the thrust vector. Instead of controlling the 6 DOF (3D position and 3 attitude angles) of the free-flying body directly, 2 position variables are controlled indirectly through the attitude which in turn controls the thrust vector and hereby the longitudinal and lateral acceleration. This allows for a 6-DOF hover with only 4 independent control variables. Most concepts use flapping power control combined with 3 external actuators—for instance, to move the roots of trailing edges [26] or drive all the flapping degrees of freedom [17]. Since actuators do not contribute to thrust generation but only add weight, these must be very light. Finding sufficiently light, fast, and strong actuators is an integral part of designing a flight-capable multi-degree of freedom flapping mechanism.

4.2.2. Actuator Review

The main driving motor must be sized to produce sufficient thrust. Sizing the control actuators is more complex. In practice, on small flapping-wing vehicles in the presence of disturbance, actuators must be fast, strong, and light. This combined requirement is not trivial.

Coil actuators (Figure 4.2 (a)) are fast but create very small moments, which makes them suitable only for actuation of conventional tail control surfaces [27]. Shape memory alloys (Figure 4.2 (b)) have shown high strength at minimal weight, but are slow, fragile, and create minimal deflections, that need to be amplified [28].

Most servos consist of small brushed motors with a reduction gearbox and include a position feedback mechanism with a potentiometer (Figure 4.2 (c)) or magnet and hall effect sensor (Figure 4.2 (d)). The gear ratio can be altered to change the speed versus force, but to increase both, a larger and heavier motor is needed; its size can even come close to the size of the main flapping motor. In contrast with the main motor which runs all the time, actuator motors are used very inefficiently and only work part of the time.

(a)

(b)

(c)

(d)
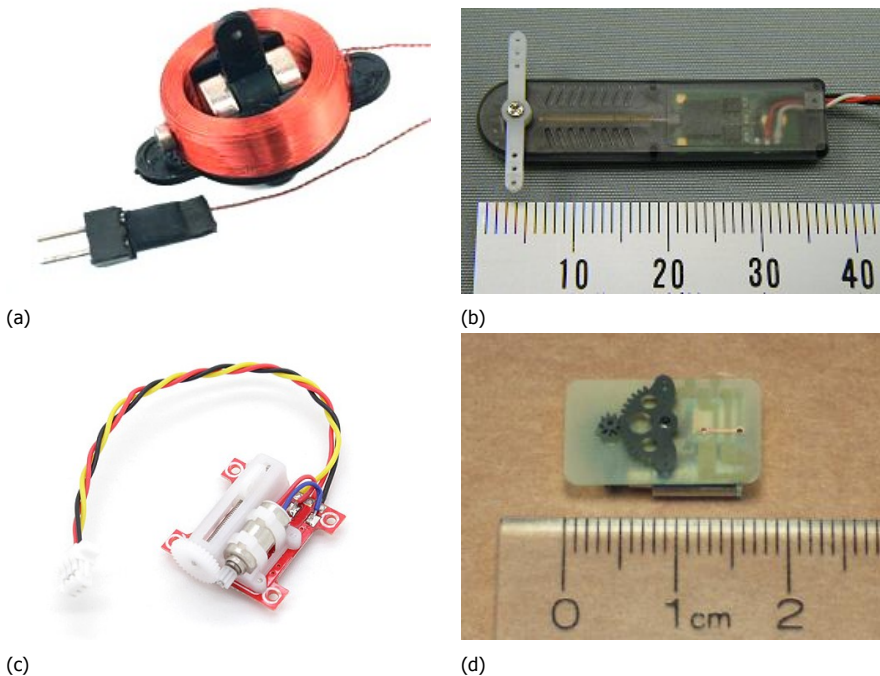
Figure 4.2: Overview of actuator types for lightweight flapping wing MAVs: (a) magnetic servos, (b) shape memory alloy servos, and servos with brushed Direct Current (DC) motors (c) and (d) (images from www.microflight.com, www.servoshop.co.uk, www.hobbyking.com, www.microflierradio.com).

4.2.3. Moment control using the flapping motor

To use most of the actuators in their efficient regime, the main flapping actuator(s) can be used to also generate the control moments. Such an idea is not novel. RoboBee [21] uses the two main flapping piezo-actuators driven with independent waveforms to generate the 4 independent controls (See Figure 4.3 (a)). The flapping amplitudes of the left and right wings can be driven independently, and a bias can be added (to both actuators) for pitch control. Finally, a speed difference in up and down-stroke can generate yaw moments, while the same flapping motion also provides the main thrust force.

The quest to achieve this same idea using traditional rotating electric motors has led some researchers to attach brushed motors directly to the wings [29] as illustrated in Figure 4.3 (b). These motors are used outside their design operational regime with very low efficiency and high wear as they vibrate back and forth instead of turning in one direction at high speed. Nevertheless, their efficiency can be improved by using resonance mechanisms. All 3 required control moments can be generated by varying amplitude of the stroke and velocity profiles within the stroke in a differential way (left/right and upstroke/downstroke).

Still, electric motors are most efficient when turning at higher speed, in which

(a)

(b)
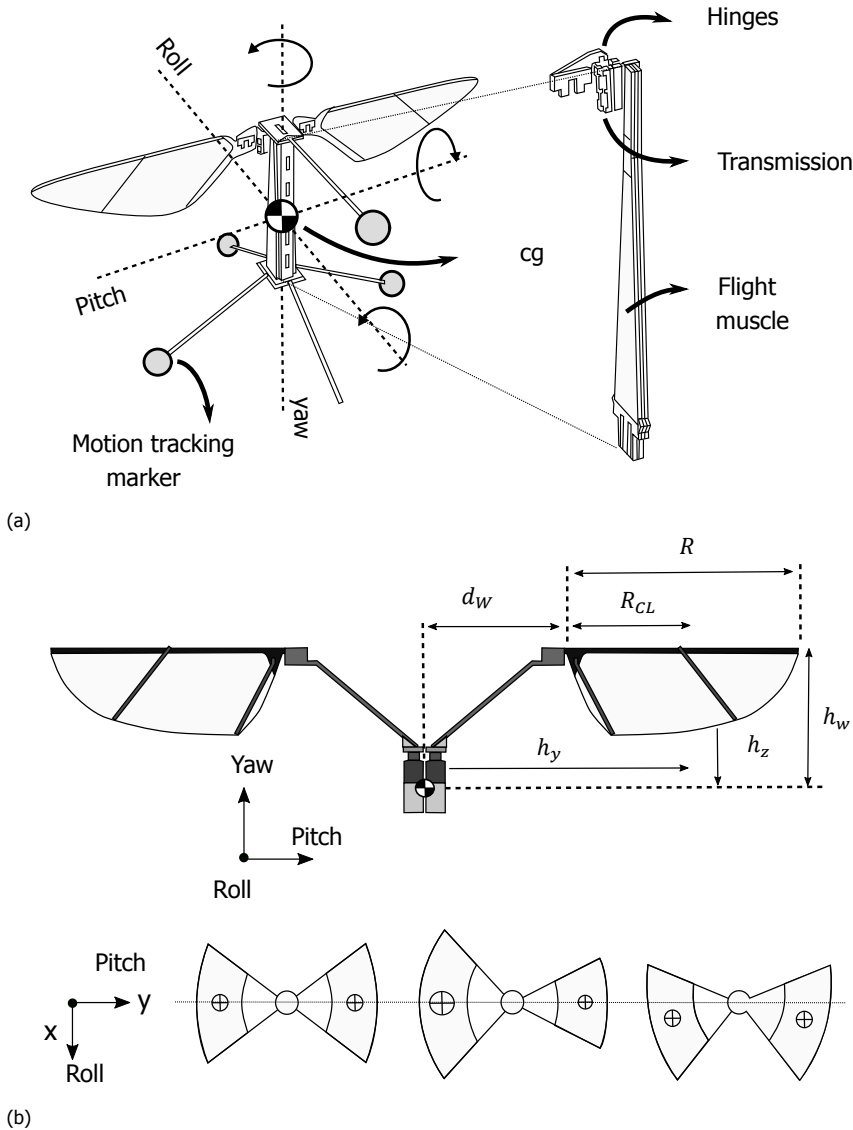
Figure 4.3: MAV designs that use their main actuators also for control: (a) piezo actuators [21] and (b) brushed DCs [29].

case a crank mechanism is required. Unless a variable crank mechanism is used—which in turn is controlled by actuators—this makes it impossible to vary amplitude anymore while also the phase and frequency become coupled.

To generate different thrusts on the left and right wings, they must be uncoupled and driven by separate motors. In this case, the motors are used efficiently, since their main task remains to be thrust generation, while variations anywhere between

zero and full power can yield very large moments with minimal response times. This, however, comes at the cost that it is impossible to keep both wings in phase.

4.3. The Quad-thopter

In order to have full control authority in hover, which requires at least an indepen-dent generation of at the three-body moments and the total thrust, one solution is to combine four sets of wings, each driven by a separate motor and a crankshaft as is shown in Figure 4.4. When the four thrust vectors can be controlled inde-pendently, this can generate moments for attitude control much like a quadrotor, allowing full 3D hover control.

But unlike in a quadrotor, where propellers have a non-zero average torque, additional control is needed for the yaw. This can be obtained by tilting the thrust vectors with respect to the average thrust vector.

This setup does still suffer from the effect described in Section 4.2 that wings can flap out of phase. This could potentially lead to very large yawing moments on the fuselage, resulting in fuselage rotation that will cause loss of flapping amplitude and loss of lift. To cope with this problem, instead of using single flapping wings, a phase-locked pair of wings as found in for instance the DelFly II [14] is used instead. This means that whatever frequency each of the four motors is running, for every

Figure 4.4: Quad-thopter. Four pairs of flapping wings are arranged in an X-configuration with a small angle between thrust vectors to allow control of the yaw axis.
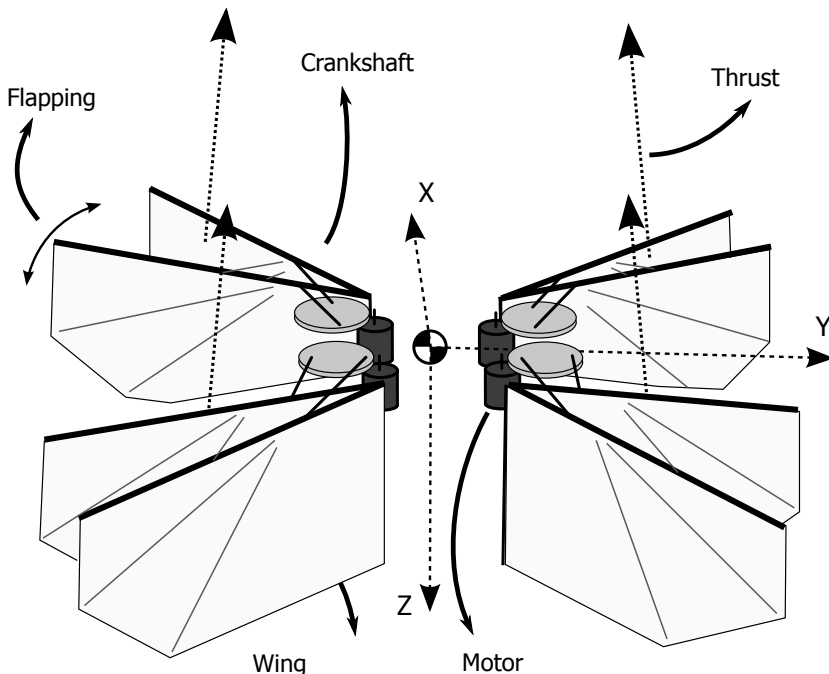
single wing moving one way there is a corresponding wing moving the other way, canceling each other out.

The resulting setup has fast and powerful attitude control while its complexity remains moderate. On the one hand, four gearboxes are needed, but on the other hand, a simple, fixed gear crankshaft can be used. Fragile, underpowered, slow, or expensive actuators are no longer needed. In terms of weight, all actuators are directly used to create thrust, which increases efficiency and maximally available thrust.

The lack of tail section significantly reduces the sensitivity for perturbations, while active attitude control with full authority controls the attitude. This enables maneuvers that were not possible with the tail, like a fast vertical descend.

The platform is capable of transitioning to forward flight in the same way as its tailed counterpart. In forward flight, the attitude must also be actively controlled. Similarly, as with hybrids like the Quadshot [9], the vehicle pitches down almost 90° and the wings start to produce lift perpendicularly to the thrust direction.

4.4. Residual Vibration

Although the moments of the flapping itself are canceled out during stationary hover as shown in Figure 4.5, the thrust generated by a wing pair is non-constant in time. The fact that all wings generate thrust and flapping-torque with peaks at different times still results in vibrations on the main central fuselage.

The DelFly concept has been using a double pair of flapping wings to minimize fuselage rocking. For every wing performing an upstroke, there is exactly one wing doing a downstroke. The double pair of wings doing clap and fling has also been shown to achieve higher thrust density [14].

This concept can be re-used in the tail-less flapper with 4 wings and 4 motors. Replacing every wing with a pair of wings flapping in anti-phase, removed the largest residual vibration. The wing mass, in this case, does not cause large inertial vibrations anymore, because for any wing moving in one direction another wing moves in the opposing direction.

The result is a vehicle with 4 main driving motors and 4 pairs of flapping wings flapping at different rates. The main residual vibration now is when 2 opposing pairs flap with 90° phase shift, with the difference between the minimal thrust during a stroke and the maximum thrust during a stroke as the driving force for the vibration. Due to their different rates, the phase shift is not constant, but varies over time; a beat phenomenon (vibration of pulsating amplitude) will be present, see Figure 4.6. When using a wing design with small thrust variation during a stroke, this vibration can be reduced to acceptably small levels.

To keep fuselage motion to a minimum, fuselage inertia $I = m \cdot r^2$ plays an important role. Maximizing the rotational inertia without increasing the weight will minimize vibrations.

(a)

(b)
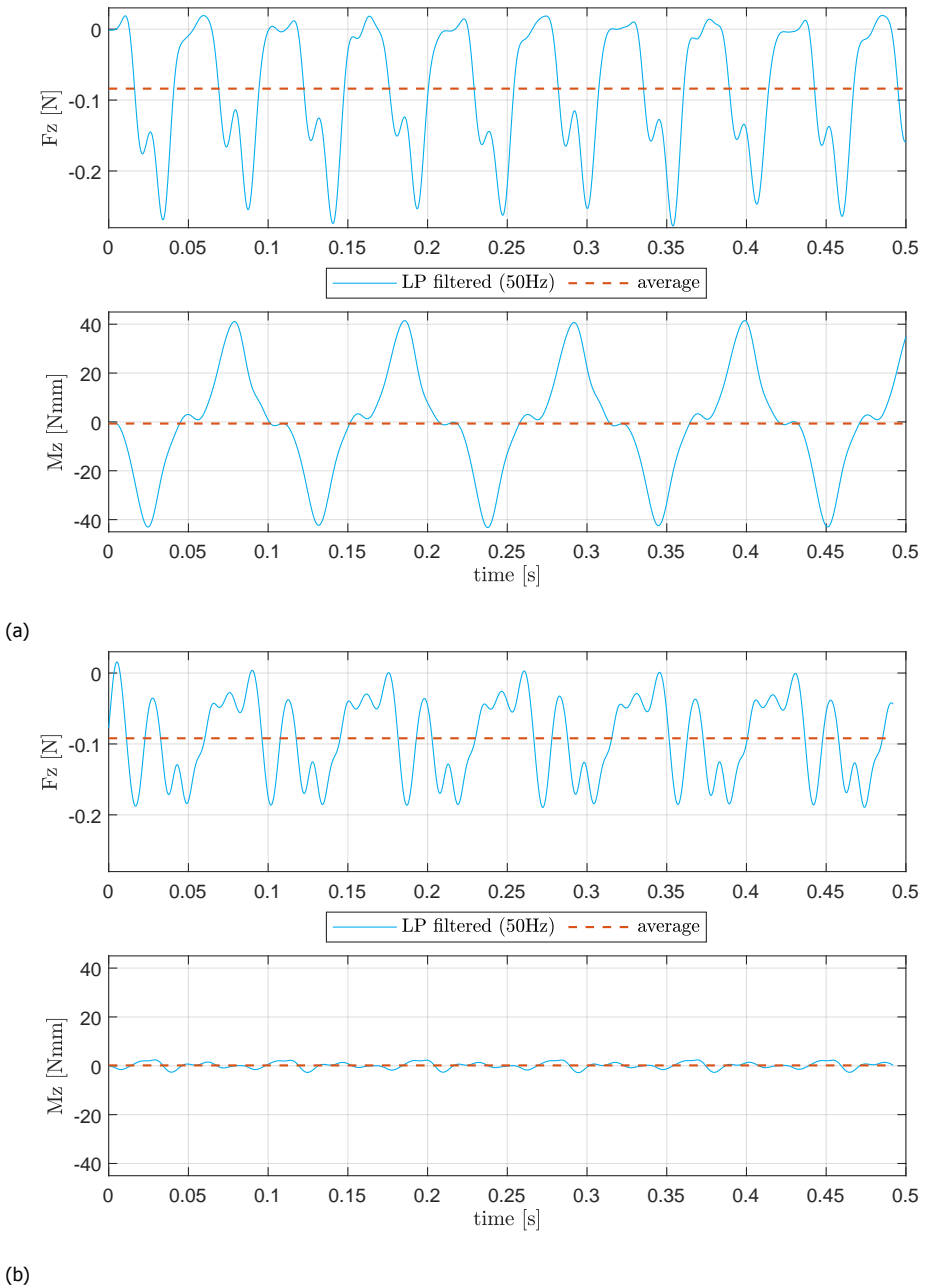
Figure 4.5: Thrust force and moment around principal body axis (data include also inertial effects): (a) single-wing flapping with 90-degree amplitude, (b) double-wing flapping in antiphase with 40-degree amplitude. The reaction torque on the body is significantly reduced when using the double-wing setup while generating a similar amount of thrust as the single wing.
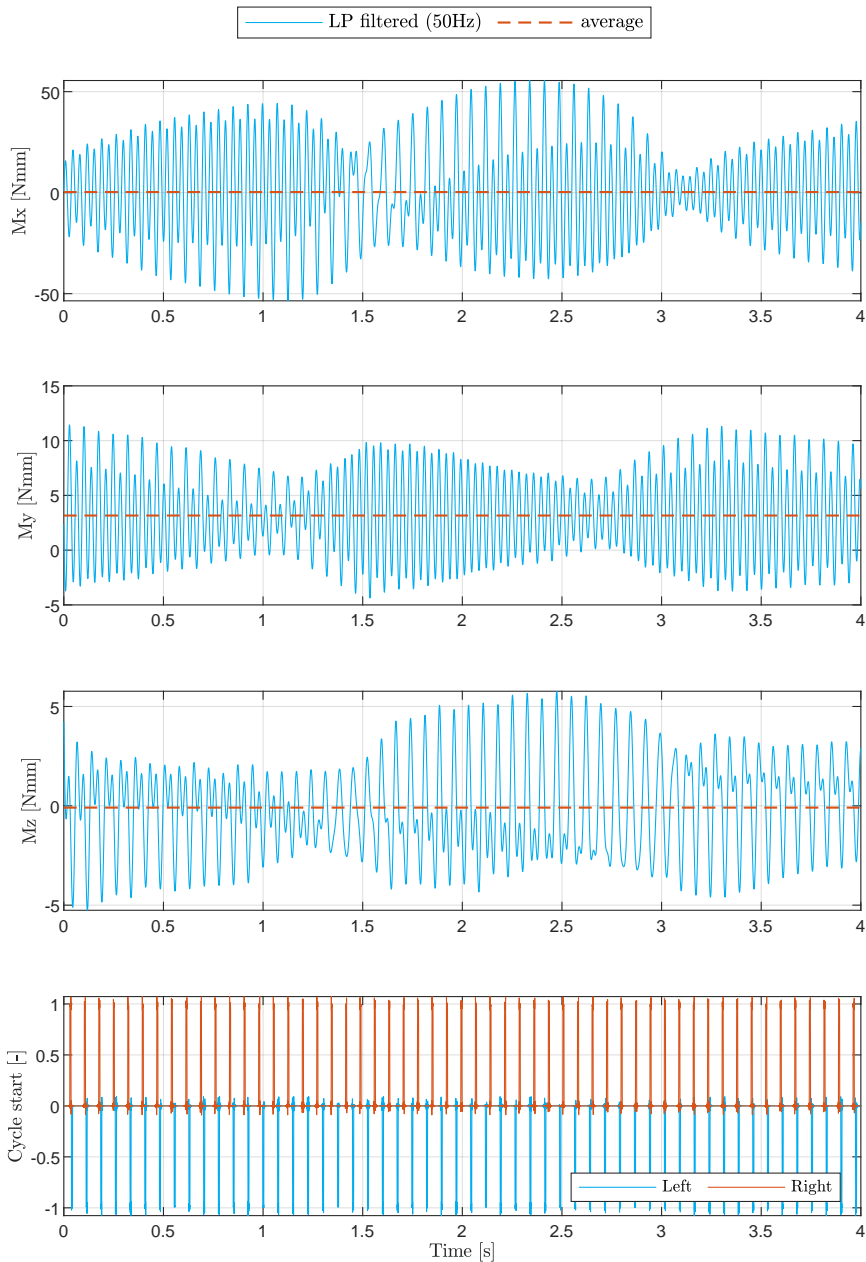
Figure 4.6: Roll, Pitch and Yaw moments of two separately driven double-wings: a beat phenomenon can be observed in the moment data when a difference in flapping frequencies of left and right double-wings is present. The cycle start is detected by a hall effect sensor and a magnet attached to the flapping mechanism. The residual vibration is especially strong around the roll (Mx) axis. Note that the average pitch (My) moment is non-zero as in the pitch direction the mounting point was not in the center of lift.

4.5. Yaw versus thrust efficiency

Pitch and roll are driven by differences in thrust generated by the left and right wings and fore and aft wings, respectively, but yaw is less evident. To achieve yaw, the lift vectors of 2 opposing wings are misaligned with respect to the vertical body axis. One diagonal is given a right-hand yawing alignment while the other pair of wings is given a left-hand yawing moment.
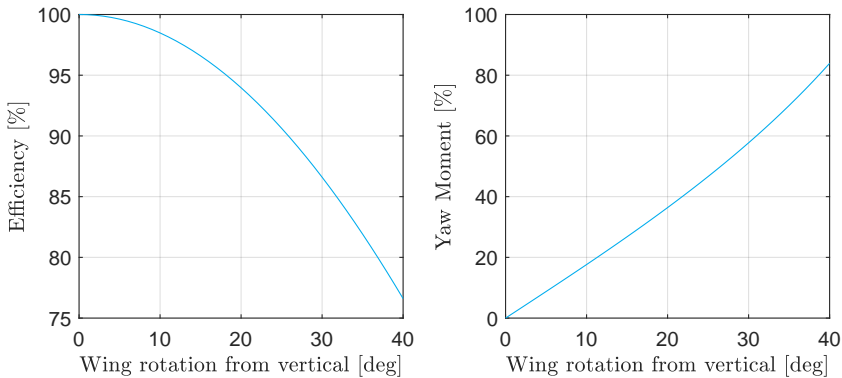
Figure 4.7: Yaw force and thrust efficiency in function of thrust rotation. Note that the yawing moment increases more than linearly with the wing rotation due to the average hover-lift increase caused by the efficiency loss.

The amount of misalignment can be used to increase the yaw control effectiveness at the cost of less efficient thrust generation as not all lift vectors now point perfectly upward (See Figure 4.7).

Since thrust efficiency is lost to achieve yaw control, the yaw channel could still benefit from using an actuator instead. Since the yaw is very well damped thanks to the wing area, a slower but more powerful actuator could still be considered to for instance deflect the trailing edges of the wing [26] to also deflect the thrust vector. In this case, only three sets of flapping wings would be required for full attitude control much like the tri-copter concept.

4.6. Flight Testing

A quad-thopter was built using DelFly II flapping mechanisms. Instead of a double pair of wings, only one side was mounted per flapping mechanism. DelFly II brushless motors were used and equipped with 3.5 A Brushless DC motor controllers. Since the vehicle is not naturally stable a paparazzi-UAV [30] Lisa-MX-S [31] autopilot was mounted. Standard rotorcraft stabilization was programmed and the Quad-thopter was tuned during manual flights in attitude direct mode.

An initial prototype was used in the high-speed camera recordings and outdoor flights. A final prototype was used in the indoor lateral steps tests. Figure 4.8 shows a photo of the final prototype. Table 4.1 gives the weight breakdown of the final prototype.
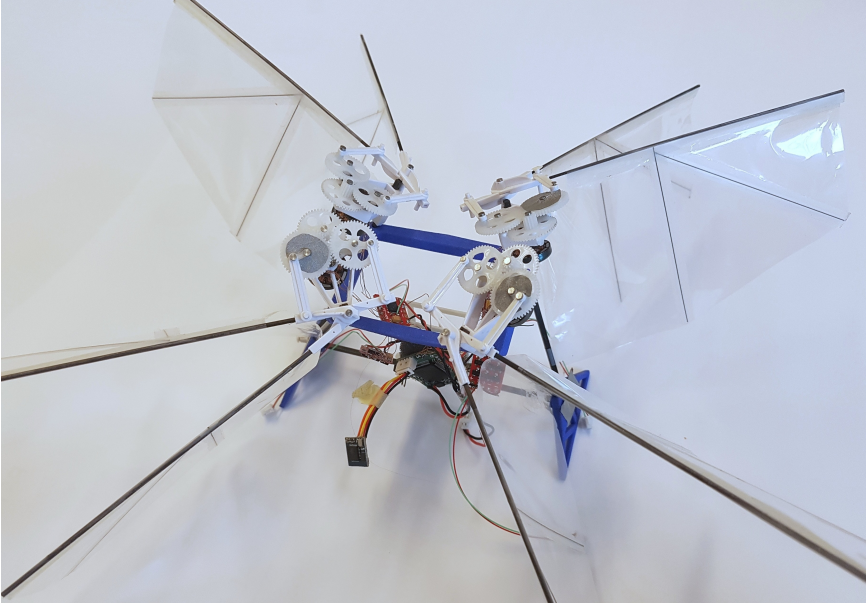
Figure 4.8: Photo of the final quad-thopter prototype. The maximal dimension is 28 cm from tip to tip and the weight is 37.9 g when equipped with a 205 mAh battery.

Figure 4.9 shows the response to a 40° step input in the roll axis. Within less than 4 beats of the fastest flapping wings (15 Hz), the attitude change was fully obtained.

(a)   (b)   (c)   (d)
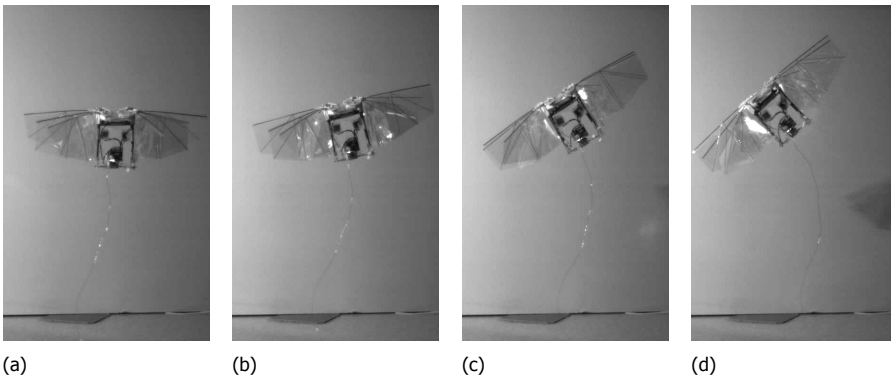
Figure 4.9: Highspeed camera recordings at 66.6 ms interval show a step in attitude from hover to a steady 40° of roll being executed in less than 266 ms or less than 4 wing beats at 15 Hz.

Position step responses were performed using the prototype shown in Figure 4.8 and measured using an Optitrack camera system. The quad-thopter was commanded in attitude mode to make a lateral step of about 2 m. A side view of the maneuver is shown in Figure 4.10. The quad-thopter will quickly reach the com-
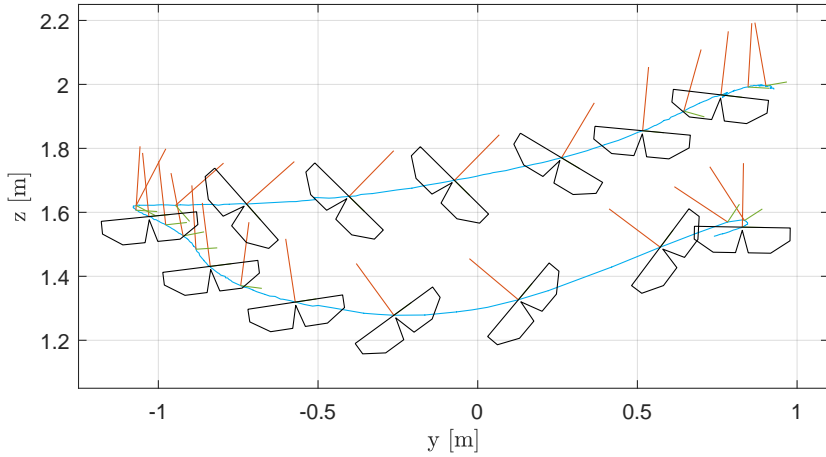
Figure 4.10: Indoor test flight recorded by the Optitrack motion tracking system. The quad-thopter starts at the bottom right and makes a 2 m step to the left and then back to the right in under 3 s. Notice that the vehicle does not need a negative roll angle during the slow down.
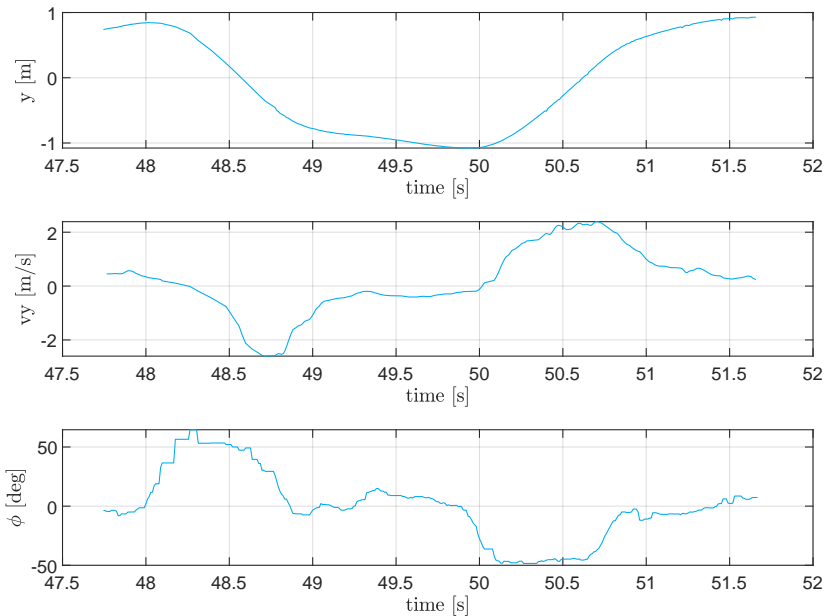
Figure 4.11: Lateral position, lateral velocity and roll angle in function of time during the lateral step shown in Figure 4.10. A left and then right 1.5 m sidestep were executed. The steps required roll angles of about 50° and resulted in speeds reaching 2.5 m/s. Each step was executed in under a second.

4
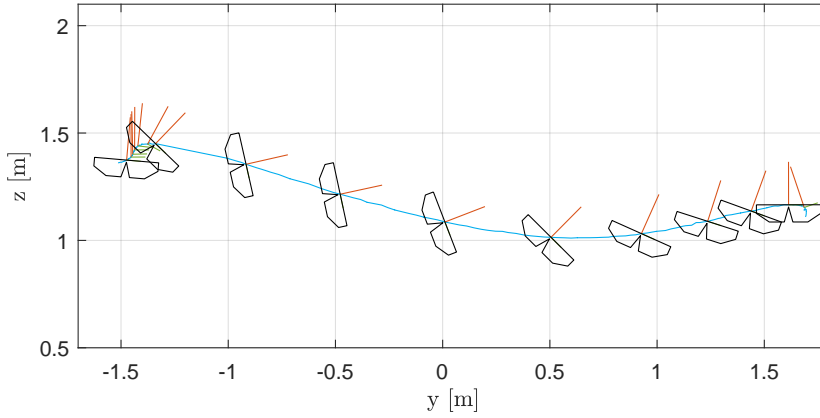
Figure 4.12: Lateral view of a manually flown 3m lateral step recorded indoors. The quad-thopter reaches a speed of 3.5 m/s and angles of 80° roll during this 1.5 s maneuver.
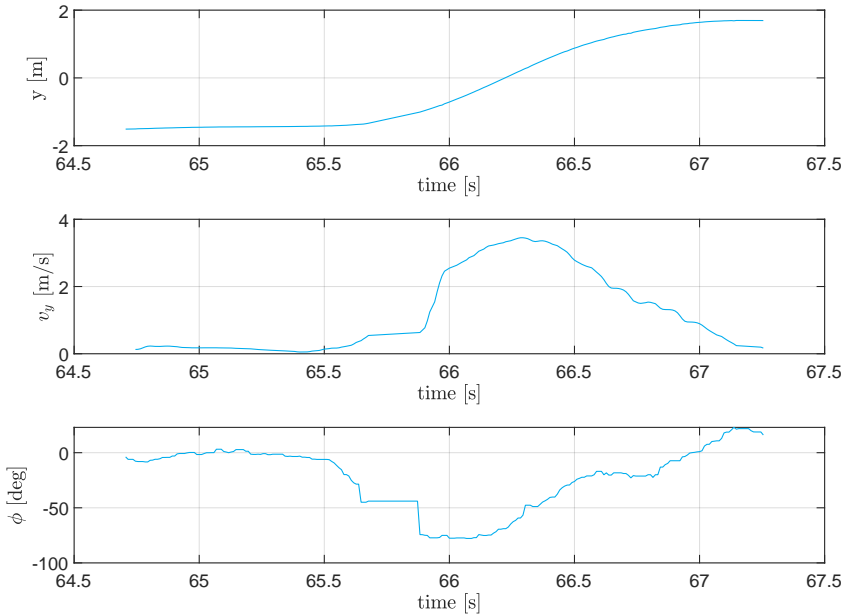
Figure 4.13: Position, speed, and roll angle captured by an external Optitrack motion tracking system during a 3 m lateral step command. Note that the Optitrack temporarily lost track at 65.55 s.

manded left roll angle of 50° and start accelerating. About half a meter before the target, the attitude is commanded to zero. Because of the lateral area of the wings and relatively low wing loading, the quad-thopter stops by itself when commanded back to a zero attitude. Then a right step is commanded. Everything combined is executed in under 3 s.

The corresponding timing of the motion is shown in Figure 4.11 left. As can be seen, the entire lateral acceleration from hover followed by the 2-meter motion and deceleration only takes about one second.

Figure 4.11 right shows the roll angle of the quad-thopter during the maneuver. It shows that roll angles of over 50° are achieved in about a quarter of a second. Finally, the speed profile of the lateral step is shown in Figure 4.11 center. Note that during the lateral step the quad-thopter was only rolled 50° and did not nearly reach its maximum speed but instead was subjected to lateral drag.

Lateral steps at higher angles were performed but often resulted in lost tracking from the Optitrack. One sequence at 80° roll was successfully recorded during a 3 m lateral step as shown in Figure 4.12. As shown in Figure 4.13 the quad-thopter reaches speeds of 3.5 m/s and roll angles of 80° while stepping sideways 3 m in less than 1.5 s.

(a)

(b)

(c)

Figure 4.14: Quad-thopter In-flight Outdoor in various phases of the flight. (a) hover (b) semi-transitioned (c) fast forward flight.

To illustrate the forward flight and disturbance handling capabilities, outdoor flights have been performed as shown in Figure 4.14. Very aggressive start and stops can be performed. When compared to DelFly II with its aerodynamic tail, the sensitivity to turbulence is reduced by an order of magnitude thanks to the fast powerful moments created by opposing wing pairs and stabilized by electronic attitude control. The maximal flight speed, however, is very close to that of DelFly II and is limited by the maximal flapping frequency that can be obtained.
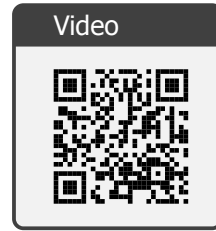
4.7. Variations

While the 'quad-thopter' can control all three angles and the total thrust with minimal residual vibration, it does require a lot of wings. While recent work proposed concepts with even more wings [32] and adding wings can help to average out vibrations, it makes the system more complex and expensive. Therefore, several solutions exist to reduce this number of wings while maintaining the advantages listed above as much as possible: the active hover control, simple crank flapping mechanism, minimal vibration without the need for flapping synchronization, and using lift-generating motors for most of the actuation.
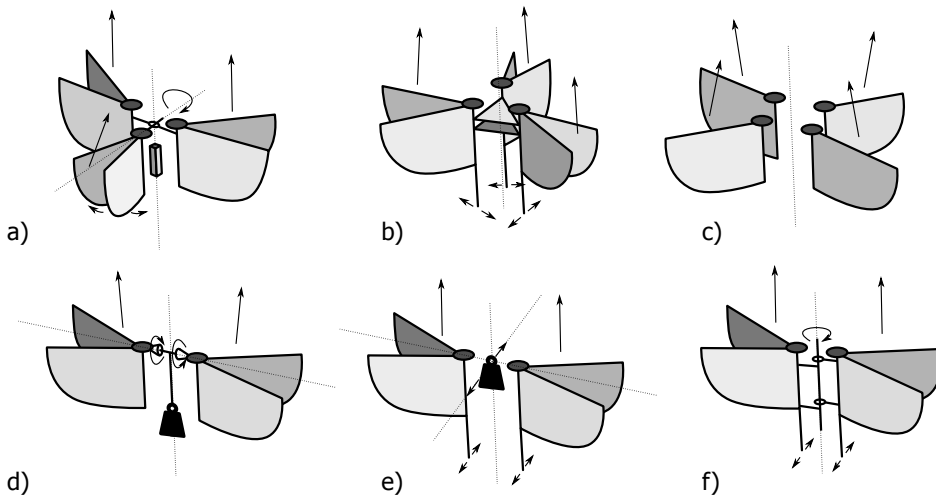
Figure 4.15: Variations of the quad-thopter concept to reduce the number of wings

The first option (Figure 4.15 (a)) is to reduce the number of wing pairs to three and make one rotatable to generate yawing moments in the same way tri-copters do [33]. While this requires an extra servo to actuate this rotation, the speed requirement on the well-damped yaw axis is typically much lower, which allows the use of slower strong servos. The extra weight is also offset by the more efficient vertical orientation of the main wings.

A second option is inspired by the results of moving the wing root spars in Chan *et al.* [26]. A single servo actuator can be used to move the bottom parts of all wing root spars (Figure 4.15 (b)). This works with 3 or 4 pairs of wings.

If higher vibration levels are acceptable and the yaw inertia is sufficiently large for the given flapping frequency (or vice-versa), the pairs of wings can be simplified to single loose wings (Figure 4.15 (c)). As seen in Figure 4.5, this does come with a much higher yaw vibration.

When adding two servos is acceptable, several intermediate options become available with only two pairs of flapping wings—similarly to the original DelFly. One way is to have both wings twist with respect to the fuselage (Figure 4.15 (d)). Alternatively, moving the wing root spars can be used to control yaw since it requires relatively little force, while the pitch can be controlled by moving the center of gravity (Figure 4.15 (e)). Finally, an apparent shift in the center of gravity can also be obtained by actuating a central hinge between both wings (Figure 4.15 (f)), while the wing root spars are moved for achieving yaw. This concept corresponds to the design of the DelFly Nimble [4].

4.8. Conclusions

This chapter proposed a novel flapping-wing design, a 'quad-thopter'. In the article, we have discussed the various design parameters relevant to a highly maneuverable, tailless flapping wing MAV. We conclude that the design represents a close-to-optimal choice in the design space consisting of the magnitude of the generated control moments, the control bandwidth, and the weight, size, and energy requirements of the actuators. In addition, the quad-thopter is relatively easy to construct with widely available current-day technology. The implementation of the design built and tested in this work has a flight time of 9 minutes or more, depending on the flight regime. This makes it suitable for real-world missions.

Although the presented design does not correspond to any (known) biological counterpart, the quad-thopter has several characteristics featured by natural fliers. For instance, the proposed quad-thopter becomes more efficient in forward flight, increasing the range and endurance. Furthermore, the wing surfaces can also be used for braking. This means that in contrast to quadrotors, quad-thopters do not have to thrust in the backward direction to brake, which also gives them the ability to slow down faster. Finally, the quad-thopter features enhanced safety because of the absence of fast-rotating rotors, so it is more suitable for flying around humans.

We hope that the presented design will be apter than previous designs for widespread use in academia and industry, helping to break the hegemony of rotorcraft and fixed wings.

Part	Mass
4 wing pairs with gears, motor and ESC	5.06 grams × 4
3D printed frame parts	5.95 gram
Frame carbon	2.2 gram
3D printed battery holder	1.2 gram
Wires	0.43 gram
Lisa-MX-S Autopilot	0.95 gram
Deltang Rx31 Receiver	0.23 gram
205mAh 1 cell LiPo Battery	6.7 gram
Total	37.9 gram

Table 4.1: Weight break-down of the final quad-thopter prototype

4

References

[1] C. De Wagter and E. J. J. Smeur, *Control of a hybrid helicopter with wings,* International Journal of Micro Air Vehicles **9**, 209 (2017).

[2] C. De Wagter, M. Karásek, and G. C. H. E. de Croon, *Quad-thopter: Tailless flapping wing robot with 4 pairs of wings,* in *International Micro Air Vehicle Conference and Flight Competition (IMAV) 2017*, edited by J.-M. Moschetta, G. Hattenberger, and H. de Plinval (IMAV, Toulouse, France, 2017) pp. 249–256.

[3] C. De Wagter, *Multiple pairs of flapping wings for attitude control,* (2017), patent NL2016130B1.

[4] M. Karásek, F. Muijres, C. De Wagter, B. Remes, and G. de Croon, *A tailless aerial robotic flapper reveals that flies use torque coupling in rapid banked turns,* Science **361**, 1089 (2018).

[5] A. Hedenström, *Extreme endurance migration: what is the limit to non-stop flight?* PLoS Biol **8**, e1000362 (2010).

[6] M. F. Platzer, K. D. Jones, J. Young, and J. S. Lai, *Flapping wing aerodynamics: progress and challenges,* AIAA journal **46**, 2136 (2008).

[7] M. Keennon, K. Klingebiel, H. Won, and A. Andriukov, *Development of the nano hummingbird: A tailless flapping wing micro air vehicle,* in *50th AIAA Aerospace Sciences Meeting including the New Horizons Forum and Aerospace Exposition* (American Institute of Aeronautics and Astronautics, 2012) pp. 1–24.

[8] R. Wood, R. Nagpal, and G.-Y. Wei, *Flight of the Robobees*, techreport Scientific American 308, 3, 60-65 (Scientific American, 2013).

[9] P. Sinha, P. Esden-Tempski, C. Forrette, J. Gibboney, and G. Horn, *Versatile, modular, extensible vtol aerial platform with autonomous flight mode transitions,* in *IEEE Aerospace Conference* (IEEE, Big Sky, MT, USA, 2012) pp. 1–17, 3-10 March 2012.

[10] C. De Wagter, R. Ruijsink, E. Smeur, K. van Hecke, F. van Tienen, E. van der Horst, and B. Remes, *Design, control, and visual navigation of the delftacopter vtol tail-sitter uav,* Journal of Field Robotics **35**, 937 (2018).

[11] O. Chanute, *Progress in Flying Machines*, edited by D. science books (Courier Corporation, 1997).

[12] W. Bejgerowski, A. Ananthanarayanan, D. Mueller, and S. Gupta, *Integrated product and process design for a flapping wing drive-mechanism,* ASME Journal of Mechanical Design **131**, 1 (2009).

[13] J. Gerdes, S. Gupta, and S. Wilkerson, *A review of bird-inspired flapping wing miniature air vehicle designs,* Journal of Mechanism and Robotics **4** (2012), 10.1115/1.4005525.

[14] G. C. H. E. de Croon, M. Perçin, B. D. W. Remes, R. Ruijsink, and C. De Wagter, *The DelFly: Design, Aerodynamics, and Artificial Intelligence of a Flapping Wing Robot*, 1st ed. (Springer Netherlands, 2016).

[15] H. Altartouri, A. Roshanbin, G. Andreolli, L. Fazzi, M. Karásek, M. Lalami, and A. Preumont, *Passive stability enhancement with sails of a hovering flapping twin-wing robot,* International Journal of Micro Air Vehicles **11**, 175682931984181 (2019).

[16] C. Paz, E. Suárez, C. Gil, and C. Baker, *CFD analysis of the aerodynamic effects on the stability of the flight of a quadcopter UAV in the proximity of walls and ground,* Journal of Wind Engineering and Industrial Aerodynamics **206**, 104378 (2020).

[17] M. Karásek, A. Hua, Y. Nan, M. Lalami, and A. Preumont, *Pitch and roll control mechanism for a hovering flapping wing MAV,* International Journal of Micro Air Vehicles **6**, 253 (2014).

[18] D. Coleman, M. Benedict, V. Hrishikeshavan, and I. Chopra, *Design, Development and Flight-Testing of a Robotic Hummingbird,* in *AHS 71st Annual Forum, Virginia Beach, Virginia, May 5–7, 2015* (2015) p. 18.

[19] H. V. Phan, T. Kang, and H. C. Park, *Design and stable flight of a 21g insect-like tailless flapping wing micro air vehicle with angular rates feedback control,* Bioinspiration & Biomimetics **12**, 036006 (2017).

[20] A. Roshanbin, H. Altartouri, M. Karásek, and A. Preumont, *Colibri: A hovering flapping twin-wing robot,* International Journal of Micro Air Vehicles **9**, 270 (2017).

[21] K. Ma, P. Chirarattananon, S. Fuller, and R. Wood, *Controlled flight of a biologically inspired, insect-scale robot.* Science **340**, 603 (2013).

[22] P. Zdunich, D. Bilyk, M. MacMaster, D. Loewen, J. DeLaurier, R. Kornbluh, T. Low, S. Stanford, and D. Holeman, *Development and testing of the mentor flapping-wing micro air vehicle,* Journal of Aircraft **44**, 1701 (2007).

[23] S. Frawley and D. Getz, *Wowwee flytech dragonfly,* Wikipedia entry, accessed May 16, 2017. (2007).

[24] N. Gaissert, R. Mugrauer, G. Mugrauer, A. Jebens, K. Jebens, and E. M. Knubben, *Inventing a micro aerial vehicle inspired by the mechanics of dragonfly flight,* in *Towards Autonomous Robotic Systems* (Springer, 2014) pp. 90–100.

[25] C. Dileo and X. Deng, *Design of and experiments on a dragonfly-inspired robot,* Advanced Robotics **23**, 1003 (2009).

[26] W. L. Chan, Q. V. Nguyen, and M. Debiasi, *Tailless control of a double clap-and-fling flapping wing mav,* in *International Micro Air Vechicle Competition and Conference 2016*, edited by P. Z. PENG and D. F. LIN (IMAV, Beijing, PR of China, 2016) pp. 291–299.

[27] J. A. Roll, B. Cheng, and X. Deng, *Design, fabrication, and experiments of an electromagnetic actuator for flapping wing micro air vehicles,* in *2013 IEEE International Conference on Robotics and Automation* (IEEE, 2013).

[28] W. Huang, *On the selection of shape memory alloys for actuators,* Materials & Design **23**, 11 (2002).

[29] L. Hines, D. Colmenares, and M. Sitti, *Platform design and tethered flight of a motor-driven flapping-wing system,* in *2015 IEEE International Conference on Robotics and Automation (ICRA)* (IEEE, 2015) pp. 5838–5845.

[30] P. Brisset, A. Drouin, M. Gorraz, P.-S. Huard, and J. Tyler, *The paparazzi solution,* in *MAV 2006, 2nd US-European Competition and Workshop on Micro Air Vehicles* (EMAV, Sandestin, United States, 2006) pp. 1–15.

[31] B. D. W. Remes, P. Esden-Tempski, F. van Tienen, E. Smeur, C. De Wagter, and G. C. H. E. de Croon, *Lisa-s 2.8 g autopilot for gps-based flight of mavs,* in *International Micro Air Vehicle Competition and Conference 2014*, edited by G. de Croon, E. J. van Kampen, C. De Wagter, and C. C. de Visser (IMAV, Delft, the Netherlands, 2014) pp. 280–285.

[32] M. Kiani, B. Davis, F. P. Quevedo, N. Cabezut, S. Hince, M. Balta, and H. E. Taha, *A new bio-inspired flying concept: The quad-flapper,* in *AIAA Scitech 2019 Forum* (American Institute of Aeronautics and Astronautics, 2019).

[33] J.-T. Zou, K.-L. Su, and H. Tso, *The modeling and implementation of tri-rotor flying robot,* Artificial Life and Robotics **17**, 86 (2012).

5

Rotor-Fuselage Interaction and Attitude Control of a Helicopter with Wings

You can never understand everything.
*But, you should push yourself to **understand the system**.*

- Ryan Dahl

This chapter investigates the design parameters and their consequences in the control of a helicopter rotor combined with a pair of fixed wings. Such a hybrid vehicle has a light and aerodynamically efficient rotor with a large range of pitch angles to enable both hover and forward flight. Because of the light stiff rotor and heavy wings, the hybrid vehicle exhibits couplings between the roll and pitch axes during hover flight. The rotor-wing interaction depends on several parameters. In this chapter, we utilize a simplified theoretic model and simulations to identify these parameters and to gain insight into the effect they have on vehicle dynamics. Finally, an attitude controller is designed that compensates for undesired coupling between pitch and roll.

5.1. Introduction

Rotorcraft dynamics have been well studied for many years [e.g. 3–6] with work ranging from rotorcraft modeling [7, 8], rotorcraft simulation [9], and matching measurement data with models [10] to the blade optimization in function of vibrations [11]. The design of controllers for conventional helicopters is equally well-understood [12, 13], and at the scale of small unmanned helicopters, models have been used for decades, for instance, to identify which parameters affect the performance [14]. More recently, non-linear models of miniature unmanned helicopters have been presented either for control purposes [8] but even to reduce vibrations or noise [15].

For less conventional designs like very low inertia rotors on very high inertia fuselages, the design choices and control problems are less mainstream. It is known that changes in fuselage dynamics affect flight performance. For instance, Ormiston [16] performed some studies into the fuselage-rotor interaction and fuselage ground interaction to identify resonance problems.

When propellers are small compared to the fuselage inertia, which is the case in for instance fixed-wing propeller aircraft, the influence of the rotor on the fuselage is often even neglected. But studies of aircraft in which the fuselage significantly interacts with the rotor are very scarce.

Figure 5.1: Novel hybrid Unmanned Air Vehicle featuring a cyclic and collective pitch controlled rotor combined with a biplane deltawing.

Research on hybrid UAVs has been investigating many possible combinations of rotors 'to hover and land vertically' and wings 'to fly forward efficiently' [17–19]. While most researchers combine quadrotors with fixed wings, having several small rotors is less efficient than using a single large rotor. Therefore, to improve hover performance by using only one large rotor, De Wagter *et al.* [20] proposed the *helicopter with wings* concept shown in Figure 5.1.

The central part consists of a model helicopter rotor head with cyclic and col-

lective pitch control. The rotor blade design is based on a compromise between efficient hover and efficient forward flight. This means the rotor significantly differs from rotors seen in conventional helicopters. It is relatively small, light, stiff and it has a high lift coefficient. While during hover the rotor points upwards, to transition to fast forward flight, the entire vehicle pitches down 90° as shown in Figure 5.2. During forward flight, the *rpm* of the rotor is reduced and its pitch angle increased to generate propulsion efficiently at high speed.

The large wings containing all the UAV systems have a large moment of inertia and combined with relatively small low-weight blades, the result is that the vehicle does not exhibit traditional helicopter dynamics in hover. Likewise, during fast forward flight, the gyroscopic effect of the rotor is much larger than in typical fixed-wings, which means it does not behave as a traditional fixed-wing vehicle either.
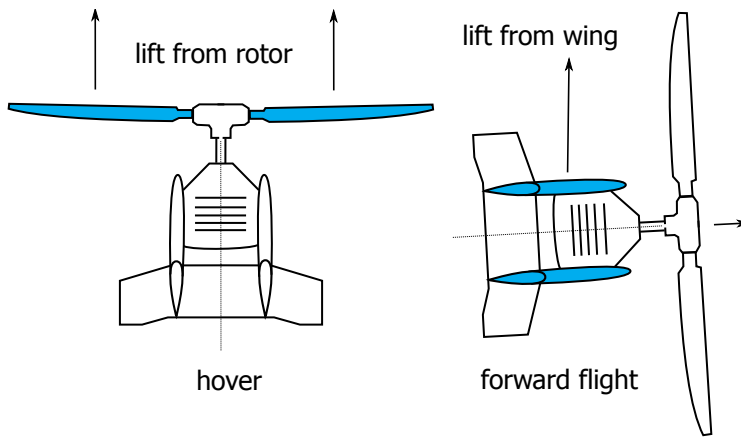
Figure 5.2: Lift generation of a helicopter with wings. In hover, the helicopter rotor points upwards and provides the lift while in forward flight, the vehicle pitches down 90°, the rotor provides thrust and the wings provide lift.

To investigate the dynamics of the *helicopter with wings* and propose a controller, this chapter presents the different parameters that affect the control and performance of a conventional cyclic and collective-pitch controlled light rotor head on top of a fixed-wing shaped body with varying inertia.

A simplified mathematical model of the rotor system with wings is created in Section 5.2. Section 5.3 presents simulation results of the model with varying rotor parameters on a fixed body. In Section 5.4 the interaction between the rotor and a free-floating fuselage is investigated in simulation for varying wing inertias, and finally, in Section 5.5 the insights are used to propose an attitude controller in hover.

5.2. Rotor Model

First, a 6 Degree of Freedom (DOF)mathematical rotor model [6] is derived as shown in Figure 5.3. The flapping angle β is measured around the spring hinge K. The rotor radius is R and it is spinning with rate ω. The feathering angle of the

rotor or pitch angle of a blade element is written as θ_B.
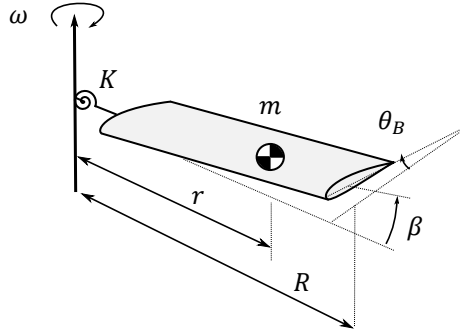
Figure 5.3: A simplified rigid rotor model turning with an angular rate ω, with mass m, radius R and spring stiffness K and yielding a flapping angle β and blade pitch angle or rotor feathering angle θ_B.

A blade element cross-section of the rotor and its corresponding angles is depicted in Figure 5.4. The model neglects the lagging angle of the rotor blade, as even in forward flight, the rotor of a tailsitter nearly only has axial flow. The velocity V_x of a blade element at distance r from the rotor axis then becomes $\omega \cdot r$ while the vertical speed of the blade element V_y is a function of the derivative of the flapping rate $\dot{\beta} \cdot r$. The path angle ν is the arctangent of V_x and V_y while θ_B is the feathering angle of the blade. The velocity of a blade element $\bar{V}$ then is:

$$\bar{V} = \begin{pmatrix} V_x \\ V_y \end{pmatrix} = \begin{pmatrix} \omega r \\ \dot{\beta} r \end{pmatrix} \tag{5.1}$$

To study the attitude control dynamics in hover, we neglect the collective pitch and hereby also the induced velocity through the rotor v_i. The angle of attack of a blade element then becomes $\alpha = \theta_B - \nu$, and for small angles $\nu = \dot{\beta}/\omega$. The lift of a blade element δr at distance r from the rotor becomes:

$$\delta L = \frac{\rho}{2}(\omega r)^2 C_L(\alpha) \cdot c \delta r \tag{5.2}$$
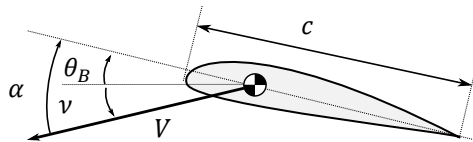
Figure 5.4: Angle of attack α of a rotor-blade element cross-section with cord c, velocity V, and blade pitch angle θ_B and path angle ν.

in which ρ is the air density and where around hover conditions the lift coefficient $C_L(\alpha)$ can be linearized to $c_{l_\alpha} \cdot \alpha$. The blade cord c, the blade pitch angle θ_B, the blade angle of attack α and rotor radius R are defined in Figure 5.3 and Figure 5.4. A so-called *Lock Number* γ from Bramwell *et al.* [6] is introduced

$$\gamma = \frac{\rho c_{l_\alpha} c R^4}{I_B} \tag{5.3}$$

with I_B being the rotational inertia of the rotor $I_B = \int r^2 \delta m$. After substitution of α and γ, δL can be expressed as:

$$\delta L = \gamma \frac{\omega^2 I_B}{R^4} \left(\theta_B - \frac{\dot{\beta}}{\omega} \right) \cdot \frac{1}{2} r^2 \cdot \delta r \tag{5.4}$$

The moments created by a blade element can then be integrated. The aerodynamic force δL perpendicular to a blade element and the centrifugal force $\omega^2 \cdot r \cos(\beta) \cdot \delta m$ acting on a moment arm $\sin(\beta) \cdot r$ together with the mass δm of the blade element at moment arm $r \cos(\beta)$ yield the following blade moment at the hinge:

$$\begin{aligned} M_B = & \int r \cdot \delta L \\ & - \int \cdot \omega^2 \cdot r \cos(\beta) \cdot r \sin(\beta) \cdot \delta m \\ & - \int r \cos(\beta) \cdot \delta m \cdot g \\ & - K \cdot \beta \end{aligned} \tag{5.5}$$

where g is the gravitational constant and $K \cdot \beta$ is the hinge spring moment with spring stiffness K. δm can be expressed in function of a length unit δr using the rotor blade density ρ_B and the blade cross-section S_B. The equation can then be integrated over the length of the rotor blade R.

To obtain the blade flapping acceleration $\ddot{\beta}$, moment M_B is divided by the blade rotational inertia I_B. When linearizing Equation (5.5), filling the lift force from Equation (5.4), neglecting the very small contribution of gravity on the blade dynamics, the following differential equation for rotor flapping is obtained:

$$\ddot{\beta} + \frac{\gamma}{8} \omega \dot{\beta} + (\omega^2 + \frac{K}{I_B})\beta = \frac{\gamma}{8} \omega^2 \theta_B \tag{5.6}$$

The terms in Equation (5.6) from left to right relate to first the inertia of the rotor, then its aerodynamic damping, the centrifugal and finally the spring forces. This concise notation shows that besides rotor rpm ω and input θ_B, the rotor dynamics depend mostly on the *Lock Number* γ. As given in Equation (5.3), this *Lock Number* physically contains aerodynamic damping terms (air density ρ, chord c, rotor radius R and lift coefficient c_{l_α}) divided by the blade flapping inertia I_B.

A discrete simulation model is created by generating a fixed number of rotor segments and solving the integral of Equation ([5.5](#)) as a summation over the segments.

The input of the system is the blade pitch angle or rotor feathering angle θ_B, which is changing over the rotor rotation and defined as a function of the cyclic control inputs δ_x and δ_y. These inputs correspond to swash-plate deflections around the body X and Y axis (See Figure [5.6](#)). A positive input δ_x increases the pitch of the blade as it passes over the Y axis and vice-versa:

$$\theta_B = \delta_y \cdot \sin(\omega t) + \delta_x \cdot \cos(\omega t) \tag{5.7}$$

5.3. Fixed Body Simulations

The derived model is analyzed in simulation. In this section, the rotor axis is kept fixed while the influence of rotor spring stiffness K is analyzed. Parameters for the model can be found in Table [5.1](#).

5.3.1. Fully Hinged Rotor Blade
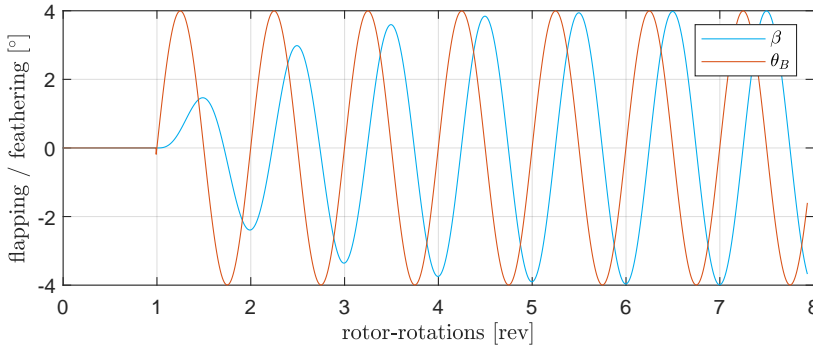
Figure 5.5: Blade dynamics β with zero spring stiffness K based on a cyclic deflection δ_y after 1 rotation which causes a periodic blade pitch angle θ_B.

Figure [5.5](#) shows the simulation result of the flapping angle β for a given deflection θ_B on a hypothetical rotor with $K = 0$. A deflection δ_y of 4 degrees is applied. The periodic deflection of β corresponds to tilting of the rotor plane. The deflection β has a phase lag of 90 degrees with the input θ_B as is the case in pure gyroscopes. The angle between the applied moment and the subsequent rotation axis of the rotor plane is called ξ and is illustrated in Figure [5.6](#)). When $K = 0$, ξ is equal to 90°. A positive cyclic deflection in pitch decreases the feathering angle θ_B whenever the rotor blade is at the right side of the vehicle with a clockwise spinning rotor ω. This results in a rolling moment but a rotor-plane inclination backward. This model corresponds to old fully hinged helicopter rotors.
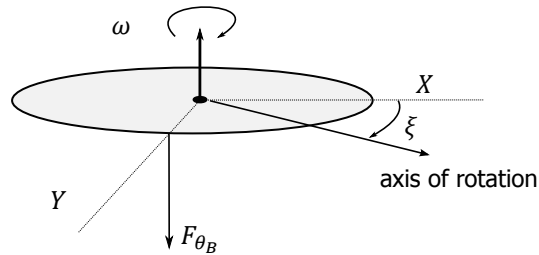
Figure 5.6: The applied force F_{θ_B} and corresponding axis of rotation at angle ξ of a spinning rotor. For non-spinning bodies, ξ is zero as a moment in the X axis will produce a rotation in the X axis. For pure gyroscopes, ξ is 90°.

5.3.2. Rotor with non-zero spring hinge

When the stiffness of the spring K is increased, the dynamics of the rotor are affected. Not only is the deflection β reduced, but the direction of maximal flapping—in other words, the rotor plane rotation—is affected. Figure 5.7 shows the results for a rotor system with a stiff spring (high K). In this case, the angle ξ, or in other words the phase difference between the point of maximum θ_B and β, is reduced from 90° to below 30° for a spring K which reduces the flapping angle β roughly by half.
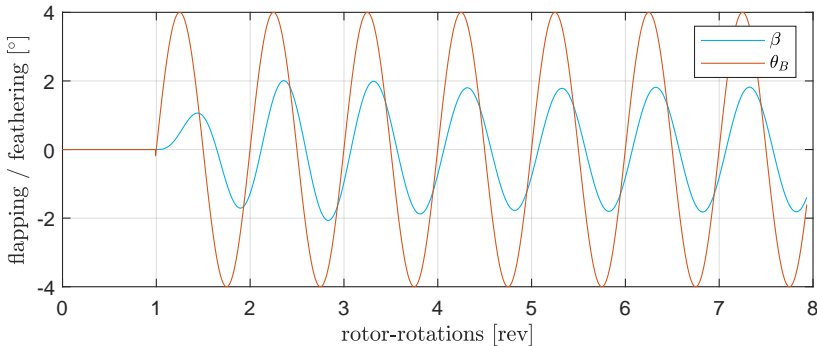
Figure 5.7: Blade dynamics β on a simulated rotor with high spring stiffness K in function of a constant cyclic deflection applied after 1 rotation.

The theoretical model and simulations give insight into how the rotor dynamics can be affected by the moments originating from the rotor axis. As shown in Equation (5.6), the dynamics of the rotor are affected by the rotor rotation rate ω, *Lock Number* γ and spring stiffness over rotor inertia K/I_B. Practically, given a rotor size and lift requirement, the *Lock Number* γ can only be significantly altered by changing the rotor weight. But although ω and γ will influence the response, the interaction of the fuselage on the rotor must come from the spring K and cyclic deflections δ_x and δ_y.

5.4. Simulation of Rotor-Fuselage Interaction

Since the previous sections have shown the importance of the hinge spring K, the model of the actual rotor is analyzed in more detail.

5.4.1. Rotor Hub Model
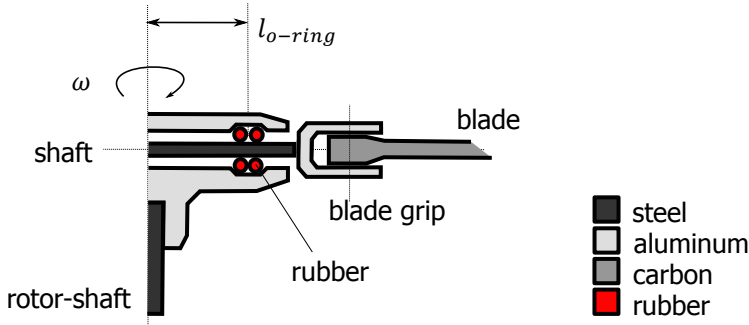
Figure 5.8: Actual Rotor Hub Simplified Schematics.

Figure 5.8 shows a simplified cross-section of the rotor head used in the helicopter with wings prototype from Figure 5.1. The center part consists of an aluminum T-shaped hub on the main rotor shaft. The feathering shaft holding both blades is only connected to the hub via rubber o-rings.

Precise modeling of the bending of all parts of the rotor is beyond the scope of this work. The feathering shaft and the blade grips can bend, and the blade itself has a structure with non-uniform properties, but most of the flexing comes from the rubber rings.
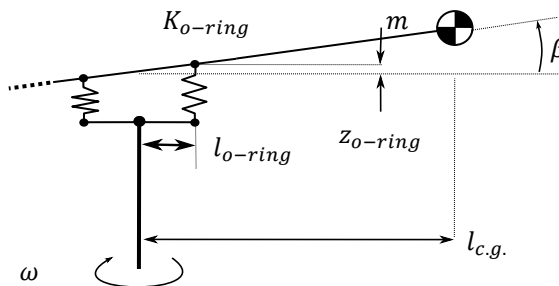
Figure 5.9: Simplified rotor hub model where the rubber o-rings holding the feathering axis are linearized as springs.

Modeling how a force is transferred from the rotor system to the main rotor shaft is therefore simplified by modeling only the rubber o-rings as a linear spring K_{o-ring} and their location l_{o-ring} as schematized in Figure 5.9. For one blade, the moment from the rotor on the rotor shaft then becomes:

$$M_{rotor-shaft} = z_{o-ring} \cdot K_{o-ring} \cdot l_{o-ring} \qquad (5.8)$$

The relation between the linear spring constant K_{o-ring} and torsional spring constant K from Equation (5.6) with $z_{o-ring} \approx l_o \cdot \beta$ is given by:

$$K = K_{o-ring} \cdot l_{o-ring}^2 \qquad (5.9)$$

The stiffness of the central rotor block rubbers was measured by hanging weights at the rotor and measuring the deflection [1]. A close-up photograph of the rotor-head and swashplate can be found in Figure 5.10.
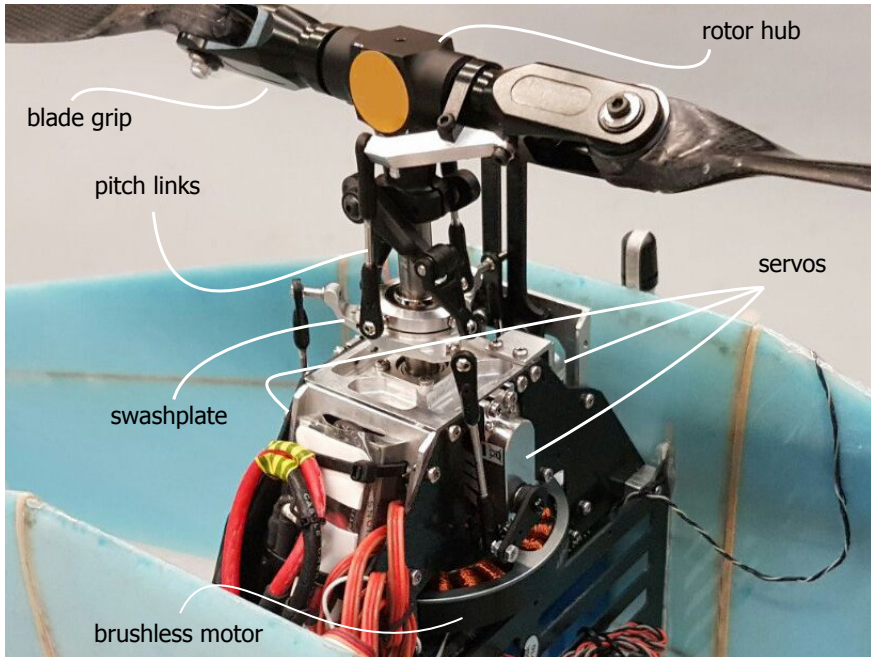
Figure 5.10: A close-up of the rotor head of the helicopter with wings vehicle. The swash-plate has 3 servos at 120° from each other. The collective pitch travel was increased and the blades have more twist to allow efficient forward flight.

5.4.2. Constrained rotor-shaft motion

When the rotor shaft is forced to rotate in pitch or roll—corresponding to a fuselage change in attitude—the rotor plane is following the fuselage motion through the blade hinge force and the cyclic mechanism. Since the swashplate moves along with the fuselage and rotor axis, it effectively changes the blade pitch θ_B. Figure 5.11 depicts the simulation results of a 10 degree pitch up of the fuselage and main rotor shaft in the case of a pure hinged rotor with $K = 0$ (left) and the case of a rotor with non-zero K (right).
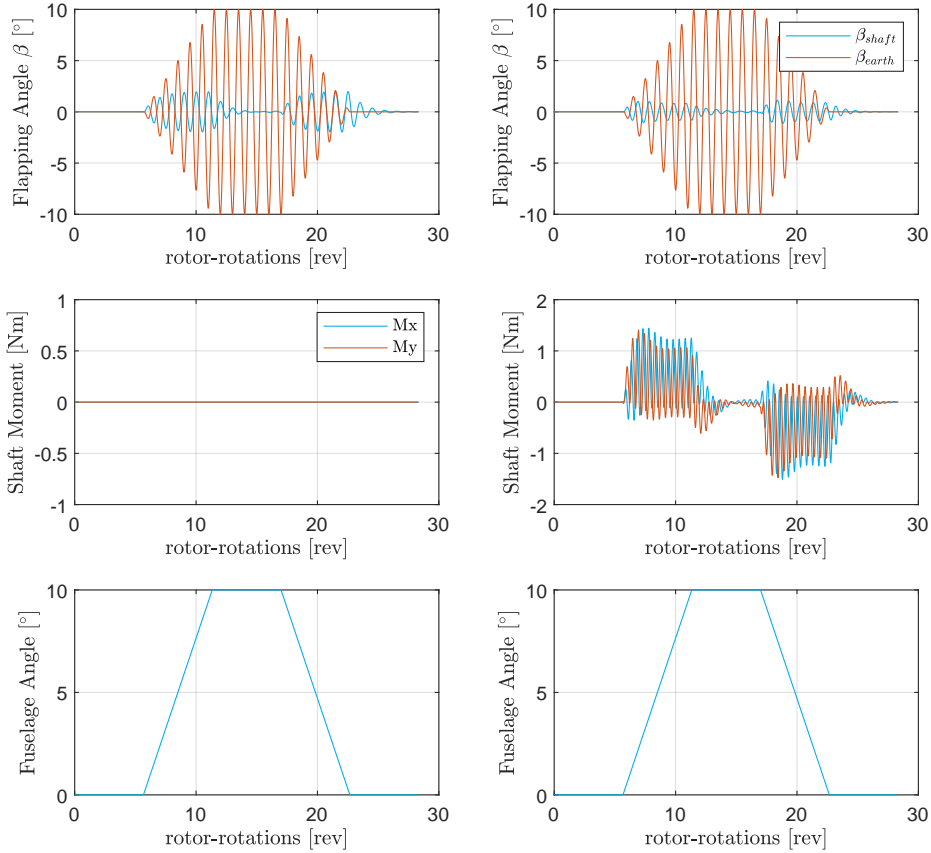
Figure 5.11: Rotor dynamics β due to imposed fuselage motion. Left $K = 0$, right $K \neq 0$. The flapping angle is given in the earth frame (β_{earth}) and with respect to the rotor shaft (β_{shaft}). Even with zero K, the rotor β follows the rotor shaft through the swashplate mechanism. With non-zero K, the rotor follows the rotor shaft faster but applies moments on the rotor shaft in both Mx and My direction. These moments are acting on the whole vehicle.

In the case of a fully hinged rotor, the rotor disc still tracks the motion of the rotor shaft, as the feathering angle θ_B of the blade follows a plane perpendicular to the rotor shaft through the swash-plate mechanism. This creates an aerodynamic force that makes the rotor plane follow the rotor shaft even without spring K. When neglecting the blade grip push-rods and swash-plate forces, the moment from the fuselage to the rotor is zero.

On the other hand, whenever a moment can be transferred from the rotor to the rotor-shaft directly via K, the relative blade flapping angle β_{shaft} creates moments M_x and M_y with a frequency of 2ω, or two times the rotor frequency.

Note that a pure imposed pitch motion will generate moments in both M_x and M_y

directions. This will also happen in free flight whenever the wing imposes a motion on the rotor. While the swashplate mechanism creates an aerodynamic force to make the rotor pitch up as above, the fuselage also applies a pitch-up moment on the rotor directly through the spring. The gyroscopic reaction of the rotor on that pitching moment is a rolling motion. This yields a roll moment from the rotor on the fuselage in return. This happens whenever the fuselage and rotor plane are not aligned. An extreme case is for instance upon landing the helicopter with wings (See Figure 5.1) with a roll angle, one tip will touch the ground first, yielding a constrained roll rate of the fuselage which resembles the constrained shaft motion of this simulation. As shown in Figure 5.11, this results in significant pitch moments imposed back from the rotor on the fuselage, which, if not compensated can make the vehicle tip over. Similarly, in forward flight, a pitching moment from the wings and its elevons will cause an undesired yawing moment from the rotor back on the fuselage.

In the next section, the dynamics of a non-constrained fuselage on the rotor system will be investigated.

5.4.3. Free fuselage dynamics

To simulate the free fuselage dynamics, the fuselage is modeled as four-point loads of a quarter of the total mass, as depicted in Figure 5.12. The fuselage is symmetric around the X and Y axis but the dimensions are not equal.
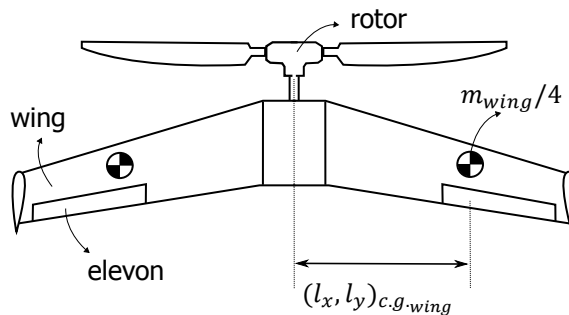
Figure 5.12: The fuselage body of the helicopter with wings is modeled as four point-masses $m_{wing}/4$ at distances l_x and l_y from the center of gravity of the vehicle.

The distance from the vehicle center of gravity to each modeled point load $m/4$ in the X direction is l_x and in the Y direction l_y.

$$I_{xx} = 4 \cdot \frac{m_{wing}}{4} \cdot l^2_{x_{c.g \cdot wing}}, \tag{5.10}$$

$$I_{yy} = 4 \cdot \frac{m_{wing}}{4} \cdot l^2_{y_{c.g \cdot wing}} \tag{5.11}$$

Assuming that there are no aerodynamic forces on the wing during hover, that there is no yaw rate, and that angles are small, the fuselage roll and pitch rates p and q are obtained through integration of the rotor shaft moments.

$$p = \int_0^t \frac{M_x}{I_{xx}} dt, \qquad q = \int_0^t \frac{M_y}{I_{yy}} dt \qquad (5.12)$$

The interaction between the rotor and the fuselage is simulated for three different values of l_x and l_y in Figure 5.13. In all three simulations, the same inputs are applied, shown in the top left figure. The distribution of fuselage inertia over the X and Y axes which is also present in the helicopter with wings prototype is seen to have a big influence on the way the vehicle reacts to inputs.
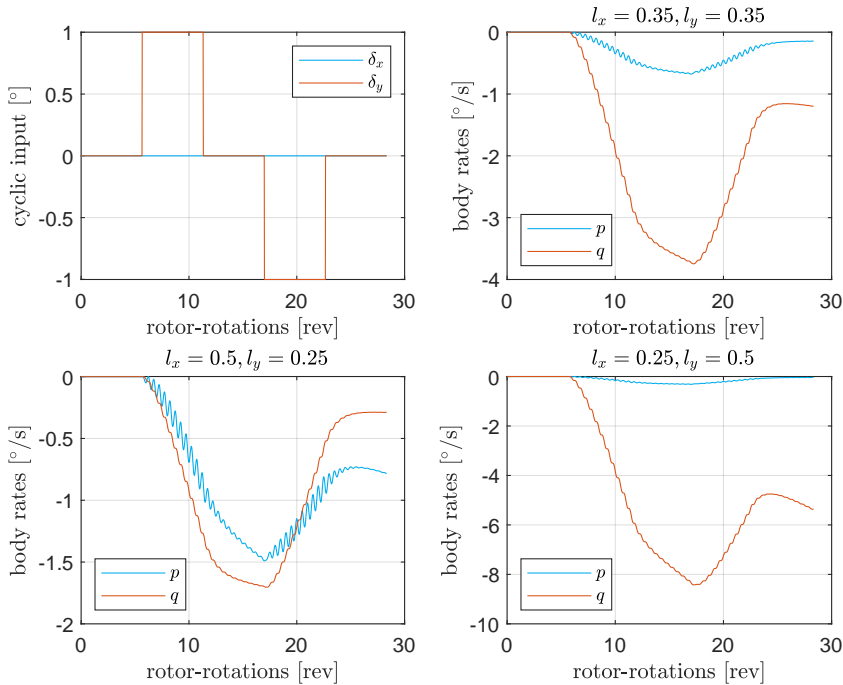
Figure 5.13: The influence of fuselage inertia on a free body helicopter with wings. Three simulations of an identical rotor with identical inputs and non-zero stiffness but different fuselage inertia distribution.

5.5. Attitude Control

The insights from the derived models were applied to the control of the helicopter with wings shown in Figure 5.1. This prototype has light, stiff, and relatively small carbon-fiber rotor blades mounted on a stiff conventional Logo-480 rotor head with modified blade grips to double the pitch range. The rotor blade airfoils are highly cambered to obtain high lift coefficients. The biplane wing-shaped fuselage contains all electronics and power and spreads the weight over the entire wingspan, giving it large rotational inertia. Similarly, as the simulation from Figure 5.13, the combination is not behaving like a conventional helicopter anymore.

To obtain real flight tests data, the vehicle was equipped with an autopilot with a simple controller shown in the next section and flown manually. A governor was also programmed to maintain a constant rpm as previous sections showed the influence of rotor speed. The flight controller is the *Lisa-MX* from the Paparazzi-UAV autopilot project as described [21–23]. Figure 5.14 shows onboard measurements of a test flight in which can be seen that rpm is kept constant even before the vehicle takes off.
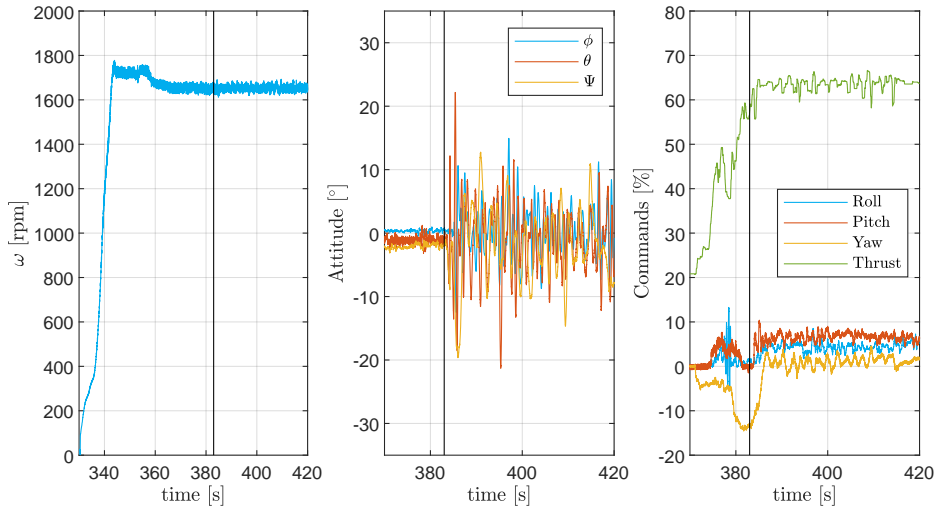
Figure 5.14: Take-off sequence of the manual identification test flight of the prototype helicopter with wings. Due to the influence of ω in the rotor dynamics, the RPM of the rotor is kept constant when the governor is enabled at 358 s. The lift-off represented by the vertical black line at 383 s.

5.5.1. Axis definitions
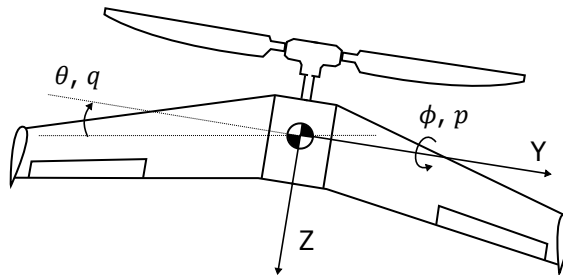
Figure 5.15: Body axis definitions, with the X axis defined by the right-hand rule. The X axis points down in forward flight. p and q are the body rates around the X and Y axes respectively.

Figure 5.15 shows the body axis definitions used in the controller. Angular rates

around the X, Y, and Z axes are denoted with p, q, and r respectively. Together, they are denoted by the vector $\bar{\omega}$.

To control the attitude, the cyclic δ_x and δ_y are controlled through the swash-plate. The swashplate also controls the collective pitch which is changing the pitch of all blades collectively to regulate the total lift.

Tip propellers provide a moment around the body Z axis in hover, and four flaps, one on each wing, can provide a moment around the body Y and Z axes.

5.5.2. Baseline attitude controller

The control of the attitude is formulated in quaternions because tail-sitter hybrid UAV pitch down 90° or more to transition from hover to forward flight and at these angles Euler representations reach singularities [24]. A reference angular rate is constructed from the vector part of the error quaternion multiplied by a proportional and integral gain K_P and K_I respectively:

$$\bar{\omega}_{\text{ref}} = K_P \begin{bmatrix} q_x & q_y & q_z \end{bmatrix}^T_{\text{err}} + K_I \sum_i \begin{bmatrix} q_x & q_y & q_z \end{bmatrix}^T_{\text{err}} \tag{5.13}$$

where the error quaternion is calculated using the Hamilton product:

$$q_{\text{err}} = q_{\text{ref}} \otimes q_m^* \tag{5.14}$$

where * denotes conjugation [24]. Equation (5.13) contains the integrator term, which sums the quaternion error over every discrete time instant i.

From the reference angular rate, the angular rate error is calculated:

$$\begin{bmatrix} p_{err} \\ q_{err} \\ r_{err} \end{bmatrix} = \bar{\omega}_{\text{err}} = \bar{\omega}_{\text{ref}} - \bar{\omega} \tag{5.15}$$

Then, roll pitch and yaw commands are calculated by multiplying the angular rate error with a linear rate gain K_D to obtain cyclic commands and yaw compensation using the tip motors.

Once the desired cyclic commands δ_x and δ_y are computed, which rotate the swash plate around the body X and Y axes respectively, the actuator deflections are computed to move the swash-plate as desired. Three servos δ_{s1}, δ_{s2} and δ_{s3} are used to control the swash-plate (See Figure 5.10):

$$\delta_{s1} = \frac{\sqrt{2}}{2}\delta_x + \frac{\delta_y}{2}, \tag{5.16}$$

$$\delta_{s2} = -\frac{\sqrt{2}}{2}\delta_x + \frac{\delta_y}{2}, \tag{5.17}$$

$$\delta_{s3} = -\delta_y \tag{5.18}$$

5.5.3. Compensating for fuselage-rotor interaction

In steady conditions, the prototype helicopter with wings can just be kept airborne with the proposed baseline controller. The feedback was initially done with $\xi = 90°$ (See Figure 5.6), such that roll feedback was applied to δ_x and pitch feedback to δ_y. Using the onboard logging on an SD-card, data was collected to identify these coupled vehicle dynamics. The pitch and roll during the resulting marginally stable flight are shown in Figure 5.16.
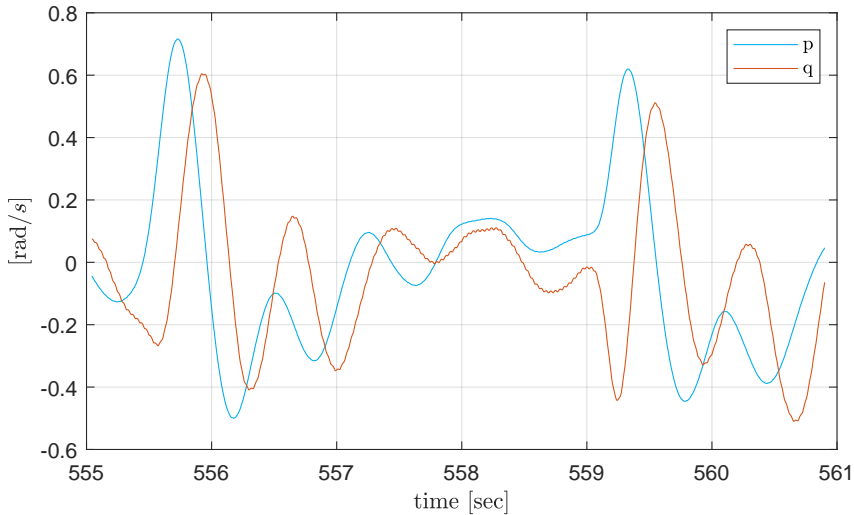
Figure 5.16: An early manual hovering test flight of the helicopter with wings prototype with a manually tuned standard helicopter rate controller from the paparazzi-UAV autopilot showed that a doublet step input right ($t = 555$ s) and then left ($t = 559$ s) on roll rate p (rotation rate around body X axis) yields an undesired but very significant pitch rate q (rotation rate around body Y axis). Pilots described this undesired and delayed effect of pitch on roll commands as 'wobbling'.

Section 5.4 found that the angular accelerations in pitch $\dot{q}$ and roll $\dot{p}$ are expected to depend on both cyclic inputs δ_x and δ_y but also on motion of the fuselage, or in other words, the rates in roll p and pitch q. To identify their relative influence, coefficients were introduced to fit the relation of the former variables on the pitch and roll accelerations. C_{A_B} denotes the influence of input A on output B. Coefficients were introduced for inputs p, q, δ_x and δ_y on outputs $\dot{p}$ and $\dot{q}$. Offsets $C_{O_{\dot{p}}}$ and $C_{O_{\dot{q}}}$ are added to the fit to compensate for trim errors. The fits are referred to as $f_p()$ and $f_q()$ and shown in Equation (5.19) and Equation (5.20):

$$\dot{p} \approx f_p() = C_{O_{\dot{p}}} + C_{\delta_{x\dot{p}}}\delta_x + C_{\delta_{y\dot{p}}}\delta_y + C_{p_{\dot{p}}}p + C_{q_{\dot{p}}}q \tag{5.19}$$

$$\dot{q} \approx f_q() = C_{O_{\dot{q}}} + C_{\delta_{x\dot{q}}}\delta_x + C_{\delta_{y\dot{q}}}\delta_y + C_{p_{\dot{q}}}p + C_{q_{\dot{q}}}q \tag{5.20}$$

Figure 5.17 shows the angular acceleration in roll and pitch along with the best fit of the coefficients for a short indoor flight fragment where the helicopter with
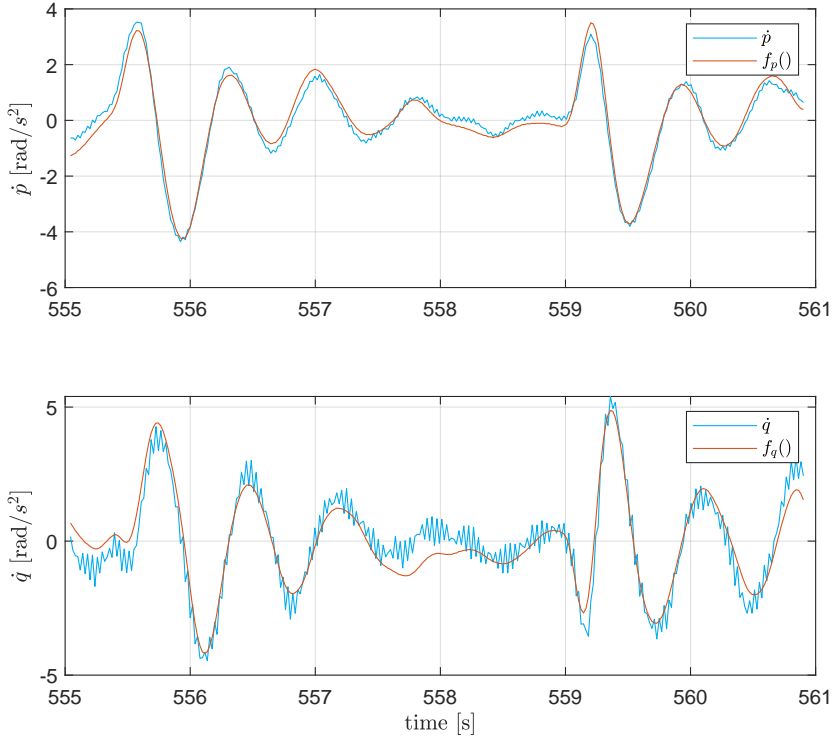
Figure 5.17: Fitting the control inputs and body rates to body accelerations $\dot{p}, \dot{q}$. The best model fits $f_p(), f_q()$ relate well to the observed filtered angular accelerations.

wings performs a step in roll angle of approximately 20 degrees. All signals were filtered with a second-order filter with a cutoff frequency of 15 rad/s [25]. From the figure, it can be seen that this model can explain most of the behavior for this part of the flight. The coefficients that were found using the data shown in Figure 5.17 are given in Table 5.2. When looking closely at the coefficients for C_p and C_q in Table 5.2, they confirm that a roll rate causes a pitch acceleration and vice-versa.

Taking into account the identified couplings, the linear controller is revised to:

$$\begin{bmatrix} \delta_x \\ \delta_y \end{bmatrix} = G^{-1} \begin{bmatrix} K_p \cdot p_{err} + q \cdot C_{q_{\dot{p}}} \cdot K_c \\ K_q \cdot q_{err} + p \cdot C_{p_{\dot{q}}} \cdot K_c \end{bmatrix}, \tag{5.21}$$

$$G = \begin{bmatrix} C_{\delta_{x_{\dot{p}}}} & C_{\delta_{y_{\dot{p}}}} \\ C_{\delta_{x_{\dot{q}}}} & C_{\delta_{y_{\dot{q}}}} \end{bmatrix} \tag{5.22}$$

Where p_{err} and q_{err} are the difference between the desired rates and the actual rates of the vehicle, and K_p and K_q are gains that can be tuned. An in-flight tuning

parameter K_c is introduced with a value between 0 and 1. It was introduced to gradually enable the compensation of angular acceleration due to rates during flight.

Test flights showed that a value of $K_c = 0.5$ gives better results than a value of $K_c = 1$. This may be caused by actuator dynamics or the filtering, as a control moment can not be instantly generated when a rate is measured. More research is necessary to better explain why $K_c = 1$ still gives a wobble.

5.5.4. Flight validation of the controller
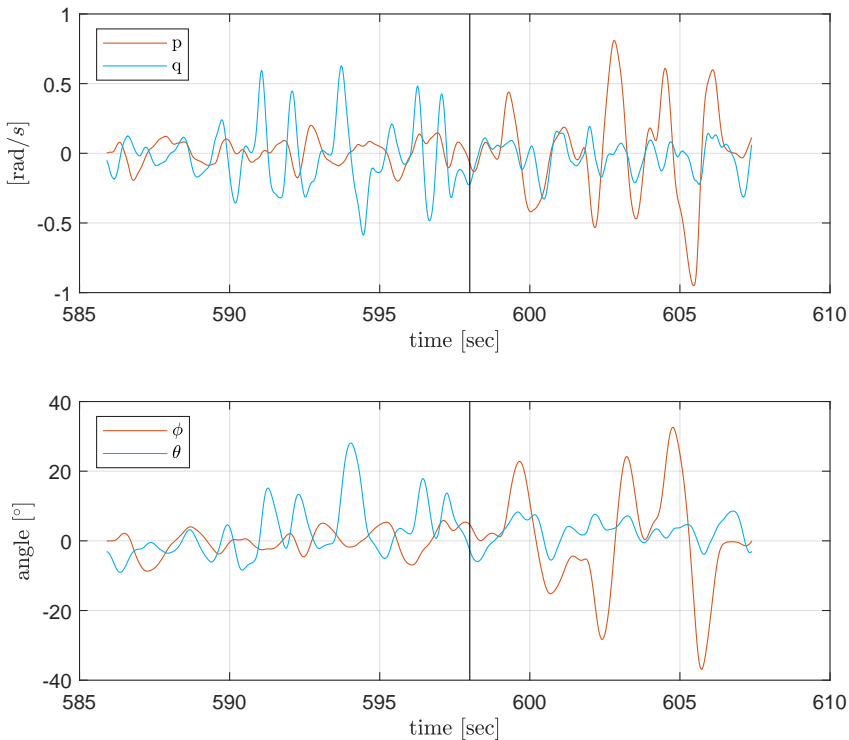
Figure 5.18: Manual test flight in attitude mode to confirm the observed coupling as seen in Figure 5.16 has been resolved with the proposed controller. In this flight, a K_c of 0.5 was selected to yield the best results. Before time $t = 598$ the test pilot was applying mainly pitch commands, and after mainly roll commands while keeping the vehicle in the flight area.

Figure 5.18 shows the measured angular rates of the vehicle during some pitch maneuvers in the first part of the flight and some roll maneuvers in the second part of the flight. The rates were filtered with a second-order filter with a cutoff frequency of 25 rad/s. In the bottom figure, the roll angle ϕ and pitch angle θ, as defined by ZYX Euler angles, are shown. From Figure 5.18 it can be seen that no wobble is present, and the motion in roll and pitch is uncoupled. When compared

back to the initial situation in Figure 5.16, it can be seen that the control was highly improved. But for every change in fuselage inertia, rotor inertia, or rotor rpm, new values need to be computed.

5.6. Conclusion

When designing combinations of conventional cyclic controlled helicopters rotors and fixed-wing aircraft, it is important to understand the interactions between rotor and wing to optimize the design. Although a very simplified simulation model cannot be used to directly identify control parameters, it can help understand the variables affecting the control.

The *Lock Number* was shown to influence the response speed of the rotor plane while the rotor hinge spring stiffness was shown to influence the amplitude of the rotor plane tilt and even its direction.

Non-homogeneous inertia of the fuselage and fuselage-rotor interactions were shown to add non-symmetrical coupling between the pitch and roll axes. Compensation for gyroscopic effects was needed in the controller to remove this coupling.

Finally, an attitude controller was formulated and tested in flight that compensates the rotor-fuselage interaction, enabling functional attitude control in hover.

Variable	Value	Unit
R	51	cm
$r_{c.g.}$	30	cm
m	55	gram
c_{tip}	3.0	cm
c_{root}	5.7	cm
c_{l_α}	2π	cm
K	88	Nm/rad

Table 5.1: Rotor blade parameters of the simulations, estimated to resemble the prototype helicopter with wings in De Wagter *et al.* [20].

Coefficient	$\dot{p}$	$\dot{q}$
C_O	-2.4661	-2.8847
C_{δ_x}	0.0032	-0.0044
C_{δ_y}	0.0011	0.0073
C_p	-0.5703	7.4479
C_q	-3.4308	-3.4487

Table 5.2: Identified control parameters of the helicopter with wings prototype.

References

[1] C. De Wagter and E. J. J. Smeur, *Control of a hybrid helicopter with wings,* International Journal of Micro Air Vehicles **9**, 209 (2017).

[2] C. De Wagter, R. Ruijsink, E. Smeur, K. van Hecke, F. van Tienen, E. van der Horst, and B. Remes, *Design, control, and visual navigation of the delftacopter vtol tail-sitter uav,* Journal of Field Robotics **35**, 937 (2018).

[3] W. Z. Stepniewski and C. Keys, *Rotary-wing aerodynamics,* edited by W. Z. Stepniewski (New York, NY : Dover Publ., Massachusetts, 1979).

[4] R. W. Prouty, *Helicopter performance, stability, and control* (Krieger Publishing Company, Melbourne, FL 32902-9542 USA, 1995).

[5] W. J. Wagtendonk, *Principles of Helicopter Flight* (Aviation Supplies & Academics Inc, 1996).

[6] A. Bramwell, G. Done, and D. Balmford, *Bramwell's Helicopter Dynamics* (American Institute of Aeronautics and Astronautics, 2001) pp. 1–397.

[7] W. Johnson, *A Comprehensive Analytical Model of Rotorcraft Aerodynamics and Dynamics. Part 1. Analysis Development,* techreport 19800019795 (NASA Ames Research Center, DTIC Document, Moffett Field, CA, United States, 1980).

[8] G. Cai, B. M. Chen, T. H. Lee, and K.-Y. Lum, *Comprehensive nonlinear modeling of a miniature unmanned helicopter,* Journal of the American Helicopter Society **57**, 1 (2012).

[9] G. D. Padfield, *Helicopter flight dynamics* (John Wiley & Sons, Hoboken, New Jersey, United States, 2008).

[10] G. K. Yamauchi, R. M. Heffernan, and M. Gaubert, *Correlation of sa349/2 helicopter flight test data with a comprehensive rotorcraft model,* Journal of the American Helicopter Society **33**, 31 (1988).

[11] D. A. Peters, T. Ko, A. Korn, and M. P. Rossow, *Design of helicopter rotor blades for desired placement of natural frequencies,* in *American Helicopter Society, 39th Annual Forum* (St. Louis, Missouri, 1983) pp. 674–689.

[12] H. Shim, T. J. Koo, F. Hoffmann, and S. Sastry, *A comprehensive study of control design for an autonomous helicopter,* in *Proceedings of the 37th IEEE Conference on Decision and Control,* Citeseer (IEEE, Tampa, FL, USA, USA, 1998) pp. 1–6.

[13] V. Gavrilets, *Dynamic model for a miniature aerobatic helicopter,* in *Handbook of Unmanned Aerial Vehicles* (Springer, Netherlands, 2015) pp. 279–306.

[14] F. Caradonna and C. Tung, *Experimental and analytical studies of a model helicopter rotor in hover,* in *European Rotorcraft and Powered Lift Aircraft Forum* (Garmisch-Partenkirchen, Germany, 1981) pp. 1–58.

5

[15] G. Bernardini, E. Piccione, A. Anobile, J. Serafini, and M. Gennaretti, *Optimal design and acoustic assessment of low-vibration rotor blades,* International Journal of Rotating Machinery **2016**, 1 (2016).

[16] R. A. Ormiston, *Rotor-fuselage dynamics of helicopter air and ground resonance,* Journal of the American Helicopter Society **36**, 3 (1991).

[17] P. Sinha, P. Esden-Tempski, C. Forrette, J. Gibboney, and G. Horn, *Versatile, modular, extensible vtol aerial platform with autonomous flight mode transitions,* in *IEEE Aerospace Conference* (IEEE, Big Sky, MT, USA, 2012) pp. 1–17, 3-10 March 2012.

[18] L. Lustosa, F. Defay, and J. Moschetta, *Development of the flight model of a tilt-body MAV,* in *International Micro Air Vehicle Competition and Conference 2014* (Delft, The Netherlands, 2014) pp. 157–163.

[19] M. Hochstenbach, C. Notteboom, B. Theys, and J. De Schutter, *Design and Control of an Unmanned Aerial Vehicle for Autonomous Parcel Delivery with Transition from Vertical Take-off to Forward Flight -VertiKUL, a Quadcopter Tailsitter,* International Journal of Micro Air Vehicles **7**, 395 (2015).

[20] C. De Wagter, R. Ruijsink, E. Smeur, K. van Hecke, F. van Tienen, E. van der Horst, and B. Remes, *Design, control and visual navigation of the delftacopter,* arXiv , 1 (2017), 1701.00860 .

[21] P. Brisset, A. Drouin, M. Gorraz, P.-S. Huard, and J. Tyler, *The paparazzi solution,* in *MAV 2006, 2nd US-European Competition and Workshop on Micro Air Vehicles* (EMAV, Sandestin, United States, 2006) pp. 1–15.

[22] B. Gati, *Open source autopilot for academic research-the paparazzi system,* in *American Control Conference (ACC), 2013* (IEEE, Washington, DC, 2013) pp. 1478–1481.

[23] G. Hattenberger, M. Bronz, and M. Gorraz, *Using the Paparazzi UAV System for Scientific Research,* in *IMAV 2014, International Micro Air Vehicle Conference and Competition 2014* (IMAV, Delft, the Netherlands, 2014) pp. 247–252.

[24] E. Fresk and G. Nikolakopoulos, *Full Quaternion Based Attitude Control for a Quadrotor,* in *European Control Conference* (IEEE, Zurich, Switzerland, 2013) pp. 3864–3869.

[25] E. J. J. Smeur, Q. P. Chu, and G. C. H. E. de Croon, *Adaptive Incremental Nonlinear Dynamic Inversion for Attitude Control of Micro Aerial Vehicles,* Journal of Guidance, Control, and Dynamics **39**, 450 (2016).

6

The DelftaCopter

Good judgment comes from experience,
and often experience comes from bad judgment

Will Rogers

To participate in the Outback Medical Express UAV Challenge 2016*, a vehicle was designed and tested that can autonomously hover precisely, take-off and land vertically, fly fast forward efficiently, and use computer vision to locate a person and a suitable landing location. The vehicle is a novel hybrid tail-sitter combining a delta-shaped biplane fixed-wing and a conventional helicopter rotor. The rotor and wing are mounted perpendicularly to each other and the entire vehicle pitches down to transition from hover to fast forward flight where the rotor serves as propulsion. To deliver sufficient thrust in hover while still being efficient in fast forward flight, a custom rotor system was designed. The theoretical design was validated with energy measurements, wind tunnel tests, and application in real-world missions. A rotor-head and corresponding control algorithm were developed to allow transitioning flight with the non-conventional rotor dynamics that are caused by fuselage-rotor interaction. Dedicated electronics were designed that meet vehicle needs and comply with regulations to allow safe flight beyond visual line of sight. Vision-based search and guidance algorithms running on a stereo-vision fish-eye camera were developed and tested to locate a person in cluttered terrain never seen before. Flight tests and competition participation illustrate the applicability of the DelftaCopter concept.*

6.1. Introduction

The possible applications of aircraft with combined efficient long-range flight and hovering capabilities are numerous [2, 3]. Typical examples are long observation missions from ships, survey operations over vast forests, or long-distance flights departing from densely built-up areas. Unfortunately, requirements for fast and slow or even hovering flight are very contradictory [4], making it difficult to design an aircraft that is efficient and controllable while having a very large flight envelope.

Though hybrid aircraft have existed for a long time [5], the first hybrid aircraft had to carry a human pilot. This created some additional constraints, as the pilot needs to be comfortable and able to see the surroundings at all times.

With the advent of UAVs, several hybrid aircraft concepts that were previously impracticable have gained new interest. This includes the so-called tail-sitter UAV.

Figure 6.1: Novel hybrid UAV which combines a cyclic and collective pitch controlled main rotor with a biplane delta-wing and torque compensating tip rotors. The biplane concept adds structural rigidity and minimizes the lateral surface area to reduce the perturbations from turbulence during hover. The large main rotor allows efficient hovering flight while the cyclic control provides large control authority in hover.

To solve the combined requirement on control authority and efficiency, a new tail-sitter concept is proposed based on two principles from conventional helicopters. The first is that conventional helicopters not only vary the pitch of the main rotor for all blades collectively, but they can also create different lift on two opposing blades. This is referred to as cyclic control, as the pitch is increased or decreased every time the blade passes a certain point in its cycle. This control of blade pitch is done through a swashplate where the top part is turning with the rotor and has pushrods to the blades while the bottom part does not rotate and connects to servos in the fuselage. While this adds complexity and maintenance, it allows the rotor to very quickly create very large control moments that, unlike aerodynamic actuators, are nearly independent on vehicle flight speed [6].

The second aspect of conventional helicopter rotor advantages, when compared to multicopters, is that propulsion theory predicts the best efficiency is obtained

with a single rotor that induces only a small velocity increment to a large surface of air [7].

Finally, for fast forward flight, the most energy-efficient way of flying is by using high aspect ratio fixed wings to provide the lift.

By combining a large efficient conventional helicopter rotor with cyclic control and a pair of delta-wings, a platform is obtained that can hover efficiently, fly forward efficiently and still maintain very good control in case of perturbations during hover.

6.1.1. Medical Express Challenge

One use-case for Vertical Take-Off and Landing (VTOL) aircraft with long-range capabilities is the Outback Medical Express UAV Challenge 2016. The Outback UAV Challenge has a long history of creating realistic but very hard challenges to stimulate the state of the art in UAV technology [8–10].

The 2016 edition of the Outback UAV Challenge was called *Medical Express* and had set its competition goals to stimulate the development of aircraft with both hovering and long-range flight capabilities. The competition requires an unmanned vehicle to take off from a model airstrip in *Dalby, Australia* and fly to a remote location 30 km away. The selected remote area had often been inaccessible due to floods for real. At the location, a lost bush-walker must be located. The unmanned vehicle must then select a suitable landing location within 80 m from the found person, but for safety reasons may never come closer than 30 m to the person [11]. After an automatic vertical landing, medical assistance is delivered before flying back to base with a medical sample.

6.1.2. Long-Distance VTOL

This chapter describes the design and application of the novel UAV concept called DelftaCopter shown in Figure 6.1, that combines efficient and high control authority hover with efficient fast long-range flight. While the design was optimized for the Outback Medical Express, it has applications far beyond. It contains all avionics and computer vision needed to turn the UAV into a flying fully autonomous vision-guided robot.

During hover, all lift is provided by the main rotor and it uses tip-rotors and ailerons to compensate for the main rotor torque resulting in the DelftaCopter becoming a helicopter. In forward flight, DelftaCopter pitches down almost 90° and transitions to a fixed-wing aircraft with a large propeller, as illustrated in Figure 5.2. The motor rpm is then reduced and the rotor blade pitch is increased to reach flight speeds of around 20 to 25 m/s. These flight speeds are necessary to cover the required 60 km in under an hour, particularly in case of winds up to 25 kt or 12.9 m/s stated as the limit in the competition rules.

The delta-wing of the DelftaCopter has the advantage of being simple and compact. Not needing a long fuselage and tail section also yields advantages in the landing phases. The natural wind has a severe wind gradient close to the ground [12]. When hovering, the top of the aircraft experiences a higher wind velocity than the lower part, which calls for aircraft without a long tail.

The choice for a biplane was made on three grounds. First, two wings have less

surface area exposed to the wind in VTOL mode, compared to a single wing that can provide the same lift. This diminishes the perturbations of take-off and landing in wind. Moreover, the two wings and fins at the tips form a box construction with landing legs at the extremities. This results in a large footprint and thereby maximal stability when landed. And finally, a biplane configuration remains non-stalled in a higher range of angles of attack [13], which gives advantages in the transition from hover to forward flight and back.

6.1.3. Outline

The outline of this chapter is as follows. First, a propulsion system for both hover and forward flight is derived in Section 6.2. Then the energy consumption (Section 6.3) is addressed. Based on the available propulsion and energy, the aerodynamic and structural design are detailed in Section 6.4. The electrical design is explained in Section 6.6. The control of the DelftaCopter is explained in Section 6.7. An overview of the on-board computer-vision follows in Section 6.8. Flight testing is described in Section 6.9 and finally the Conclusions and Recommendations follow in Sections 6.10 and 6.11.

6.2. Propulsion design

The design of a propulsion system that is efficient in the wide range from fast forward flight down to stationary hovering flight remains a challenge. For the DelftaCopter, the propulsion is designed to be a compromise between efficient hover and efficient forward flight. This results in a rotor blade that is different from rotors seen in conventional helicopters.

Maximum efficiency for hover is obtained using a single large rotor with a low pitch angle [6]. Also for forward flight, a single rotor is the most efficient solution to provide propulsion, albeit with a higher pitch angle [4]. While in theory, a single-blade rotor is more efficient than a two-blade rotor, in practice to balance vibrations at all power settings, the dual blade is more practicable than the single blade.

Blade twist is the change in angle of attack between tip and root. Since the tip of a propeller or rotor moves a lot faster than the root, it needs a different angle of attack to be optimal. The DelftaCopter rotor blades are designed with blade twist. Conventional helicopters suffer from blade-twist as in fast forward flight the rotor undergoes a lot of sideward airflow [14]. This lateral flow hits both tip and root of the blades at the same speed, hereby changing the optimal blade angles and reducing efficiency in case of twist. In the DelftaCopter, the use of twist is possible thanks to the transitioning as the rotor can always be kept in an axial flow regime.

6.2.1. Propeller design

For efficient hovering, the diameter has to be big enough to reach a reasonable figure of merit [6]. For forward flight where the power is significantly less than for hover, the big diameter is only acceptable when the rpm is reduced and the pitch is increased [7]. The DelftaCopter, therefore, uses a large rotor to hover efficiently and create large control moments and increases the pitch in forward flight. This

is achieved by modifying a flybarless 480-sized model helicopter rotor head and reducing the size of the pitch links, more than double the collective pitch range was achieved; namely from $-40°$ to $40°$.
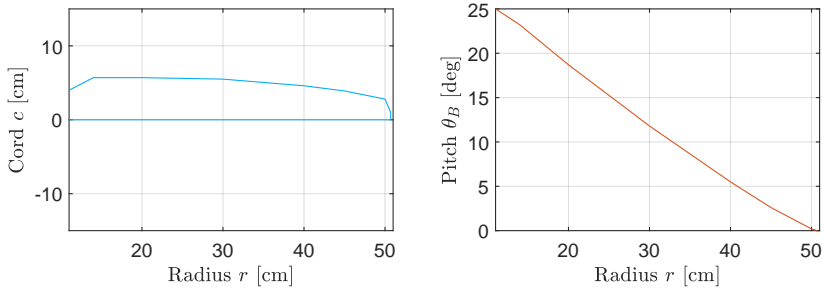
Figure 6.2: Blade cord $c(r)$ and blade pitch angle $\theta_B(r)$ of the designed rotor blade in function of the radial location r.

The design of the propeller was iteratively performed with the support of *Prop-Calc 3.0*[1] [15] to minimize both hover power and forward flight power for a given weight of the DelftaCopter. A diameter of 1 meter was selected as a compromise between hover and forward flight requirements. A blade twist of $25°$ from root to tip was applied. For the airfoil, the *MA409* section was chosen, targeted at a *Reynolds* numbers of $Re_{0.7} = 200.000$ and below. The resulting propeller is shown in Figure 6.2.

Figure 6.3 shows computations of the thrust T generated by the DelftaCopter rotor in function of the incoming airflow V_a for various collective pitch and rpm settings of the blades. A higher thrust for hover or forward acceleration can only be obtained at higher rpm. Lower airspeeds V_a correspond to hovering conditions or slow vertical climb as a low V_a means the rotor moves little compared to the air. Higher V_a occur in fast forward flight. The corresponding predicted required shaft power P to achieve this thrust is shown in Figure 6.4. These figures must be taken into account when designing the automatic flight control of the DelftaCopter. Finally, Figure 6.5 shows the computed efficiency η of the propulsion, showing that at each forward speed, another blade pitch angle is optimal. The rotor is producing the required hover thrust (See Figure 6.3) at 1500 rpm with 10° tip pitch angle. For fast forward flight, the best efficiency at 25 m/s (See Figure 6.5) is obtained using 500 rpm with 50° tip pitch angle. The propeller should then be able to produce about 5.5 N thrust.

During the wind tunnel measurements (See Section 6.5) and flight tests (See Section 6.9), the drag of the DelftaCopter was found to be higher than initially estimated. To overcome this higher drag, a higher thrust is needed, which can only be obtained (See Figure 6.3) by using a lower pitch and increased rpm. While this results in a slightly lower maximal forward cruise speed, it has the advantage to improve the control responsiveness and allows to climb more quickly when re-

[1]See http://www.drivecalc.de/PropCalc/
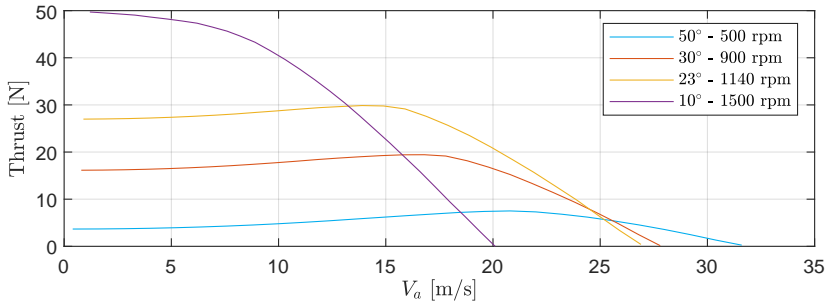
Figure 6.3: Calculated propulsion thrust T in function of the incoming free stream airspeed V_a at selected rotor-blade tip pitch angles and rpm. Low V_a corresponds to hovering flight while high V_a corresponds to cruising flight. In hover, all the weight of the DelftaCopter ($\approx$ 43 N) must be carried by the rotor. This can only be done at low pitch angles and an rpm of 1500. On the other hand, at low pitch angles, the DelftaCopter would never be able to reach 20 m/s as the thrust becomes zero at that speed. Meanwhile, using very high pitch angles of 50°, thrust can be generated up to at least 30 m/s.
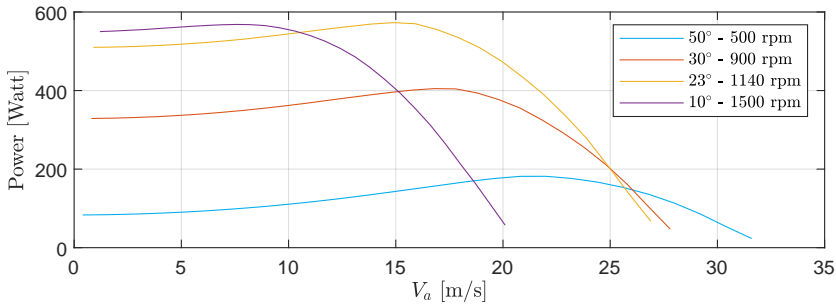
Figure 6.4: Calculated available propulsion power at selected rotor-blade tip pitch angles and rpm. The lower V_a corresponds to hover while the higher V_a corresponds to fast forward flight. Note that the actual lift, motor efficiency, and electronic control efficiency have to be taken into account before the total used power is found.
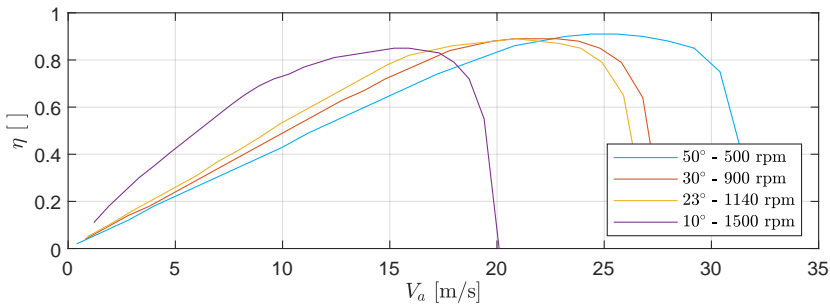
Figure 6.5: Calculated propulsion efficiency η defined as power obtained divided by power applied at selected pitch angles and rpm in function of airspeed. This shows the most efficient pitch setting in function of airspeed V_a. Up to airspeeds V_a of about 16 m/s, the most efficient pitch setting is 10°. For a speed of 20 m/s the pitch setting of 10° is not possible anymore but $\approx$ 23° seems quite efficient. The pitch setting of 50° only becomes more efficient than 30° at speeds over 23 m/s.

quired. For forward flight at this slightly lower cruise speed of ≈21 m/s, the most efficient setting is a pitch angle of about 23° combined with a reduced rpm of about 1140 rpm.

6.2.2. Motor

To deliver the required torque and power, a 105 kV direct-drive sensorless Brush-Less Direct Current (BLDC) motor was selected. The *iPower MT8017* motor rated for 900 W and 40 A was used and powered at a nominal voltage of 22.2 V from the 6 cell lithium-polymer pack (LiPo). This 90 mm diameter outrunner weighs 385 g and was able to spin the 1 m diameter rotor at 1650 rpm in hover at full load. A higher torque motor able to achieve the same rpm would have been preferred but was not available at the moment of the design.

The absence of gears in the direct-drive system with a low-rpm motor on a large efficient low rpm main rotor reduces the three main sources of sound. In hover, the DelftaCopter produces noise equivalent to a medium-sized quadrotor, with most noise originating from the high rpm fixed-pitch counter-torque wingtip propellers. But when transitioning to forward flight, the tip propellers are shut off completely and the main rotor rpm is reduced, which enables the DelftaCopter to become very silent. This reduced noise production is a benefit of using one large efficient rotor with low disc-loading, low rpm, and a gearless direct-drive motor.

6.3. Energy subsystem design

Common high energy density battery technologies for electric UAVs are lithium-polymer and lithium-ion batteries. Even higher energy densities can be achieved using fuel cells [16]. But because of the short mission time of less than 1 hour and high flight speed involved in the competition, the power these systems can deliver is also important. No fuel cell systems could be found within the weight budget and power rating, so instead, lithium cells were selected.

The choice between the more energy-dense lithium-ion and high-current-rated lithium-polymer types is not obvious. Two cells were found that in theory should have sufficient energy to fly the mission; namely the 3300 mAh *LG-HG2-3300* lithium-ion battery and the 2700 mAh *Extron 2700* lithium-polymer battery. While the former has 22 % more energy, it becomes very inefficient at loads close to or over 3.3 A per cell or so-called *1C*: one time the capacity. Since batteries can behave differently than specified under non-constant loads, the selected cells were submitted to a load that simulates an actual flight. The energy profile consists of an initial *high-load phase* during vertical take-off, followed by an endurance *low load-phase* during the cruise and another *high-load phase* during the landing. After a short downtime, there is also a return flight with the same profile.

DelftaCopter needs six lithium cells in series to boost the voltage to the required 22.2 V nominal as single lithium cells have a nominal voltage of 3.7 V. Three series of cells are then placed in parallel to increase the maximally allowed discharge current and be able to deliver the required peaks of 600 W during the climb. The average current during hover was computed to be about 7.5 A per cell and is further referred
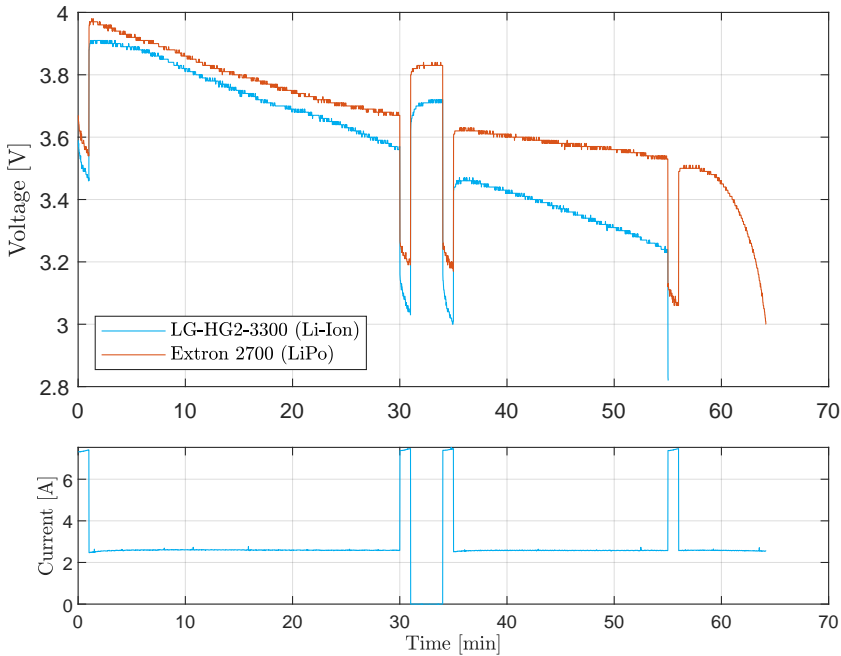
Figure 6.6: *Battery Discharge Test*: Voltage in function of time and current for a single lithium-polymer versus lithium-ion cell subjected to the mission load profile, emulating a 1-minute hovering take-off, followed by an efficient 29 min forward cruising flight, a 1 min hovering landing, 3 min of waiting time and the same return flight. DelftaCopter uses six cells in series to boost the voltage to 22.2 V nominal and three series in parallel to reach the required about 500 W peak. Although the *LG-HG2-3300* contains 22 % more energy than the *Extron 2700*, under the load of the DelftaCopter mission it is the first to be depleted as it cannot handle high discharge rates well.

to as the *high-load* while during forward flight the current per cell is about 2.5 A, which is referred to as the *low-load*.

Figure 6.6 shows the battery discharge test results for the best lithium-polymer and the best lithium-ion battery for the DelftaCopter. Large differences can be observed in the discharge voltage while both are loaded with the same current. It can be seen that the voltage of the lithium-ion cell reaches critically low levels of 2.7 V before the end of the flight. While the lithium-ion cells contain 22 % more mAh under ideal conditions, namely 3300 mAh compared to 2700 mAh for the lithium-polymer cell, under the mission load it delivers less energy and could not deliver the power needed for the final landing. The *Extron 2700* lithium-polymer cells were selected for the DelftaCopter as they could better cope with the high loads of the hover and the fast discharge rate imposed by the relatively short competition time.

6.4. Airframe design

Given the propulsion system, energy package, and performance requirements, a fixed-wing airframe was designed. The airframe needs to generate lift during fast forward flight with little drag, but at the same time, it must also accommodate all the systems of the flying robot, including a swash-plate system for the control of the main rotors blades. Finally, it must provide structural integrity for the airframe to land as a rotorcraft as shown in Figure 6.7.
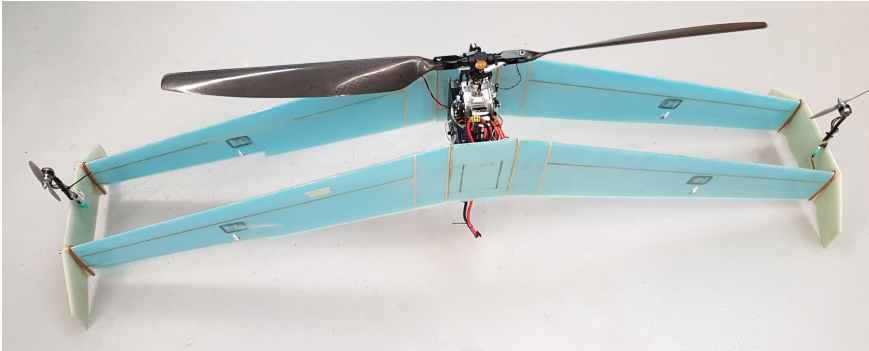
Figure 6.7: Photo of the DelftaCopter standing on the ground using the wingtips as landing legs and utilizing the double-wing structure to increase rigidity and ground stability.

6.4.1. Structural

When the DelftaCopter is in hover, the wings make the helicopter more sensitive to lateral gusts. The biplane configuration has the advantage that the total lateral surface area in hover is reduced by almost a factor of two when compared to a single wing. This in turn means the size of the vehicle and the moments from external perturbations are reduced, while the two wings also provide a stable rectangular basis for landing as shown in Figure 6.7. The wings are kept together by a central assembly that also supports the rotor head. Based on the blade size, parts from a rotor-head and swash-plate system from a *LOGO480*[2] were used and built into an own carbon-aluminum frame. The rotor-head was equipped with shorter blade grid handles to achieve a higher range of pitch angles. Figure 6.16 in Section 6.7 shows a close-up of the rotor system and central fuselage.

6.4.2. Aerodynamic design

A delta-shaped auto-stable flying wing concept was selected for efficient forward flight while removing the need for a long fuselage with a stabilizer that would conflict with the landing. A 'Peter Wick' *PW51*[3] airfoil was manually selected. The *PW51* is an airfoil designed for and proven in flying wings at Reynolds numbers from 100 000 until 800 000. This marginally stable relatively thin airfoil with reflex was designed to

---

[2]MIKADO Model Helicopter
[3]https://tracfoil.com/airfoils/uploads/files/profils/p/PW51i.dat
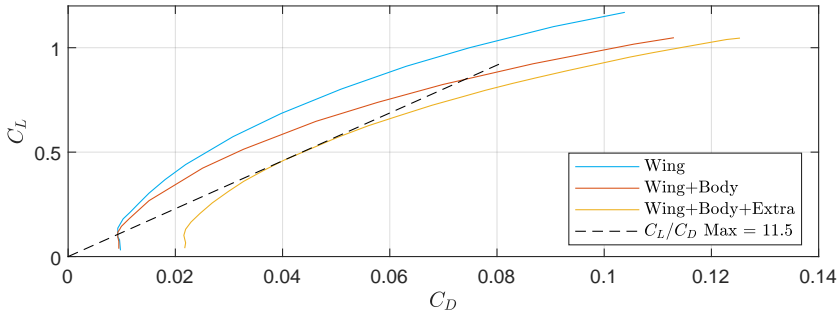
Figure 6.8: Lift-Drag computation using XFLR for a 4.5 kg DelftaCopter. The figures show computed drag polars in the case of wings only, wings with an ideal fuselage, and the total vehicle including drag from rotor head and all protruding items like antennas. The best glide ratio $(C_L/C_D)_{max}$ is 11.4.
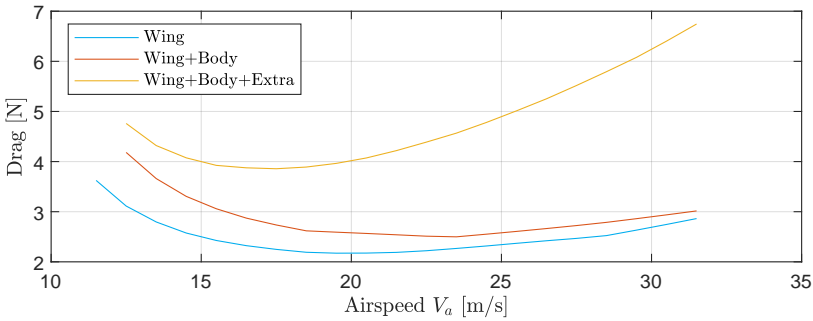
Figure 6.9: The total aerodynamic drag in function of airspeed V_a. When compared to the available thrust from the propulsion from Figure 6.3, one can see that at about 25 m/s the drag becomes larger than 5 N while the maximal achievable thrust with any blade setting becomes lower than 5 N. If the real drag of a built prototype is higher, this will reduce the maximal speed.
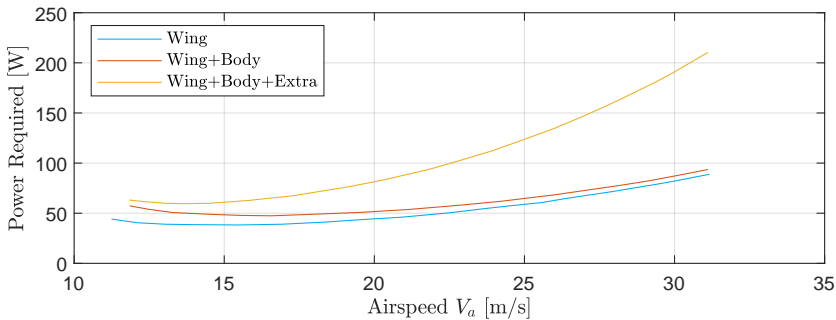
Figure 6.10: The required aerodynamic power in function of forward airspeed V_a computation using XFLR. It is visible that especially at higher speeds, which correspond to lower C_L, a lot can still be gained by reducing the parasitic drag of the DelftaCopter. The actual power used depends on the propulsion setting used and all electrical losses.

have low drag at C_L=0 for fast flight and a high $C_{L_{max}}$ of around 1.2 for sharp turning or slow flight. The pitching moment curve is as flat as possible and the zero pitching moment is around C_L=0 so that no flap deflections are needed at high speeds to get minimal drag. Finally, it has gentle stall properties, which is important during the transitioning phase. Passive longitudinal stability in forward flight is achieved when the delta-wing is given 18° of sweepback and 1° of washout. The wingspan is set at 1.5 m and the cord decreases from 20 cm at the root to 12 cm at the tip. Lift and drag computations were performed using XFLR [17].

Figure 6.8 shows the drag polars which relate the amount of drag for a given amount of lift [4]. Higher angles of attack correspond to higher lift coefficients at lower speeds. It can be seen that the insertion of the fuselage "Body" has almost no influence on C_D at C_L=0 due to the inviscid calculation used in XFLR. The drag due to the non-streamlined fuselage, the rotor head, motor cooling, and all protrusions like antennae, etc is therefore added as an extra term and initially set at C_{D_0}=0.012.

Using the drag polar from Figure 6.8 in the formula of lift $L = 0.5\rho V_a^2 \cdot S \cdot C_L$ with a total wing surface of S=0.496 m^2 and ρ at sea-level of 1.225 kg/m^2 the total drag can be computed. This is shown in Figure 6.9 and can directly be compared with the available propulsion thrust in Figure 6.3 to determine which flight speeds are possible, namely, according to these calculations, speeds of up to 25 m/s.

Figure 6.10 shows the power needed in function of forward speed given the previously computed drag polar in Figure 6.8 and given a total system weight of 4.5 kg. When compared with the propulsion power required to hover with the same weight in Figure 6.4, one can see that flying with the wing requires an order of magnitude less power. From Figure 6.3, one can also see that in pure helicopter mode without wing, the maximal airspeed where the rotor can still provide enough thrust to carry the entire weight of 4.5 kg or 44 N is about 7 m/s. In that case, more than 500 W is used. In comparison, Figure 6.10 shows that thanks to its wings the DelftaCopter can fly using much less power and also reach much higher speeds.

6.5. Wind tunnel analysis

To find optimal settings for energy-efficient forward flight, a wind tunnel experiment was performed in the Open Jet Facility of the Delft University of Technology. The vehicle was placed in the middle of the 2.85 m by 2.85 m wind tunnel outlet, with zero angle of attack. The DelftaCopter was rigidly attached to a pole, which was mounted on a force-moment balance below the wind tunnel outlet as shown in Figure 6.11. Measurements were taken at several representative airspeeds, namely at 15, 19, 24, and 27 m/s. For each airspeed, a range of main rotor collective pitch angles and power settings was tested as shown in Figure 6.12. These settings were manually selected based on the earlier predictions and adapted during the test such that no rpm, current, or motor temperature limitation was breached.

Compared to the theoretic predictions from Section 6.2, the wind tunnel observations show several differences. First of all that the actual reserve thrust ($Thrust - Drag$) of the tested prototype is smaller than predicted, which means that the maximal velocity will be less than the design value and measurements show it will lie
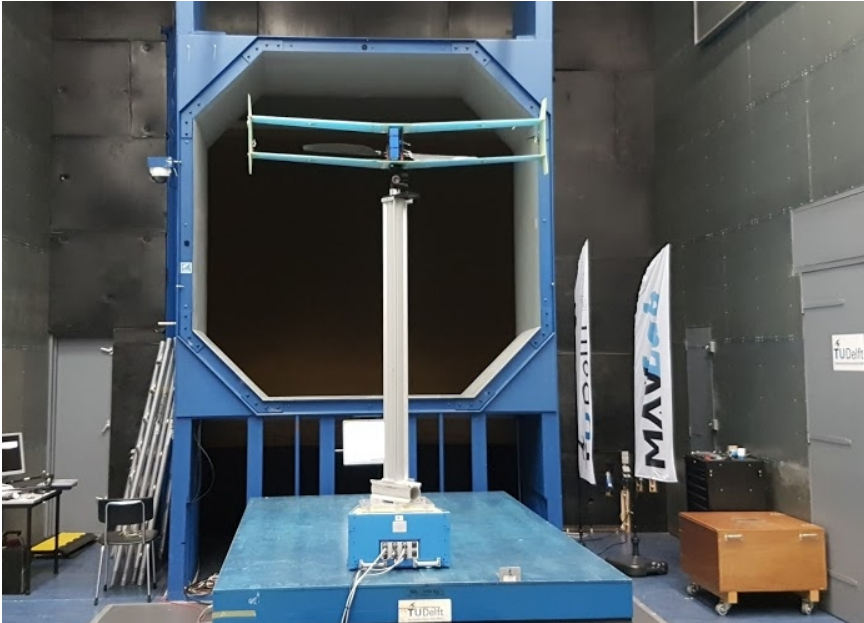
Figure 6.11: The DelftaCopter in the Open Jet Windtunnel of TUDelft. The tunnel outlet measures 2.85 m by 2.85 m and can reach 30 m/s wind speeds. DelftaCopter was mounted on a 1.8 m aluminum pole which was standing on a force and moment balance. The Y-axis of the balance points into the tunnel opening. The X-axis points right in the picture and the Z-axis up.

between 19 and 24 m/s. Similarly, the rpm values below 700 rpm can not produce sufficient thrust to fly at even 19 m/s cruise speed. Increasing the rpm allows having more thrust. While the optimal forward speed for a given power or *kilometer per mAh* can not be extracted precisely from the wind tunnel data as this would have required to tune the angle of attack to produce the correct amount of lift, it could be seen through the lack of thrust that high pitch settings become very inefficient. To further investigate this, the main motor temperature was measured by the onboard avionics using an Negative Temperature Coefficient (NTC) thermistor glued to the inner coils of the main motor. High motor temperatures were only observed at high power combined with low rpm. Hereby the electrical motor efficiency was shown to reduce significantly at high torque. This counteracts the increase in aerodynamic efficiency predicted with higher pitch settings in Figure 6.5. Because of this, it was found that pitch and rpm can be exchanged without a significant difference in power efficiency. Figure 6.13 shows the produced net thrust in function of power for various throttle sweeps at several flight speeds and pitch settings. The reduced electric motor efficiency at lower rpm appears to precisely cancel out the gain in propeller efficiency at lower rpm for the main operating conditions since the thrust-to-power ratio remains nearly constant (except 3 low-rpm sweeps where it is assumed from the vibrations and noise that the rotor was stalled). This shows that at normal cruise conditions, the selected rpm and blade pitch combination do not
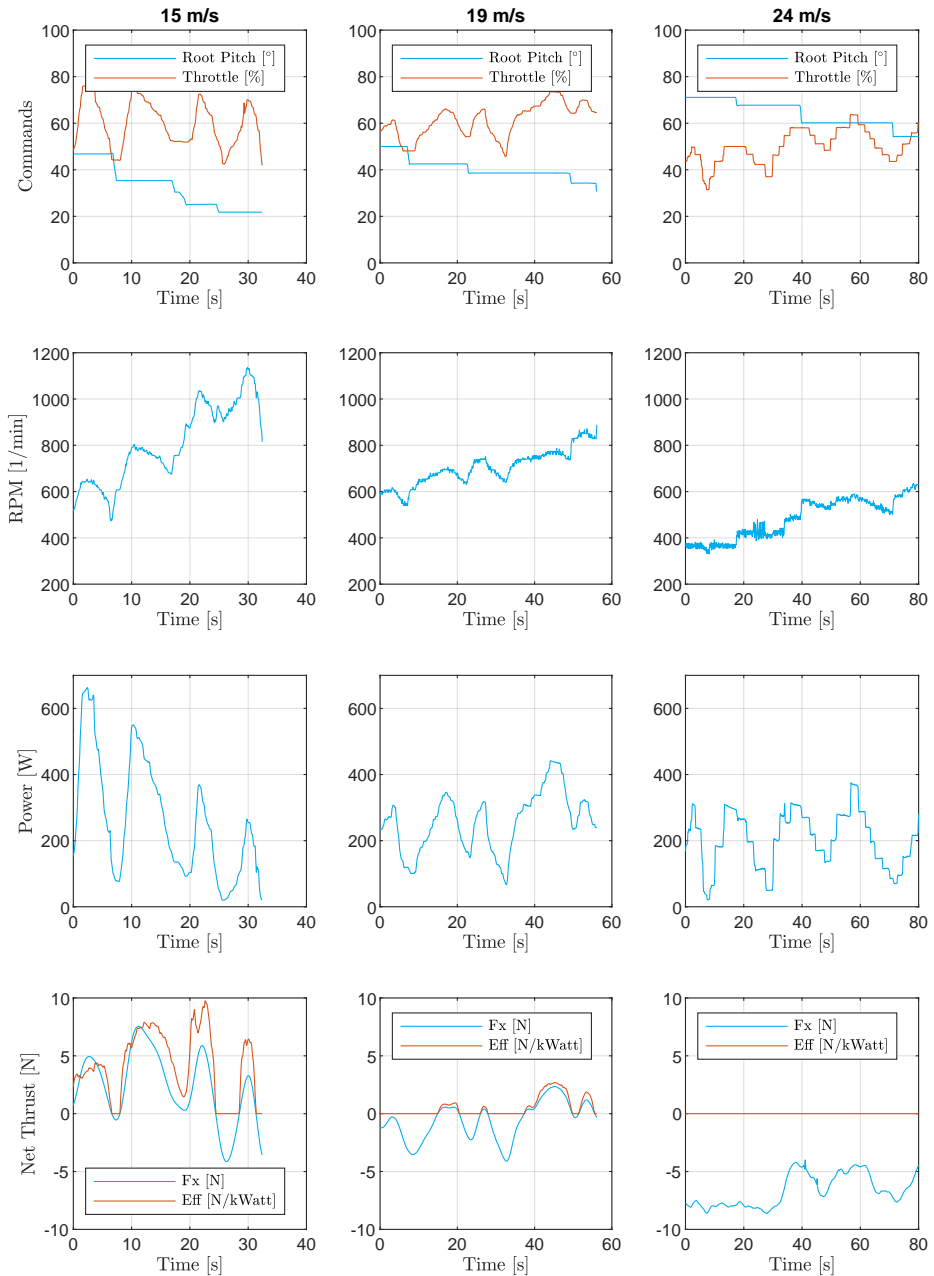
Figure 6.12: Raw windtunnel data and onboard measurements for the tunnel setting at 15, 19, and 24 m/s. For every pitch setting all acceptable throttle settings are visited and the effect on power use and forward thrust is measured. Note that the tip pitch is 25 deg smaller than the root pitch.
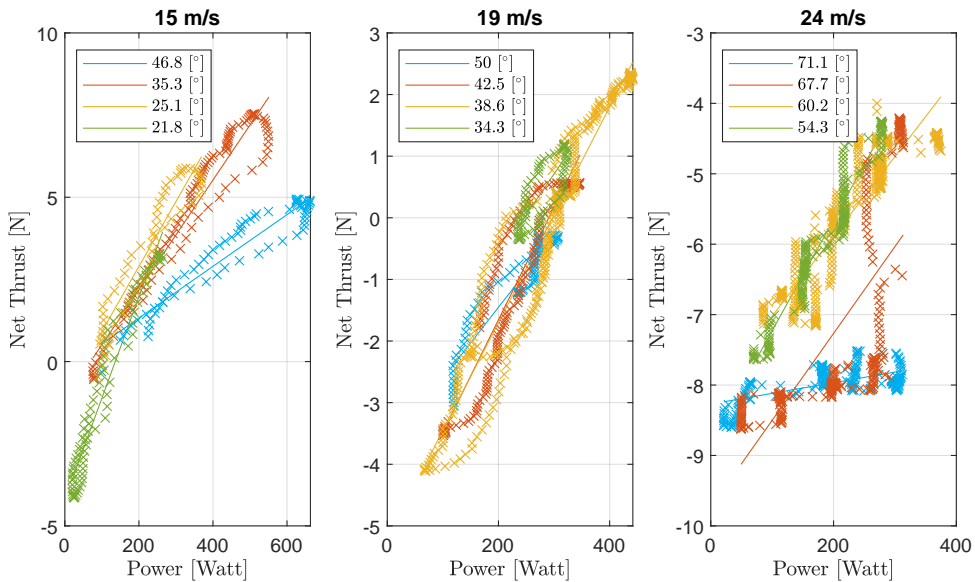
Figure 6.13: Measured thrust in function of the power for various up and down throttle sweeps at various pitch settings. Except a few very inefficient cases, around the zero net thrust most pitch angles require the same amount of power. Note that there are about three runs where the rotor is much less efficient while the motor is unable to provide the requested torque.

influence the power efficiency very much.

Overall it can be concluded that in the cruise regime, the DelftaCopter can operate at a large range of rpm and pitch settings without important change in efficiency as the aerodynamic rotor efficiency increase at reduced rpm is canceled out by electrical motor efficiency loss.

This led to the following compromise to select an ideal rpm for the forward flight. The rotor needs time to spin up and can only hover at over 1500 rpm. From Figure 6.5 we know head rotor speeds below 1000 rpm are only useful for speeds over 22 m/s, but wind tunnel measurements showed that these speeds can not be reached. The DelftaCopter can operate at a large range of rpm and pitch settings while cruising at about 19 m/s without significant change in total efficiency as increases in aerodynamic efficiency are canceled out by the reduced electrical motor efficiency. In the case of low motor efficiency, its temperature can grow dangerously hot. Because it is safer in case of quick deceleration to hover and puts less thermal stress on the motor, in its current form the DelftaCopter can best fly in forward flight with high rotor speeds.

6.6. Electronic design

To comply with the strict requirements of the Outback Medical Challenge [11] dictated by the Australian aviation safety organization Civil Aviation Safety Au-
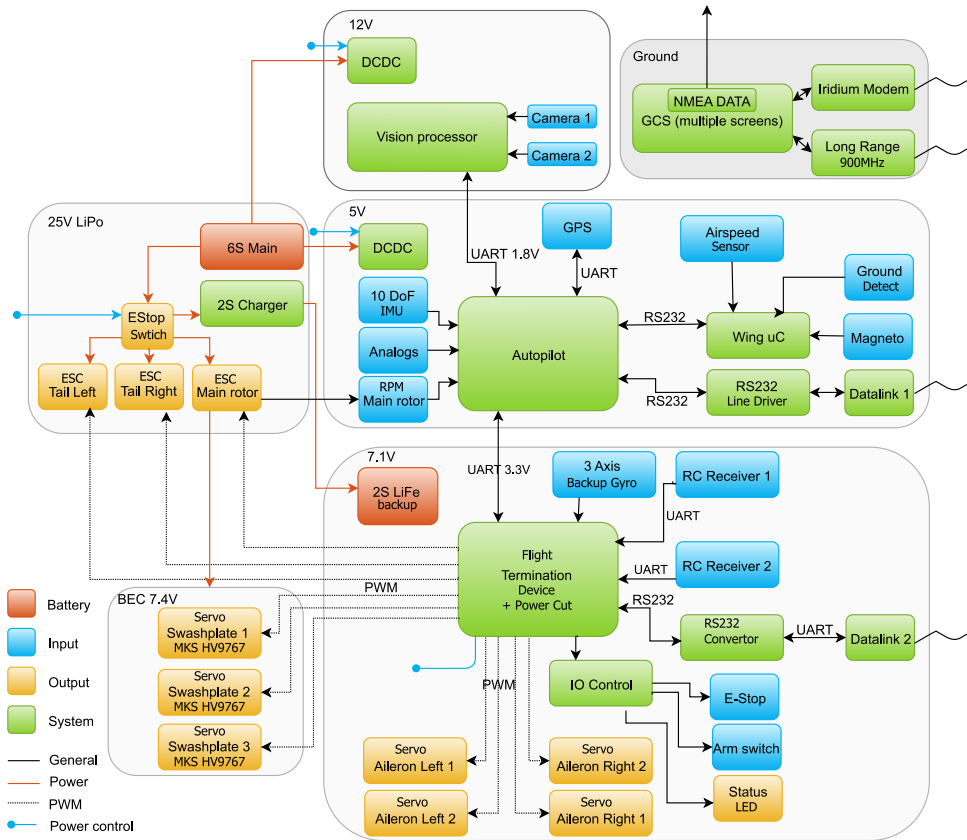
Figure 6.14: Schematic overview of the DelftaCopter electronics

thority (CASA) and be allowed to fly Beyond Visual Line of Sight (BVLOS) missions of up to 30 km, custom electronic are required (See Figure 6.15).

The electronics board consists of two independently powered circuits. As seen in Figure 6.14, the first part is called the 'flight termination device'. This part has all the safety-critical functions like driving actuators but also geo-fencing and long-range kill switches, motor un-powering, and arming.

All navigation and control functions together with the flight plan logic are in the second part called 'autopilot'. Both parts are modifications of the Paparazzi-UAV [18] Lisa-MX autopilot [19].

Because of the number of extra functions and boards, like SD-card logging, master power cut-off, line drivers to modems in wings, power converters, current sensors, voltage sensors and, temperature sensors, the design started to grow larger. To minimize interconnection failures and minimize the total weight, a custom Printed Circuit Board (PCB) was designed with all needed functions. The custom system is shown in Figure 6.15.
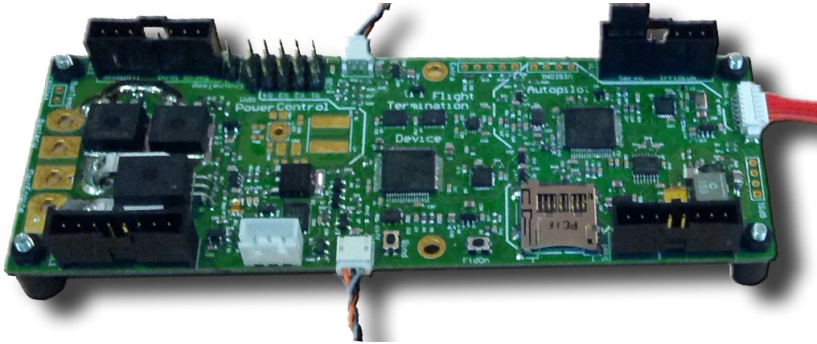
Figure 6.15: All central electrical functions of the DelftaCopter are integrated into a single board PCB for minimal weight and minimal interconnection failure. The four corner connectors lead to the systems in all four wings. From left to right the board contains power, flight termination, and autopilot.

6.7. Control

In hover, the DelftaCopter is a helicopter and is controlled with blade pitch changes of the main helicopter rotor through a conventional swashplate. Rotorcraft dynamics have been well studied for many years [6, 14, 20–26]. But the properties of the light efficient rotor on a large heavy fuselage found in the DelftaCopter are different from what is seen in similarly sized conventional helicopters. In conventional helicopters, the gyroscopic effect of the rotor dominates in the total system dynamics, and roll is steered by changing the lift at the front and back of the rotor. Opposingly, in conventional quadrotor control, the inertia of the body dominates over the precession of the propellers. Roll is steered by altering the lift of the left or right rotors. The DelftaCopter seems to be precisely in between both [27].

6.7.1. Attitude control in hover and forward flight

The total weight of the DelftaCopter with all its batteries is well over 4 kg while the power-efficient 60 g rotor blades with high camber and lift coefficients only require low rotor speeds. The rotational inertia of the wings is increased as its weight is spread over the high aspect ratio wings with a lot of electronics like radios and antennas being placed in the wingtips for reasons of interference and antenna placement. Previous work (covered in Chapter 5) has shown that this high fuselage inertia is altering the control of the light DelftaCopter rotor in hover [27] and proposed a rate controller in the form:

$$\begin{bmatrix} \delta_x \\ \delta_y \end{bmatrix} = G^{-1} \begin{bmatrix} K_p \cdot p_{err} + q \cdot C_{q_{\dot{p}}} \cdot K_c \\ K_q \cdot q_{err} + p \cdot C_{p_{\dot{q}}} \cdot K_c \end{bmatrix}, \quad G = \begin{bmatrix} C_{\delta_{x_{\dot{p}}}} & C_{\delta_{y_{\dot{p}}}} \\ C_{\delta_{x_{\dot{q}}}} & C_{\delta_{y_{\dot{q}}}} \end{bmatrix} \quad (6.1)$$

where δ_x and δ_y are the desired swashplate cyclic deflections, p_{err} and q_{err} are the rate errors between the actual rate and desired rate, K_p, K_q, and K_c are tunable gains, p and q are the body rotational rates and C_x represent the identified coefficients. Around this rate control loop with compensation for the coupled dynamics,

an attitude PID controller is implemented.

Rotor in forward flight

In forward flight, the rotor-fuselage interaction will change due to the large dependency of rotor dynamics on rotor rpm [27]. Moreover, it was found to take several seconds to accelerate a slow turning rotor back to hovering speed. Finally, wind tunnel testing in Section 6.5 showed only a little decrease in total efficiency at higher rpm Therefore, it was chosen to initially fly forward with the same rotor rpm as in hover so a single set of rotor head coefficients needed to be identified while the vehicle could instantly go back from forward flight to hover in the case of a problem[4]. Detailed identification of the rotor dynamics in forward flight is left to future work.

Control allocation of the aerodynamic surfaces

Figure 6.16: Close up of the rotor head of the DelftaCopter. The swashplate has three leverage points at 120° from each other. The collective pitch can reach from -40 to 40°, which is double that of a conventional helicopter. The blades have high camber, a high lift coefficient, and 25° of blade twist from root to tip. Hovering flight is performed at a designed tip angle of attack of around 10° with 1500 rpm. In forward flight, the tip angle of attack can change up to 50° at 500 rpm. The root angle of attack is then about 75°. Having blade twist is possible because the flow is always axial as the DelftaCopter transitions. This allows the rotor to be efficient from hover to fast forward flight.

Besides the swashplate for the control of the rotor blade pitch, the DelftaCopter also has two fixed-pitch torque compensating tip rotors and four aerodynamic surfaces. A control allocation module was developed with sends the commands to the

---

[4]The DelftaCopter was developed for a competition and was on a very strict and short schedule.

various actuators for the flaps, the tip motors, and the swashplate. In parallel with the swashplate control, the pitch rate error q_{err} was also sent to the elevator, and the hover yaw rate or fixed-wing roll was sent to the top motors and ailerons:

$$\begin{bmatrix} \delta_{\text{elevator}} \\ \delta_{\text{ailerons}} \\ \delta_{\text{tipprops}} \end{bmatrix} = \begin{bmatrix} K_{q_a} \cdot q_{err} \\ K_{r_a} \cdot r_{err} \\ K_{r2} \cdot r_{err} \end{bmatrix} \tag{6.2}$$

The flaps and swashplate are both always active at the same time in hover and in forward flight and the gains K_x are scaled such that a 100 % deflection of the swashplate corresponds to a 100 % deflection of the elevator or ailerons. The tip motors are only active in hover and disabled in forward flight. The actual aerodynamic surfaces mix the elevator and aileron linearly and act as elevons.

To cope with the large differences in actuator effectiveness of these actuators in function of airspeed, different PID gains are implemented for hover and forward flight.

6.7.2. Horizontal position control
The horizontal position control of the DelftaCopter differs based on the flight mode: hover or forward flight.

Hover
The control of the horizontal position during the hover phase is done with the Incremental Nonlinear Dynamic Inversion (INDI) controller from Smeur *et al.* [28]. This sensor-based control approach avoids the need for precise aerodynamic modeling but instead exploits the fact that accelerometers measure the sum of forces acting on the vehicle. This sum contains external forces acting on the airframe, but also the control forces, such as the thrust vector. Therefore, a change, or *increment*, in acceleration can be achieved by incrementing the control forces. INDI therefore only requires a precise actuator model.

The position control of the DelftaCopter in hover is purely based on the thrust vector from the rotor and does not take the wing into account. However, because of the large wing area, wind gusts can result in significant forces. However, because these forces are directly sensed by the accelerometer even before an actual displacement occurs, INDI immediately compensates them even though no knowledge of the wing is provided.

Forward flight
During forward flight, the goal of horizontal navigation is to fly towards waypoints, and the direction of flight is controlled by making coordinated turns. Vehicle pitch and roll are controlled with PID controllers based on the altitude error and heading error. For the heading, a coordinated turn is made purely on a feedforward basis, where the heading change is proportional to the tangent of the roll angle:

$$\dot{\psi} = \frac{g \cdot tan(\phi)}{V_A} \tag{6.3}$$

Because there is no measurement of the sideslip, in the controller it is not actively controlled but is reduced passively by the vertical tip fins.

6.7.3. Altitude control

When the rotor points upwards, the vertical axis is controlled using the thrust of the main rotor via a classical controller. During forward flight, the vertical axis is controlled with the pitch angle of the vehicle while, thrust controls the airspeed. Additionally, a proportional feed-forward gain compensates for the loss of lift during turns.

6.7.4. Transition control

In this work, the first generation of DelftaCopter is controlled either in hover mode or forward mode. Transitions between the two flight modes are governed by the flight plan. Practically, during a transition, the roll angle is kept zero and the heading is kept constant, while the pitch angle is gradually increased or decreased during about 3 s. When going from hover to forward flight, the tip propellers are turned off when the transition is halfway. The rotor thrust is set to maximal practical safe values to quickly build airspeed. In forward flight, the flaps become sufficiently effective to counter the rotor torque due to the increased airflow, and energy is saved by not using the tip propellers.

This first-generation DelftaCopter controller was limited by conservative maximum bank angles, which only allowed it to hover up to and including maximum wind speeds of 7 m/s. Although this open-loop transition method does not keep the altitude constant during the transition particularly during the slow down, it was shown to be very reliable.

6.8. Onboard computer vision

To enable automatic landing site selection, the DelftaCopter was equipped with the state-of-the-art computer vision system shown in Figure 6.17: a prototype of the Parrot SLAMdunk[5].

Figure 6.17: Parrot SLAMdunk vision system with a dual fish-eye lens at a baseline of 20 cm and an Nvidia Tegra TK1 processor.

The SLAMdunk Application Programming Interface (API) provides access to a 96x96 pixels depth map and a 1280x1024 pixel color image. The depth map is

---

[5]https://www.parrot.com/

generated at 30 fps, employing Semi-Global Block Matching (SGBM) accelerated by the Graphics Processing Unit (GPU). The hardware specifications are shown in Table 6.1.

Figure 6.18: The SLAMdunk vision system was mounted on the side of the center fuselage DelftaCopter looking away from the main rotor. In hovering flight, this means the camera has a perfect view of the ground, and in forward flight, the camera looks backward. Thanks to the wide field of view fisheye lenses the camera can also look vertically down during forward flight.

On the DelftaCopter, the SLAMdunk looked straight down towards the ground when in hover mode, as can be seen in Figure 6.18. This system was used for the detection of targets, for flat landing spot selection, and determining the ground altitude at the remote landing site.

Processor	Nvidia Tegra TK1
Cameras	1280x1024 RGB
Depth map	96x96 corresponding to the central 640x480 pixels
Frame rate	30 fps
Stereo base line	20 cm
Lenses	Fish eye
Sensors	10-DOF Inertial Measurement Unit (IMU) and sonar

Table 6.1: SLAMdunk prototype properties.

6.8.1. Visual target detection

The outback medical challenge requires UAV to find a lost bushwalker called 'Outback-Joe' located at a roughly known GPS position (± 100 m accuracy) [29]. The UAV has to land as close as possible to the target but shall at all times keep a minimum distance of 30 m from Joe in all directions. Joe is to be recognized standing upright in a field near a farm, wearing normal blue jeans and an Australian Akubra hat. No example visual data was available beforehand and vision test flights in representative environments were very limited due to the ongoing development of the platform. This does not favor detection methods that need many training samples [30]. Instead of using a real human as Joe, the challenge used a full-size dressed dummy. This means no movement or thermal features could be used [31]. The overall quality of the images of Joe taken from a moving and vibrating platform at 40 m height was also low. Since Joe was reported to be standing upright, a birds-eye view is advantageous to detect it [32].

A Hue Saturation Value (HSV) color filter combined with a shape filter[6] was used as a salience detector to select possible targets Joes. These were clustered based on their projected GPS locations over time and sent over the low bandwidth long-range data link to the Ground Control Station (GCS) in the form of thumbnails accompanied with their projected GPS positions and Joe likelihood scores. At GCS, a human operator would select the best candidate and update the landing waypoint.

6.8.2. Ground model and altitude
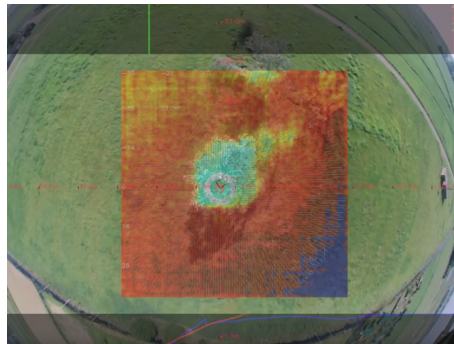
Figure 6.19: Image from the landing avoidance system based on the SLAMdunk disparity map. The colored disparity map in the center of the image shows a high tree where the red represents the landable area.

The stereo disparity images provide direct measurements of the height above the terrain and obstacles and can measure up to a maximum of 30 m and the SLAMdunk also has a sonar to measure precisely up to 10 cm from obstacles. This was used to estimate the ground altitude, ground flatness and find obstacles [33, 34]. To prevent false positives from the noise in the depth map at small disparities, the stereo vision was only enabled at heights below 20 m Above Ground Level (AGL). Additionally,

---

[6]The OpenCV simple blob detector

reference textures of areas with a known good surface (farmer's land, grass, desert, road, etc) and non-landable surface (water, trees, roofs, etc) were annotated and classified during flight with a simple Euclidean distance texture comparison on 11x11 pixel patches [35].

Finally, a proportional gain was used to steer the DelftaCopter laterally away from the closest obstacle or non-landable area towards the flattest landable area while adjusting the descending speed in case of close obstacles. This simple strategy was shown to cope well with simple sceneries like farm setups with trees, buildings, and fences but a lot of landable areas. An example landing view is shown in Figure 6.19.

6.9. Flight performance

During the flights, data are logged onboard the autopilot on an SD-card at 512 Hz and can be followed in real-time with low bandwidth through the telemetry. The logged data consists of gyroscopic body rates and body accelerations, magnetometer readings, dual air pressure from inside the fuselage and from a static port in the wing, total pressure converted to airspeed, main rotor rpm, main battery voltage, auxiliary battery voltage, propulsion current, and the main motor coil temperature. In this section, the flight performance of the DelftaCopter is evaluated from the onboard logs.

6.9.1. Transitioning flight

Figure 6.20 shows a flight with six transitions from hover to forward flight and back. During a transition from hover to forward, the DelftaCopter has a small increase in altitude due to the applied power to accelerate the vehicle. During the transition from a fast forward flight back to hover a non-negligible large altitude overshoot is observed of about 17 m due to excess energy during the fast transition. This has the advantage of only reaching stall speeds when the DelftaCopter is already nearly vertical and results in visually smooth transitions. The flight in this test is performed in a very confined area of about 150 by 150 m and in forward flight, the DelftaCopter is turning most of the time. Figure 6.20 also shows how during every hover the engine temperature is rising due to the increased load.

Figure 6.21 shows a close up of a transition from the same flight as Figure 6.20. The figure shows a smooth transition from hover at body pitch angles around zero to forward flight with body pitch angles down to $-90°$ with the X axis pointing to earth in that configuration. During the short thirty-second forward flight, four turns are performed during which the pitch angle is increased (less negative) to maintain the correct altitude. During the transition from hover to forward flight, the main rotor thrust is increased to accelerate. The result is a peak in power used. During the forward flight, altitude is well maintained even during the turns. During the transition from forward flight to hover, the vehicle has a lot of excess energy to dissipate. The transition is made based on timing and the excess energy results in a climb of more than 15 m. The hover controller then slowly returns the vehicle to the desired altitude.
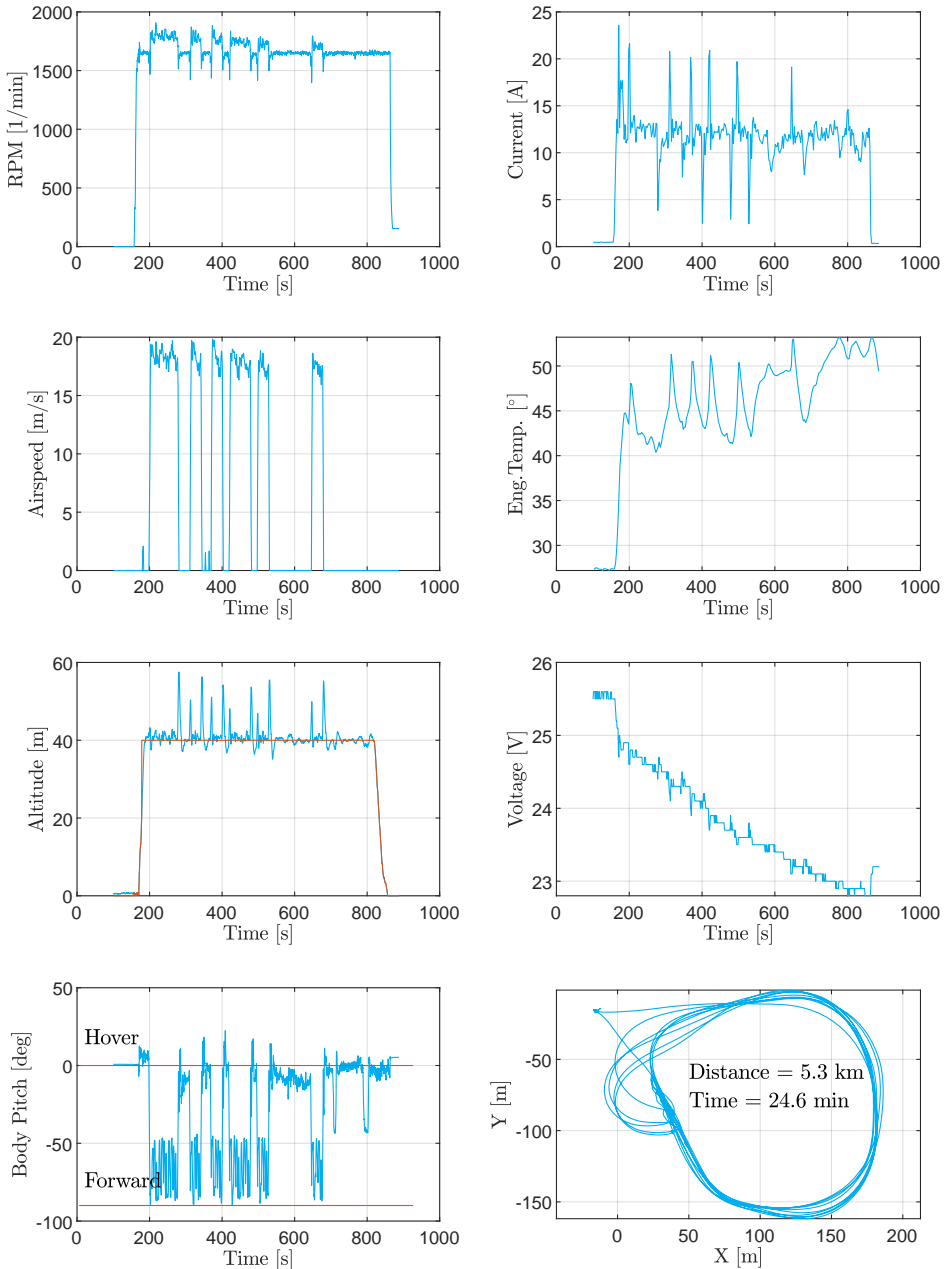
Figure 6.20: Onboard measurements (main rotor rpm, current, airspeed, main motor temperature, altitude, battery voltage, pitch angle, and ground track) from a test flight containing six transitions from hover to forward flight and back.
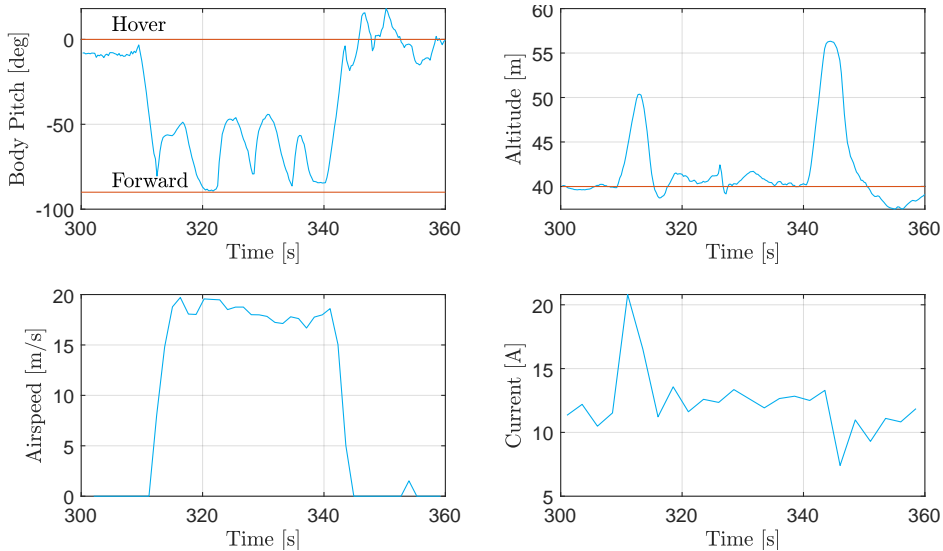
Figure 6.21: Close-up of a single transition. The DelftaCopter is starting from hover and transitions to forward flight. The current temporarily increases to over 20 A during the acceleration phase and altitude increases during this open-loop transition. It then flies a square pattern while the body pitch angle is used to control altitude. During each of the four turns, a significant pitch up is required to keep the altitude constant. Finally, the DelftaCopter transitions back to hover in a 3 s open-loop maneuver where all excess kinetic energy is transformed into altitude.

6.9.2. Efficiency testing

During another test flight shown in Figure 6.22 an attempt is made to find the optimal forward flight regime. According to the design from Section 6.2, a lower rotor rpm in forward flight should be more efficient. The actual flight data does however not clearly show an efficiency increase. This corresponds exactly to the wind tunnel observations from Section 6.5. The rising motor temperature shows that the high motor load does decrease the electrical efficiency. Since no loss of total efficiency is observed, this means the propeller efficiency indeed increases but is undone by the loss of electric motor efficiency.

6.9.3. Competition flight

The goal of the DelftaCopter was to bring medical aid to an isolated person in need. This was tested during the 2016 Medical Express competition held in Dalby, Australia. The remote location of 'Outback-Joe', namely the dummy person in need, was never visited before and his appearance was not known. On average, weather conditions were good with only mild ≈5 m/s winds, no precipitation, and more than 10 km visibility. However, there were occasional whirlwinds, sucking sand and butterflies 100 m into the air. The team had 15 min to set up all equipment like laptops, antennas, and prepare the DelftaCopter. After a thorough preflight inspection, the DelftaCopter performed a great autonomous take-off and transition to forward flight in front of all spectators.
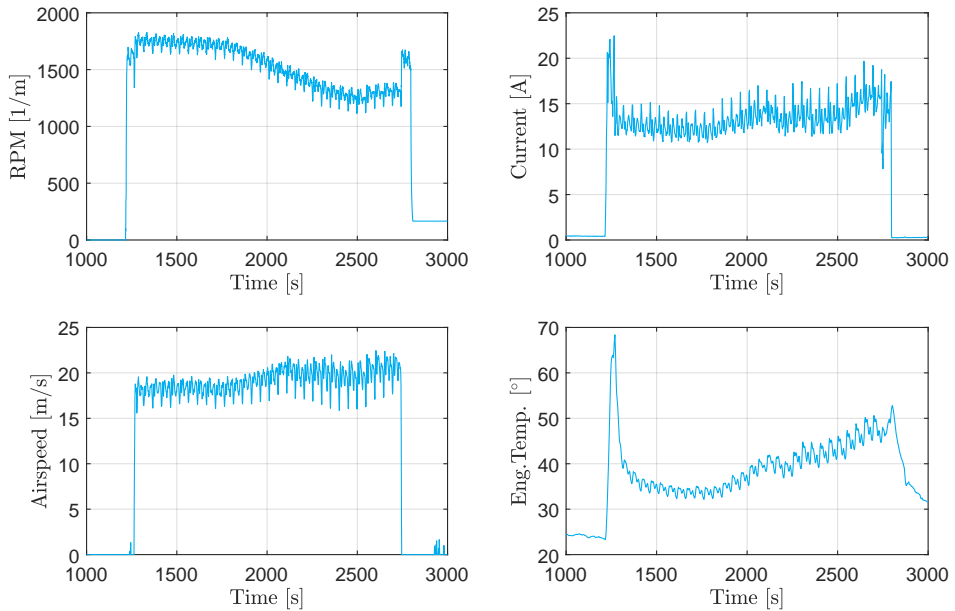
Figure 6.22: In search for a rotor rpm for the most efficient forward flight, a long outdoor flight was performed on a very calm evening in which a large range of pitch and throttle settings were tested.

6

As can be seen in Figure 6.23, the flight started at Waypoint 1 and the path passed the take-off location again at Waypoint 5 after approximately 10 km of flying. This was done for safety reasons. Waypoint 3 was located over agricultural areas with very little danger for people on the ground. Safely flying this return segment increased the chances that the unmanned air vehicle was operating properly before attempting the flight over roads near Waypoint 6 and towards a farm at Waypoint 9.

The total traveled distance to Joe is 21.1 km or 11.4 Nm one-way.

During the flight, all systems worked as desired and performance was consistent with all the test flying data. The DelftaCopter was carrying a full 10.5 Ah 6 cell lithium-polymer battery weighing 1.6 kg and the Parrot SLAMdunk stereo camera. The total weight was 4.3 kg.

Figure 6.24 shows that its cruise airspeed was a little under the designed 40 kt, which corresponds to 20.5 m/s. The eastern wind meant that DelftaCopter has a head-wind during most of the flight and therefore the altitude was selected to be as low as allowed to exploit wind gradient effects which yield lower wind speeds close to the ground. At the remote location, the DelftaCopter successfully made a scan, transitioned back to hover, and initiated a landing. In the 2016 Outback Medical Challenge, no participant managed to complete the challenge, but the DelftaCopter nevertheless won the second prize. Overall this novel helicopter with wings concept called DelftaCopter[7] was shown to successfully handle real-world conditions, hover efficiently, fly fast forward efficiently, and transition seemingly between both.

---

[7]http://www.delftacopter.nl/
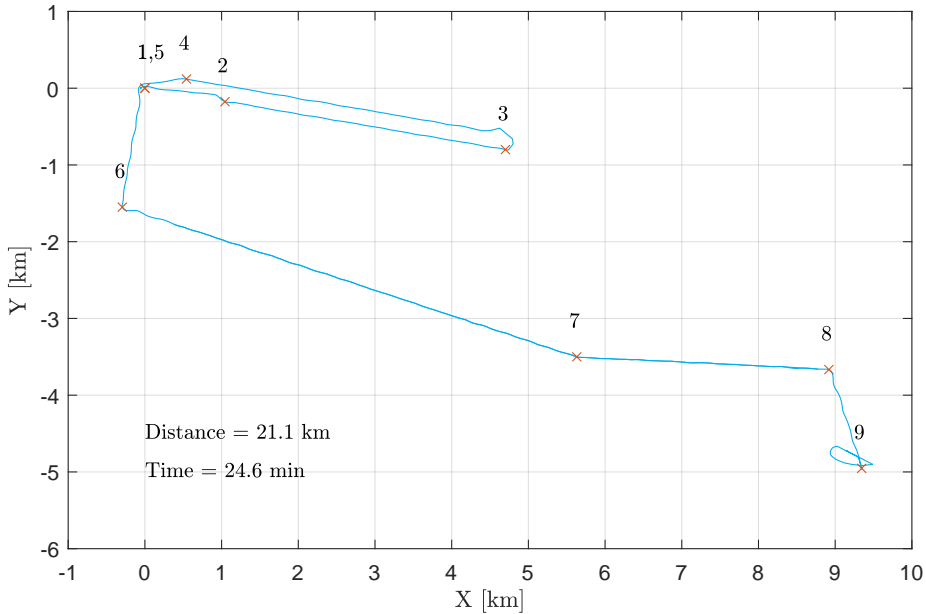
Figure 6.23: Competition flight ground track. The flight starts at Waypoint 1 and searches for Joe around Waypoint 9. Including the hovering take-off and landing, the flight to Joe took 24.6 min and the total distance of the flight was 11.4 Nm or 21.1 km.

6.10. Conclusion

The novel DelftaCopter concept was proposed which exhibits efficient hovering with one large rotor, good control authority in hover with fast cyclic control, a simple and structurally strong biplane delta-wing design that also serves as landing gear and yields improved stall behavior over single wings. The biplane also reduces the lateral surface affected by turbulence and wind during hover of this tail-sitter VTOL aircraft. While the swash-plate adds mechanical complexity and maintenance, it yields very fast large control moments and the collective pitch change is crucial to the efficiency of both hover and forward flight. The DelftaCopter was built, tested in a wind tunnel and in-flight. Finally, the DelftaCopter participated in the *Outback Medical Express Challenge 2016* where it won the second prize. The concept applies to a variety of scenarios, especially when long-distance and efficient hovering at minimal weight are driving requirements. It was about five times lighter than the concept winning the first prize.

The hover efficiency of the DelftaCopter is high thanks to its large single low rpm optimized rotor. The energy efficiency during fast forward flight turned out to be lower than expected from computations. This is most likely due to the electrical
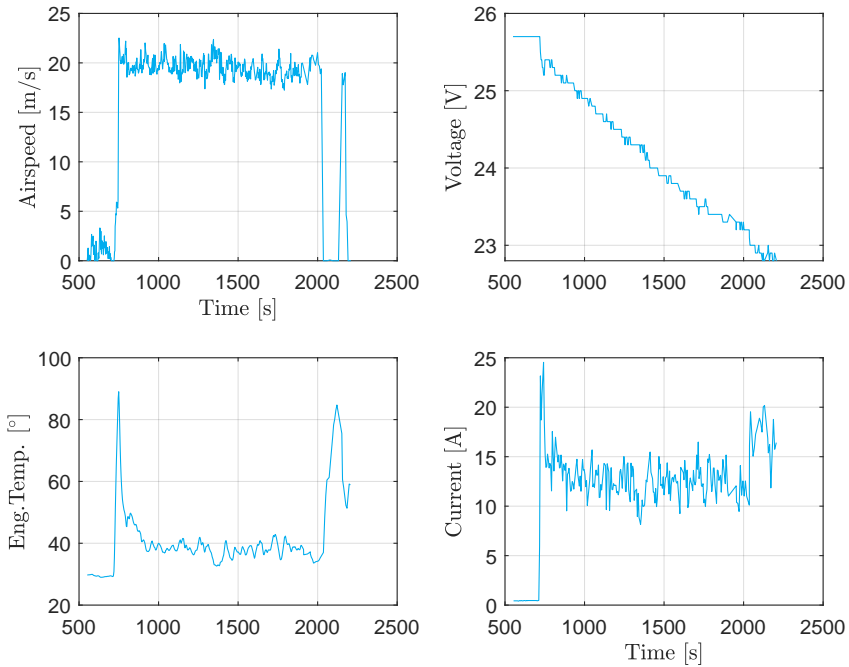
Figure 6.24: Competition flight data of the flight to Joe. The average airspeed during the flight was roughly 40 kt or 20.5 m/s. During hover, the engine temperature rises to 80° but during forward flight, it settles at a value of about 40°. The current during the climbing hover in the first phase is about 23 A, 540 Watt. During the cruise, the current reduces to about 12 A or power of 280 W. Non-climbing hover is achieved at 18 A or 420 W.

inefficiency of the motor at high torque. The maximal forward speed was also lower than expected due to the higher than expected drag of the final airframe.

The cyclic control of the DelftaCopter yields very fast and effective attitude control. Previous work proposed a controller that compensates for the different lateral and longitudinal inertia of the fuselage and the fuselage-rotor interactions with couplings between the pitch and roll. This controller was extended to handle forward flight and fly trajectories and perform transitions.

The stereo depth map of the SLAMdunk allows path planning around obstacles and selection of flat areas during landing. The large field of view provided by the fisheye lens enabled the DelftaCopter to perform its mission with one fixed stereo camera, even though the aircraft tilts 90°. A salient detector with human feedback option was developed to find a lost bushwalker. The DelftaCopter is also capable of autonomously selecting a safe landing spot based on texture analysis and flatness

analysis. During the landing phase, an autonomous obstacle avoidance algorithm ensures safe landing based on the depth map provided by stereo vision.

6.11. Recommendations and future work

The current design has shown outstanding efficiency in hovering flight and slightly less efficiency than predicted during forward flight. During the Outback Medical Express Challenge but also most other application scenarios of the DelftaCopter, the forward flight phase is the predominant mode of flight. A future design could therefore place slightly less emphasis on hover efficiency and more on forward flight where some efficiency gains highly affect the operational range and flight speed. A smaller diameter rotor/propeller will also put less demand on the torque requirements of the direct-drive motor which was currently overloaded in fast forward flight. When higher torque direct drive brushless motors become available, they could also yield efficiency improvements in fast forward flight.

Although sufficient information about the flight dynamics was gathered in this work to allow successful flight, many aspects could benefit from further research. One particular topic of interest is the interaction between the wing and the rotor. Especially the influence of wing forces on the rotor was not studied for higher frequencies and for forward flight. This will be the topic of Chapter 7.

6

Appendix

Key specification values of the DelftaCopter are repeated in Table 6.2. Figure 6.25 gives an overview of the team. Finally, Figure 6.26 shows the three views of the DelftaCopter with sizing information.

Figure 6.25: DelftaCopter team at the *Outback Medical Express UAV Challenge 2016*, Dalby Australia. From left to right: Bart Remes, Christophe De Wagter, Freek van Tienen, Ewoud Smeur, Kevin van Hecke, Rick Ruijsink and Erik van der Horst.
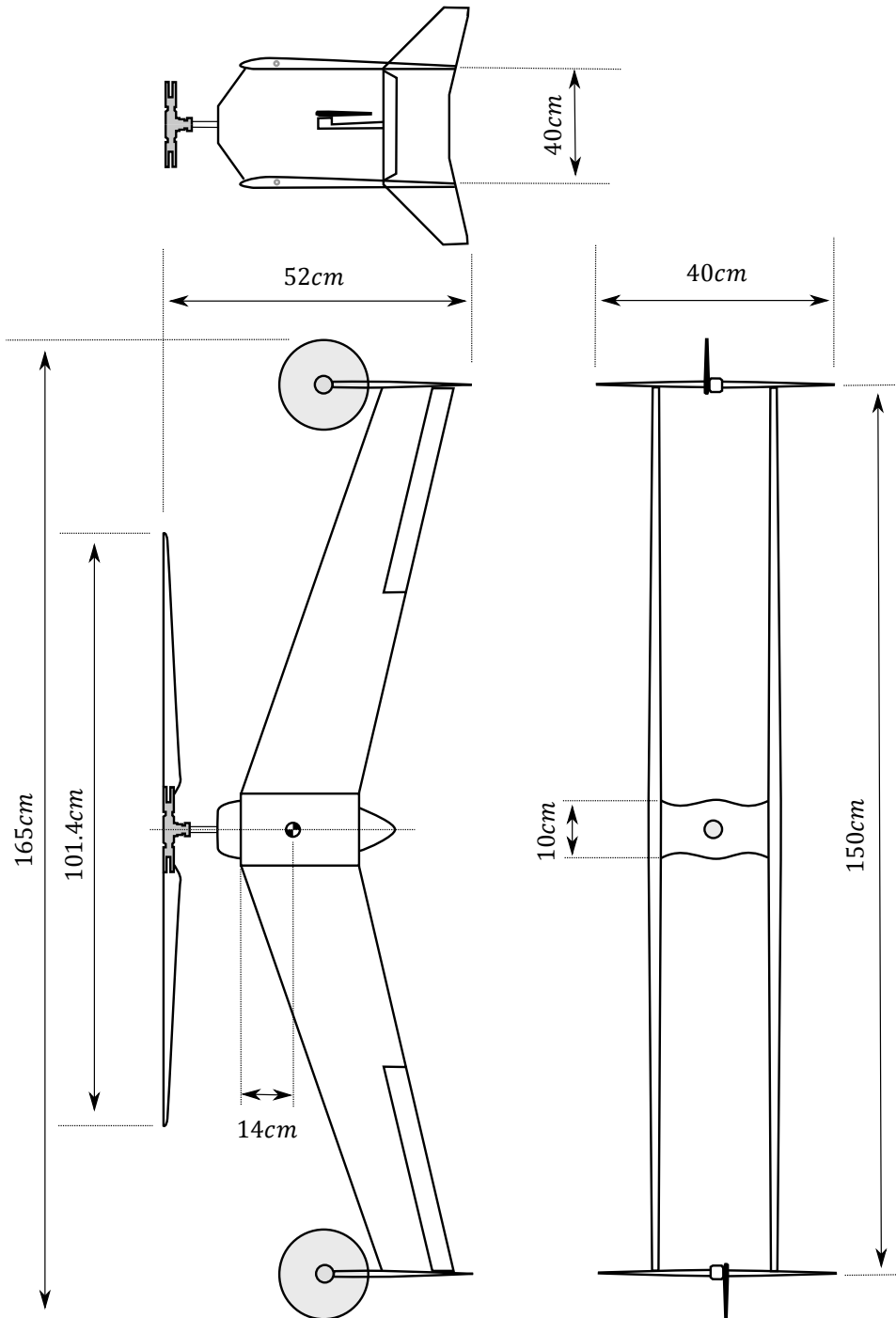
Figure 6.26: Plan view of the DelftaCopter. The center part consists of a 480-sized helicopter head with a direct drive motor. Two pairs of delta-wings form a box structure. The wingtips are stabilizing the delta-wing by increasing its C_{m_β}, they connect the top and bottom wing and provide structural strength while housing modems and acting as landing gear.

Property	Value
Weight	4.3 kg
MTOW	4.5 kg
Wing Area	0.496 m^2
Wing Loading	8.7 kg/m^2
Span	1.54 m
Length	0.6 m
Height	0.4 m
Design cruise speed	20.5 m/s (40 kt)
Measured cruise speed	19.5 m/s to 20.5 at 4.3 kg
Measured cruise power	300 W at 4.3 kg 20 m/s
Theoretical most efficient speed	18.0 m/s (|SI35kt)
Measured power at most efficient speed	280 W at 18.0 m/s
Theoretical maximum speed	25.5 m/s (49.5 kt)
Measured maximum speed	23.5 m/s
Measured hover power (4.3 kg)	420 W at 1650 rpm
Measured climb power (4.3 kg)	600 W at 1650 rpm
Main battery	10.5 Ah 6 Cell LiPo
FTD battery	250 mAh 2 Cell LiFe

Table 6.2: DelftaCopter key specifications

References

[1] C. De Wagter, R. Ruijsink, E. Smeur, K. van Hecke, F. van Tienen, E. van der Horst, and B. Remes, *Design, control, and visual navigation of the delftacopter vtol tail-sitter uav,* Journal of Field Robotics **35**, 937 (2018).

[2] F. Nex and F. Remondino, *UAV for 3d mapping applications: a review,* Applied Geomatics **6**, 1 (2013).

[3] G. Pajares, *Overview and current status of remote sensing applications based on unmanned aerial vehicles (UAVs),* Photogrammetric Engineering & Remote Sensing **81**, 281 (2015).

[4] J. D. Anderson, *Aircraft Performance & Design*, 1st ed., edited by K. T. Kane (WCB McGraw-Hill Education, 1998).

[5] S. B. Anderson, *Historical overview of V/STOL aircraft technology*, techreport 19810010574 (NASA Ames Reseach Center, Moffett Field, CA, United States, 1981).

[6] A. Bramwell, G. Done, and D. Balmford, *Bramwell's Helicopter Dynamics* (American Institute of Aeronautics and Astronautics, 2001) pp. 1–397.

[7] J. Roskam and C.-T. E. Lan, *Airplane aerodynamics and performance* (DARcorporation, 1997).

[8] D. Erdos and S. E. Watkins, *Uav autopilot integration and testing,* in *Region 5 Conference, 2008 IEEE*, IEEE (IEEE, Kansas City, MO, USA, 2008) pp. 1–6.

[9] D. Boura, D. Hajicek, and W. Semke, *Automated air drop system for search and rescue applications utilizing unmanned aircraft systems,* Infotech@ Aerospace, St. Louis, Missouri , 29 (2011).

[10] D. Erdos, A. Erdos, and S. E. Watkins, *An experimental uav system for search and rescue challenge,* IEEE Aerospace and Electronic Systems Magazine **28**, 32 (2013).

[11] R. A. Clothier, B. P. Williams, and N. L. Fulton, *Structuring the safety case for unmanned aircraft system operations in non-segregated airspace,* Safety science **79**, 213 (2015).

[12] C. Thornthwaite and P. Kaser, *Wind-gradient observations,* Eos, Transactions American Geophysical Union **24**, 166 (1943).

[13] E. C. Olson and B. Selberg, *Experimental determination of improved aerodynamic characteristics utilizing biplane wing configurations,* Journal of Aircraft **13**, 256 (1976).

[14] G. D. Padfield, *Helicopter flight dynamics* (John Wiley & Sons, Hoboken, New Jersey, United States, 2008).

[15] H. Schenk, *PropCalc - propeller calculator software,* `http://www.drivecalc.de/PropCalc/` (2007).

[16] J. Larminie and A. Dicks, *Fuel cell systems explained*, 2nd ed. (J. Wiley Chichester, UK, 2003).

[17] M. Drela, H. Youngren, M. Scherrer, and A. Deperrois, *Xflr-5,* (2012).

[18] P. Brisset, A. Drouin, M. Gorraz, P.-S. Huard, and J. Tyler, *The paparazzi solution,* in *MAV 2006, 2nd US-European Competition and Workshop on Micro Air Vehicles* (EMAV, Sandestin, United States, 2006) pp. 1–15.

[19] B. Gati, *Open source autopilot for academic research-the paparazzi system,* in *American Control Conference (ACC), 2013* (IEEE, Washington, DC, 2013) pp. 1478–1481.

[20] R. W. Prouty, *Helicopter performance, stability, and control* (Krieger Publishing Company, Melbourne, FL 32902-9542 USA, 1995).

[21] W. J. Wagtendonk, *Principles of Helicopter Flight* (Aviation Supplies & Academics Inc, 1996).

[22] W. Johnson, *A Comprehensive Analytical Model of Rotorcraft Aerodynamics and Dynamics. Part 1. Analysis Development*, techreport 19800019795 (NASA Ames Research Center, DTIC Document, Moffett Field, CA, United States, 1980).

[23] W. Z. Stepniewski and C. Keys, *Rotary-wing aerodynamics*, edited by W. Z. Stepniewski (New York, NY : Dover Publ., Massachusetts, 1979).

6

[24] V. Gavrilets, *Dynamic model for a miniature aerobatic helicopter,* in *Handbook of Unmanned Aerial Vehicles* (Springer, Netherlands, 2015) pp. 279–306.

[25] H. Shim, T. J. Koo, F. Hoffmann, and S. Sastry, *A comprehensive study of control design for an autonomous helicopter,* in *Proceedings of the 37th IEEE Conference on Decision and Control*, Citeseer (IEEE, Tampa, FL, USA, USA, 1998) pp. 1–6.

[26] G. Cai, B. M. Chen, T. H. Lee, and K.-Y. Lum, *Comprehensive nonlinear modeling of a miniature unmanned helicopter,* Journal of the American Helicopter Society **57**, 1 (2012).

[27] C. De Wagter and E. J. J. Smeur, *Control of a hybrid helicopter with wings,* International Journal of Micro Air Vehicles **9**, 209 (2017).

[28] E. J. J. Smeur, de G.C.H.E de Croon, and Q. Chu, *Gust disturbance alleviation with incremental nonlinear dynamic inversion,* in *International Conference on Intelligent Robots and Systems (IROS)*, IEEE/RSJ (IEEE, Daejeon, South Korea, 2016) pp. 5626–5631.

[29] UAVChallenge, *Uav challenge medical express competition rules 2016 v4,* https://uavchallenge.org/ (2016).

[30] D. C. De Oliveira and M. A. Wehrmeister, *Towards real-time people recognition on aerial imagery using convolutional neural networks,* in *Real-Time Distributed Computing (ISORC), 2016 IEEE 19th International Symposium on* (IEEE, 2016) pp. 27–34.

[31] A. Gaszczak, T. P. Breckon, and J. Han, *Real-time people and vehicle detection from uav imagery,* in *Intelligent Robots and Computer Vision XXVIII: Algorithms and Techniques*, Vol. 7878, International Society for Optics and Photonics (SPIE, 2011) pp. 71–83.

[32] P. Rudol and P. Doherty, *Human body detection and geolocalization for uav search and rescue missions using color and thermal imagery,* in *Aerospace Conference, 2008 IEEE* (IEEE, Big Sky, MT, USA, 2008) pp. 1–8.

[33] G. C. H. E. de Croon, H. W. Ho, C. De Wagter, E. Van Kampen, B. Remes, and Q. P. Chu, *Optic-flow based slope estimation for autonomous landing,* International Journal of Micro Air Vehicles **5**, 287 (2013).

[34] H. W. Ho, C. De Wagter, B. D. W. Remes, and G. C. H. E. de Croon, *Optical flow for self-supervised learning of obstacle appearance,* in *Intelligent Robots and Systems (IROS), 2015 IEEE/RSJ International Conference on*, IEEE (IEEE, Hamburg, Germany, 2015) pp. 3098–3104.

[35] T. Cover and P. Hart, *Nearest neighbor pattern classification,* IEEE transactions on information theory **13**, 21 (1967).

7

Identification of DelftaCopter Dynamics from Flight Data

To be conscious that you are ignorant is a great step to knowledge.

Benjamin Disraeli

The DelftaCopter is a tilt-body tailsitter UAV which combines a large swash-plate controlled helicopter rotor with a biplane delta-wing. Previous research has shown that the large moment of inertia of the wing interacts with the dynamics of the rotor but did not investigate the higher frequency dynamics nor the forward flight dynamics. In this work, a Cylinder Dynamics (CD) is compared with a Tip-Path Plane (TPP) model and then extended to include the wing and elevon dynamics in forward flight. Flight test data are used to identify the model parameters using grey-box modeling while flying with a feedback controller. This is made possible by identifying one axis at a time while injecting white noise on all other axes. The TPP model is shown to accurately reproduce the high-frequency attitude dynamics including the significant rotor-wing interaction. Finally, a Linear-Quadratic Regulator (LQR) controller based on the TPP model is derived and tested to further validate the model.

7.1. Introduction

Unmanned Air Vehicles have enabled new applications in many areas [3]. A wide range of those applications benefits from long endurance combined with VTOL capability. Hybrid UAVs combine the hovering capabilities of helicopters with the range efficiency and speed of fixed-wing aircraft [4]. One of the many concepts for combining this long-range with VTOL is the tailsitter or tilt-body hybrid UAV [5]. This concept has its rotors pointed upwards during hover, but can tilt downward by 90° to transition to fast foward flight. During forward flight, the wing provides the required lift while the rotor only counters the drag.

Figure 7.1: The DelftaCopter tailsitter UAV in hovering flight. DelftaCopter has a single large rotor with collective and cyclic blade pitch control, two small torque countering tip propellers, and a pair of delta-wings placed in a biplane configuration. The tips form the landing legs and provide yaw stability in forward flight. It weighs 4.3 kg and was designed to fly 60 km in the Outback Medical Challenge 2016 [6] [7]

Many tailsitter concepts have been proposed. Using at least four rotors in hover combined with traditional multicopter control is the earliest and most common solution. Examples include the QuadShot [8] and the VertiKUL [9]. A dynamic model for such platforms has been proposed by [10].

Reducing the number of rotors, [11] have proposed two counter-rotating in-line propellers on their Vertigo platform. The counter-rotating small propellers reduce the gyroscopic effects of the propellers on the body to levels where it does not need to be compensated by the attitude controller. Similarly, when both propellers are in-plane but side by side, the gyroscopic effect of both counter-rotating propellers cancel each other out pretty well. This was for instance shown in the control of the MAVION by [12] and the Cyclone by [13]. [14] have proposed a similar concept but with variable pitch propellers, and show that a controller based on a simple 2nd order model achieves acceptable control. But for all three, the biggest difficulty was coping with the highly non-linear and imprecisely modeled effectiveness of the aerodynamic control surfaces.

To further increase hovering efficiency and control moments, [15] have proposed

the DelftaCopter tailsitter (See Figure 7.1) which has a single rotor with cyclic and collective blade pitch control. The rotor inertia of the DelftaCopter was shown to be sufficiently large to affect the dynamics of the rigid body, yet is too small to act as a pure gyroscope as in conventional helicopter models [16]. Several other single rotor concepts were proposed like the AeroVel Flexrotor [17], but these do not report the same properties as the DelftaCopter.

The initial work on the DelftaCopter allowed the creation of a working controller, but only modeled the low-frequency dynamics in hover [15]. While black-box modeling has recently shown practical results in modeling unconventional UAV [18], this work will extend a helicopter model to capture the tailsitter dynamics in hover and forward flight by using grey-box parameter estimation.

Section 7.2 first compares the different models that can be applied to single rotor tailsitters, and Section 7.3 formulates the state-space model. Section 7.4 describes how system identification is performed in-flight on an unstable platform. Section 7.5 describes the results of the system identification. With the fitted models, a controller was designed and implemented for hover in Section 7.6. The model is extended to model the forward flight dynamics in Section 7.7. Finally, the conclusions are presented in Section 7.8.

7.2. Single Rotor Tailsitter Modeling

Modeling helicopter rotor dynamics can be categorized into roughly three levels of simplification in blade flapping dynamics.

7.2.1. Flapping dynamics

The first and most elaborate approach is to deal with the blade flapping explicitly and to include all the degrees of freedom of every individual blade as states of the model [19]. The blades can at least change their pitch angle θ_B, flap up and down with angle β, and lead and lag, for instance, due to sideward wind. More complex models can include blade bending and hinge dampers. This requires too many physical parameters to be identified to allow identification from onboard logfiles without adding sensors to measure rotor blade positions.

7.2.2. Tip-Path-Plane

A first simplification is to relate the attitude dynamics of the helicopter to the Tip-Path Plane (TPP). This is the approximate plane in which the tips of the rotor travel and is shown in Figure 7.2. Mettler [20] have derived a TPP model by neglecting high-frequency dynamics of the rotor. The TPP is represented by the longitudinal and lateral angles a and b in radians between the TPP and a plane perpendicular to the rotor axis. These correspond to the steady-state flapping angles when the blade is aligned with the X and Y axis. The TPP angles change under influence of control inputs, rotations of the fuselage, and gyroscopic precession of the rotor. The fuselage is a separate rigid body and a moment is transferred from the rotor to the fuselage if the a and b angles are non-zero, due to the effective spring between the rotor blade and axis and the offset of thrust application point on the rotor and

the center of mass of the fuselage [20, 21].
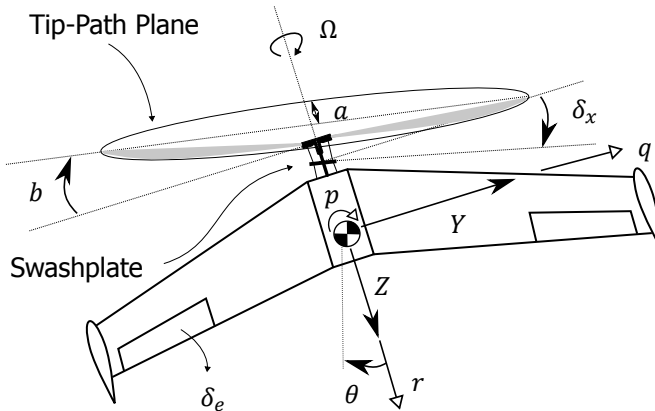
Figure 7.2: Helicopter Tip-Path Plane (TPP) model showing the tip angles a and b, the cyclic deflections δ_x and δ_y as well as the body X, Y and Z axes and p, q and r turn rates. Ω is the rotor speed.

7.2.3. Cylinder Dynamics Model

A final simplification is to ignore the flapping dynamics completely and treat the rotor as a rigid disc or cylinder. This model is widely used for small helicopters [22–24]. A TPP model can be transformed into a model without flapping dynamics by setting the derivatives of the a and b angles to zero. This simplification can still yield accurate results if the relative fuselage inertial compared to the rotor inertial is very small or the hinge spring forces are very large [21]. The model without flapping dynamics is referred to as a Cylinder Dynamics (CD) model.

7.3. State Space Description

The TPP and CD models will be given as linear time-invariant models in state-space form:

$$\dot{\bar{x}} = A\bar{x} + B\bar{u} \tag{7.1}$$

$$\bar{y} = C\bar{x} + D\bar{u} \tag{7.2}$$

7.3.1. TPP Model

The Tip-Path Plane (TPP) model has been adapted from [20]. Only the attitude dynamics are considered and the "Hiller bar" dynamics are removed since the DelftaCopter does not have one. The state vector becomes $\bar{x} = (p, q, a, b)^T$ with p and q being the roll and pitch rates expressed in radians per second. The input vector is $\bar{u} = (\delta_x, \delta_y)^T$ where δ_x and δ_y are measured in percent. The observable states are $\bar{y} = (p, q)$. The state-space A and B and C matrices for the TPP model are given in Equations (7.3) and (7.4). The C-matrix shows that only the body rates are measurable and the D-matrix consists of only zeros. The model has nine parameters

that need to be identified: L_b and M_a represent the spring constants of the Tip-Path Plane and consist of the combined stiffness of the blade and blade hinge and the offset between the rotor thrust vector and center of mass of the fuselage. τ_{f_n} is the time constant of the TPP dynamics. A_{b_n} and B_{a_n} are cross-coupling terms that describe how the TPP interchanges the a and b angles over time. The four parameters in the B-matrix give the actuator effectiveness. The dependence of several parameters on the rotor Rotations Per Minute (RPM) Ω is reflected in $\tau_f = \tau_{f_n}/\Omega$, $A_b = A_{b_n}/\Omega^2$ and $B_a = B_{a_n}/\Omega^2$ [20, sec. 2.3]. This results in :

$$
A_{\text{TPP}} = \begin{bmatrix}
0 & 0 & 0 & L_b \\
0 & 0 & M_a & 0 \\
0 & -1 & -\dfrac{\Omega}{\tau_{fn}} & \dfrac{A_{b_n}}{\Omega \tau_{fn}} \\
-1 & 0 & \dfrac{B_{a_n}}{\Omega \tau_{fn}} & -\dfrac{\Omega}{\tau_{fn}}
\end{bmatrix}
\tag{7.3}
$$

$$
B_{\text{TPP}} = \begin{bmatrix}
0 & 0 \\
0 & 0 \\
\dfrac{A_{\text{lat}} \Omega}{\tau_{fn}} & \dfrac{A_{\text{lon}} \Omega}{\tau_{fn}} \\
\dfrac{B_{\text{lat}} \Omega}{\tau_{fn}} & \dfrac{B_{\text{lon}} \Omega}{\tau_{fn}}
\end{bmatrix}, \qquad
C_{\text{TPP}} = \begin{bmatrix}
1 & 0 & 0 & 0 \\
0 & 1 & 0 & 0
\end{bmatrix}
\tag{7.4}
$$

7.3.2. CD Model
The Cylinder Dynamics (CD) model state variables are only the body rates $\bar{x} = (p, q)^T$, and the input is the same as for the TPP model. Both the A- and B-matrices consist of four identifiable parameters, as shown in Equation (7.5) below.

$$
A_{cyl} = \begin{bmatrix} L_p & L_q \\ M_p & M_q \end{bmatrix}, \qquad
B_{cyl} = \begin{bmatrix} L_{lat} & L_{lon} \\ M_{lat} & M_{lon} \end{bmatrix}
\tag{7.5}
$$

7.3.3. Relation between CD and TPP
In the TPP model, only the a and b states drive the angular accelerations in the q and p states, and control inputs first affect the dynamics of this TPP.

When substituting the a and b values of the steady-state solution $\dot{a} = \dot{b} = 0$ in the $\dot{p}$ and $\dot{q}$ equations then results in a comparable system as the CD model, with every CD model parameter linked directly to a combination of parameters in the steady-state TPP model [21].

7.4. Unstable platform System Identification

To identify the parameters from the derived models, a grey-box parameter estimation procedure is used based on the input-output response found in flight test data. To get the best identification results, the system should be measured open-loop [25]. In the case of the DelftaCopter, this is not possible because it has an unstable attitude and requires at least a rate controller to fly. Constraining the motion to one axis at a time is not an option as the rotor dynamics create couplings between pitch and roll that would then not be identified. Initial attempts

by hanging the DelftaCopter using a rope introduced too many external forces on the system and made identification impossible. Therefore system identification was finally performed in free flight using a minimal linear rate feedback controller, and is a simplified version of the one described in Chapter 3 [26] in which the rate coupling compensations are removed as given in:

$$
\begin{bmatrix} \delta_x \\ \delta_y \end{bmatrix} = G^{-1} \begin{bmatrix} K_p p_{err} \\ K_q q_{err} \end{bmatrix}
\tag{7.6}
$$

where K_p and K_q are proportional gains, p_{err} and q_{err} are the rate errors and 2 by 2 matrix G^{-1} is the inverted control effectiveness.

7.4.1. Noise

To lower the risk of false correlation between different inputs and states that become coupled through the attitude controller, [27] suggested adding white noise to every axis independently. This reduces the chance of false correlations and hereby allows in-flight system identification of an unstable platform if a simple baseline controller is available. Finally, further complicating system identification, not all states can be measured in flight since only the body rates can be measured and the a and b states are not directly observable. Absolute values of a and b are thereby not validated.

7.4.2. Flight Maneuvers

Flight tests were performed in an indoor environment without wind nor turbulence. As proposed by [27], a "chirp-shaped" actuator deflection is applied on each control input separately. A chirp is a sine wave with a frequency increasing continuously over time. White noise is injected on all axes during the chirp after filtering with a first-order low-pass filter with the cut-off at the highest frequency of the chirp. An exponential-time chirp is used to have enough content at the lower frequencies. The resulting actuator signal is stored with the gyroscope measurements on an SD-card at a frequency of 512 Hz using a custom Paparazzi-UAV autopilot [28].

The exponential-time chirp formulation by [27] was implemented as:

$$
K = C_2 \left(e^{\left(C_1 \cdot \frac{t}{\Delta_t} \right)} - 1 \right) \qquad \phi = 2\pi \left(f_0 \cdot t + (f_1 - f_0) \cdot \left(\frac{\Delta_t}{C_1} \cdot K - C_2 \cdot t \right) \right)
\tag{7.7}
$$

where C_1 and C_2 are coefficients, t is the time, Δ_t is the chirp duration in seconds, f_0 and f_1 are the start and stop frequencies, ϕ is the phase of the chirp and the amplitude of the chirp in funtion of time is $s(t) = \sin(\phi)$. The lower frequency and amplitude are limited by the maximal roll angle that the system is allowed to reach during the test. The maximal attitude angles were not permitted to grow larger than about 30 deg. The chirp settings are given in Table 7.1. The noise fraction is the ratio between the amplitude of the chirp and the standard deviation of the white noise that is filtered and added to the chirp signal.

Variable	Value
Start frequency f_0	0.5 Hz
End frequency f_1	10 Hz
Noise fraction	0.2
C_1	4
C_2	$\frac{1}{e^{C_1-1}}$

Table 7.1: Exponential-time chirp settings.

7.4.3. Post-processing

To cope with the sensor noise in the measured data, some post-processing was performed as in [29]. The measurements were filtered digitally using an ideal low-pass filter with a cut-off frequency of 15 Hz. This removes vibrations caused by the DelftaCopter rotor which rotates at about 27.5 Hz. The inputs bias was removed and the resulting time-domain chirp log files were used to fit the parameters using the MATLAB 2018a system identification toolbox `greyest` function.

7.5. Identification Results in Hover

The full time-sequences including fitted models for a roll chirp are shown in Figure 7.3. The figure shows the measured pitch and roll rates together with the predicted pitch and roll rates from both CD and TPP models. The predicted pitch and roll rates are obtained by feeding the logged inputs into the respective identified models. The CD model can accurately predict the response up to a certain frequency but does not include the eigenfrequency which is excited at around 28.5 s. The TPP dynamics model has four states and was found to have two pairs of complex poles which leads to 2 eigenfrequencies. The slowest eigenfrequency is the same as in the CD model while the highest eigenfrequency corresponds to the faster oscillations seen in the chirp plots. Particularly intereting is that after 25 s or roughly 3 Hz, the roll chirp drives pitch more than roll. A pitch chirp is shown in Figure 7.4. In this chirp, the difference between the CD model and the measurements is even larger.

7.5.1. Validation maneuvers

To validate the identified model parameters, pitch and roll doublets were recorded separately and not used in the identification. Figure 7.5 shows pitch and roll commands manually given by a pilot, which represent normal flight maneuvers of the DelftaCopter. While the roll rate is relatively well captured by both models, even at these relatively low-frequency doublets, the pitch rate dynamics shows important differences in the CD model.

Table 7.2 shows the eigenfrequencies of both identified TPP and CD state-space systems. The first pole-pair has almost the same eigenfrequency in both models, which means that at lower frequencies both models respond comparably. However, the higher eigenfrequency of the flapping dynamics model is not present in the CD model, which explains why high-frequency dynamics are missing (See Figure 7.4).
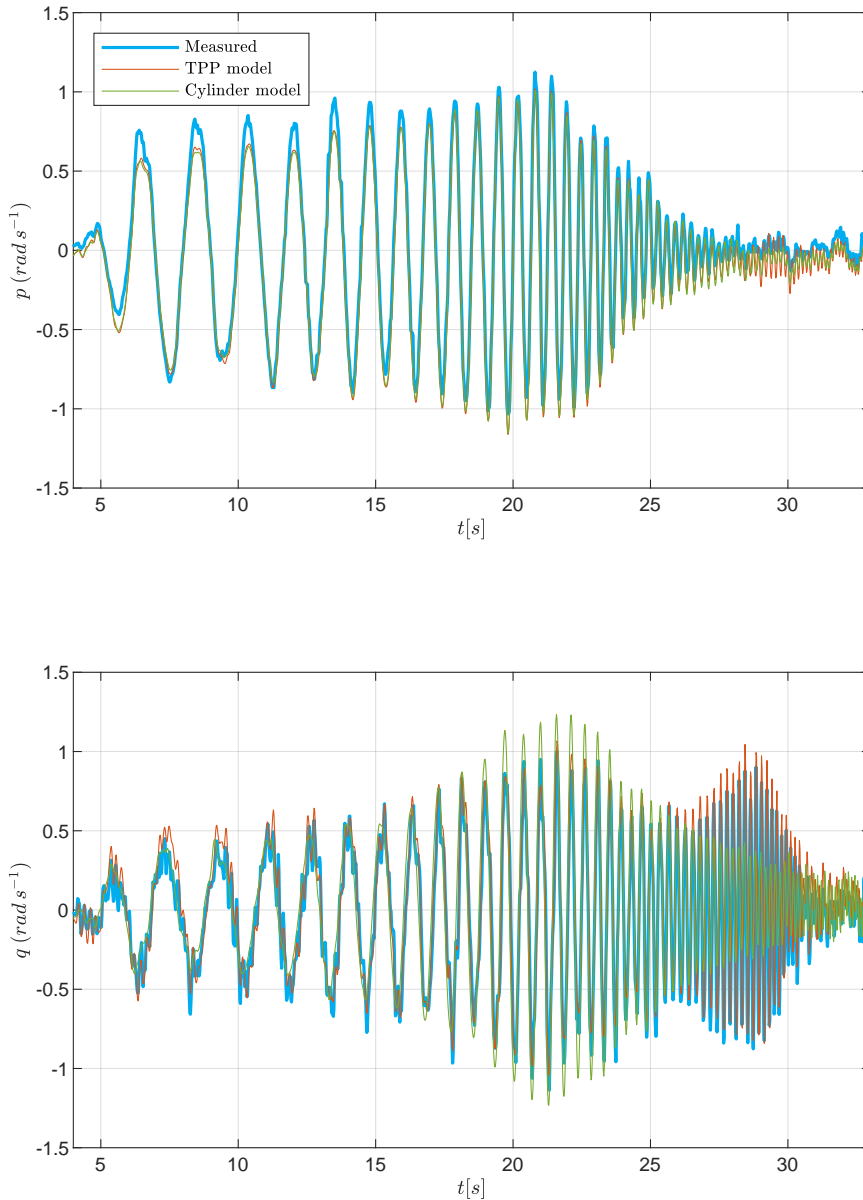
Figure 7.3: A chirp on the roll axis in hover. The pitch response to the roll chirp is due to pitch-roll couplings of the system. The TPP model is much better at reproducing the measured pitch signals in the higher frequency range.
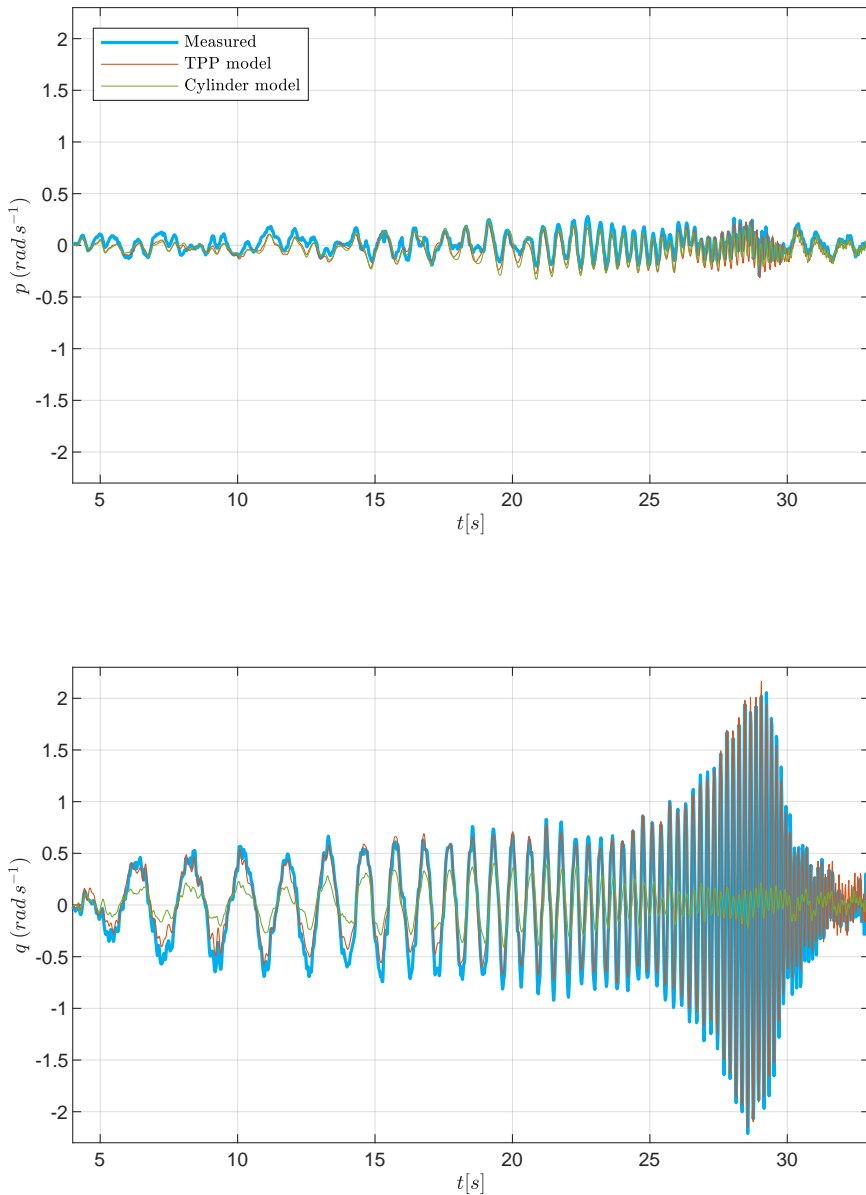
Figure 7.4: A chirp on the pitch axis in hover. The roll motion due to pitching is not as pronounced as the pitch due to roll since the roll inertia of the fuselage is much larger than the pitch inertia. Here, the CD model accuracy is also worse than the TPP model at low frequencies.

	Pole	Frequency [Hz]	Damping [−]
CD model	1-2	1.54	0.35
TPP model	1-2	1.64	0.39
	3-4	5.04	0.22

Table 7.2: Comparison of eigenfrequencies of the TPP and CD models.
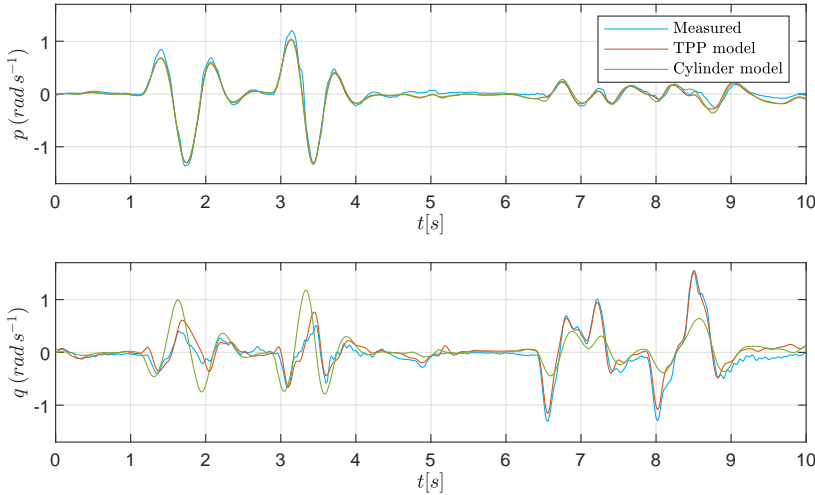
Figure 7.5: Validation flight test sequence flown in manual control consisting of first a roll doublet and then a pitch doublet. The roll response is quite accurately modeled by both models while the pitch response is better in the TPP model.

7.5.2. Results

Table 7.3 lists all the identified model parameters. These are the matrix elements in Equations (7.3) to (7.5) where the following substitutions were performed:

$$\tau_f = \tau_{f_n}/\Omega, \qquad A_b = A_{b_n}/\Omega^2, \qquad B_a = B_{a_n}/\Omega^2 \qquad (7.8)$$

The difference in roll and pitch inertia of the DelftaCopter is apparent from the L_b and M_a values, which differ by a factor of 4.8 in the identified parameters. Furthermore the principal components for actuation of pitch and roll A and B are different than in helicopters and are not perpendicular but are at a 43.2° angle with eachother.

7.5.3. Fitting quality

To assess the fitting quality, the Coefficient of Multiple Correlation (CoMC) is used as given in Equation (7.9), where 100% constitutes a perfect match:

TPP	Value	CD	Value
A_b	−1.338	L_p	−2.056
B_a	1.448	M_p	10.536
L_b	147.548	L_q	−7.900
M_a	713.378	M_q	−4.777
τ_f	0.091	L_{lat}	−5.361
A_{lat}	−0.282	M_{lat}	−67.573
A_{lon}	0.296	L_{lon}	9.917
B_{lat}	0.524	M_{lon}	11.136
B_{lon}	−0.050		

Table 7.3: The identified TPP and CD model parameters.

$$R = \left(1 - \frac{||s - \hat{s}||}{||s - \bar{s}||}\right) \tag{7.9}$$

in which R is the CoMC, s is the measured signal, $\hat{s}$ is the model output and $\bar{s}$ is the average of the measured signal. The CoMC of both identified models on the indentification and validation data is given in Table 7.4. For both the chirp and validation doublet, the CoMC of the roll response of both models is very similar. Interestingly, the CoMC of the pitch on the validation doublet is lower than on the chirp data. This shows that even the TPP does not capture all the dynamics or the optimizer might overfit the chirp data. When looking back at Figure 7.5, the time series of q shows that the biggest error in pitch seems to occur when large roll rates occur at t=1.5 and 3.5 seconds. This points to uncaptured couplings, which could, for instance, come from hinge spring non-linearities.

	Axis	TPP model	CD model
Chirp	p	77.8%	77.2%
	q	77.3%	25.9%
Doublets	p	77.6%	76.7%
	q	64.7 %	20.0%

Table 7.4: CoMC of the TPP and CD model fits on identification chirps and validation doublets.

7.5.4. Reproducibility
To validate that the parameters were not overfitted to a particular chirp, the TPP model was fitted to two different sets of chirp data and their fitted parameters were compared. The highest single change in model parameter between the two sets of chirps was 7.7 %, but the eigenfrequencies and damping ratios of the systems differed not more than 0.9 % and 1.8 % respectively.

7.5.5. RPM dependence of parameters
The model from Equations (7.3) to (7.5) contains the rotor RPM Ω and is expected to compensate changes in rotor speed. To assess if the identified model parameters

remain constant at different rotor rotational speeds, measurements were performed at a range of rotor speeds between 1500 and 1650 RPM.

Although the rotor speed was varied only 10 %, some model parameters, which should stay constant, showed changes of up to 185 % (B_{lon}) with many others changing tens of percents as shown in Table 7.5. The importance of these changes in model parameters in terms of model response is analyzed by comparing the eigenfrequency and damping of the model fitted on the 1650 RPM data with the model fitted on 1500 RPM and then corrected to 1650 RPM using Equation (7.8). The largest change in eigenfrequency was only 4 %, while the largest change in damping ratio was up to 28 %. This leads to the conclusion that mainly the damping properties still contain unmodeled dynamics. The CoMC of this model fitted on 1500 RPM was 72.4 % in roll and 67.1 % in pitch when tested on the same 1650 RPM chirp as in Table 7.4. Further research is thus needed to obtain models that generalize well with different rotor RPMs.

Rpm	1499.8	1549.8	1599.7	1649.6
A_{b_n}	−45350	−55960	−54590	−57000
B_{a_n}	46180	49720	57790	62700
L_b	176.100	179.400	178.100	181.200
M_a	746.800	754.000	754.200	760.900
τ_{f_n}	14.010	15.980	18.370	19.350
A_{lat}	−0.157	−0.173	−0.243	−0.268
A_{lon}	0.240	0.270	0.291	0.302
B_{lat}	0.484	0.494	0.564	0.599
B_{lon}	−0.040	−0.063	−0.098	−0.114

Table 7.5: The identified TPP parameters in function of RPM.

7.6. Controller Derivation

To test the applicability of the model, it was used to derive a linear rate controller which was subsequently tested. Since the tip-path plane angles a and b are not measured onboard the DelftaCopter, a linear observer was created in the form:

$$\dot{\hat{x}} = A\hat{x} + B\bar{u} + L(\bar{y}_{measured} - \hat{y}), \qquad \hat{y} = C\hat{x} + D\bar{u} \tag{7.10}$$

in which $\hat{x}$ is the current state estimate and L is the correction matrix. The A, B and C matrices are as given in Equations (7.3) and (7.4) and the parameters are shown in Table 7.3. The L matrix is chosen using pole placement such that the error dynamics of the observer are asymptotically stable with sufficient speed to capture the dynamics but filter the main rotor vibrations. The poles where placed at $(-50, -50, -51, -51)$. The controller is then designed using the feedback law:

$$\bar{u} = -K\hat{x} + g\bar{y}_{ref} \tag{7.11}$$

in which $\bar{y}_{ref}$ is the reference attitude rate and the steady-state gain of the controlled system is g.

The gain matrix K is selected using Linear Quadratic Regulator (LQR). This finds the optimal gain matrix K for the system minimizing a cost function J consisting of a combination of states and inputs $J = \int_0^\infty (x^T Q x + u^T R u) dt$. The cost parameters for the states p and q in Q are set to 1 and since the actual values of the a and b states do not matter, they were given a cost of only 0.001. The costs on the inputs R were varied to yield several controllers, where the lower the cost on the input, the larger the allowed deflections and the faster the controller steers the system. The input cost of 5 made the system the fastest without introducing oscillations nor saturating the actuators.
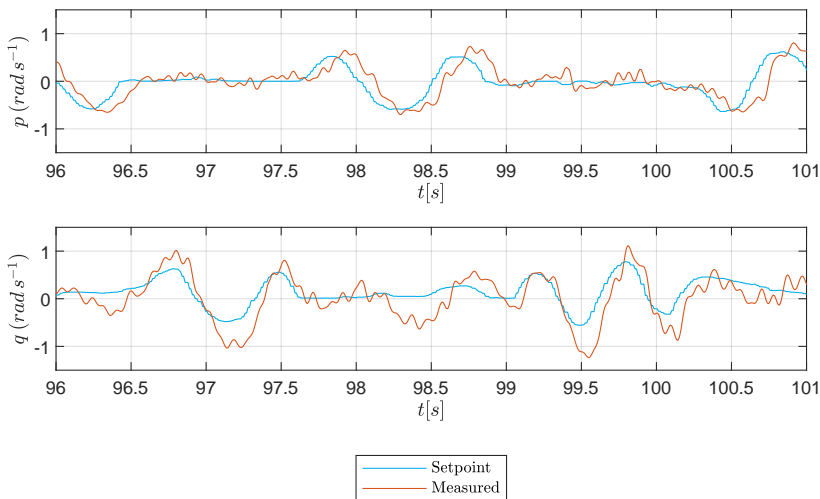
Figure 7.6: Performance test of an LQR controller derived directly from the identified TTP DelftaCopter model. The pilot manually commands the attitude rate of the DelftaCopter. The roll response has a small delay with the command but otherwise has adequate tracking performance. The pitch rate shows coupling with the roll and the response shows larger values than the command.

The controlled system response is shown in Figure 7.6. It can be seen that the roll response has a small delay, but the roll measurement follows the command well. The pitch response shows a coupling when larger roll rates are present. The pitch response is also larger in magnitude than the commanded rate, but the fact that the model can be used to design a controller for the DelftaCopter, further confirms that the TPP model covers the most essential dynamics of the platform.

7.7. Forward Flight Modeling

In forward flight, the DelftaCopter pitches down 90° such that the wings provide the required lift while the main rotor is providing forward pointed thrust, as shown in Figure 7.7. The aerodynamic surfaces then play a significant role in the balance of moments of the DelftaCopter attitude dynamics. Both models are therefore extended with linear aerodynamic moments for the aerodynamic actuators.
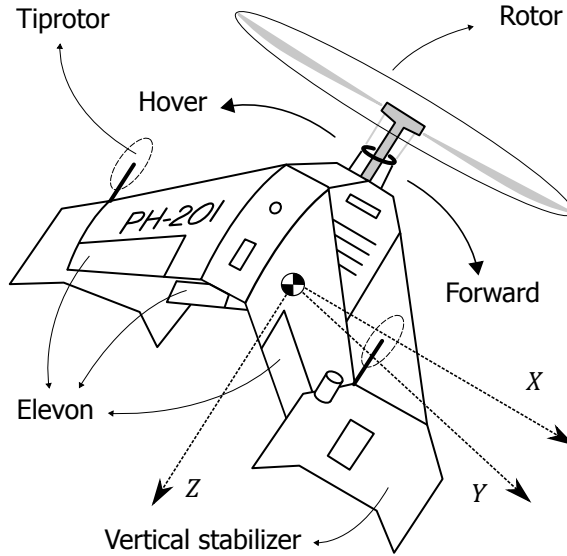
Figure 7.7: The DelftaCopter tailsitter UAV has a single main rotor that points up and provides lift during hover. Two tip props provide counter-torque in hover, and the swashplate gives lateral and altitude control. In forward flight, the entire vehicle tilts 90° down, and the rotor provides thrust while the biplane delta-wings provide lift, and the elevons provide most of the control.

7.7.1. Aerodynamic surface models

The DelftaCopter has four movable surfaces that together perform the role of aileron and elevator for the delta-wing. The ailerons apply a moment on the body along the Z axis, which is the axis of rotation of the rotor and points forward during forward flight. Since the yaw angle is not included in the model and differential aileron drag of the ailerons is further neglected, it is not added to the model. The elevator can generate a significant moment in the pitch axis and is included in the model as parameter M_{elev}. The longitudinal damping moment of the wings due to a pitch-rate q is named M_q and lateral damping due to rate p is called L_p. Note that for the DelftaCopter, the body X axis points down in forward flight and represents the yawing of the delta-wing. In the CD model, these extra effects are lumped into the parameters already present. The state vector x is the same as the model in hover while the input vector is extended to $\bar{u} = (\delta_x, \delta_y, \delta_e)^T$, with δ_e being the elevator deflection. The aileron deflection δ_a represents a rotation along the rotor axis which is not part of the rotor model. The resulting TPP state space system for forward flight thereby becomes:

$$A_{\mathrm{FW}} = \begin{bmatrix} \mathrm{L_p} & 0 & 0 & \mathrm{L_b} \\ 0 & \mathrm{M_q} & \mathrm{M_a} & 0 \\ 0 & -1 & -\dfrac{\Omega}{\tau_{fn}} & \dfrac{\mathrm{A_{b_n}}}{\Omega\tau_{fn}} \\ -1 & 0 & \dfrac{\mathrm{B_{a_n}}}{\Omega\tau_{fn}} & -\dfrac{\Omega}{\tau_{fn}} \end{bmatrix}, \quad B_{\mathrm{FW}} = \begin{bmatrix} 0 & 0 & 0 \\ 0 & 0 & M_{elev} \\ \dfrac{\mathrm{A_{lat}}\,\Omega}{\tau_{fn}} & \dfrac{\mathrm{A_{lon}}\,\Omega}{\tau_{fn}} & 0 \\ \dfrac{\mathrm{B_{lat}}\,\Omega}{\tau_{fn}} & \dfrac{\mathrm{B_{lon}}\,\Omega}{\tau_{fn}} & 0 \end{bmatrix} \quad (7.12)$$

The parameters L_b and M_a of the TPP model contain the spring constants of the rotor and their physical meaning is given by [20, sec. 3.1] where M_a is defined as:

$$M_a = \frac{k_\beta + hT}{I_{yy}} \tag{7.13}$$

This relates the angle a to the angular acceleration $\dot{q}$ of the body and contains a rotor stiffness term k_β and moment due to the offset h of where the thrust T acts on the body compared to the center of gravity. Chapter 3 estimated the rotor blade spring stiffness k_β to be $\approx 88\,\mathrm{N\,m\,rad^{-1}}$. The contribution to the moment caused by the thrust at maximum weight $hT \approx hmg \approx 0.15 \cdot 4.5 \cdot 9.81 = 6.6\,\mathrm{N\,m\,rad^{-1}}$. In forward flight, the actual thrust will be much smaller than the full weight. Therefore the contribution of the variable thrust on the parameters L_b and M_a is assumed to be very small and the parameters L_b and M_a are further assumed to be constant.

The $A_{cyl,FW}$ matrix in the CD model in forward flight is the same as in hover given in Equation (7.5), and the damping moments from the rotor and wing are mixed. The $B_{cyl,FW}$ matrix is as given in Equation (7.5) and has the addition of the third input δ_e which is modeled to yield a linear pitch acceleration $\dot{q}$ through parameter M_{elev}.

7.7.2. Results

The parameters are fitted from measurements obtained during several chirp maneuvers on all three actuators $\bar{u}$ in steady level flight. The model fitting is always done using a different set of chirps than the validation chirps depicted in this chapter. Due to perturbations from amongst others the chirp itself, the airspeed fluctuates between $17\,\mathrm{m\,s^{-1}}$ and $19.5\,\mathrm{m\,s^{-1}}$, while the RPM fluctuates between 1550 and 1720. This RPM range is quite broad compared to the hover experiments, especially considering the observed sensitivity of parameters to the RPM.

TPP	Value	CD	Value
A_b	−0.908	L_p	−10.690
B_a	0.999	M_p	14.899
L_b	147.550	L_q	−9.251
M_a	713.380	M_q	1.050
τ_f	0.075	L_{lat}	6.605
A_{lat}	−0.196	M_{lat}	−70.459
A_{lon}	0.214	L_{lon}	−2.903
B_{lat}	0.440	M_{lon}	11.532
B_{lon}	−0.026	M_{elev}	10.263
L_p	−0.930		
M_q	4.691		
M_{elev}	37.752		

Table 7.6: The fitted values for the TPP and CD models in forward flight.

The parameters of the TPP and CD models are given in Table 7.6. Comparing these to the hover parameters in Table 7.3 shows that both have comparable param-
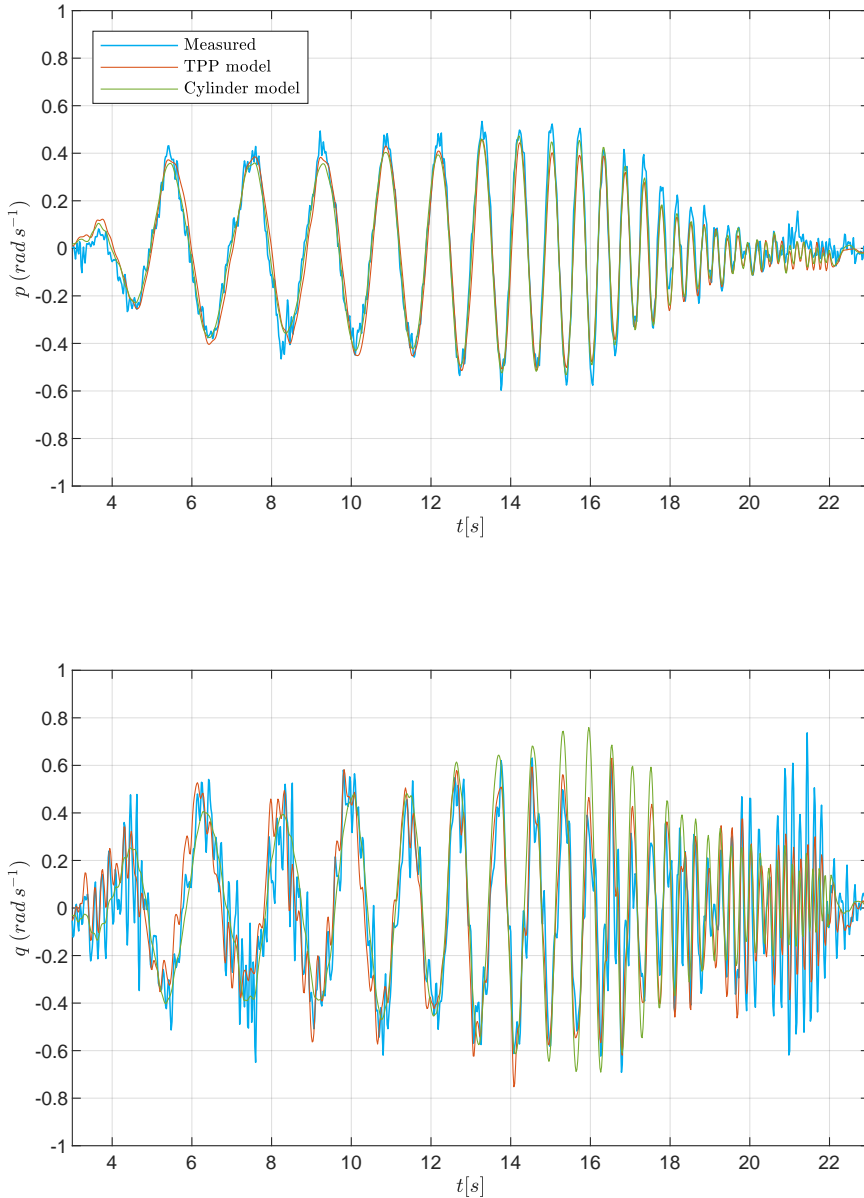
Figure 7.8: A validation chirp on the roll axis in forward flight. The pitch motions are mainly due to pitch-roll coupling. The TPP and CD models have a similar response. The high-frequency fluctuations in the pitch are due to the attitude controller which is active during the chirp.
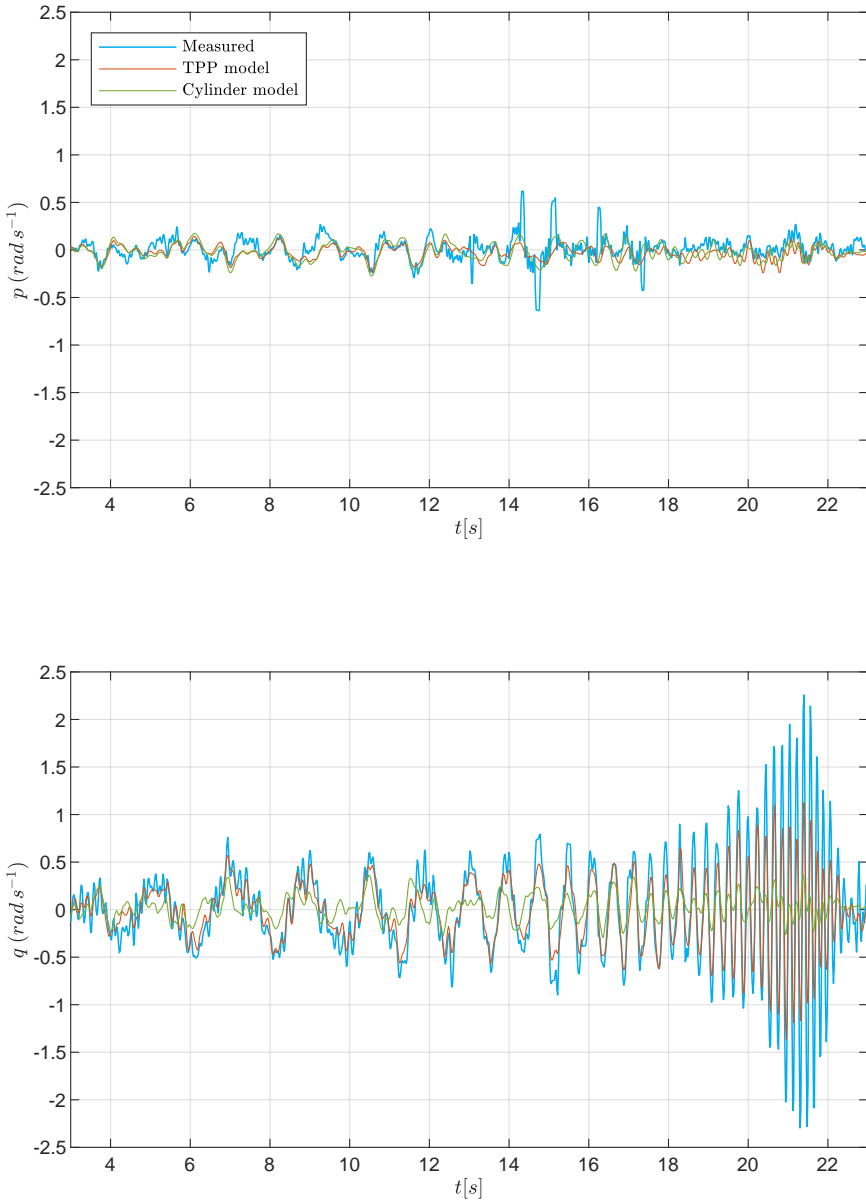
Figure 7.9: A validation chirp on the pitch axis in forward flight. The CD model accuracy is much worse than the TPP model, while the latter is also unable to follow the measurements at higher frequencies.
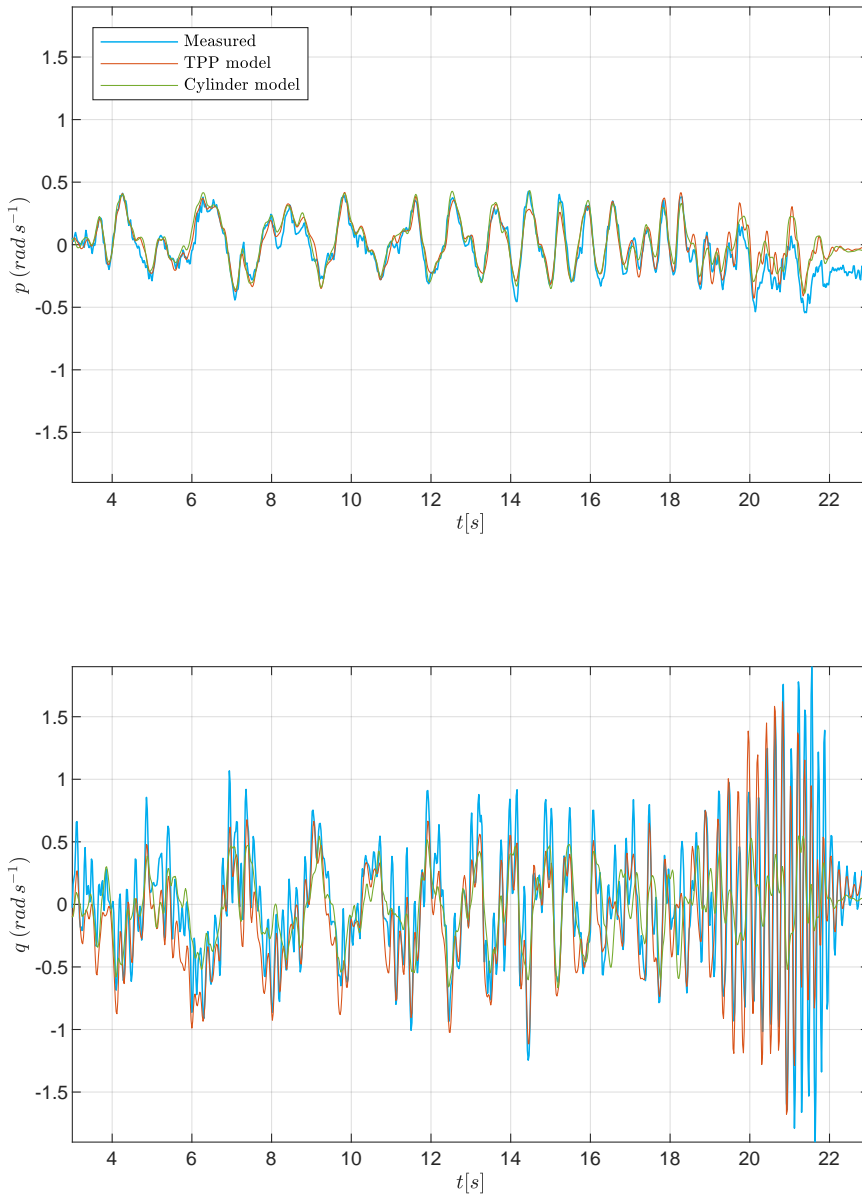
Figure 7.10: Validation chirp on the elevator axis in forward flight. The roll response p (yaw in fixed-wing aircraft reference frame) is fitted accurately by both TPP and CD models, while in the pitch response q, the TPP models start to show significant difference around 20 s and the CD model is unable to replicate those frequencies at all.

eters for the rotor dynamics in the TPP model. The fact that the roll rate damping is very small is to be expected since the vertical stabilizing tips of DelftaCopter have a small moment arm to the center of mass.

Figures 7.8 to 7.10 show the measurements and the model responses of chirps on roll, pitch and elevator respectively. The resulting TPP and CD model fits are overlayed in the figures and clearly show which frequencies are not well modeled. It is clear that the TPP model is better at predicting the high-frequency response than the CD model, but the fit is not as good as for the hover model. This can be due to the RPM fluctuations or the TPP model. Another cause of model inaccuracy could be unmodeled aerodynamic effects or the energy exchange during the chirps. Atmospheric conditions are also less steady during outdoor forward flights than during the indoor hover tests. The angle of attack and sideslip are not part of the model either and were not measured, but could have an important influence. Surprisingly, the M_q parameter is identified as being positive, implying a positive feedback loop on the pitch rate. The CoMC of the fits can be found in Table 7.7. While the p axis in the CD model is better than the TPP model, the q axis is so much worse that this advantage is completely lost. Both fitting and validation percentages are obtained from three chirps, one in roll, one in pitch, and one with the elevator. The validation chirps and model responses can be found in Figures 7.8 to 7.10.

	Axis	TPP model	CD model
Fitting	p	66.0%	70.8%
	q	54.7%	21.7%
Validation	p	49.7%	53.1%
	q	47.1%	17.0%

Table 7.7: Comparison of the CoMC percentage as given in Equation (7.9) for forward flight.

7.8. Conclusion

The DelftaCopter is a tailsitter UAV consisting of a single rotor with cyclic and collective pitch control on top of a delta-wing biplane. Previous research developed a Cylinder Dynamics (CD) model which assumes a rigid rotor [26]. This work compared the CD model with a linearized Tip-Path Plane (TPP) model of the attitude dynamics based on work by [20]. A system identification modeling approach was chosen and chirps were used as system identification maneuvers to fit a wide frequency range. The TPP model is shown to be much better at modeling the high-frequency response than the CD model. This is validated using data from manually flown doublets, for which the TPP response also shows better accuracy. In particular, the flapping dynamics modeled as the Tip-Path Plane significantly influence the pitch dynamics of the DelftaCopter at about 5 Hz. It was shown that this model can be used for controller design by deriving an LQR attitude rate controller. The relationship between the identified parameters and rotor RPM was found to be different than predicted from theory. This may be due to the lumping together of unmodeled effects into the present parameters, but is likely to be due to non-linear

effects that the current state-space model has linearized. In particular, the rotor hinge spring is believed to have very non-linear characteristics.

For forward flight, the TPP and CD models were extended to include roll rate and pitch rate damping and include a constant for the elevator effectiveness. Furthermore, the model confirmed particular characteristics of the DelftaCopter, namely: the principal components for the actuation of pitch and roll are different than in traditional helicopters and are not even perpendicular and the roll actuator mainly drives roll at low frequencies and mainly drives pitch at high frequencies. Overall, the derived linear state-space model captures most of the dynamics of the Delfta-Copter in the frequency range up to 10 Hz. Nevertheless, the data clearly shows that not all dynamics are modeled and more states and non-linearities have to be included to improve the modeling.

7.9. Recommendations

Due to technical constraints, the a and b angles of the TPP could not be measured. They were estimated using the derived model, but could not be validated. The angle of attack α or fuselage sideslip angle β of the delta-wing in forward flight could also not be measured, but could better model errors like the end of Figure 7.10 where sideslip or increased angle of attack could be the cause of the steady-state error. Although separate tests have shown that the used *MKV HV9767* servos could track the required chirp commands with small deflections up to frequencies of over 20 Hz, the role of servo dynamics on the faster dynamics should be further investigated. Finally, in forward flight, it is recommended to generalize the flight model for different airspeeds and RPM as these values do change during normal flight conditions.

References

[1] C. De Wagter and J. Meulenbeld, *Modeling the unstable DelftaCopter vertical take-off and landing tailsitter unmanned air vehicle in hover and forward flight from flight test data,* International Journal of Micro Air Vehicles **11**, 1 (2019).

[2] J. Meulenbeld, C. De Wagter, and B. Remes, *Modeling delftacopter from flight test data,* in *10th International Micro Air Vehicle Competition and Conference*, edited by S. Watkins (IMAV, Melbourne, Australia, 2018) pp. 18–29, iMAV2018-1.

[3] K. K. Valavanis, *Advances in unmanned aerial vehicles: state of the art and the road to autonomy*, edited by Springer (Springer, 2012) p. 543.

[4] A. S. Saeed, A. B. Younes, C. Cai, and G. Cai, *A survey of hybrid unmanned aerial vehicles,* Progress in Aerospace Sciences **98**, 91 (2018).

[5] S. Herbst, G. Wortmann, and M. Hornung, *Conceptual design studies of vertical takeoff and landing remotely piloted aircraft systems for hybrid missions,* CEAS Aeronautical Journal **7**, 135 (2016).

[6] UAVChallenge, *Uav challenge medical express competition rules 2016 v4,* https://uavchallenge.org/ (2016).

[7] J. Roberts, D. Frousheger, B. Williams, D. Campbell, and R. Walker, *How the outback challenge was won: The motivation for the UAV challenge outback rescue, the competition mission, and a summary of the six events,* IEEE Robotics & Automation Magazine **23**, 54 (2016).

[8] A. Oosedo, S. Abiko, A. Konno, T. Koizumi, T. Furui, and M. Uchiyama, *Development of a quad rotor tail-sitter VTOL UAV without control surfaces and experimental verification,* in *2013 IEEE International Conference on Robotics and Automation* (IEEE, 2013) pp. 317–322.

[9] M. Hochstenbach, C. Notteboom, B. Theys, and J. De Schutter, *Design and Control of an Unmanned Aerial Vehicle for Autonomous Parcel Delivery with Transition from Vertical Take-off to Forward Flight -VertiKUL, a Quadcopter Tailsitter,* International Journal of Micro Air Vehicles **7**, 395 (2015).

[10] E. J. J. Smeur, Q. P. Chu, G. C. H. E. de Croon, B. Remes, C. De Wagter, and E. van der Horst, *Modelling of a hybrid uav using test flight data,* in *International Micro Air Vehicle Competition and Conference 2014*, edited by G. de Croon, E. J. van Kampen, C. De Wagter, and C. C. de Visser (IMAV, Delft, the Netherlands, 2014) pp. 196–203.

[11] B. Bataillé, J.-M. Moschetta, D. Poinsot, C. Bérard, and A. Piquereau, *Development of a VTOL mini UAV for multi-tasking missions,* The Aeronautical Journal **113**, 87 (2009).

[12] L. Lustosa, F. Defay, and J. Moschetta, *Development of the flight model of a tilt-body MAV,* in *International Micro Air Vehicle Competition and Conference 2014* (Delft, The Netherlands, 2014) pp. 157–163.

[13] M. Bronz, E. Smeur, and H. de Marina, *Development of A Fixed-Wing mini UAV with Transitioning Flight Capability,* in *35th AIAA Applied Aerodynamics Conference* (Denver, Colorado, 2017).

[14] K. Wong, J. Alfredo Guerrero, D. Lara, and R. Lozano, *Attitude Stabilization in Hover Flight of a Mini Tail-Sitter UAV with Variable Pitch Propeller,* IEEERSJ International Conference on Intelligent Robots and Systems (2007).

[15] C. De Wagter, R. Ruijsink, E. Smeur, K. van Hecke, F. van Tienen, E. van der Horst, and B. Remes, *Design, control, and visual navigation of the delftacopter vtol tail-sitter uav,* Journal of Field Robotics **35**, 937 (2018).

[16] K. Kondak, M. Bernard, N. Losse, and G. Hommel, *Autonomously Flying VTOL-Robots: Modeling and Control,* in *Proceedings 2007 IEEE International Conference on Robotics and Automation* (IEEE, 2007) pp. 736–741.

7

[17] D. Vorsin and S. Arogeti, *Flight transition control of a multipurpose uav,* in *13th IEEE International Conference on Control Automation ICCA* (IEEE, Ohrid, Macedonia, 2017) pp. 507–512.

[18] M. S. Gandhi, L. Whitcher, E. Theodorou, and E. N. Johnson, *Practical system identification for small VTOL unmanned aerial vehicle,* in *AIAA Scitech 2019 Forum*, 1–24 No. 2019-1982 (AIAA, San Diego, California, 2019).

[19] A. Bramwell, G. Done, and D. Balmford, *Bramwell's Helicopter Dynamics* (American Institute of Aeronautics and Astronautics, 2001) pp. 1–397.

[20] B. Mettler, *Identification Modeling and Characteristics of Miniature Rotorcraft* (Springer US, Boston, MA, 2003).

[21] B. Mettler, C. Dever, and E. Feron, *Scaling Effects and Dynamic Characteristics of Miniature Rotorcraft,* Journal of Guidance, Control, and Dynamics **27**, 466 (2004).

[22] K. Kondak, M. Bernard, N. Losse, and G. Hommel, *Elaborated modeling and control for autonomous small size helicopters,* in *Proc. ISR/ Robotik*, Vol. 1956 (VDI-Verlag, München, Germany, 2006) p. 207.

[23] S. Bhandari, R. Colgren, P. Lederbogen, and S. Kowalchuk, *Six-DoF dynamic modeling and flight testing of a UAV helicopter,* in *AIAA Modeling and Simulation Technologies Conference and Exhibit*, August, edited by AIAA (AIAA, San Francisco, California, 2005) pp. 992–1008.

[24] L. A. Sandino, M. Bejar, A. Ollero, L. A. Sandino, A. Ollero Grvc, M. Bejar, and A. Ollero, *A Survey on Methods for Elaborated Modeling of the Mechanics of a Small-Size Helicopter. Analysis and Comparison,* Journal of Intelligent & Robotic Systems **72**, 219 (2013).

[25] V. Klein and E. A. Morelli, *Aircraft System Identification: Theory And Practice* (AIAA (American Institute of Aeronautics & Astronautics), 2006).

[26] C. De Wagter and E. J. J. Smeur, *Control of a hybrid helicopter with wings,* International Journal of Micro Air Vehicles **9**, 209 (2017).

[27] M. B. Tischler and R. K. Remple, *IEEE Control Systems*, edited by J. A. Schetz (AIAA, 2012).

[28] G. Hattenberger, M. Bronz, and M. Gorraz, *Using the Paparazzi UAV System for Scientific Research,* in *IMAV 2014, International Micro Air Vehicle Conference and Competition 2014* (IMAV, Delft, the Netherlands, 2014) pp. 247–252.

[29] A. Dorobantu, A. Murch, B. Mettler, and G. Balas, *System Identification for Small, Low-Cost, Fixed-Wing Unmanned Aircraft,* Journal of Aircraft **50**, 1117 (2013).

8

The Nederdrone: a hybrid lift, hybrid energy hydrogen UAV

*If we all would be willing to change our mind when proven wrong
then the world would be a better place.*

Lawrence Maxwell Krauss

Many Unmanned Air Vehicle (UAV) applications require vertical take-off and landing and very long-range capabilities. Fixed-wing aircraft need long runways to land, and electric energy is still a bottleneck for helicopters, which are not range efficient. In this paper, we introduce the Nederdrone, a hybrid lift, hybrid energy hydrogen-powered UAV that can perform vertical take-off and landings using its 12 propellers while flying efficiently in forward flight thanks to its fixed wings. The energy is supplied from a combination of hydrogen-driven Polymer Electrolyte Membrane fuel-cells for endurance and lithium batteries for high-power situations. The hydrogen is stored in a pressurized cylinder around which the UAV is optimized. This work analyses the selection of the concept, the implemented safety elements, the electronics and flight control and shows flight data including a 3h38 flight at sea while starting and landing from a moving ship.

8.1. Introduction

UAVs offer solutions in a large variety of applications [3–6]. While a lot of applications can be performed with current battery technology, for many others the energy requirements cannot be met [7]. In particular, when combined with the requirement to have VTOL capabilities, the traditional efficient fixed-wing aircraft concept is not an option. For these applications, hybrid concepts have been proposed which combine the most efficient way of flying, namely using fixed wings, with the capability to land vertically.

(a) DelftaCopter [8]   (b) VertiKUL [9]   (c) DHL Parcelcopter 3 [10]

Figure 8.1: Hybrid UAV able to take-off and land vertically while using fixed-wings to increase flight efficiency in forward flight.

The most common categories of hybrid lift UAV are the tail-sitters, dual-systems, and transforming UAV [11]. Tail-sitters pitch down 90° during the transition from hover to forward flight, and while they have important drawbacks for pilot comfort [12], they have gained a lot of interest for UAV. They do not require any mechanical reconfiguration and allow the re-use of the same propulsion systems in several phases of the flight [9] (See Figure 8.1b). Many different types of tail-sitters exist. They can either be optimized to maximize the hovering efficiency with a single large rotor [8] (See Figure 8.1a) or to minimize complexity [13–15]. Other tail-sitters were optimized for maximal redundancy [1] or were given re-configurable wings to minimize sensitivity to gusts in hover [16]. The second category is formed by 'dual systems' like quad-planes. These UAVs contain a complete hovering vehicle combined 'in-plane' with a separate fixed-wing vehicle. Both parts are typically operated separately [17]. The last category consists of transforming vehicles that try to re-use propulsion systems in hover and forward flight by either tilting the entire wings with respect to the fuselage [10] (See Figure 8.1c) or by only tilting the propulsion system [18]. These hybrid concepts increase the endurance of UAV while maintaining the ability to hover and land vertically.

Despite large improvements in battery technology, battery capacity is still a bottleneck for the endurance of UAVs. This is why recent lightweight robust fuel-cell technology advancements [19] have led to increased interest from UAV applications [20–23]. Fuel-cells can be divided into five types: alkaline [24], Polymer Electrolyte Membrane (PEM) [25], phosphoric acid [26], solid oxide [27], and molten carbonate

batteries [28]. The most suitable for portable micro-systems are the PEM [29] as they can work at room temperature, have a small size, are lightweight, and have anti-aging. PEM fuel cells can be powered by fuels like liquid methanol [29] or hydrogen [30].

Apart from storage [31], hydrogen is ideal as a synthetic fuel because it is lightweight, highly abundant and its oxidation product is environmentally benign. Moreover, the hydrogen to electricity cycle is bi-directional [32]. Hydrogen can be generated in a variety of ways even without generating COx [33]. It can be generated off-grid [34], and recent research even addresses the generation of hydrogen without the need for rare and expensive platinum (Pt) [35] nor Ruthenium (Ru) [36] by using hybrid nano-plates as catalytic material instead [37].

Fuel-cells do come with power constraints and developing small reliable membranes for power-hungry UAVs can be a challenge [38]. So, while flight with a single energy source is the most weight-efficient solution [39], in most hydrogen-powered UAVs the fuel-cell power had to be complemented with batteries [40]. Hovering also requires a higher power density than forward flight [11]. So while hydrogen fuel-cell powered quadrotors have been developed [21], their flight times have never reached the endurance seen in fixed-wings. This power efficiency is why so many fixed wing hydrogen UAVs have been proposed like the 16 kg 500 W demonstrator from [41] in 2007, the 1.5 kg 100 W UAV from [21] in 2012, the 11 kg 200 W from [22] in 2017 to the 2020 6.4 kg 250 W [23].

As even hydrogen's energy storage capacity is limited, the combination of hydrogen power with solar power has also been investigated [42] and effectively helped to double the flight time in ideal conditions. This combination has also been proposed to cross the Atlantic [43] with a fixed-wing UAV. But the mainstream solution remains a combination of battery power for high-demand situations and hydrogen power for endurance. This combination is further referred to as "hybrid energy" [44].

To combine the advantages of a hybrid lift UAV with those of hybrid energy from batteries and hydrogen fuel-cells, a new concept is developed called: *the Nederdrone.*

Section 8.2 investigates the selected type of fuel-cell and safety aspects of flying with hydrogen. Section 8.3 explains the design choices of the hybrid UAV built around the fuel-cell system. Section 8.4 describes the essential aerodynamic properties. Section 8.5 explains the hybrid power wiring and dual control bus of the Nederdrone. Section 8.6 explains the control. Section 8.7 shows actual test flight data. Finally Section 8.8, 8.9 and 8.10 give a discussion, conclusions, and recommendations respectively.

8.2. Selection of the hydrogen systems

Hydrogen-powered fuel-cells form an attractive solution for sustainable aircraft if the remaining technological problems can be solved [45]. The following section will address the selection of the fuel-cell, the selection of the fuel storage solution, and its safety considerations.
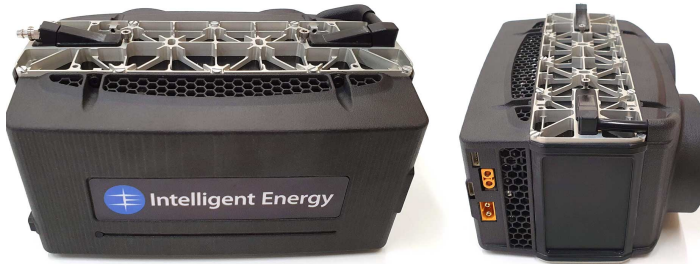
8.2.1. Fuel-cell

Figure 8.2: Intelligent Energy's 800 W fuel-cell system with dual fan.

The three most common fuel-cells used to power UAVs are: 1) hydrogen PEM fuel-cells, 2) direct methanol PEM fuel-cells, and 3) solid oxide fuel cells [46]. But the availability of ready-to-use systems at the time of selection also plays an important role. Although PEM fuel-cell efficiency drops with altitude [25, 47, 48], and their membrane must be re-humidified to unlock their full power when not used for a few days [49], their small size and weight form an attractive choice for UAV. Two options within the power range from 300 W to 1000 W were available, namely PEM fuel-cell systems from Intelligent Energy[1] (**IE**) and HES Energy Systems[2] (**HES**).

Unit	P [W]	P_{max} [W]	Lipo [cell]	ζ [%]	W [kg]	P/W [W/kg]
HES	250	250	6	50%	0.73	342.5
	500	500	7	52%	1.4	357.1
IE	650	1000	6	56%	0.81	802.5
	800	1400	6	55%	0.96	833.3

Table 8.1: Available fuel-fell power P, system maximum power P_{max}, number of auxiliary battery lithium cells, hydrogen efficiency ζ, weight W and weight efficiency P/W.

The **IE** 800 W air-cooled PEM fuel-cell running at ambient temperatures was selected, which is packaged as a small light-weight cost effective and robust system and shown in Figure 8.2. It runs at the easily available 6-cell lithium output voltage and—at the time of selection—had the better hydrogen efficiency ζ and weight efficiency P/W of the two.

The Lower Heating Value (LHV) efficiency Eff_{PEMFC} of the 800 W system is between 53 % at 800 W and 56 % at 700 W[3]. The fuel consumption ff_{H_2} in g/h at the predicted forward flight conditions of 600 W average power then becomes:

$$ff_{H_2} = \frac{P_{mean}}{E_{specific_{H_2}} \cdot Eff_{PEMFC}} \quad (8.1)$$

[1]http://www.intelligent-energy.com
[2]https://www.hes.sg/
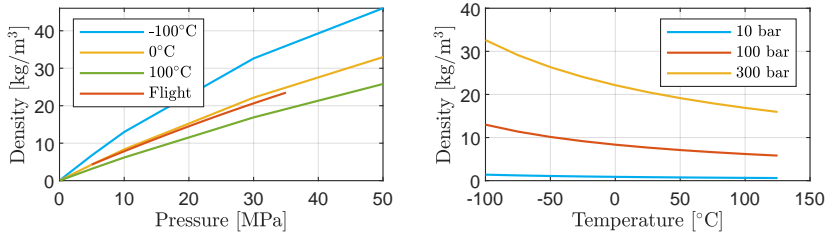[3]IE: uploads/product_docs/61126_IE_-_Cylinder_Guide_May_2020.pdf

Figure 8.3: Density of pressurized hydrogen in function of temperature Equation (8.2).

A hydrogen LHV of 33.3 Wh/g is used in further computations. This results in a fuel consumption (8.1) of not more than 34 g/h at 600 W average power and up to 45.3 g/h at full power. To fly at least 3 h at maximum fuel-cell power—to also deliver payload power and be able to climb, hover and recharge hover batteries in-flight—about 140 g of hydrogen would be desired.

The corresponding Intelligent Energy Transportable Pressure Equipment Directive (TPED) regulator weighs 0.28 kg, is 40 by 35 mm (diameter x length), 20 to 500 bar 'in' and 0.55 bar 'out' and is equipped with an electronic shut-off valve, pressure sensors and a standard 8 mm Pre-Charged Pneumatic (PCP) fill port. The fuel-cell system weighs 0.96 kg and measures 196 by 100 by 140 mm. Its output voltage ranges from 19.6 V to 25.2 V. It is equipped with a 1800 mAh 6-cell lithium-polymer auxiliary battery of 0.3 kg which enables the combined system to deliver 1400 W of peak power for a short time.

8.2.2. Hydrogen storage

At room temperature, the main two options to store hydrogen are as a pressurized gas in a pressure cylinder, or as a chemical solution that releases hydrogen [50]. Sodium borohydride ($NaBH_4$) is often used in UAV and portable applications as a hydrogen source to power PEM fuel-cells [30, 51, 52].

The downside of pressure cylinders is that they weigh much more than the hydrogen inside them [53]. But because of sustainability, overall system weight, off-grid recharge options [34], price, and availability, the choice was made to use pressure cylinders.

The mass of hydrogen m_{H_2} based on the cylinder volume V and pressure p in flight conditions is fitted as[4]:

$$m_{H_2} = (-0.00002757p^2 + 0.074969p + 0.6187) \cdot V \qquad (8.2)$$

It should be noted that the actual value varies with temperature. At 300 bar, values change from 20.7 g/L at 25 °C to 21.2 g/L at 15 °C (See Figure 8.3) and a 25 °C drop in temperature leads to a 7.8 % increase in hydrogen per liter. In this paper, the more pessimistic values at 25 °C are used. Figure 8.4 shows an overview of available cylinder options. The cylinders are compared for the weight percentage

---

[4]https://h2tools.org/hyarc/hydrogen-data/hydrogen-density-different-temperatures-and-pressures
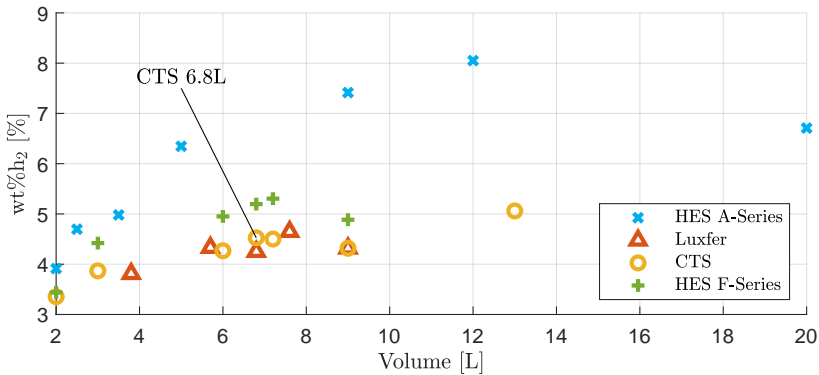
Figure 8.4: Overview of the specific hydrogen weight $wt\%H_2$ which should be as high as possible, for various cylinders that were available at the time of selection. It can be seen that the actual hydrogen weight is only a fraction of the storage weight.

of hydrogen they can contain compared to the total cylinder weight which is further called $wt\%H_2$ [2]. The cylinders should be as light as possible for a given pressure and volume to result in the highest weight percentage of hydrogen [54].

Figure 8.5: CTS 6.8 L 300 bar ultralight Type-4 pressure cylinder in a certified transport case.

Due to price, commercial availability, and availability of EU certification, the 6.8 L Composite Technical Systems (CTS) Polyethylene Terephthalate (PET) Liner Type-4 cylinder[5] was selected and is shown in Figure 8.5. This is the heaviest certified cylinder that still fitted in the weight budget of the ≈10 kg UAV. The graph does however illustrate that doubled specific hydrogen weights can be expected in the future.

8.2.3. Safety of handling pressurized hydrogen
Hydrogen gas is flammable in concentrations from 4 % up to 75 % when mixed with air and burns optimally at a concentration of 29 %. It has a self-ignition temperature

---

[5]http://www.ctscyl.com/prodotti/h2/cts-ultralight-6-8l-300-bar-h2

585 °C, but a very low required ignition energy of 17 µJ. Human body models show that a person without static protection can easily cause a 40 mJ discharge. To avoid ignition, anti-static shoes and clothes are therefore required when leakages are expected, for instance during filling. Refueling should be done at temperatures in between −20 °C and 40 °C to stay within cylinder's limitations. Hydrogen is roughly 14 times lighter than air and therefore easily gets trapped inside rooms and ceiling cavities and can degrade material properties [55].

Pressure cylinders also have inherent risks. A lot of research has been done on pressure cylinder rupture, but most research has been focusing on metal cylinder gasses like air and Compressed Natural Gas (CNG) [56]. For composite high-pressure cylinders, models and methods have been developed and validated [57], but these do not show all risks of hydrogen cylinder failures. Actual crush-tests of composite hydrogen cylinders have been performed [58] to simulate a car crash. But they used mainly cylinders with aluminum liners (type 3A/B). The blast from hydrogen cylinders exposed to vehicle fires was also investigated [59]. They suggest that the blast from a cylinder failure through fire (with combustion) can throw debris up to 80 m, but also shows that 35 m would be a no-harm distance for the shock-wave of a 12 L 700 bar cylinder.

(a) 12m high drop tower   (b) Tank impact   (c) Damage

Figure 8.6: Drop-test of a hydrogen-filled cylinder on steel-covered concrete did cause a leak at the regulator but did not visibly damage the cylinder and did not lead to fire nor detonation.

The cylinder selected for this platform has been tested by the manufacturer according to the *NEN-EN12245+A1* norm. But since no data were available about the safety of the combined cylinder and pressure regulator, a drop test was organized that simulated the fall on the metal deck of a ship (See Figure 8.6b). While this does not represent the worst-case scenario of a crash involving hydrogen, it does address the operational scenario in which the hydrogen drone moves away from the ship as soon as possible after take-off and only moves over the ship at low speed and low altitude upon landings. A test was performed according to the *STANAG 4375*. The cylinder was dropped from a 12 m high tower (See Figure 8.6a) on a metal plate on top of a concrete floor while filled with about 140 g of hydrogen (285 bar) [60]. High-speed camera footage was made and the post-impact damage was assessed. The metal regulator broke (See Figure 8.6c) which resulted in a leak. After a few minutes, all hydrogen had escaped and the cylinder was inert. No combustion occurred.

8.3. Design of the hybrid lift UAV

After the selection of the fuel-cell system and hydrogen storage, a UAV was designed around it from the ground up. Fitting a hydrogen cylinder and fuel-cell in a hybrid UAV poses specific constraints [20, 21, 44]. The large and bulky cylinder highly influences the aerodynamic shape. To cool the fuel-cell and remove the formed water vapor, airflow through the fuel-cell radiator is important. The relatively large weight of the energy supply and payload combined with the weight of the propulsion needed to hover poses strict limitations on structural weight and flying with pressure cylinders and expensive equipment comes with redundancy requirements. This section will discuss these challenges.

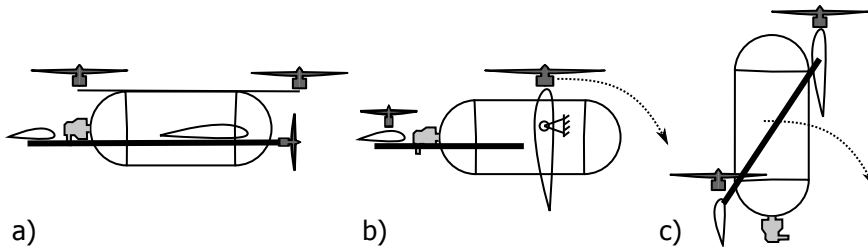### 8.3.1. Hybrid lift UAV concept trade-off

Figure 8.7: Hybrid lift UAV concepts around a hydrogen cylinder.

First, a trade-off is made between the three main classes of hybrid lift UAVs. The dual-system VTOL UAV like quad-planes have a separate propulsion system for hover and forward flight (Figure 8.7a). To minimize weight, a minimalistic hover system is often used as this is only dummy weight during the largest part of the flight. The hover propulsion blows perpendicularly to the wing and therefore needs additional arms to support the motors at a distance from the wing, which also adds weight and drag in forward flight. The tilt-wing (or tilt-motor) concept (Figure 8.7b) has a mechanism to rotate the entire wing, thereby removing the need for separate motor support arms and re-using part of the propulsion from hover in forward flight. The downsides are the increased mechanical complexity, higher mechanical weight, and the control complexity of flying with a changing morphology. The tail-sitter concept shown in Figure 8.7c, re-uses the same motors in both flight regimes while minimizing mechanical complexity. The propulsion can be attached to the wing, which is already designed to carry the weight of the vehicle and this reduces overall structural weight. As the vast majority of the flight is typically in forward flight, the propulsion can be optimized for this phase. The drawbacks are that the UAV must pitch down 90° during the transition and therefore pass through the stall regime of the wing. Moreover, the cylinder is vertical after landing which makes it prone to tipping over, especially on moving platforms like ships.

To minimize structural weight and complexity while re-using the hover propulsion in forward flight, the tail-sitter concept was selected for the Nederdrone.
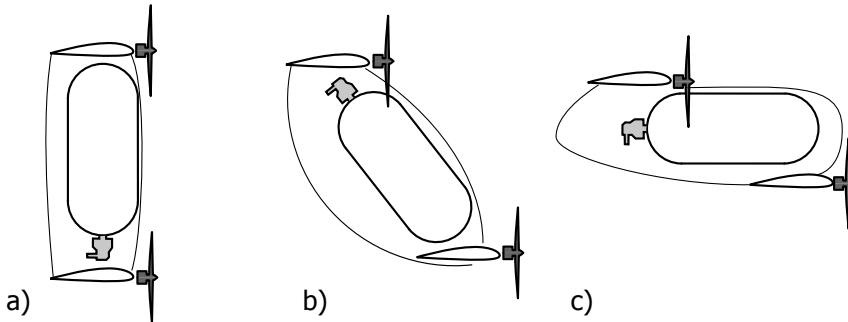
8.3.2. Cylinder placement into the UAV

Figure 8.8: Hybrid lift Tail-sitter UAV concepts with several cylinder orientations.

Within the class of tail-sitter UAVs, three variables form a trade-off for the orientation of the cylinder: drag, ground stability, and control authority in hover. The best control authority in hover is achieved by maximizing the distance between the motor center lines as shown in Figure 8.8a. With this setup, larger control moments can be created through differences in thrust. After landing the cylinder lies flat and stable on the ground. But this configuration has the highest fuselage drag in forward flight as the frontal surface is determined by the cylinder surface in the length direction. Moreover, in forward flight, the wings are exactly on top of each other which results in an aerodynamically unstable aircraft without an S-shaped airfoil or significant wing sweep angle.

Previous work [1] made a compromise and placed the cylinder at a negative 30° angle with the incoming flow as shown in Figure 8.8b. Upon landing, the fuselage would roll down 30° until the cylinder was flat on the ground. But a shock-absorbing landing gear was nevertheless needed to protect the propellers. Moreover, the design goal of staying below 600 W in forward flight could not be achieved. Therefore, for the Nederdrone, the cylinder was placed completely in line with the flow as in Figure 8.8c, as any reduction in drag is crucial to increase the endurance and maximal forward flight speed.

8.3.3. Sizing the wings, stabilizer, and fuselage

The next step of the hybrid lift UAV design is the sizing of the wings, horizontal stabilizer, and fuselage to achieve stable forward flight characteristics. The selected concept has the cylinder and the fuel-cell placed in-line to minimize drag which increases the longitudinal mass distribution. To improve the damping of the short period pitch motion in forward flight, either a large elevator or a long fuselage is required [61]. But since this is a tailsitter UAV, a long fuselage conflicts with the ground stability requirement and is at high risk of tipping over.

The combined requirements are addressed by giving the Nederdrone a short fuselage and a tandem wing configuration. The tandem wing has the best pitch damping for a given fuselage length [61]. Moreover, it has a shorter wingspan for a given amount of wing area at a given aspect ratio compared to a conventional large
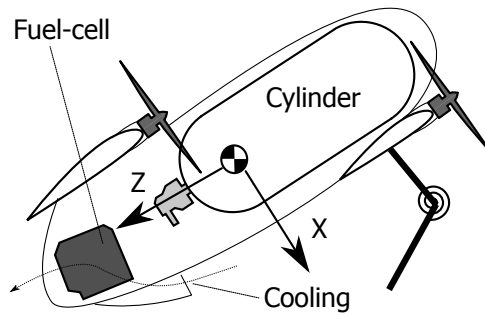
Figure 8.9: The Nederdrone concept: a *drop-down* tail-sitter with an in-flow oriented hydrogen pressurized cylinder, rear-mounted fuel-cell with bottom cooling airflow vent, low front-wing, and high tail-wing.

main wing and a small horizontal stabilizer. These shorter wings help to reduce the influence of perturbations in hover, as they provide less leverage than longer wings.

8.3.4. Ground stability
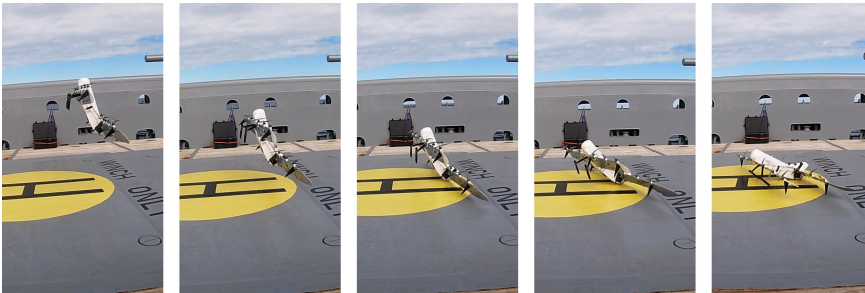
Figure 8.10: Landing sequence of the Nederdrone on a ship.

Since the pressure cylinder is placed in the direction of the airflow during forward flight, it is upright during the landing and its stability after landing must nevertheless be guaranteed, even on a moving platform like a ship.

The option was investigated to slowly *drop-down* the nose after landing by using the hover propellers. Once the hover propellers start to point forward beyond a certain angle, the ground friction is overcome and the drone starts to slide forward. Just before this point, the thrust is cut off and the nose drops down. A sprung landing gear then absorbs the last part of the gentle drop. The result is a UAV which lies stably on the ground after landing.

To further minimize the impact of the landing, the center of gravity was moved backward and closer to the ground while landing by choosing a canard configuration with the largest wing at the back. The resulting landing sequence is shown in Figure 8.10.

8.3.5. Take-Off

(a) Take-off with 2m/s wind

(b) Take-off with 7m/s wind
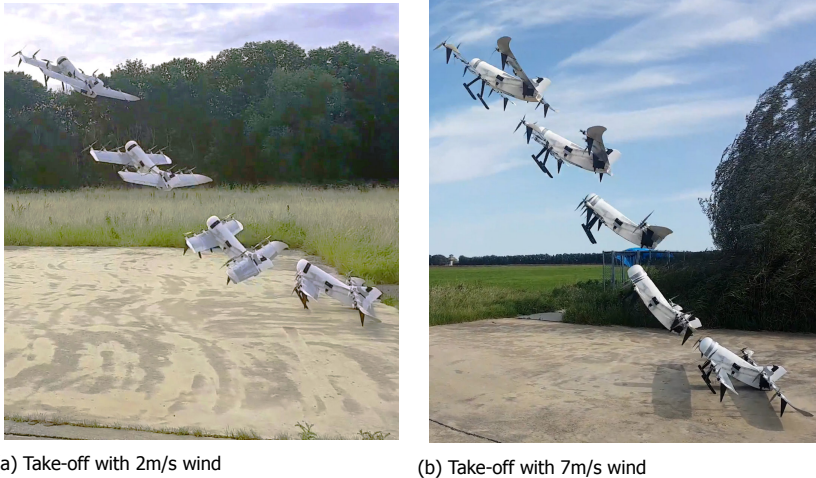
Figure 8.11: Composite image of the Nederdrone take-off.

In tail-sitter UAVs, the ground stability requirement is conflicting with the vertical take-off requirement of the tail-sitter. The Nederdrone was designed to sit in a stable 60° nose down from hover. This means for take-off the nose points only 30° up, but test flights showed that even in worst-case 'no-wind' conditions the UAV only slides less than a foot before taking off as shown in composite image Figure 8.11. The high thrust to weight, the ground effect of the propeller flow over the wing squeezed between the wing and the ground, and the spring in the landing gear makes the Nederdrone take-off into what will be referred to as an angled take-off.

The resulting hybrid-hybrid vehicle designed around a pressure cylinder has minimal drag in forward flight, has tandem wings that also serve as structural support for the 12 propellers, does not require mechanical reconfiguration but uses its redundant propulsion in both flight regimes, can take-off and land vertically and is stable on the ground before take-off and after landing.

8.4. Aerodynamics

Once the general concept shape was determined, the aerodynamics properties were designed and tested. The airfoil for the wings has been chosen to yield a good compromise between 'gentle stall' and 'low drag throughout the lift curve' using the *XFoil* module within XFLR5[6]. The resulting airfoil is based on a *MH32* airfoil but was modified to allow construction from Expanded Polypropylene (EPP). Wind tunnel measurements were performed in the TUDelft OJF [62], in which the full-scale Nederdrone was tested (See Figure 8.12).

The lift and drag forces were measured at different speeds and angles of attack α from zero to over 60 degrees. The resulting lift coefficient C_L and drag coefficient

---

[6]http://www.xflr5.tech/
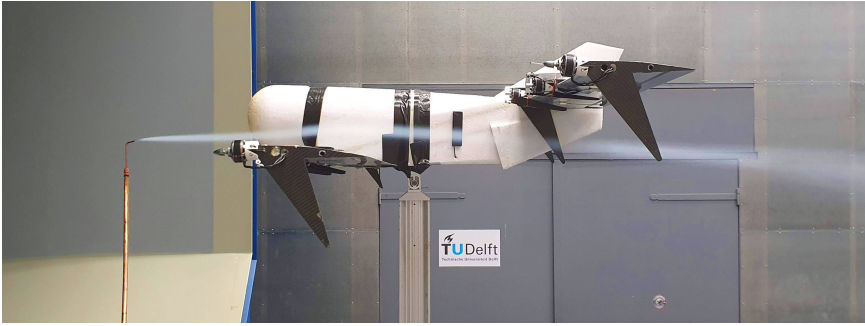
Figure 8.12: The Nederdrone placed in the TUDelft Open Jet Facility (OJF). Smoke analysis shows that in forward flight there is no interference between the wings and the cooling air reaches the rear inlet to cool the fuel-cell.
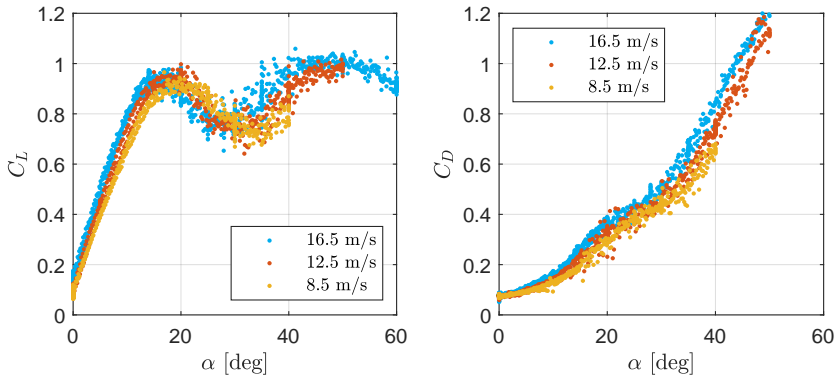
Figure 8.13: Lift and drag curves (lift coefficient C_L and drag coefficient C_D in function of angle of attack α) of the Nederdrone as measured during wind tunnel testing. The stall starts at about 15° but is very gentle. This is important during the transition phase of the tail-sitter UAV as abruptly changing lift forces complicate the control.

C_D curves are shown in Figure 8.13. The smooth reduction in lift coefficient after $\alpha > 20°$ confirms that the airfoil has gentle stall properties and that the front and back wings of the tandem aircraft do not cause detrimental interactions with each other. These two properties are very important for flight control as abrupt changes in the lift or drag highly affect the control of the platform.

8.5. Electronics

With the concept design to fit the available fuel-cell power in forward flight finished, the required power to hover was analyzed.
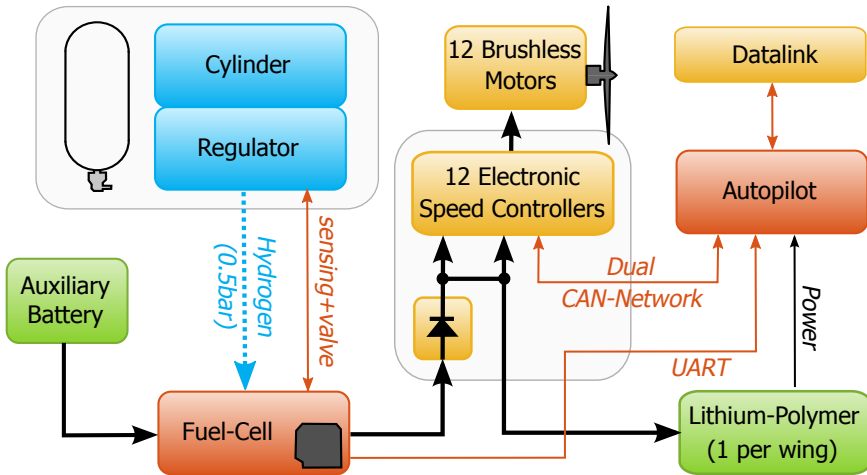
Figure 8.14: Dual power bus and dual Controller Area Network (CAN) controller area network brushless ESC.

8.5.1. Hybrid electric power

Hovering a roughly 10 kg platform in gusts while the propulsion is optimized for the forward flight regime is taking more than the 1400 W maximum of the selected fuel-cell system. To complement the fuel-cell during the short high power phases, high C-rating lithium polymer batteries are added to the Nederdrone. This is traditionally done with two DC-DC converters and a power management system. This allows the application of various types of intelligent power management strategies, for instance, based on fuzzy logic [63]. But even with state-of-the-art technology, the mass of DC-DC converters is not negligible [64]. To avoid heavy power electronics merging both energy sources, a passive approach is designed where both power sources are connected in parallel. The company proprietary DC-DC converter inside the **IE800** fuel-cell system is tuned to act as a 25 V constant voltage source when the used power is less than 800 W, while beyond 800 W its voltage drops depending on the load.

The six-cell lithium-polymer battery recommendations state that they can safely be charged up to 25.2 V, which is compatible with the fuel-cell voltage range including a safety margin of 0.2 V to prevent over-charge. To minimize weight, the batteries are therefore connected directly to the motors in parallel to the fuel-cell. To prevent the hover batteries from feeding current into the fuel-cell, the fuel-cell current is run through a pair of *SBRT15U50SP5-13* 15 A continuous power diodes at each motor. This allows the very high currents to go from the lithium battery directly to the ESC without loss and allows the fuel-cell to re-charge the batteries to about 25 V minus the diode forward drop voltage of about 0.2 V in cruise conditions. To minimize power loss, maximize redundancy and distribute heat production, two diodes are used per motor, which results in lower current per diode and thereby also lower diode forward voltage V_F. This means the lithium-polymer batteries are

charged up to about 24.8 V which corresponds to at least 95 % full at a maximal rate of 8 A per pack. Since this is within specifications, the fuel-cell and lithium batteries can thus safely be placed in parallel without the need for heavy power electronics nor additional charging circuits. The full diagram is shown in Figure 8.14.

The hover batteries have been selected to provide 800 W for 30 min in case the fuel-cell would fail in-flight to allow the UAV to safely return and land. The selected batteries are four *Extron X2* 4500 mA h 6S 1P lithium-polymer batteries with a nominal voltage of 22.2 V and a discharge rate of 25C to 50C. They contain just under 100 W h of energy at 640 g each and can supply 90 A continuous current and 180 A burst current, which is more than sufficient to handle the largest peak currents. The four batteries are placed as close as possible to the four wings to supply the 3 motors on each wing through short high power wires for minimal loss.

8.5.2. Redundant control and status of 20 actuators
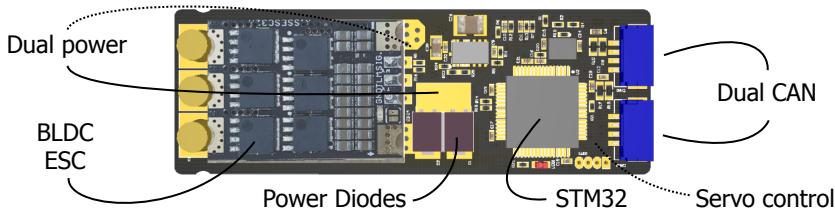
Figure 8.15: Dual power bus and dual Controller Area Network (CAN) ESC for BLDC motors (dashed lines are on the bottom).

For redundancy and structural weight distribution purposes the Nederdrone has twelve motors. Moreover, it has 8 aerodynamics flaps. To reduce wiring and connector failures and create a system that is still able to fly even if any of the wires would fail, the power and control wires need to be duplicated. This would lead to 24 control wires going to the 12 motors, excluding the motor status feedback wires and dual power bus and 16 additional control wires to servos. To reduce this large amount of wiring and weight, the Nederdrone uses a network bus instead as shown in Figure 8.14. The Controller Area Network (CAN) is an automotive industry technology that has been proposed as a low-cost solution in several aerospace applications [65]. The popular [66] *UAVCAN*[7] implementation was selected with custom messages. The result is a system where any control or power wire can be cut without dramatic consequences while the weight and complexity are kept to a minimum. The PCB design for the 12 CAN BLDC motor controllers with servo control outputs is shown in Figure 8.15.

8.6. Flight control

The flight control of the Nederdrone tail-sitter UAV poses several special challenges. First, the lift and moments generated by the wings are hard to model

---

[7]https://uavcan.org/

at large angles, which occurs when tail-sitters fly slowly. Sudden changes in the aerodynamic forces and moments can occur when the flow over the wings stalls or re-attaches, and require fast and powerful control actions to compensate. In hover, the large exposed up-pointing wing surfaces make tail-sitters susceptible to wind gusts, which need to be compensated by the controller. Moreover, specifically to the Nederdrone with its tandem-wing configuration, the slipstream from the front wing can hit the back wing at certain hover attitudes. Finally, the experimental nature of the project required a control method that could be easily adapted to changes made to the platform, without needing new wind tunnel measurements.

To cope with these challenges, an INDI controller was selected as it does not rely heavily on aerodynamic modeling but uses a sensor-based approach to identify external forces. INDI has been successful implemented on tail-sitters with similar challenges like the Cyclone tail-sitter UAV [15].

8.6.1. Cascaded INDI Control
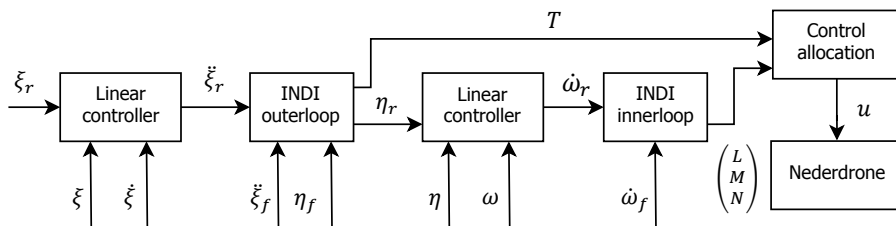
Figure 8.16: A schematic overview of the cascaded INDI control approach used in the Nederdrone. ξ is the position, η is the attitude, and ω the angular rate of the vehicle. The control moments are denoted by L, M and N, the total thrust is T, and the command vector to the servos and motors is u. Signals that are filtered have a subscript f.

INDI is a control method that makes use of feedback of linear and angular acceleration to replace much of the modeling needs since these signals provide direct information on the forces and moments that act on the vehicle [67]. The angular acceleration can be obtained through differentiation of the gyroscope signal, and the linear acceleration is directly measured with the accelerometer. To ensure a timely and well-scaled response to these external forces, INDI does require modeling of the actuators' responses and their control effectiveness. Based on the difference between desired and measured linear and angular acceleration, control *increments* are then calculated using this control effectiveness. The disturbance rejection properties of INDI have been shown theoretically and experimentally in previous research [68, 69] and its successful implementation on a tail-sitter has been detailed in [15].

The general structure of the controller is given in Figure 8.16, in which ξ is the position, η is the attitude, and ω the angular rate of the vehicle. The control moments are denoted by L, M, and N, the total thrust is T, and the command vector to the servos and motors is u. Signals that are filtered with a low pass filter have a subscript f.

The controller is split into an outer loop that controls the position and an inner loop that controls attitude. Both start with a linear controller to generate the desired

reference signals $\ddot{\xi}_r$ and $\dot{\omega}_r$. These signals are then compared with the filtered measurements $\ddot{\xi}_f$ and $\dot{\omega}_f$. The INDI blocks then compute increments in actuator deflection using the actuator effectiveness and dynamics to exactly cancel the errors in linear or rotational acceleration [68].

8.6.2. Structural Modes

One particular property of the tandem-wing tail-sitter UAV which was found during flight testing, is the relatively low frequency of some of the structural modes—in particular the longitudinal torsion mode. This is due to the large spread in mass over the wings, the relative flexibility of the wings combined with the relatively low torsional stiffness of the fuselage frame around the cylinder. To avoid interaction between the controller and the structural modes, the common procedure in aerospace is to give the controller a sufficiently small open-loop gain at the structural resonance frequency [70].

This can be achieved by including a low pass or a notch filter on the relevant feedback signals $\ddot{\xi}_f$ and $\dot{\omega}_f$. For the INDI inner loop, there is already a low pass filter to cope with the high-frequency vibrations from the motors. To minimize complexity, this filter was re-used by reducing the cutoff frequency of this second-order Butterworth low pass filter to 1.5 Hz for the pitch rate and roll rate, and 0.5 Hz for the yaw rate and linear acceleration. It should be noted that these filter cutoff frequencies are relatively low, and lead to reduced disturbance rejection performance. Increasing the stiffness of the platform and hereby the frequencies of the structural body modes can therefore improve the disturbance rejection.
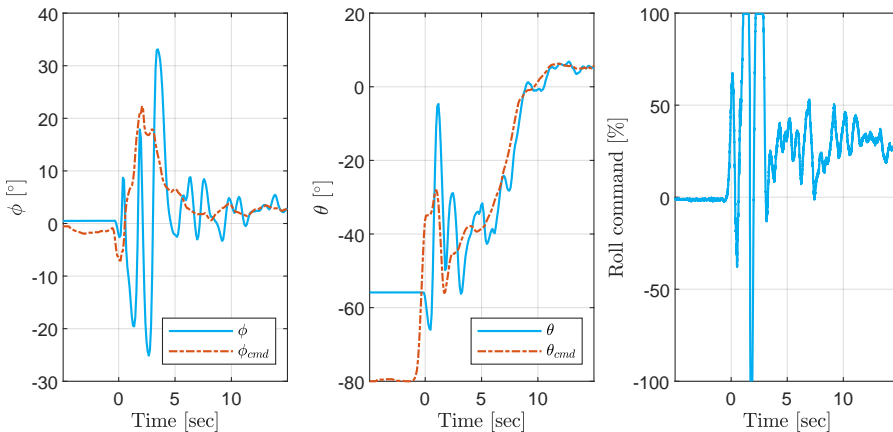
8.6.3. Disturbance rejection

Figure 8.17: Time sequence of a take-off (t=0) with a tip propeller spinning in reverse, causing a very large roll disturbance. The INDI controller needs 100 % deflections to counteract the disturbance but finds the required trim command within seconds. Notice the 55° nose down θ when standing on the ground.

To illustrate the ability of INDI to handle very large perturbations, a test flight was performed in which one tip propeller was configured to turn in the reverse direction. Not only does this tip propeller thereby create negative lift and a very large roll moment, but it also acts as a variable disturbance as it is being changed by the controller. Figure 8.17 shows the resulting perturbed take-off of the Nederdrone. Although some initial oscillations can be seen during the first five seconds, the INDI controller keeps the Nederdrone within acceptable attitudes and applies 100 % actuator deflections to cope with the unexpected perturbation. Within three seconds it stabilized the platform and found the new equilibrium which requires a 25 % roll command to compensate for the perturbation, while at the same time tracking aggressive outer-loop commands.

8.7. Results

The concept was built and tested in real flight. The wings are made of EPP cut with hot-wire and strengthened with dual carbon spars. Carbon ribs connect the spars to the motor mounts. Various parts like the motor mounts were built with the increasingly popular and powerful 3D printing technology [71]. To withstand the motor heat, the motor mounts were printed from a high-temperature resistant Ultimaker CPE+ filament.

The autopilot software is the Paparazzi-UAV autopilot [72, 73] project, which has support for various key features like low-level CAN drivers to INDI control implementations for hybrid aircraft, together with the ability to easily create custom modules to interface with the fuel-cell systems. The autopilot hardware is the Pixhawk PX4 *MBS-ENTB-24* board. The motors are 12 T-Motor *MN3510-25-360* motors equipped with *APC 13x10* propellers. Servos are the waterproof *HS-5086WP* metal gear, micro digital waterproof servos. Telemetry is exchanged via the *HereLink* system.

8.7.1. Battery-only flight testing

Before flying with hydrogen, a mock-up hydrogen system was 3D printed and filled with batteries and metal to achieve the same component weight. The mock-up cylinder was equipped with a 21 A h 1.865 kg 6S6P lithium-ion battery (*NCR18650GA*) to simulate the power delivered from the fuel-cell. This allowed the battery-powered Nederdrone to safely fly over 30 min. A sample flight is shown in Figure 8.18 in which the pitch angle on the ground, take-off, hover, transition, forward flight, and forward turns can be seen. Once the Nederdrone with mock-up hydrogen components had flown dozens of flight hours successfully including many test flights from a ship, it was equipped with the hydrogen systems.

8.7.2. First hybrid lift hybrid energy hydrogen flight at sea

To demonstrate the capabilities of the Nederdrone, a test flight at sea was performed in real-world conditions. On September 30th 2020, the Nederdrone with fuel cell took off from a sailing coast guard ship. The flight lasted 3 hours and 38 minutes. A composite image of the take-off is shown in Figure 8.19a.
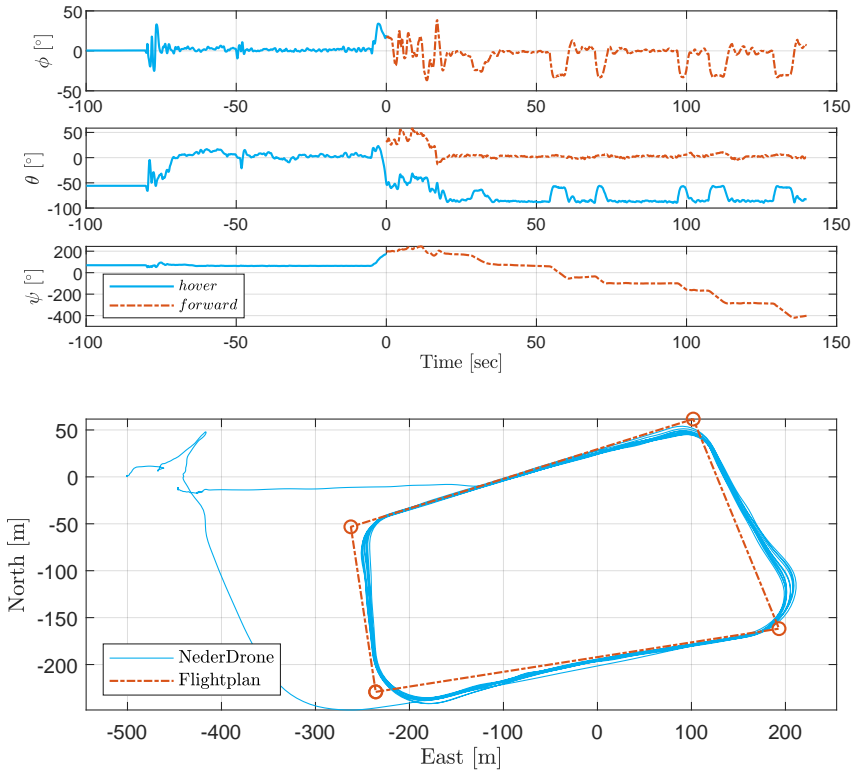
Figure 8.18: Test flight with take-off, hover, transition to forward and forward flight through a set of waypoints. The Euler angles in the plots swap from the hover frame to the forward frame upon transition. Onboard computations are performed in quaternions.

8

The onboard video of the pan-tilt HD camera protruding from the top of the Nederdrone was streamed via the 2.4GHz ISM-band HereLink datalink. A live video view of the Nederdrone following the ship is shown in Figure 8.19b. All data links and video systems were also charging from the hydrogen energy and remained fully charged during the entire flight.

After landing, the empty cylinder can be replaced with a new full cylinder in seconds, before taking off again. The presented test flight does not push endurance to its limits. There were at least 20 min worth of hydrogen and 15 min of battery left after landing. All systems were running at full power and the weather was rough with 5 Beaufort or 20 kn wind with moderate turbulence. This illustrates that the hybrid lift hybrid power UAV called Nederdrone can handle real-world operations and has considerable safety, performance, and energy margins.

8.7.3. Energy profile of the 3h38 flight

The hydrogen cylinder was filled with 285 bar remaining after settling at ambient temperature. During take-off and landing, lithium batteries provided the required
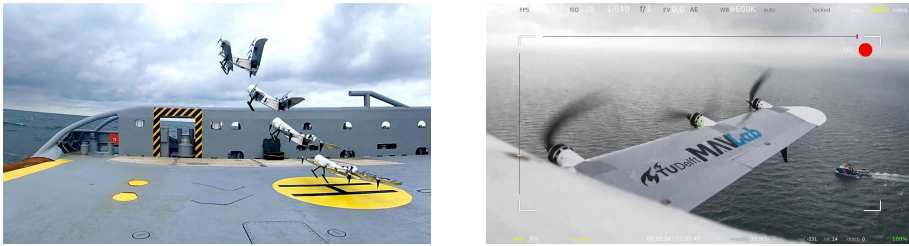
(a) Composite image from take-off from the moving vessel. (b) Live-view of the telemetry.

Figure 8.19: Hydrogen powered flight at sea departing from the coast-guard vessel the *Guardian*.
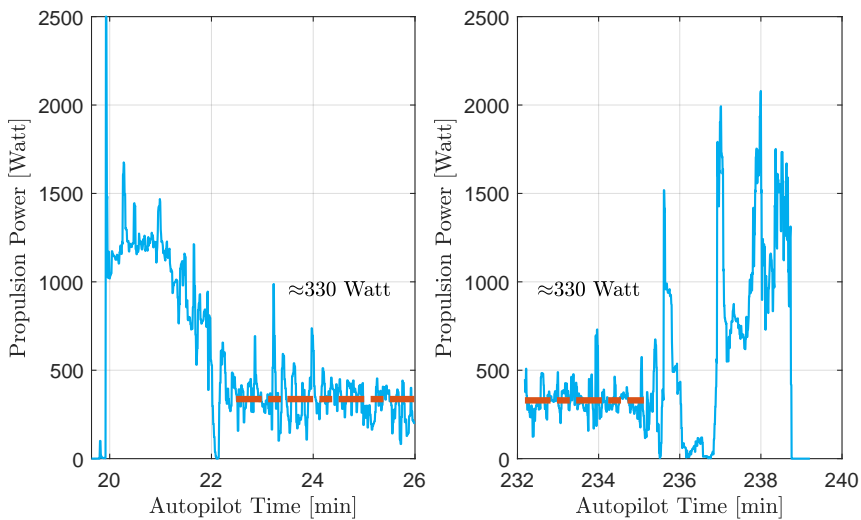
Figure 8.20: Flight power as reported by the ESC during the take-off and landing.

extra power while the fuel-cell was running at maximum power. Figure 8.20 shows the reported power used by the ESCs. This excludes the power used by the fuel-cell itself and its cooling, power losses in the long wires, power loss over the diodes, and power used by the payload and video link. The descent power becomes nearly zero at moments when the Nederdrone is gliding in forward flight with the propellers windmilling. The climbing power (from 20 to 21 min) is about 1250 W during the angled take-off with the wings not stalled and thus significantly helping in lift production. The hover power required in the last phase of the landing while fighting turbulence with the wing stalled (238 min) consumed nearly 1500 W with peaks of over 2000 W. This is much more than the raw fuel-cell system can handle but is supplied from the high current rated lithium hover batteries with ease. Figure 8.21 shows that the power delivered by the fuel-cell in those cases is about 800 W as by design.
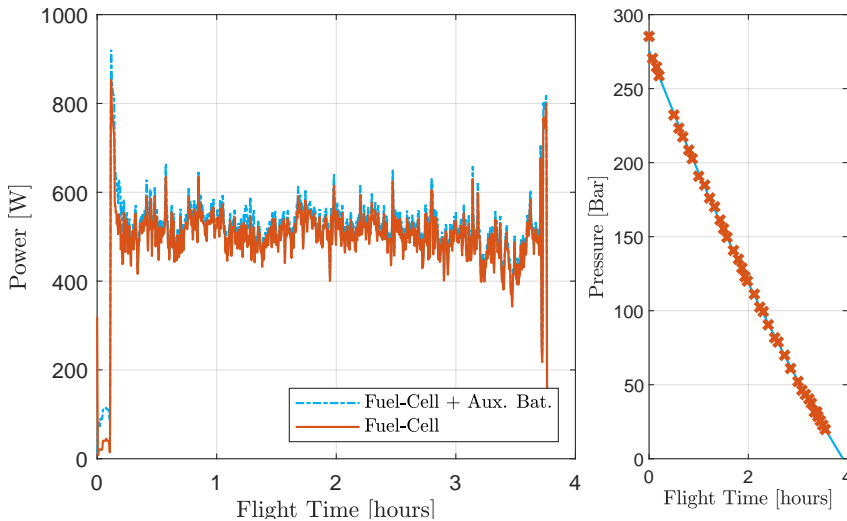
Figure 8.21: Power generation of the IE800 fuel-cell system depletion rate of the hydrogen pressure.

The Intelligent Energy fuel-cell system comes with an auxiliary battery, which powers the fuel-cell electronics before the fuel-cell becomes active and helps in powering the system when more than 800 W is used. Figure 8.21 shows that since most of the extra power is delivered by the much larger flight batteries, the auxiliary battery mainly serves to power the fuel-cell electronics. While a power control loop could help to choose which battery is used or charged at each point in time, it would also add a lot of weight. The current fully passive setup performs as expected without any heavy electronics.

Two minutes after the take-off, the Nederdrone transitions to forward flight and starts using much less power. The sum of the flight power, payload power, and fuel-cell systems (including cooling) power are an average of 550 W. After the take-off, the fuel-cell slowly re-charges the lithium batteries that were used during take-off. This means the hovering lithium batteries are fully charged before landing.

Figure 8.21 also shows the depletion of the hydrogen cylinder as measured by the onboard sensors. It follows the inverse of the density profile from (8.2). Having reached the desired 3 flight hours, the flight was stopped at a remaining pressure of 20 bar, although previous tests proved that the Nederdrone can continue to fly safely on battery power after complete depletion of the cylinder and shutdown of the fuel-cell.

8.8. Discussion

Hydrogen is seen as a highly promising future fuel for aviation thanks to its high energy density. But the limited power that can be generated by fuel-cells requires help from alternative power sources. Furthermore, the onboard storage of pure hydrogen requires a pressure cylinder with a weight that is easily one-quarter of the vehicle weight and has shape constraints.

To allow the successful application of hydrogen in UAVs, operational limitations have to be minimized and safety must be guaranteed, as the consequences of accidents with onboard pressure cylinders filled with hydrogen can be significant. This requires platforms with redundant flight modes, redundant energy, and redundant control. The shape of the UAV also plays a role in the protection of the cylinder. Light foam around the cylinder provides both an aerodynamic shape and a large crumple zone for low weight. By placing the sensitive high-pressure regulators backward in the middle of the vehicle, safety can be further increased. Last but not least, by having dual flight modes, an additional recovery mode is created in case of failure. When for instance aerodynamic actuators would fail, then the platform can return and land in hovering flight. If on the other hand, many motor controllers would fail, then the platform can still be flown in forward flight by exploiting the efficiency of its fixed wings. This combined versatility and safety are expected to play an important role in the development of hydrogen-fuelled flight.

8.9. Conclusions

A novel hydrogen UAV was presented called the Nederdrone[8]. It is a tail-sitter hybrid lift vehicle with tandem wings for forward flight, and 12 propellers for hover. The power comes from a PEM fuel-cell with hydrogen stored in a pressurized cylinder around which the UAV is optimized. The dual automotive CAN control bus, redundant power source, wiring, propulsion, dual flight modes, and model-less INDI control make the Nederdrone particularly resilient to failures. The versatility and flight endurance of the Nederdrone is shown with a 3h38 test flight at sea from a moving ship with 20 kt winds. The main advantages and disadvantages are summarized in Table 8.2.

8.10. Recommendations

Several aspects of the concept could be the subject of improvement. First of all, the presented flight time can be greatly extended by fitting larger amounts of hydrogen. The Nederdrone was built with a 350 bar cylinder and tested with 285 bar while 700 bar cylinders are available. This would require a new analysis of the safety aspects. Aerodynamically, airfoils with even smoother stall behavior but very low drag in forward flight should be developed to accommodate the specific needs of tail-sitter UAVs. Electrically, a lot of power is lost in the cooling of the fuel-cell which could be done passively thanks to the incoming air. To reduce the risk of overheating, this was not addressed in the present research as the temperature of

---

[8]http://www.nederdrone.nl/

	Advantage	**Disadvantage**
Propulsion	Re-use motors in forward and hover.	Reduced efficiency in hover.
Mechanical	Light: wings support the motors & props.	Transitioning 90° nose down.
Control	Redundant high authority control with excess power.	Need for high current batteries during hover.
Hybrid power	Passive parallel fuel-cell & batteries.	Power loss over diodes.
Redundancy	Redundant wiring, 12 props, 8 flaps.	Reduced propulsion efficiency.

Table 8.2: Overview of the main advantages and disadvantages of the Nederdrone concept

the fuel-cell could not be measured in real-time. The control of the Nederdrone is also the topic of future work. In hovering flight, the yaw axis of the Nederdrone is controlled using the torque of the propellers and the induced flow of the propellers over the aerodynamic surfaces. Both moments are very small compared to pitch and roll moments and this results in a lower performance of the yaw axis. Furthermore, the pitch angle of the Nederdrone should not be allowed to move higher than about 20°-30° nose up in hover. Since during hover the Nederdrone has a 90° higher pitch angle than during forward flight, pitching up even further will effectively place the fixed-wings in an inverted attitude (See Figure 8.9 rotated 90 degrees counterclockwise). While this is in itself not a problem, the flapping drag of the rotors while hovering backward bends the thrust vectors in the opposite direction than the direction of motion, which is such that it reduces the moment arm with respect to the center of gravity. In other words, since in hover, not all rotors are in the same plane, when translating in the positive X-direction (See Figure 8.9), the maximally achievable pitch moment of the rotors is increased while in the negative X-direction the maximally achievable pitch moment is decreased. In both cases, the forward flight stability of the wings causes a disturbing moment. While this can be solved by climbing or avoiding the situation altogether, further research is recommended. Finally, a lot of small improvements can still be made to the concept like retracting the landing gear in forward flight to reduce drag, reducing the small and underutilized auxiliary battery, and reducing the power loss over the diodes, which combined could result in additional improvements in performance and allow faster or longer operation in even tougher real-world conditions.

References

[1] C. De Wagter, B. Remes, R. Ruijsink, F. van Tienen, and E. van der Horst, *Design and testing of a vertical take-off and landing UAV optimized for carrying a hydrogen fuel cell with a pressure tank,* Unmanned Systems **8**, 279 (2020).

[2] C. De Wagter, B. D. W. Remes, E. Smeur, F. van Tienen, R. Ruijsink, K. van Hecke, and E. van der Horst, *The nederdrone: a hybrid lift, hybrid energy hydrogen uav,* International Journal of Hydrogen Energy **46**, 16003 (2021).

[3] G. Pajares, *Overview and current status of remote sensing applications based on unmanned aerial vehicles (UAVs),* Photogrammetric Engineering & Remote Sensing **81**, 281 (2015).

[4] T. Adão, J. Hruška, L. Pádua, J. Bessa, E. Peres, R. Morais, and J. Sousa, *Hyperspectral imaging: A review on UAV-based sensors, data processing and applications for agriculture and forestry,* Remote Sensing **9**, 1110 (2017).

[5] N. Yin, R. Liu, B. Zeng, and N. Liu, *A review: UAV-based remote sensing,* IOP Conference Series: Materials Science and Engineering **490**, 062014 (2019).

[6] H. Yao, R. Qin, and X. Chen, *Unmanned aerial vehicle for remote sensing applications—a review,* Remote Sensing **11**, 1443 (2019).

[7] M. N. Boukoberine, Z. Zhou, and M. Benbouzid, *A critical review on unmanned aerial vehicles power supply and energy management: Solutions, strategies, and prospects,* Applied Energy **255**, 113823 (2019).

[8] C. De Wagter, R. Ruijsink, E. Smeur, K. van Hecke, F. van Tienen, E. van der Horst, and B. Remes, *Design, control, and visual navigation of the delftacopter vtol tail-sitter uav,* Journal of Field Robotics **35**, 937 (2018).

[9] M. Hochstenbach, C. Notteboom, B. Theys, and J. De Schutter, *Design and Control of an Unmanned Aerial Vehicle for Autonomous Parcel Delivery with Transition from Vertical Take-off to Forward Flight -VertiKUL, a Quadcopter Tailsitter,* International Journal of Micro Air Vehicles **7**, 395 (2015).

[10] P. Hartmann, M. Schütt, and D. Moormann, *Control of departure and approach maneuvers of tiltwing VTOL aircraft,* in *AIAA Guidance, Navigation, and Control Conference* (American Institute of Aeronautics and Astronautics, 2017) pp. 1–18.

[11] A. S. Saeed, A. B. Younes, C. Cai, and G. Cai, *A survey of hybrid unmanned aerial vehicles,* Progress in Aerospace Sciences **98**, 91 (2018).

[12] S. B. Anderson, *Historical overview of V/STOL aircraft technology*, techreport 19810010574 (NASA Ames Reseach Center, Moffett Field, CA, United States, 1981).

[13] J. Escareño, A. Sanchez, O. Garcia, and R. Lozano, *Modeling and global control of the longitudinal dynamics of a coaxial convertible mini-UAV in hover mode,* Journal of Intelligent and Robotic Systems **54**, 261 (2008).

[14] M. Bronz, E. Smeur, and H. de Marina, *Development of A Fixed-Wing mini UAV with Transitioning Flight Capability,* in *35th AIAA Applied Aerodynamics Conference* (Denver, Colorado, 2017).

8

[15] E. J. Smeur, M. Bronz, and G. C. de Croon, *Incremental control and guidance of hybrid aircraft applied to a tailsitter unmanned air vehicle,* Journal of Guidance, Control, and Dynamics , 1 (2019).

[16] K. Wang, Y. Ke, and B. M. Chen, *Autonomous reconfigurable hybrid tail-sitter UAV u-lion,* Science China Information Sciences **60** (2017), 10.1007/s11432-016-9002-x.

[17] Y. Govdeli, S. M. B. Muzaffar, R. Raj, B. Elhadidi, and E. Kayacan, *Unsteady aerodynamic modeling and control of pusher and tilt-rotor quadplane configurations,* Aerospace Science and Technology **94**, 105421 (2019).

[18] G. R. Flores, J. Escareño, R. Lozano, and S. Salazar, *Quad-tilting rotor convertible MAV: Modeling and real-time hover flight control,* Journal of Intelligent & Robotic Systems **65**, 457 (2011).

[19] Z. Pan, L. An, and C. Wen, *Recent advances in fuel cells based propulsion systems for unmanned aerial vehicles,* Applied Energy **240**, 473 (2019).

[20] M. K. Furrutter and J. Meyer, *Small fuel cell powering an unmanned aerial vehicle,* in AFRICON 2009 (IEEE, 2009) pp. 1–6.

[21] T. Kim and S. Kwon, *Design and development of a fuel cell-powered small unmanned aircraft,* International Journal of Hydrogen Energy **37**, 615 (2012).

[22] N. Lapeña-Rey, J. Blanco, E. Ferreyra, J. Lemus, S. Pereira, and E. Serrot, *A fuel cell powered unmanned aerial vehicle for low altitude surveillance missions,* International Journal of Hydrogen Energy **42**, 6926 (2017).

[23] E. Özbek, G. Yalin, S. Ekici, and T. H. Karakoc, *Evaluation of design methodology, limitations, and iterations of a hydrogen fuelled hybrid fuel cell mini UAV,* Energy **213**, 118757 (2020).

[24] J. Banjong, A. Therdthianwong, S. Therdthianwong, S. Yongprapat, and N. Wongyao, *High performance alkaline-acid direct glycerol fuel cells for portable power supplies via electrode structure design,* International Journal of Hydrogen Energy **45**, 2244 (2020).

[25] T. Hordé, P. Achard, and R. Metkemeijer, *PEMFC application for aviation: Experimental and numerical study of sensitivity to altitude,* International Journal of Hydrogen Energy **37**, 10818 (2012).

[26] M. Pareta, S. R. Choudhury, B. Somaiah, J. Rangarajan, N. Matre, and J. Palande, *Methanol reformer integrated phosphoric acid fuel cell (PAFC) based compact plant for field deployment,* International Journal of Hydrogen Energy **36**, 14771 (2011).

[27] F. Yu, T. Han, Z. Wang, Y. Xie, Y. Wu, Y. Jin, N. Yang, J. Xiao, and S. Kawi, *Recent progress in direct carbon solid oxide fuel cell: Advanced anode catalysts, diversified carbon fuels, and heat management,* International Journal of Hydrogen Energy (2020), 10.1016/j.ijhydene.2020.10.259.

8

[28] S. Koomson and C.-G. Lee, *Lifetime expectancy of molten carbonate fuel cells: Part i. effect of temperature on the voltage and electrolyte reduction rates,* International Journal of Hydrogen Energy (2020), 10.1016/j.ijhydene.2020.07.218.

[29] X. Chen, T. Li, J. Shen, and Z. Hu, *From structures, packaging to application: A system-level review for micro direct methanol fuel cell,* Renewable and Sustainable Energy Reviews **80**, 669 (2017).

[30] T. Kim, *NaBH4 (sodium borohydride) hydrogen generator with a volume-exchange fuel tank for small unmanned aerial vehicles powered by a PEM (proton exchange membrane) fuel cell,* Energy **69**, 721 (2014).

[31] L. Schlapbach and A. Züttel, *Hydrogen-storage materials for mobile applications,* in *Materials for Sustainable Energy* (Co-Published with Macmillan Publishers Ltd, UK, 2010) pp. 265–270.

[32] Y. Luo, Y. Shi, and N. Cai, *Bridging a bi-directional connection between electricity and fuels in hybrid multienergy systems,* in *Hybrid Systems and Multienergy Networks for the Future Energy Internet* (Elsevier, 2021) pp. 41–84.

[33] J. Zhao, Y.-J. Sheng, Y.-L. Cai, Y.-L. Teng, L. Wang, C. Ping, M. Shen, and B.-X. Dong, *Efficiently generating COx-free hydrogen by mechanochemical reaction between alkali hydrides and carbon dioxide,* International Journal of Hydrogen Energy **44**, 18159 (2019).

[34] E. Troncoso, N. Lapeña-Rey, and O. Valero, *Off-grid test results of a solar-powered hydrogen refuelling station for fuel cell powered unmanned aerial vehicles,* International Journal of Hydrogen Energy **39**, 11267 (2014).

[35] D. Xu, H. Zhang, and W. Ye, *Hydrogen generation from hydrolysis of alkaline sodium borohydride solution using pt/c catalyst,* Catalysis Communications **8**, 1767 (2007).

[36] E. Keçeli and S. Özkar, *Ruthenium(III) acetylacetonate: A homogeneous catalyst in the hydrolysis of sodium borohydride,* Journal of Molecular Catalysis A: Chemical **286**, 87 (2008).

[37] J. Liao, Y. Feng, W. Lin, X. Su, S. Ji, L. Li, W. Zhang, B. G. Pollet, and H. Li, *CuO–NiO/co3o4 hybrid nanoplates as highly active catalyst for ammonia borane hydrolysis,* International Journal of Hydrogen Energy **45**, 8168 (2020).

[38] A. Gong and D. Verstraete, *Fuel cell propulsion in small fixed-wing unmanned aerial vehicles: Current status and research needs,* International Journal of Hydrogen Energy **42**, 21311 (2017).

[39] E. L. González, J. S. Cuesta, F. J. V. Fernandez, F. I. Llerena, M. A. R. Carlini, C. Bordons, E. Hernandez, and A. Elfes, *Experimental evaluation of a passive fuel cell/battery hybrid power system for an unmanned ground vehicle,* International Journal of Hydrogen Energy **44**, 12772 (2019).

8

[40] C. Herwerth, C. Chiang, A. Ko, S. Matsuyama, S. B. Choi, M. Mirmirani, D. Gamble, R. Paul, V. Sanchez, A. Arena, A. Koschany, G. Gu, T. Wankewycz, and P. Jin, *Development of a small long endurance hybrid PEM fuel cell powered UAV,* in *SAE Technical Paper Series* (SAE International, 2007) pp. 1–8.

[41] T. Bradley, B. Moffitt, D. Parekh, and D. Mavris, *Flight test results for a fuel cell unmanned aerial vehicle,* in *45th AIAA Aerospace Sciences Meeting and Exhibit* (American Institute of Aeronautics and Astronautics, 2007) pp. 1–8.

[42] M. Gadalla and S. Zafar, *Analysis of a hydrogen fuel cell-pv power system for small uav,* International Journal of Hydrogen Energy **41**, 6422 (2016).

[43] N. Gavrilovic, D. Vincekovic, and J.-M. Moschetta, *A long range fuel cell/soaring uav system for crossing the atlantic ocean,* in 11th *International Micro Air Vehicle Competition and Conference*, edited by P. Campoy (IMAV, Madrid, Spain, 2019) pp. 121–131, iMAV2019-16.

[44] M. Rottmayer and R. Miller, *Fuel cell hybrid power system development for extended endurance SUAS applications,* in *AIAA Centennial of Naval Aviation Forum "100 Years of Achievement and Progress"* (American Institute of Aeronautics and Astronautics, 2011) pp. 1–3.

[45] I. E. L. Stephens, J. Rossmeisl, and I. Chorkendorff, *Toward sustainable fuel cells,* Science **354**, 1378 (2016).

[46] B. Wang, D. Zhao, W. Li, Z. Wang, Y. Huang, Y. You, and S. Becker, *Current technologies and challenges of applying fuel cell hybrid propulsion systems in unmanned aerial vehicles,* Progress in Aerospace Sciences **116**, 100620 (2020).

[47] N. Kaya, Önder Turan, T. H. Karakoç, and A. Midilli, *Parametric study of exergetic sustainability performances of a high altitude long endurance unmanned air vehicle using hydrogen fuel,* International Journal of Hydrogen Energy **41**, 8323 (2016).

[48] Z. U. Bayrak, U. Kaya, and E. Oksuztepe, *Investigation of PEMFC performance for cruising hybrid powered fixed-wing electric UAV in different temperatures,* International Journal of Hydrogen Energy **45**, 7036 (2020).

[49] J. Kim, D.-M. Kim, S.-Y. Kim, S. W. Nam, and T. Kim, *Humidification of polymer electrolyte membrane fuel cell using short circuit control for unmanned aerial vehicle applications,* International Journal of Hydrogen Energy **39**, 7925 (2014).

[50] A. Züttel, *Hydrogen storage methods,* Naturwissenschaften **91**, 157 (2004).

[51] K. Kim, T. Kim, K. Lee, and S. Kwon, *Fuel cell system with sodium borohydride as hydrogen source for unmanned aerial vehicles,* Journal of Power Sources **196**, 9069 (2011).

8

[52] A. Boran, S. Erkan, and I. Eroglu, *Hydrogen generation from solid state NaBH4 by using FeCl3 catalyst for portable proton exchange membrane fuel cell applications,* International Journal of Hydrogen Energy **44**, 18915 (2019).

[53] Y. Lee, E.-T. Park, J. Jeong, H. Shi, J. Kim, B.-S. Kang, and W. Song, *Weight optimization of hydrogen storage vessels for quadcopter UAV using genetic algorithm,* International Journal of Hydrogen Energy (2020), 10.1016/j.ijhydene.2020.09.014.

[54] U. Nour, S. Awad, S. Yusup, and S. Sufian, *Technical evaluation of current hydrogen storage technologies for vehicles,* Journal of Applied Sciences **10**, 1200 (2010).

[55] M. Molnarne and V. Schroeder, *Hazardous properties of hydrogen and hydrogen containing fuel gases,* Process Safety and Environmental Protection **130**, 1 (2019).

[56] M. Mashayekhi, *Prediction of all-steel cng cylinders fracture in impact by using damage mechanics approach,* Scientia Iranica **21**, 609 (2014).

[57] M. Bertin, D. Halm, B. Magneville, J. Renard, P. Saffré, and S. Villalonga, *One year osirhys iv project synthesis: mechanical behaviour of 700 bar type iv high pressure vessel code qualification.* in *HAL-00801409* (2012) pp. 1–8.

[58] H. Mitsuishi, K. Oshino, and S. Watanabe, *Dynamic crush test on hydrogen pressurized cylinder,* Disp **2000**, 1 (2005).

[59] V. Molkov and S. Kashkarov, *Blast wave from a high-pressure gas tank rupture in a fire: Stand-alone and under-vehicle hydrogen tanks,* International Journal of Hydrogen Energy **40**, 12581 (2015).

[60] C. De Wagter, B. Remes, E. Smeur, F. van Tienen, R. Ruijsink, K. van Hecke, and E. van der Horst, *The nederdrone: A hybrid lift, hybrid energy hydrogen uav,* arXiv , 1 (2020), 2011.03991 .

[61] L. V. Schmidt, *Introduction to Aircraft Flight Dynamics* (American Institute of Aeronautics and Astronautics, 1998).

[62] L. Vermeer, *A review of wind turbine wake research at TU delft,* in *20th 2001 ASME Wind Energy Symposium* (American Institute of Aeronautics and Astronautics, 2001) pp. 1–11.

[63] F. Aymen, *Internal fuzzy hybrid charger system for a hybrid electrical vehicle,* Journal of Energy Resources Technology **140** (2017), 10.1115/1.4037352.

[64] J. M. Martinez-Heredia, F. Colodro, J. L. Mora-Jimenez, A. Remujo, J. Soriano, and S. Esteban, *Development of GaN technology-based DC/DC converter for hybrid UAV,* IEEE Access **8**, 88014 (2020).

[65] J. Sparks, *Low cost technologies for aerospace applications,* Microprocessors and Microsystems **20**, 449 (1997).

8

[66] N. Ravi and M. El-Sharkawy, *Integration of UAVs with real time operating systems using UAVCAN,* in *2019 IEEE 10th Annual Ubiquitous Computing, Electronics & Mobile Communication Conference (UEMCON)* (IEEE, 2019) pp. 0600–0605.

[67] E. J. J. Smeur, Q. P. Chu, and G. C. H. E. de Croon, *Adaptive Incremental Nonlinear Dynamic Inversion for Attitude Control of Micro Aerial Vehicles,* Journal of Guidance, Control, and Dynamics **39**, 450 (2016).

[68] E. Smeur, G. de Croon, and Q. Chu, *Cascaded incremental nonlinear dynamic inversion for mav disturbance rejection,* Control Engineering Practice **73**, 79 (2018).

[69] E. J. J. Smeur, de G.C.H.E de Croon, and Q. Chu, *Gust disturbance alleviation with incremental nonlinear dynamic inversion,* in *International Conference on Intelligent Robots and Systems (IROS)*, IEEE/RSJ (IEEE, Daejeon, South Korea, 2016) pp. 5626–5631.

[70] A. Preumont, *Vibration Control of Active Structures* (Springer International Publishing, 2018).

[71] G. Goh, S. Agarwala, G. Goh, V. Dikshit, S. Sing, and W. Yeong, *Additive manufacturing in unmanned aerial vehicles (UAVs): Challenges and potential,* Aerospace Science and Technology **63**, 140 (2017).

[72] P. Brisset, A. Drouin, M. Gorraz, P.-S. Huard, and J. Tyler, *The paparazzi solution,* in *MAV 2006, 2nd US-European Competition and Workshop on Micro Air Vehicles* (EMAV, Sandestin, United States, 2006) pp. 1–15.

[73] B. Gati, *Open source autopilot for academic research-the paparazzi system,* in *American Control Conference (ACC), 2013* (IEEE, Washington, DC, 2013) pp. 1478–1481.

8

9

The AI behind the winning entry to the 2019 AIRR Competition

One of the great challenges in this world is knowing enough to think you're right but not enough to know you're wrong.

Neil deGrasse Tyson

A major challenge in robotics is formed by autonomous drone racing as it signifies tackling fundamental problems in AI under extreme resource restrictions. Here we show how an AI-based approach surpassed the fastest state-of-the-art vision-based indoor navigation in the first AI Robotic Racing (AIRR) World Championship season 2019. The proposed human-inspired approach combines computationally light but race-speed resistant gate detection using a deep neural segmentation network and active vision with model-based predictions, robust state estimation, and risk-based control. We present an in-depth analysis of the performance of each component using competition data and simulations. The work addresses the fundamental problem of how AI can best be designed so that flying robots need minimal time and data to reach robust and highly agile flight. It represents a promising direction to close the gap with human drone pilots and bring AI to the real world.

9.1. Introduction

Artificial Intelligence has seen tremendous progress over the last decade, especially due to the advent of deep neural networks [3, 4]. The major milestones in the history of AI have always been associated with competitions against human experts. These competitions clearly show the increasing complexity in the tasks in which AI can extend beyond human performance. In 1997, IBM's Deep Blue showed the power of search methods combined with expert systems [5] by beating the world champion in the game of chess, Garry Kasparov. Chess is a fully observable, turn-based game, with $\approx 10^{123}$ possible game states. After chess, the AI community started to aim for the game of Go, which has a much larger branching factor that also results in a much higher number of $\approx 10^{360}$ possible game states, rendering most search methods ineffective. In 2017, the Master version of Google Deepmind's AlphaGo beat Ke Jie, the top-ranked Go player at the time. AlphaGo used an elegant combination of Monte Carlo tree search and deep neural networks for evaluating board positions [6]. In 2019, Google Deepmind's AlphaStar reached a GrandMaster status in the real-time strategy game StarCraft II. This game represents yet a higher complexity, as it involves real-time instead of turn-based play, partial observability, and a large and varied action space.

Robotics will form a new frontier in AI research since the associated problems are even more complex [7]. Typical robotics problems are high-dimensional, continuous, and only partially observable. Moreover, and most importantly, robots have to operate in the real world, of which many relevant aspects remain hard to model or simulate. Sample-intensive learning methods may apply to simplified robot models in simulation, allowing for faster than real-time learning, but transferring them to an actual robotic system typically leads to a reality gap [8–10] that substantially reduces performance. One part of the reality gap is the difference in sensory input like visual appearance and sensor noise. The other part of this reality gap is the specifics of a robot itself, concerning both its "body" (energy source, structure, sensors, actuators) and "brain" (processing power, memory). For example, there may be unmodeled aerodynamic effects or different timings in the perception-action cycle of the actual robotic hardware.

One extreme challenge at the moment for AI in robotics is formed by autonomous drone racing. Similar to human drone races, the goal for the drones is to finish a pre-determined racing track in as short a time as possible. The drones have to race by using only their onboard resources, such as onboard sensors and processing, which are heavily restricted in terms of Size, Weight, and Power (SWaP) [11]. To be successful, the drones will have to fly through complex tracks at very high speeds (human racers reach speeds of up to 190 km/h). This means that they need a fast perception-action cycle on lightweight hardware, which additionally should be robust, as the margin for error is small.

The research on autonomous drone racing finds its roots in seminal work on agile and aggressive flight [12–14]. The focus of many of these early studies was mostly on high-performance control, outsourcing sensing, and state estimation to external motion tracking systems and associated central computers. Later studies focused on also getting the sensing and state estimation onboard, allowing the drones to

perform quick maneuvers through gaps [15, 16]. A real drone race additionally requires the drone to detect racing gates in more complex spaces, with multiple gates and potential distractors in view, while not only passing one gate, but flying a full trajectory in sequence, dealing with unforeseen deviations on the way. The research on drone racing received a boost by the first-ever Autonomous Drone Racing (ADR) competition, organized in conjunction with the IROS robotics conference in 2016, in Daejeon, South Korea [17]. This competition let the participants free in their choice of platform and only required that all sensing and processing took place onboard. The first competition showed the difficulty of the problem, with the winner reaching 10 gates at an average speed of 0.6 m/s. This is in stark contrast to the impressive racing performance reached a year later by Morrell *et al.* [18], whose drone only lost by a few seconds from an expert human pilot on their track. In-competition flight speeds remained inferior to out-of-competition flight speeds also over the ensuing years, with IROS drone race speeds of the winner reaching 2.5 m/s in 2018 [19]. The reason for this mostly lies in the real-world aspects of the competitions. They take place in environments previously unknown by the teams, with no opportunity for benign, solution-specific changes, and little time for adapting the developed solution to the environment in situ. Moreover, competitions often pose a more challenging environment, with gates located slightly differently than on the pre-communicated maps or even moving during the race, unforeseen lighting effects optimized for spectators rather than for drones, and large crowds of moving people around the flight arena.
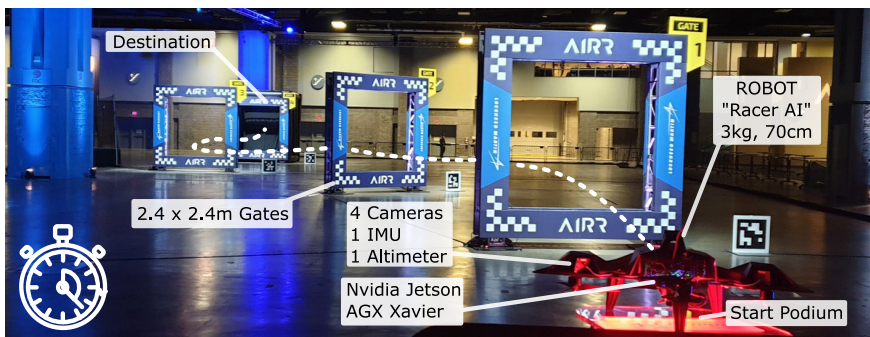
Figure 9.1: Setup of the Washington Seasons race.

In this chapter, the winning approach to the 2019 Artificial Intelligence Robotic Racing (AIRR) competition is presented (see Figure 9.1). This competition which is also refered to as *AlphaPilot*, was organized by Lockheed Martin (LM) and the Drone Racing League (DRL) in 2019 and had a grand prize for the best AI of 1M$. The AIRR competition strives to support the development of AI for racing drones that will be able to surpass human drone racing pilots. It is completely different from the previous autonomous drone racing competitions in many aspects. For example, the competition did not take place on a single day at a conference but had two phases: a qualifier phase and a competition phase. In the qualifier phase, 424 teams registered worldwide and had to qualify by performing a computer vision task, racing

in simulation, and describing their proposed approach and team composition. The competition phase was also unique as it was organized as a complete season with three seasonal races and a championship race. The races themselves were organized by DRL as e-sports events, also aiming for the amusement of the audience, adding specific requirements on the teams and robots. Moreover, the organization provided all teams with the same type of racing drone, developed by the organizers. These drones were equipped with four high-resolution, wide field-of-view cameras, and an NVIDIA AGX Xavier board to run the embedded AI (see Figure 9.1). Hence, the robotic hardware was the same for all teams, making the competition only about the difference between the AI software. Moreover, the teams had very little direct access to the racing drone hardware, making it very hard to get acquainted with the hardware, perform calibrations, and identify potential reality gaps. The amount of flight testing was low and happened in different conditions than the races in terms of light, room size, and even air density. Finally, during the races, the AI code was uploaded to refurbished drones that had never flown this particular code before without the possibility to improve in between the runs. Consequently, the AI developed for the competition had to be very data efficient and robust.

The goal was to mainly develop AI solutions on the provided DRL simulator, which figured a substantial reality gap in terms of drone dynamics and sampling characteristics of especially the camera. The simulator did have a hardware-in-the-loop setup for the processing, i.e., it communicated with the same NVIDIA AGX Xavier board and allowed teams to accurately test the computational effort of the developed algorithms.

9.2. Human-inspired, gate-based approach

In our approach to developing an AI for the AIRR competition, we used the characteristics and restrictions of the competition as a point of departure (Figure 9.1, Figure 9.2). First and foremost, we desired to fly as fast as possible, ideally close to the physical limits of the drone. This implied that we did not use perception methods that would restrict the drone's maximum speed. Importantly, it meant the exclusion of state-of-the-art methods for feature-based Visual-Inertial Odometry (VIO) cf. e.g. Delmerico and Scaramuzza [20], since the blurry images that occur at higher speeds lead to more difficulties in finding and tracking features. The reliance on this type of VIO was one of the main reasons that the runner-up team limited their velocity to 8 m/s [21]. Moreover, current accurate VIO methods have the disadvantage that they are computationally intensive. For similar reasons, we did not employ feature-based Simultaneous Localization and Mapping (SLAM) methods, e.g. Mur-Artal *et al.* [22] as used by the winning team in the IROS 2017 competition [23]. Additionally SLAM methods have difficulties handling changes in the map, like the foreseen gate displacements.

Instead, we drew inspiration from human pilots who focus greatly on the gates, while combining their observations with knowledge of the drone's responses to control inputs and an approximate map of the track (see Figure 9.2). Hence, we developed an accurate, robust, and computationally efficient monocular gate detection method. We aimed to process images at frame-rate at the fastest speeds the drone
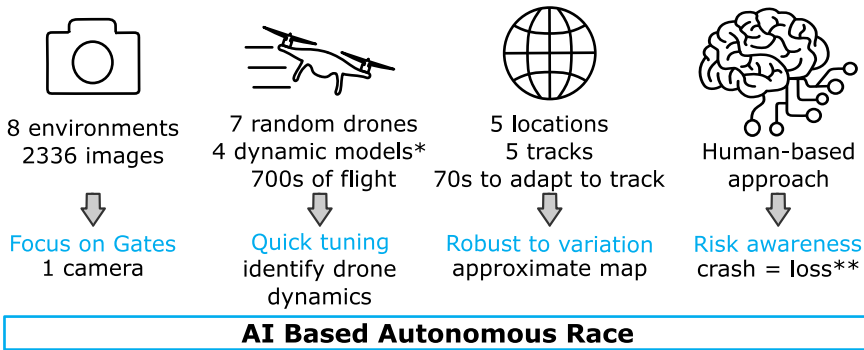
Figure 9.2: The human-inspired approach to drone racing using single-camera position estimation, dynamics prediction, a rough model of the track, and risk-aware control followed from the training data overview. *) 2 simulators, 5000 ft-dynamics, sea-level-dynamics **) loss of log files, test opportunities, or races

could achieve. Whereas previous competitions contained gates of a uniform, unique color [17, 23], the AIRR competition featured more complex gates, precluding hand-designed detection methods as in Li *et al.* [24, 25]. Relative localization can also not be done with standard rectangle-based detectors such as Single Shot MultiBox Detector (SSD) [26, 27] since the bounding boxes generated by such methods by themselves do not allow for an accurate determination of the drone's relative pose. Furthermore, we did not choose a deep neural network that immediately maps images to relative pose, as in Kaufmann *et al.* [19], Cocoma-Ortega and Martínez-Carranza [28]. Such networks experience difficulties when multiple gates are in sight and are more difficult to analyze and fix.

We developed a novel gate segmentation deep neural network called "GateNet" to create a fast vision pipeline that is minimally sensitive to the various known perturbations at high velocities. This includes the increasing levels of motion blur, rolling shutter deformation, the possible absence of texture in large parts of the scene due to the lack of features in parts of the man-made environment. The Deep Neural Network (DNN) also was used to overcome over-exposure as teams could control neither the exposure settings of the camera nor the light conditions. The vision pipeline also had to deal with the presence of moving unknown entities, the absence of precise frame timing information, and unknown shutter-times.

Subsequently finding gate corners was done with very efficient active perception [24]. Especially on flying robots where every gram matters, active vision is highly relevant [29–31] and we show it can be part of successful engineering designs. Pose estimates finally can then be computed using Perspective-n-Point (PnP) combined with the racecourse map.

Further inspired by human First Person View (FPV) pilots' ability to predict drone motion, we enhanced the drone's state estimates with model-based predictions from a dynamic model fitted on flight data. Merging the visual measurements with the predictions is then done with a Random Sample Consensus (RANSAC) based Moving Horizon Estimator (MHE) from previous work [25] but extended to better estimate

the drone's yaw angle during the race.

Concerning control, we designed a strategy that would permit high speeds but would allow flying very early on and would have short intuitive tuning cycles, given the little available flight time. As a result, promising methods such as deep reinforcement learning [32] or imitation learning [33] were ruled out. The short timeline and little flight time would not allow for a thorough investigation of the reality gap between the drone and the simulator with methods like abstraction [10, 34]. Even online adaptation [35] would yield limited benefits in a race where every drone only flew once, measurements could be very noisy and the time to the first gate is a mere 2 seconds. Moreover, the long downtimes, loss of log files (stored in RAM) and failed competition runs in case of a crash, made risk management a crucial part of the control development. Finally, while perception-aware trajectory generation [36] can optimize speed and perception, it does not take into account that collision risks depend on relative position to the gate.

The control is therefore designed from a gate-centered perspective in which risks and constraints but also position uncertainty vary depending on the distance to the gate. The controller makes use of classical control theory but was gradually augmented to fly increasingly close to the platform limits. This allowed us to start flying early in the process and gather crucial log files to steadily investigate drone limitations while minimizing risks.
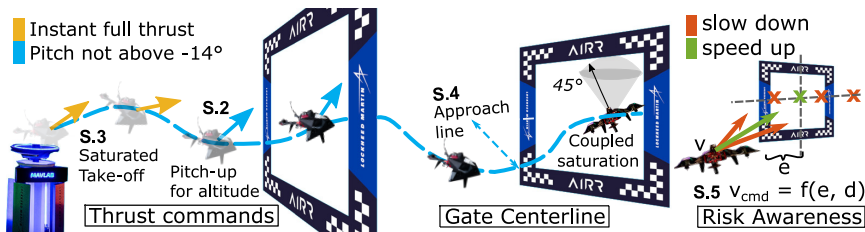
Figure 9.3: Illustration of the various controller modifications **S.2**–**S.5**.

On top of the initial scheme, we implemented an open-loop full-throttle take-off called "Boost" to overcome sensor boot-time delays (see Figure 9.3). We adopted a pitch-for-altitude controller to maintain altitude when thrust saturated and an offline optimized gate-approach-line strategy. Finally, we developed a human-inspired risk-aware strategy that speeds the robot up substantially when far from obstacles or when it is aligned with the next gate but slows down when uncertain or misaligned. By reaching various hardware limitations we expect it to be not very far of the performance of optimal control methods that employ multiple simplifications (like minimizing snap [14] instead of time) or have short time horizons to allow real-time computation onboard of a drone [37]. This was confirmed in the online qualification where our approach was only slightly slower than the winning optimal control approaches. *Whereas both in computer vision and robotics a lot of research effort is invested in increasing the accuracy of methods, we put computational efficiency at the core of our approach.* The reason for this is that control performance is not only determined by accuracy but also by the control delay, two factors which are most

often on a trade-off with each other. Moreover, not saturating processing power allowed us to have additional threads logging all data (images, states, measurements, etc.). This logged data was extremely important to estimate the drone's model and fusion parameters and for retraining and improving the perception pipeline.
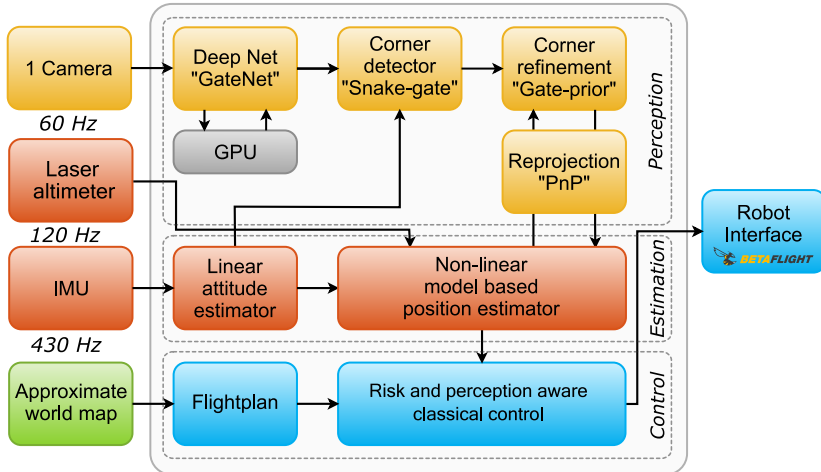

Figure 9.4: System schematic of the approach.

The full scheme is shown in Figure 9.4, and in the next section, we give an in-depth explanation of the implementation used in the competition and our approach.

9.3. Implementation

9.3.1. Drone specifications

All participating teams in the 2019 AIRR competition operated the same race drone type called "Racer AI" (see Figure 9.1). This plus-configuration quad-copter was approximately 70 cm in diameter, weighed around 3 kg, and had a thrust-to-weight ratio of about 1.4. It was equipped with two sets of forward-facing stereo camera pairs which looked sideways with an angle of $\pm 30°$ and up with an angle of 15° (see Figure 9.8). The cameras were the global-shutter, color Sony IMX 264 sensor, which provided 1200×720 resolution images at a rate of 60 Hz. The wide-field-of-view lens had a focal length of ± 590 pixels. Besides cameras, the Racer AI had a Bosch BMI088 IMU, with a measurement range of ± 24 g and ± 34.5 rad/s (with a resolution of 7×10^{-4} g and 1×10^{-3} rad/s) provided at an update rate of 430 Hz; and a downward-facing laser rangefinder Garmin LIDAR-Lite v3 with a measurement range up to 40 m (resolution of 0.01 m) and update rate of 120 Hz. As the embedded computer, the Racer AI was equipped with an NVIDIA Jetson AGX Xavier, containing a GPU with 512 CUDA cores and an 8-core ARM Central Processing Unit (CPU). It ran Linux with the PREEMPT RT kernel patch. Lastly, the Racer AI had a BetaFlight low-level autopilot controlling the angular velocities of the drone and accepting commands at a rate of 50 Hz.

9

9.3.2. Perception

The perception modules were executed sequentially in a dedicated thread, while a separate thread did the logging of images. We only used one out of the four cameras, as this setup matches the challenge that human pilots have to face. Although monocular vision is more challenging in terms of depth perception, it entails less computational load and calibration requirements. Moreover, it allows for lighter and hereby faster drones to be created in the future. Since none of the cameras faced forward, we flew in the direction of the optical axis of the selected camera. The original 1200×720 images provided by the camera were first centrally cropped to 720×720 to remove parts of the own robot that were in sight, and then downsized to 360×360 using OpenCV's bilinear interpolation function. No radial lens undistortion was performed on the images, but instead, the lens distortion was corrected for in the pose estimation. The correction of only a few corners through reverse lens parameters saves a lot of CPU load when compared to correcting all pixels.
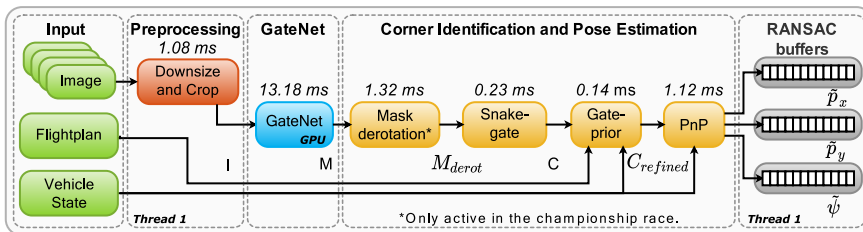

Figure 9.5: Overview of the perception pipeline and execution time of each of the submodules on the Jetson AGX Xavier. RANSAC was running on a separate CPU thread while the remaining vision pipeline was running on a separate thread. The DNN was executed on the GPU.

GateNet: Gate detection by semantic segmentation

In the first stage of our perception pipeline, GateNet was used to transform each resized input image $\mathbf{I}$ into a binary mask $\mathbf{M}$ that segments all visible gates regardless of their distance to the camera. GateNet is a fully convolutional deep neural network architecture that consists of a 4-level U-Net [38] with [64, 128, 256, 256] convolutional filters of size 3×3 and (elementwise-sum) skip connections. All layers use ReLU activation functions except the final prediction layer, which uses a sigmoid to keep $\mathbf{M}$ in the range [0, 1]. GateNet was trained in a supervised manner through a weighted combination of the binary cross-entropy and soft-Dice loss functions on a dataset eventually consisting of 2336 images recorded in 8 distinct environments (see Figure 9.7). The ground-truth mask for each sample in the training dataset was manually annotated. We augmented the training data through random affine transformations and variations in the HSV color space and artificial motion blur. The blur consists of the convolution of a squared averaging filter of random size between 5 and 15 pixels and random orientation. For the deployment on NVIDIA's Jetson AGX Xavier, we ported the network to TensorRT 5.0.2.6 with a batch size of 1 and full precision FP32 mode. The network contains 1723713 trainable parameters.

We deployed a different GateNet version in each competition race, with the only
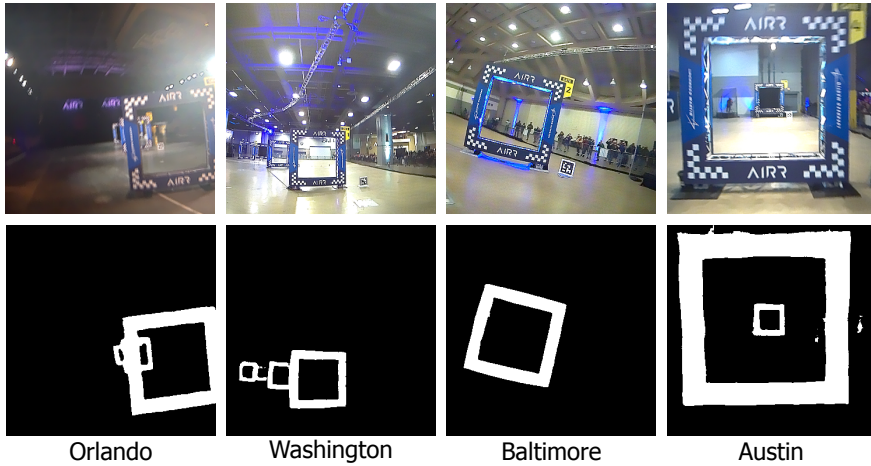
| Orlando | Washington | Baltimore | Austin |

Figure 9.6: Qualitative results of the generated segmentation masks by the final GateNet model from onboard images of each of the events.

differences being the size of the training dataset and the data augmentation mechanisms. Networks were always trained from scratch when changing the augmentation mechanisms. The otherwise fine-tuning previous models when expanding datasets. Before new races, we quickly fine-tuned the models to deployment environments with training data from the test sessions through incremental training after adding hand-labeled training data from typically roughly 50 manually selected difficult images.

Snake-gate: Active vision for corner identification

To then retrieve the inner and outer corners of only the next gate, even when multiple gates were in sight, we employed a variation of the lightweight, active-vision algorithm [31] known as snake-gate and first presented in Li *et al.* [24]. This two-stage, iterative sampling method reports the desired gate corners in a fixed order. The first stage starts at the intersection of the vertical and horizontal histograms of $\mathbf{M}$. The histograms represent the number of white pixels per column or row and the maxima in the histogram point to the pixel with a high probability of belonging to the closest (largest) gate. From that point, it starts sampling white pixels in a fixed direction in the image space (i.e., top-left, top-right, bottom-right, or bottom-left) until the corresponding outer corner is found. Thereafter, the sampling direction changes until all corners have been identified. A pixel is considered to be a corner if the sampling method cannot progress in the specified direction. Once the outer contour was identified, we used the centroid of this set of corners as the starting point to identify the inner corners of the gate by sampling black pixels. To overcome incorrect corner association at bank angles greater than $|45|°$, the mask $\mathbf{M}$ was first de-rotated using the drone's estimated roll angle around the optical axis.

Snake-gate requires (i) the mask of a gate to be continuous, and (ii) no gate overlap in the image space. The first requirement was normally met thanks to our
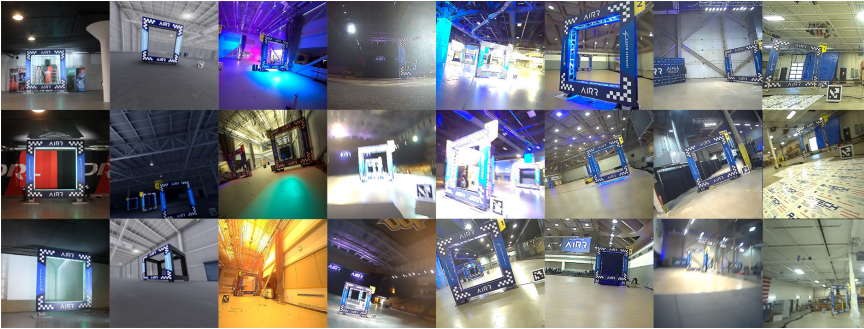
Figure 9.7: Overview of training images: from left to right per column: qualification data, simulator, workshop, Orlando, Washington, Baltimore, Austin and the testing area in Littleton.

robust and accurate GateNet model (see Figure 9.6). However, most of the AIRR tracks had gates placed in front of each other, violating the second requirement. To cope with this, we developed gate-prior.

Gate-prior: Sanity check on the identified corner locations

Snake-gate does not provide any form of confidence metric regarding the identified corners. Therefore we developed a sanity check. The expected 3D location of the next gate based on the internal flight plan was projected into the image space, and is called "gate-prior". We then compared the sides and angles of both inner and outer contours of this projection to those of the identified gate and only accepted the validity of a corner if the error of the associated sides and angle was below 25 %. Rejected corners of a contour with at least two valid corners were corrected using the shape of the gate-prior (see Figure 9.11). This actively reduced the number of outliers and it improved the robustness to challenging scenarios that could lead to discontinuous masks (e.g., High Dynamic Range (HDR) scenes, fast motion, partial gate in the image) and gate overlap (see Figure 9.11). If no valid corners were found for two full seconds, a recovery mechanism would override "gate-prior" and accept any gate corners given by "snake-gate".

Localization via perspective-n-point

The size, approximate location, and orientation of the AIRR gates were known in all races. The estimation of the drone's position and orientation was found by solving the PnP problem, using the identified corner locations in the image space and their corresponding 3D locations (maximum 8 corners). As in Li *et al.* [24, 25], instead of relying on pure vision-only PnP, we combined it with the onboard attitude estimate of the drone to retrieve the camera's 3D location, as this was shown to be more robust in drone racing conditions. We used the OpenCV library to solve the PnP problem, or more specifically: an iterative method based on Levenberg-Marquardt optimization, which minimizes the reprojection error and requires at least three point-correspondences.
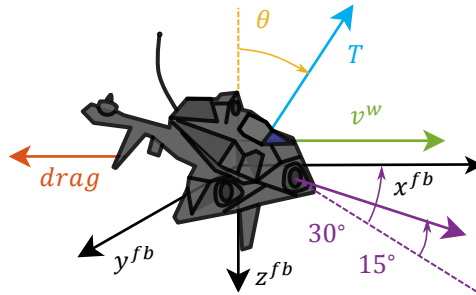
9.3.3. State estimation

Figure 9.8: Axis definition of the drag-based model with the camera viewing angle and its 30° degree offset in the x-y plane and 15° up.

Attitude estimation was performed using a complementary filter fed with gyroscope and accelerometer data. Position and velocity estimates were propagated using a drag and thrust model in the "flat-body" frame $^{fb}R_W$ shown in Figure 9.8, which is a local tangent plane rotated by the yaw ψ of the drone. The predicted drag specific forces in the flat-body frame (a_x^{fb}, a_y^{fb}) were modeled as:

$$
\begin{bmatrix} a_x^{fb} \\ a_y^{fb} \end{bmatrix} = \begin{bmatrix} \hat{d}_x & 0 \\ 0 & \hat{d}_y \end{bmatrix} \underbrace{\begin{bmatrix} c_\psi & s_\psi \\ -s_\psi & c_\psi \end{bmatrix}}_{^{fb}R_W} \begin{bmatrix} v_x^W \\ v_y^W \end{bmatrix}
\tag{9.1}
$$

where c_ψ and s_ψ present the cosine and sine of the yaw angle, (v_x^W, v_y^W) the velocities in the world frame and the linear drag parameters $\hat{d}_x$ and $\hat{d}_y$ were found by fitting the integrated path to best match the know gate locations using flight logs. To reduce the drift of drag-model predictions in the world frame a^W, an additional first-order linear filter called "alpha" fused the drag specific force model with accelerometer measurements (subscript m). The resulting prediction model is:

$$
\mathbf{a}^W = \alpha \cdot {}^W R_{fb} \begin{bmatrix} a_x^{fb} \\ a_y^{fb} \\ 0 \end{bmatrix} + (1-\alpha) {}^W R_B \begin{bmatrix} a_x^B \\ a_y^B \\ 0 \end{bmatrix}_m + \begin{bmatrix} 0 \\ 0 \\ g \end{bmatrix} + {}^W R_B \begin{bmatrix} 0 \\ 0 \\ a_z^B \end{bmatrix}_m
\tag{9.2}
$$

where α determines the ratio between predictions based on drag model or accelerometers, $^W R_B$ is the rotation from body-to-world, g is the local gravitational acceleration and $\mathbf{a}_{x,y,z}^B$ are the accelerometer measurements. A value of $\alpha = 85\%$ was found to yield the best predictions. The predicted velocity v^w and position p^w in the world frame were obtained through integration: $\mathbf{v}^W = \int \mathbf{a}^W$ and $\mathbf{p}^W = \int \mathbf{v}^W$.

For the altitude, a Kalman filter merged the low-pass filtered (6Hz cutoff) vertical accelerations and the low-pass filtered (50Hz cutoff) attitude-corrected downward-facing laser range measurements.

Position corrections in the horizontal plane were performed by merging the PnP estimates in world coordinates from the perception pipeline with the predicted path (see Figure 9.9). As vision estimates occasionally still contained large errors, a

Moving Horizon Estimator (MHE) based on RANSAC was used. It is directly adopted from Li *et al.* [25], but besides position and velocity corrections, yaw corrections were also made to account for initial heading alignment errors and yaw integration drift. The corrections were done by running the MHE filter independently on each axis (p_x, p_y, ψ). Separate buffers with a maximum of 180 samples hold information about PnP estimates and delay-compensated inertial estimates.
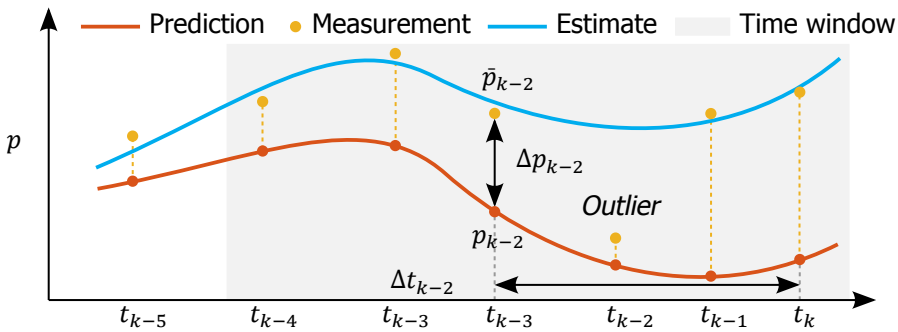

Figure 9.9: **Moving Horizon Estimator**: The predictions x_k at various time steps k is scaled ($\hat{e}_{v_{x,y}}$) and offset ($\hat{e}_{p_{x,y}}$) to best match the visual measurements $\bar{x}_k$ within the 2 second time window. Random sample consensus is used to remove outliers by sampling N random points from the buffer.

Samples older than 2 seconds were removed. The delay was fixed to 20 measurements at 0.04 s intervals on the drone and 110 when run as HiL (Hardware in the Loop) simulation. Using random sample consensus with 200 iterations with 80% of the samples, the filter fitted the predicted world path and heading with the PnP measurements. The result was a position correction $\hat{e}_{p_{x,y}}$ and a velocity correction $\hat{e}_{v_{x,y}}$ on top of the predicted estimates to obtain the current state at each time step. The heading correction $\hat{e}_\psi$ on the other hand, was only applied once upon passing each gate. The least-squares fit for RANSAC was written as $\hat{x} = (A^T A + \partial I)^{-1} A^T y$ where the prior δ ensured a preference for small corrections in velocity estimates, and $\hat{x}$, A and y were defined to map the position and velocity errors in function of time Δt over the buffer with samples $n = 1$ to N (given only for p_x):

$$
\underbrace{\begin{bmatrix} \Delta p_x|_{n=1} \\ \Delta p_x|_{n=2} \\ \vdots \\ \Delta p_x|_{n=N} \end{bmatrix}}_{y} = \underbrace{\begin{bmatrix} 1 & \Delta t|_{n=1} \\ 1 & \Delta t|_{n=2} \\ \vdots & \vdots \\ 1 & \Delta t|_{n=N} \end{bmatrix}^\dagger}_{A} \cdot \underbrace{\begin{bmatrix} \hat{e}_p \\ \hat{e}_v \end{bmatrix}}_{x} \tag{9.3}
$$

This estimator ran in a separate thread and was executed each time there were enough samples in the buffers. When a gate was crossed, the prediction was reset to the value of the state and the MHE buffers were cleared. A minimum number of 27 PnP estimates (18 in simulation due to lower frame rates) were then required before the solution was allowed to jump to the new estimate.

9.3.4. Flight planning

Path planning was done by tracking position waypoints from a list of approximate gate locations. We used the locations provided by the organizers during the practice runs and a manually updated flight plan during the races to better correspond to the perceived gate locations, which corresponds to true locations only in case of perfect calibrations. The altitude setpoint was kept constant at 1.75 m since all gate heights were identical and fixed. To better align with gates, the current commanded position $p_{x,y,z(cmd)}$ was not the gate waypoint itself, but a temporary waypoint placed 6 m perpendicularly in front of the gate along its so-called "centerline." When the robot got closer than 7 m to this target, the point remained at 7 m from the drone and moved towards the gate along the centerline until reaching the gate center.

9.3.5. Control

The heading ψ was commanded to align the active camera with the next gate center. The selected active camera was either the right-center camera for tracks with right turns or the left-center camera for tracks with only left turns. This maximized the time gates were in-view and minimized the open-loop odometry phases. When arriving close to a gate, heading commands could get unnecessarily aggressive and reduce the quality of the model-based predictions. The yaw rate was therefore limited to 180 deg/s and the robot even stopped aligning the camera with the current gate when getting closer than 2.2 m from the gate. This corresponds to the point where the gate would not be completely visible anymore.

The proportional position controller mapped the horizontal position errors in the flat-body frame $\Delta p_{x,y}^{fb}$ to commanded horizontal velocities $v_{x,y}^{fb}$. An additional proportional term was be mixed in the lateral axis to have to robot align with the gate sooner by computing the perpendicular distance towards the gate centerline Δp_y^{gate}. The total lateral control became:

$$v_y^{fb} = (1 - \alpha_{center}) \cdot k_{p1} \cdot \Delta p_y^{fb} + \alpha_{center} \cdot k_{p2} \cdot \Delta p_y^{gate} \qquad (9.4)$$

where $k_{p1} = 0.45$ and $k_{p2} = 0.45$ were gains and the mixing parameter α_{center} would determine if the robot flew directly to the waypoint along the shortest path or followed the gate centerline to improve perception and improve approach angles at the cost of increased distance to fly. Since the distance between gates was small in the last races, no obstacles were present along the gate centerlines, and some gates were placed at shallow angles, in the end, a value of $\alpha_{center} = 60\%$ was used.

The forward velocity was a function of the distance to the gate Δp_x^{fb} and the current motion vector. Far from the gate ($>$10 m), the winning version used a commanded velocity of 7.5 m/s. Then the speed was reduced to an alignment speed of 5.5 m/s. Once the state estimation predicted that the robot was sufficiently well aligned to pass through the gate within 80 cm of the center, it was allowed to speed up as much as possible. If the robot got so close to the gate that the gate was not in sight anymore, to minimize the open-loop time spent in the gate it would always accelerate if it had not reached at least the gate-crossing speed of 7.5 m/s.
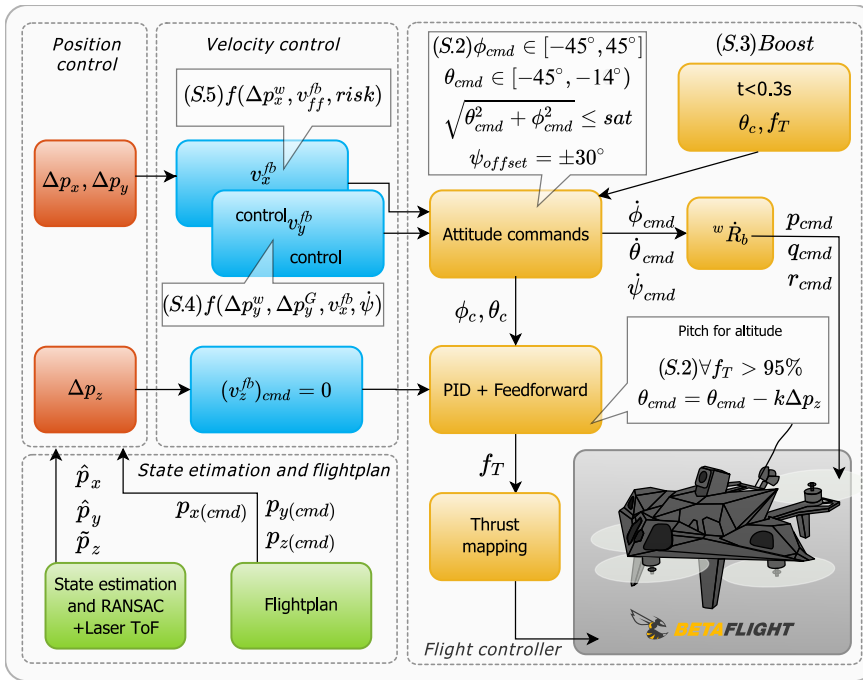
9

Figure 9.10: Schematic representation of the cascaded PID control pipeline with several enhancements for fast and risk-aware flight S.2–S.5.

A velocity control loop converted the velocity commands to desired pitch and roll angles using a feedforward gain of 0.009 rad/m/s and a velocity error feedback gain of 0.4 rad/m/s. The commanded pitch angle was constrained between -45 and $-14°$ pitch down, hence preventing pitching up. This served in keeping a good forward speed and helped perception as the fixed 15° upward-looking angle of the camera meant that the bottom of the gate could fall outside the field of view when pitching up. Moreover, slower speeds and fast deceleration into the own propeller downwash also led to a larger drift of our drag-based odometry approach. The total bank angle was saturated at 45° by maintaining the ratio between pitch and roll and is referred to as coupled saturation. Finally, a rate limiter of 320 °/s was applied to reduce the effects of attitude changes on the available throttle.

Thrust commands were generated using traditional PID with a feedforward hover-thrust of 67 % at sea-level and 73 % in Littleton, which scaled with the inverse cosine of the total bank angle of the drone. Saturation was applied to the altitude error Δp_z^w (± 2 m) and T_{cmd} (15 - 100 %). An integrator windup protection was added to the PID loop by not integrating when the T_{cmd} saturation was active.

When the throttle would saturate in full throttle, a "pitch-for-altitude" controller was activated. As the throttle saturation could occur both in forward flight as well as in turns, instead of implementing a traditional "pitch-up to climb" controller, a max-bank reduction was added. In fast forward flight, the pitch-for-altitude controller

would command pure pitch-up while during saturating turns the maximum roll angle of 45° of roll was also reduced by the same amount.

Attitude control was achieved by computing feedforward rate commands for the BetaFlight low-level autopilot that was running a fixed rate controller tuned by DRL. This was augmented with a bounded feedback controller on the error between the commanded and the current attitude. The errors in attitude are given as e_ϕ, e_θ, e_ψ while the feedback and feedforward gains are $k_p = 0.12$ and $k_{ff} = 1/dt$. The change in desired pitch and roll angles in the given discrete time step are noted $\Delta\theta_{cmd}$ and $\Delta\phi_{cmd}$ with time step dt. The rate commands in roll, pitch, and yaw $p_{cmd}, q_{cmd}, r_{cmd}$ then become:

$$\begin{bmatrix} p_{cmd} \\ -q_{cmd} \\ r_{cmd} \end{bmatrix} = \begin{bmatrix} 1 & 0 & -s_\theta \\ 0 & c_\phi & c_\theta s_\phi \\ 0 & -s_\phi & c_\theta c_\phi \end{bmatrix} \begin{bmatrix} k_{ff}\Delta\phi_{cmd} + k_p e_\phi \\ f_{ff}\Delta\theta_{cmd} + k_p e_\theta \\ k_p e_\psi \end{bmatrix} \tag{9.5}$$

These were scaled and sent together with the commanded thrust to the BetaFlight low-level controller at 50 Hz.

The gains were tuned based on a total of 60 short remote outsourced flight tests, lasting from 5 to 15 s, after which logs would be returned. The test flights were performed at a separate roughly 60 % smaller track with a different density altitude than at the competition locations. This altered the drone dynamics, made flights very short, limited the types of maneuvers, and made it hard to reach full speed. The parameters were then manually fine-tuned during the 1-hour test slot the day before the races.

9.4. Analysis and Results

In this section, we show the impact of the various elements of our approach on its performance, for perception, state estimation, and control. These experiments are conducted with a combination of real data collected with the drone, and synthetic data from the hardware-in-the-loop simulation platform provided by the competition organizers. Regarding perception, we assess the accuracy and robustness of the GateNet model qualitatively and quantitatively. Additionally, we provide an overall view of the computational expenses of the perception pipeline. Subsequently, we compare the performance of the developed state estimation scheme with that used in previous competitions. Concerning our control strategy, we conduct a detailed investigation of the various control improvements we introduced. Then, we determine the robustness of our approach to inaccuracies in the internal drone race map. Lastly, we discuss the results of the competition, for the qualification stage, the seasonal races, and the final winning championship race.

9.4.1. Perception

To quantitatively analyze the GateNet model, we collected and manually annotated a dataset consisting of 165 images logged during our 12-second winning run in the championship race. This dataset is characterized by (i) motion blur on the images due to the high-speed profile achieved in this run, (ii) strong illumination changes,

and (iii) a challenging environment with banners containing visual features similar to those of the gates along the course of the track. The reason for only using logged images from this race in this evaluation is that it is the only data that was not used in any training dataset. The GateNet model deployed for the championship race achieves an average Intersection over Union (IoU) of 87 %. After the third race, we added an artificial motion blur data augmentation mechanism to the training pipeline which notably improved the resilience towards blur. Note that this artificial blur was not applied to the ground truth masks to still promote sharp segmentations (see Figure 9.11, left).
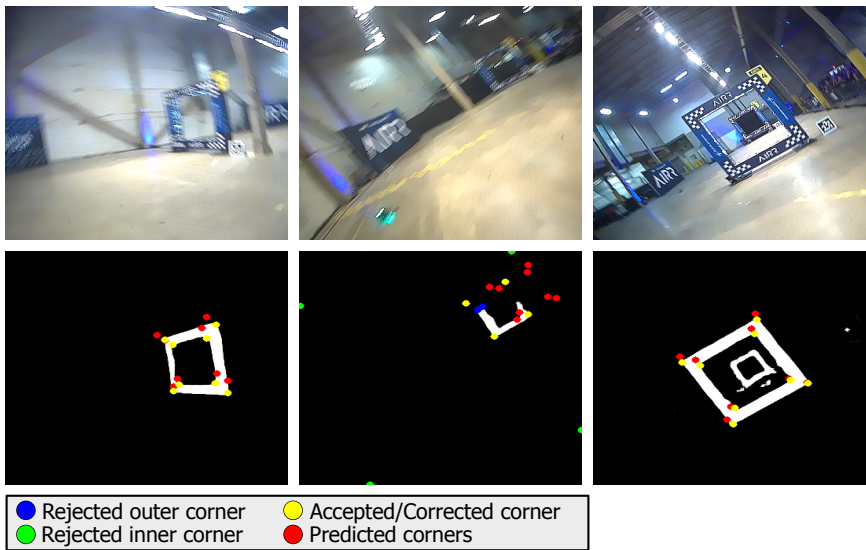

Figure 9.11: Robustness of our GateNet-based perception pipeline and corner refinement to motion blur (left), distant gates leading to incomplete segmentation masks (middle), and gate overlap, and aggressive bank angles (right).

The example images and segmentations in Figure 9.11 show the performance of GateNet in challenging scenarios like motion blur, distant gates, and adverse lighting conditions. They also show the robustness of our corner association algorithm. Our computationally efficient gate corner detector called "snake-gate" identifies the inner and outer corners of the front panel of the gates by actively sampling a small percentage of the pixels of the segmentation result. Then, our state-prediction-based sanity check and refinement of identified corner locations called "gate-prior," compares the sides and angles of the inner and outer contours of both the detected and expected gate in the image plane to neglect distractor gates when multiple gates are in sight (like overhead projected gates from the live video stream). It also corrects the location of the estimated corners in case snake-gate didn't identify a corner properly. The resulting corrected corners are finally fed to the PnP-based pose estimation. This allows the drone to localize itself with respect to the next gate even in the case of a discontinuous GateNet mask (see Figure 9.11, center) or

gate overlap in the image space (see Figure 9.11, right).

Computing the forward pass of GateNet on the GPU models requires on average 13.18 ms and thus can be performed faster than the camera update rate (i.e., 60 Hz). The estimated gate mask from the cropped and downsized input image is de-rotated using the estimated camera roll angle around the optical axis to prevent incorrect corner association and requires an average of 1.32 ms computing time (see Figure 9.5). The active-vision-based snake-gate method requires accessing the intensity information of only 1.64 % of the pixels of a 360×360 mask, which translates to a workload of 0.23 ms per image. We used the full horizontal and vertical histograms of the masks for snake-gate initialization even though computationally more efficient alternatives exist [24, 25]. Gate-prior takes on average 0.14 ms to correct the identified corners, and lastly, solving the PnP to localize the drone with respect to the gate requires 1.12 ms. Combined with the 1.08 ms import and pre-processing, the perception pipeline takes 17.07 ms while the thread runs at an average of 54 Hz, as it occasionally needs to wait a few milliseconds for delayed images. Note that the full image derotation was only added just before the championship. It was not implemented in the active-vision-based corner detector for risk mitigation purposes, although this could allow the vision pipeline to execute under 16 ms.

9.4.2. State estimation
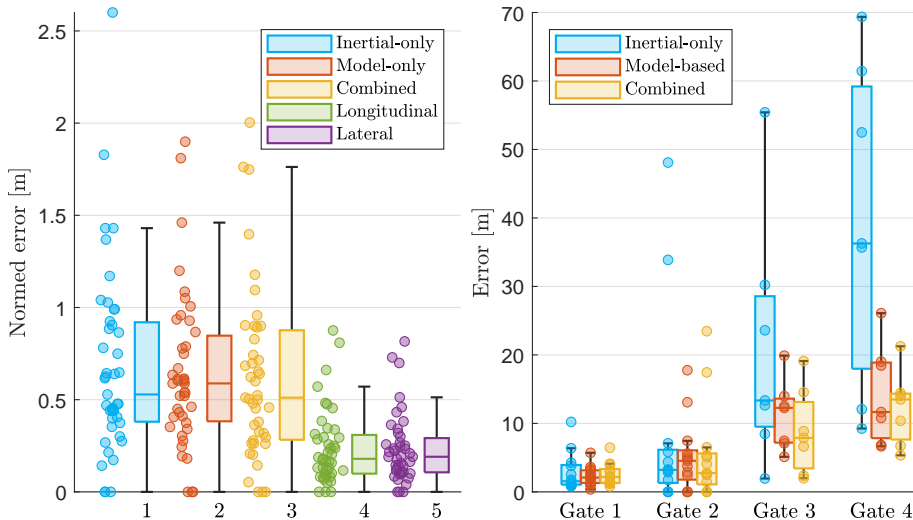
Figure 9.12: Odometry results based on the real-world data from all competition and training runs. Left: average of errors in odometry of the three dynamic models (inertial-only, model-only "flat-body" and combined "alpha", and the lateral and longitudinal components of "alpha") after 1.8 s of prediction, where the gate size is indicated as a dashed line. Right: statistics of the total accumulated odometry errors from the starting podium to each gate for the 13 full tracks flown competition tracks.

The vision-based position estimates are fused with model-inertial-based odom-

etry to smoothen the measurements and overcome periods in which no gates are detected. This odometry is primarily based on a linear drag model of the quadrotor in the "flat-body" frame (see Figure 9.8). The values of the linear drag were fitted with the scarce data from the real flights. Under low flight speed and constant altitude assumptions, this easy-to-identify model was shown to be a reasonable approximation [25]. To improve the predictions during more aggressive maneuvers, instead of fitting a more complex model for which insufficient data was available, we chose to fuse accelerometer data in the odometry (see Equation (9.2)). The difference in performance was compared between the drag-only model called "flat-body", the combined model-inertial "alpha" method (named after its α parameter to set the relative importance of the drag-model versus accelerometer odometry), and traditional body-frame accelerometer-only odometry.
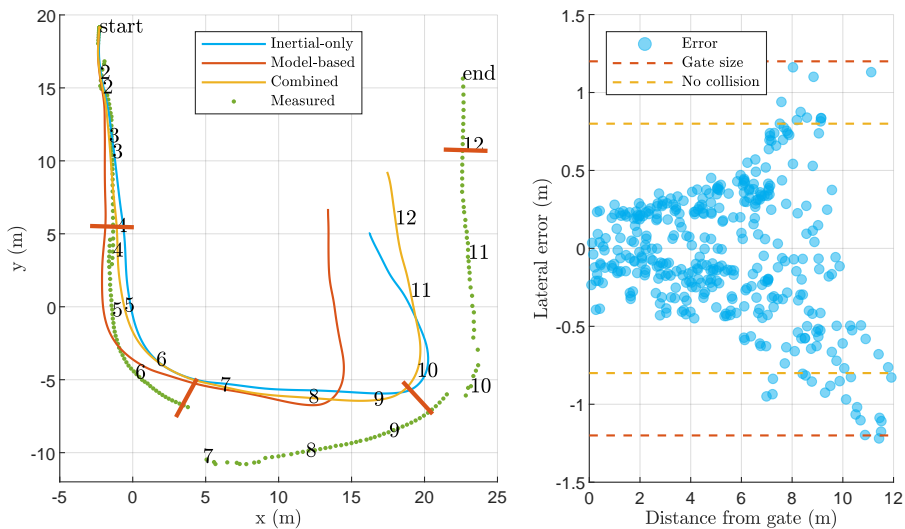
Figure 9.13: Odometry-based position estimate top view for a typical track based on the real-world data from the Baltimore track. Note that the third gate had a different orientation than expected from the flight plan, which causes the vision measurements to appear rotated. The flight times in seconds is indicated, with the total track lasting about 12 seconds.

Since no position ground truth is available for the competition flights, the comparison is made with drone observations and track knowledge instead. *This can in theory be subject to scaling and offset errors, but as long as the robot perception matches its predictions, they can successfully be merged, just like walking animals merge step-based odometry with visual observations without the need for a calibrated meter representation.*

Position measurements close to the gate are very precise thanks to the very good geometry of the PnP triangulation. In other words, small changes in position appear as large changes in pixel position of gate corners. Moreover, passing the gate is a crucial part of the race and relies on odometry only for the last few meters. We therefore first compared the odometry methods on 1.8-second stretches

just before a gate (see Figure 9.12 for the statistics and Figure 9.13 for example stretches). Subsequently, we integrated the odometry methods from start to end on 13 full tracks and compared it with the end-gate in the relatively accurate gate map (<1 m displacements). The results can be seen in Figure 9.12 and a specific track in Figure 9.13. They show that the model-inertial "alpha" method obtains the best results, which is why we used it in the final championship race. In general, the model-inertial-based odometry can obtain very good results given the scarce resources it requires (50 % within <15 m endpoint error without calibration for a 12 s prediction horizon). Nevertheless, it only seems well-suited for tracks that have sufficient gates to perform position corrections.

9.4.3. Control and path planning

To qualitatively validate the contribution to speed and reliability of the different control additions, a simulation study was performed. The initial classical control setup, marked as S.1 and shown in Table 9.1 and Figure 9.14, only finished the track half the time when configured to fly at competitive speeds. Four modifications were made to increase its speed and reliability.

The first modification to the classical control scheme combines the maximum roll and pitch angles into a single maximum bank called "coupled saturation" since separate maximum pitch and roll angles could yield 42 % higher bank angles when saturating together. Moreover, instead of putting a low and safe maximum bank angle of about 35° to never saturate thrust, we increased the limit past this point to 45°. This would occasionally lead to insufficient thrust, which was addressed by introducing a pitch-for-altitude control loop. As shown in Table 9.1 S.2, the pitch-for-altitude control loop leads to higher robustness, now finishing 8 / 10 runs with only a minor loss in speed.

An open-loop take-off with 100 % thrust and a saturating nose-down attitude called "boost" (S.3) was added that took off before the slow laser-range altitude sensor had finished booting. Likewise, a saturating pitch down was applied just before the final gate to get an even quicker finish in case the drone sensed it was well aligned. This reduces robustness (6 out of 10 runs finishing the track) but leads to slightly quicker flight times in simulation and much quicker finish times in real races by skipping the up to 1.5 s laser-range startup delay (not present in simulation).

Instead of moving along the shortest path towards the gate, an optimal approach line called "gate-centerline" was defined to prevent sharp approach angles to gates. Too sharp angles not only significantly decrease the safety margin of passing through gates but also affect the position dilution of precision (PDOP) of PnP corners, in turn reducing the quality of state estimates. This addition (S.4) increased the robustness to a success rate of 9 out of 10 through safer gate crossing angles and increased quality of perception.

The final addition to the pipeline is an adaptive, risk-based longitudinal velocity controller (Figure 9.3, S.5). At large distances from the gate, the drone is allowed to accelerate to a higher speed until it arrives at the optimal gate viewing distance, where it has to make sure the camera sees the gate. Once the drone is sufficiently
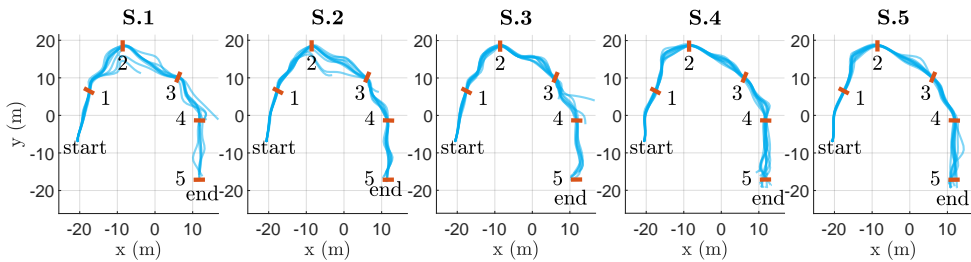
9

Figure 9.14: Contribution of the various controller modifications in simulation on the Austin track. Top view of the simulation test results of the different controllers S.2–S.5.

Setting number	S.1	S.2	S.3	S.4	S.5
Pitch for altitude & coupled saturation	×	✓	✓	✓	✓
Boosted take-off	×	×	✓	✓	✓
Gate centerline	×	×	×	✓	✓
Risk-awareness	×	×	×	×	✓
Robustness**	5 / 10	8 / 10	6 / 10	9 / 10	10 / 10
Completion time (s)	13.25±0.12	13.95±0.26	13.71±0.25	13.77± 0.32	12.08±0.27
Avg. speed (m/s)	4.57±0.52	4.55±0.25	4.62±0.23	4.73±0.22	5.38±0.18
Max. speed (m/s)	7.82±0.51	7.51±0.40	7.82±0.44	8.84±1.03	9.69±0.74

Table 9.1: Contribution of the various controller modifications in simulation on the Austin track.

confident that it is aligned properly with the gate, it can accelerate again. On the other hand, when a gate is not at the expected location or takes longer to identify, or if the control fails to align quickly, the drone slows down. This combination of risk and perception awareness was simple to implement, very light, intuitive to tune, and resulted in robust fast behavior. Table 9.1 S.5 shows that including risk-aware accelerations led to 10 successes out of 10 runs, while substantially increasing the average speed from 4.7 m/s to 5.4 m/s in simulation.

9.4.4. Robustness
Robustness was required to deal with possible camera calibration issues, the random initial starting podiums, the uncertainty about which drone was used for which race, and the inability to measure the track precisely (initially gate locations were even planned to change between runs).

Variations in the track
To evaluate the robustness of our approach to changes in the racing environment, we performed a set of simulation experiments in which we perturb our drone's internal representation of the individual gates and starting podium. Both position and orientation are altered. The drone is thereby forced to react to unanticipated gate locations. This is evaluated in the DRL simulator, which has fixed gate locations,
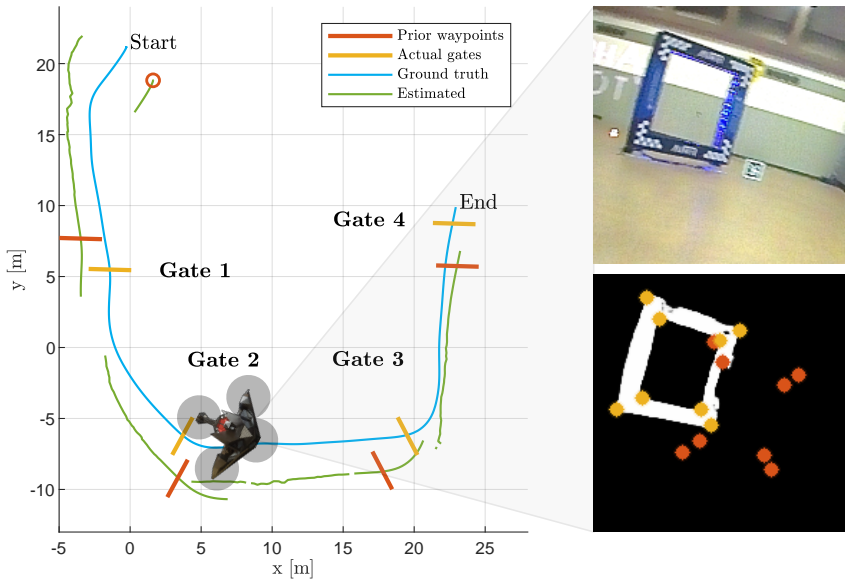
by adding uniform errors to the flight plan.

Figure 9.15: Robustness to errors in internal track representation in simulation. The onboard state estimation based on the internal model (red gates) jumps to the correct relative solution (green track) after gathering sufficient evidence.

Figure 9.15 shows that the state estimates quickly jump to the correct *relative location* with respect to the internally gate locations (prior waypoints). These red gates represent the (deliberately biased) expected gate locations in the robot's internal map while the yellow gates mark the actual locations. The black line is the simulator's ground-truth of the drone trajectory, while the green line represents the drone's internal state estimates. The advantage of this approach in a race with only a single lap is that the drone does not need to distinguish between its state error and internal map error.

Cases	Original	Gate position error		Gate yaw error	
Flightplan error	0m, 0°	3 m	5 m	20°	40°
Completion time (s)	13.01±0.19	13.02±0.31	12.79±0.81	13.03±0.25	13.60±0.48
Runs completed	10/10	10/10	6/10	9/10	6/10

Table 9.2: Robustness to errors in internal track representation in simulation. Overview of the perturbed flight plans and the effect on lap completion times.

Figure 9.16 show that our pipeline can finish the course even with 3 m perturbations in the course map or about 25 % of the 12 m inter-gate distance, albeit with lateral swings due to the control initially aligning with a wrong gate location and then needing to correct. Figure 9.16 also shows simulation with flight plan perturbations
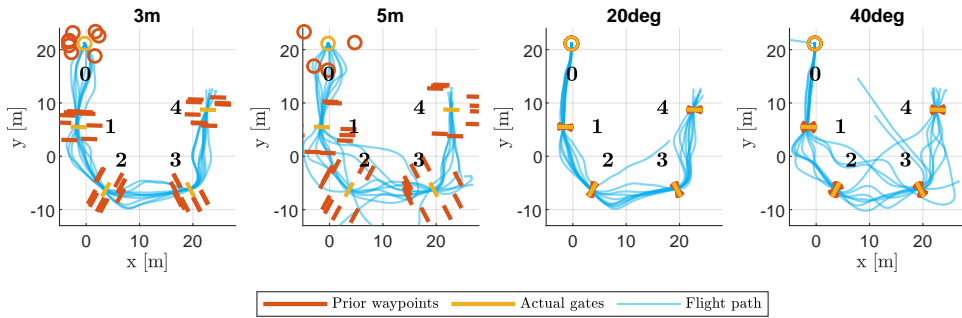
Figure 9.16: Robustness analysis in simulation on the Baltimore track with uniform flight plan gate position errors of 3 m and 5 m and uniform gate orientation errors of 20° and 40°. Perturbations in trajectories can be seen when the drone aligns with expected position of gates, but quickly have to correct after observing the real positions.

of 5 m, 20° and 40°. The table in Table 9.2 summarizes the robustness of the approach for various perturbations. The success rate only starts to drop substantially (to 6/10 runs) when gates are displaced 5 m on a track where the inter-gate distance is about 12 m or about 41 % of the inter-gate-distance.

9.4.5. Competition outcome
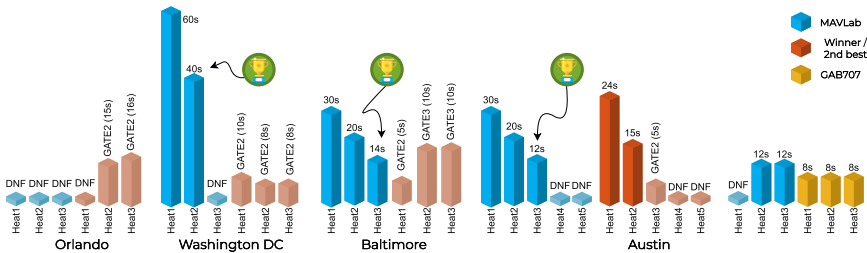
Figure 9.17: Overview of our performance through the 2019 AIRR competition: completion times at the different tracks.

Figure 9.17 represents our competition results for the three seasonal races and the championship race and that of the best opponent. Each race consisted of several "heats" which could use a different version of the code. This allowed teams to ensure completion of the track with a steady speed in the initial heats and setting best finish times in the later heats. Figure 9.19 shows the trajectories flown by our best run during all races. Since there was no ground-truth position measurement system, we show the onboard position estimates (marked in green).

The first race of the season in Orlando was won by team KAIST from South Korea, who were able to fly through two gates of the track. Our drone was not able to pass any gate primarily due to unanticipated enormous differences in illumination between testing and competition. The second race took place in Washington DC

1	MAVLab	Finish	12s
2	UZH RPG	Finish	15s
3	USRG @ KAIST	Gate 2	14s
4	Warsaw MIMotaurs	Gate 1	7s
5	KEF Robotics	Gate 1	8s
6	Formula Drone	DNF	
7	Team Puffin	DNF	
8	XQuad	DNF	
9	ICARUS	DNF	

Figure 9.18: Leader-board of the championship race, indicating the time it took for each team to reach their farthest waypoint on the track. (DNF = "did not finish"). Right: our MAVLab autonomous drone taking off at the championship race, before finishing the 74 m course in 12 s (Picture credit: DRL)

and our team was the first to fully finish any track. Since then, our racing speed has increased over the seasonal races. The championship race held at Austin was a tight competition as multiple teams were finishing the track during their training and qualification runs. The best performance of the finalists is shown in Figure 9.18. Our finish time of 12 s with an average velocity of 6.75 m/s and maximum velocity of 9.19 m/s was the prize-winning run.

After winning the AI v/s AI challenge, our drone was staged against the DRL champion GAB707 in a Human v/s AI challenge. In this race where we were not allowed to change any parameter, our first deployment led to a crash into the first gate, due to a change in starting position of more than 50 % of the distance to the gate. Both other heats against the human also started from unanticipated podiums but were within the robustness of the system and finished with the same 12 s lap time.

9.5. Conclusion

9

We presented our approach to the AIRR competition, which led to winning two out of three seasonal races, the championship race, and the title of "AIRR World Champion 2019". Our approach was human-inspired in the sense that the developed AI focuses on the drone racing gates, which serve as waypoints for the race trajectory, relies a lot on model-based odometry, and accelerates as much as possible when the situation is safe. The approach successfully dealt with the scarcity of data and was highly computationally efficient, allowing for a very fast perception and action cycle. By having a deep neural network vision front end, our approach proved to be particularly resilient to frequent changes in the environment. The only occasion that the changes proved to be too much was during the first season race where all training was done in ambient light conditions while the race took place in showbiz illumination conditions that over-exposed the gates.
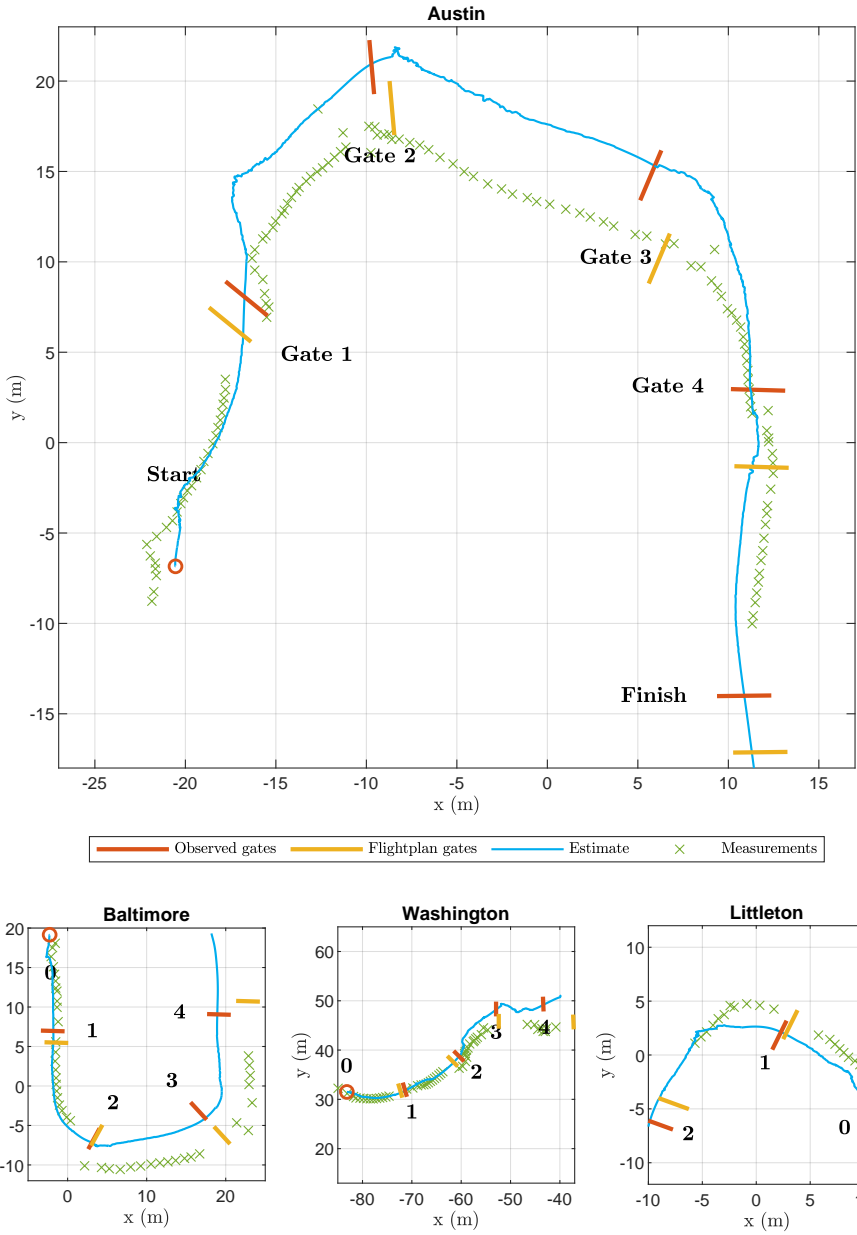
Figure 9.19: Overview of our performance through the 2019 AIRR competition. Top view of the estimated executed path with the rough map of each track received by the organizers. Estimated speed profile at the championship race. Our drone flew with an average speed of 6.75 m/s and reached a top speed of 9.19 m/s.
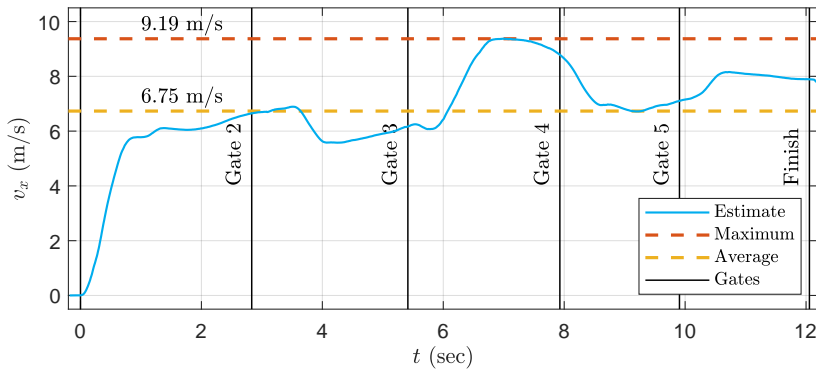
Figure 9.20: Estimated speed profile at the championship race. Our drone flew with an average speed of 6.75 m/s and reached a top speed of 9.19 m/s.

The constraints of the event drove the current implementation to make several simplifications. First of all the vertical, lateral, and longitudinal dynamics are decoupled in the controller and the estimator. The current model also makes extensive use of the constant altitude properties of the competition. Finally, the navigation solution is tailored towards detecting specific gates. But the light monocular approach opens the road to implementation onboard much lighter and hereby faster robots. Finally, the approach of merging sparse visual observations with a dynamic model which is capable of predicting the drone motion for longer distances has shown great results and allowed record in-competition velocities.

9.6. Discussion

AI purists may raise the question of how much the competition, and our approach, was actually about AI. In a "pure" AI scenario, the drone's perception and control would have been learned from scratch, making use of the provided simulator. Such an approach would, however, have clashed with the competition setup and timeline. The simulator was ready only a few weeks before the first race and had a substantial reality gap in terms of the drone's dynamics and image capturing. For example, the images in the simulation had a variable delay, going up to 0.5 s (which was worse than on the real platform). Combined with the extremely scarce access to the drone and outsourced testing, this would have left very little time for end-to-end training and a successful crossing of the reality gap.

Robotics competitions like AIRR reveal highly relevant research areas for AI. In this case: *How can AI best be designed, so that robots need minimal time and data to reach robust and highly agile flight?* A monolithic neural network trained end-to-end purely in simulation likely requires too many training samples to form

the best answer to this question. And, if we equate the experience accumulated in a simulator with the evolutionary experience before the birth of an animal, this is not the strategy that we observe in animals either. Animals "even from the same species" are all different physically, and their intelligence is set up in such a way as to deal effectively with these differences. Whereas humans need a long development time before becoming operational, many flying insects can almost immediately fly and perform successful behaviors. The reason for this is that evolution has put in place various mechanisms to deal with, e.g., the physical differences between members of the same species, ranging from adaptation to various learning mechanisms. This means that true AI will require not only reinforcement learning [39], but also, various types of self-supervised learning [40], unsupervised learning [41], and lower-level adaptations as used for instance in adaptive control [35, 42]. This last level of learning, arguably at the lowest level, is hugely important for crossing the reality gap in robotics [10].

9.7. Future directions

To make our approach work in time and robustly enough for the competition, the employed AI still relied quite a lot on us as human system designers. We learned the drone's model based on flight data, used supervised learning with human labeling of images, and designed an active vision algorithm for finding corners in the segmented images. In the future, the generation of large amounts of training data from simulation could reduce this manual work, but in this event, the qualification round forced teams to label large amounts of images to at least assess the quality of their detector (see Figure 9.7 first column). Using this data for training resulted in a DNN that segmented so well that it was only complemented with actual flight data.

Please note though that we and others are quickly developing deep learning approaches that can cross the reality gap for performing visual odometry [43], tracking of predetermined optimal trajectories [34, 44] or even for full optimal control [45, 46]. AIRR has already been a driving force to develop AI methods that will successfully bridge the reality gap, even for robots that are difficult to model in detail upfront.

But to beat human pilots in multi-robot races in random complex windy environments with multiple gate types, a lot of elements still need further development. Game theory on balancing risks of collisions with the ambition to overtake other drones, detection of randomly shaped gates after having been shown their appearance only minutes before the race, and adapting to competitor tactics are just a few of the many additional challenges that future robotics research will need to face in the competition against human pilots.

Ultimately, reducing the computational load while increasing the speed of algorithms, or in other words *improving the computational efficiency*, will play a deciding role in determining how fast and maneuverable flying robots can become, as power and especially weight spent in computing adversely influence performance. Facing these robotic challenges will bring the technology closer to applications for the benefit of the real world. We expect the applications of very fast, agile, and

situation-aware flying robots to range from ambulance drones or package delivery drones swiftly planning around obstacles in cluttered environments, to search and rescue drones. But most of all, autonomous racing helps develop solutions that sooner or later improve the characteristics of all flying robots, and we succeed to do this in heavily resource-constrained and time-pressed racing drones, then it will also generalize to other types of robots and tasks, such as autonomous vacuum cleaners and self-driving cars.

References

[1] C. De Wagter, F. Paredes-Vallés, N. Sheth, and G. C. H. E. de Croon, *The sensing, state-estimation, and control behind the winning entry to the 2019 artificial intelligence robotic racing competition,* Field Robotics **2** (2022), 10.55417/fr.2022042.

[2] C. De Wagter, F. Paredes-Vallés, N. Sheth, and G. C. H. E. de Croon, *Learning fast in autonomous drone racing,* Nature Machine Intelligence **3** (2021), 10.1038/s42256-021-00405-z.

[3] A. Krizhevsky, I. Sutskever, and G. E. Hinton, *Imagenet classification with deep convolutional neural networks,* in *Advances in neural information processing systems* (2012) pp. 1097–1105.

[4] J. Schmidhuber, *Deep learning in neural networks: An overview,* Neural networks **61**, 85 (2015).

[5] M. Campbell, A. J. Hoane Jr, and F.-h. Hsu, *Deep blue,* Artificial intelligence **134**, 57 (2002).

[6] D. Silver, A. Huang, C. J. Maddison, A. Guez, L. Sifre, G. Van Den Driessche, J. Schrittwieser, I. Antonoglou, V. Panneershelvam, M. Lanctot, and Others, *Mastering the game of Go with deep neural networks and tree search,* Nature **529**, 484 (2016).

[7] G.-Z. Yang, J. Bellingham, P. E. Dupont, P. Fischer, L. Floridi, R. Full, N. Jacobstein, V. Kumar, M. McNutt, R. Merrifield, and Others, *The grand challenges of Science Robotics,* Science robotics **3**, eaar7650 (2018).

[8] N. Jakobi, P. Husbands, and I. Harvey, *Noise and the reality gap: The use of simulation in evolutionary robotics,* in *European Conference on Artificial Life* (Springer, 1995) pp. 704–720.

[9] S. Koos, J.-B. Mouret, and S. Doncieux, *The transferability approach: Crossing the reality gap in evolutionary robotics,* IEEE Transactions on Evolutionary Computation **17**, 122 (2012).

[10] K. Scheper and G. de Croon, *Abstraction as a mechanism to cross the reality gap in evolutionary robotics,* in *From Animals to Animats 14 (Lecture Notes in Computer Science),* Vol. 9825, edited by E. Tuci, A. Giagkos, M. Wilson, and J. Hallam (Springer International Publishing, Cham, 2016) pp. 280–292.

9

[11] D. Floreano and R. J. Wood, *Science, technology and the future of small autonomous drones,* Nature **521**, 460 (2015).

[12] S. Lupashin, A. Schöllig, M. Sherback, and R. D'Andrea, *A simple learning strategy for high-speed quadrocopter multi-flips,* in *2010 IEEE international conference on robotics and automation* (IEEE, 2010) pp. 1642–1648.

[13] D. Mellinger, N. Michael, and V. Kumar, *Trajectory generation and control for precise aggressive maneuvers with quadrotors,* The International Journal of Robotics Research **31**, 664 (2012).

[14] D. Mellinger and V. Kumar, *Minimum snap trajectory generation and control for quadrotors,* in *2011 IEEE international conference on robotics and automation*, IEEE (IEEE, Shanghai, China, 2011) pp. 2520–2525.

[15] D. Falanga, E. Mueggler, M. Faessler, and D. Scaramuzza, *Aggressive quadrotor flight through narrow gaps with onboard sensing and computing using active vision,* in *2017 IEEE international conference on robotics and automation (ICRA)* (IEEE, 2017) pp. 5774–5781.

[16] G. Loianno, C. Brunner, G. McGrath, and V. Kumar, *Estimation, control, and planning for aggressive flight with a small quadrotor with a single camera and IMU,* IEEE Robotics and Automation Letters **2**, 404 (2016).

[17] H. Moon, Y. Sun, J. Baltes, and S. J. Kim, *The IROS 2016 competitions [competitions],* IEEE Robotics & Automation Magazine **24**, 20 (2017).

[18] B. Morrell, M. Rigter, G. Merewether, R. Reid, R. Thakker, T. Tzanetos, V. Rajur, and G. Chamitoff, *Differential flatness transformations for aggressive quadrotor flight,* in *2018 IEEE International Conference on Robotics and Automation (ICRA)* (IEEE, 2018) pp. 1–7.

[19] E. Kaufmann, M. Gehrig, P. Foehn, R. Ranftl, A. Dosovitskiy, V. Koltun, and D. Scaramuzza, *Beauty and the beast: Optimal methods meet learning for drone racing,* in *2019 International Conference on Robotics and Automation (ICRA)* (IEEE, Montreal, QC, Canada, 2019) pp. 690–696.

[20] J. Delmerico and D. Scaramuzza, *A benchmark comparison of monocular visual-inertial odometry algorithms for flying robots,* in *2018 IEEE International Conference on Robotics and Automation (ICRA)* (IEEE, 2018).

[21] P. Foehn, D. Brescianini, E. Kaufmann, T. Cieslewski, M. Gehrig, M. Muglikar, and D. Scaramuzza, *AlphaPilot: Autonomous Drone Racing,* in *RSS 2020* (RSS, Corvalis, Oregon, USA, 2020) pp. 1–9, 2005.12813 .

[22] R. Mur-Artal, J. M. M. Montiel, and J. D. Tardos, *ORB-SLAM: a versatile and accurate monocular SLAM system,* IEEE transactions on robotics **31**, 1147 (2015).

[23] H. Moon, J. Martinez-Carranza, T. Cieslewski, M. Faessler, D. Falanga, A. Simovic, D. Scaramuzza, S. Li, M. Ozo, C. De Wagter, G. C. H. E. de Croon, S. Hwang, S. Jung, H. Shim, H. Kim, M. Park, T.-C. Au, and S. J. Kim, *Challenges and implemented technologies used in autonomous drone racing,* Intelligent Service Robotics **12**, 137 (2019).

[24] S. Li, M. Ozo, C. De Wagter, and G. C. H. E. de Croon, *Autonomous drone race: A computationally efficient vision-based navigation and control strategy,* Robotics and Autonomous Systems **133**, 103621 (2020).

[25] S. Li, E. van der Horst, P. Duernay, C. De Wagter, and G. C. H. E. de Croon, *Visual model-predictive localization for computationally efficient autonomous racing of a 72-gram drone,* Journal of Field Robotics **37**, 667 (2020).

[26] W. Liu, D. Anguelov, D. Erhan, C. Szegedy, S. Reed, C.-Y. Fu, and A. C. Berg, *SSD: Single shot MultiBox detector,* in *Computer Vision – ECCV 2016* (Springer International Publishing, 2016) pp. 21–37.

[27] S. Jung, S. Hwang, H. Shin, and D. H. Shim, *Perception, guidance, and navigation for indoor autonomous drone racing using deep learning,* IEEE Robotics and Automation Letters **3**, 2539 (2018).

[28] J. A. Cocoma-Ortega and J. Martínez-Carranza, *Towards high-speed localisation for autonomous drone racing,* in *Advances in Soft Computing* (Springer International Publishing, 2019) pp. 740–751.

[29] J. Aloimonos, I. Weiss, and A. Bandyopadhyay, *Active vision,* International Journal of Computer Vision **1**, 333 (1988).

[30] N. J. Sanket, C. D. Singh, K. Ganguly, C. Fermuller, and Y. Aloimonos, *GapFlyt: Active vision based minimalist structure-less gap detection for quadrotor flight,* IEEE Robotics and Automation Letters **3**, 2799 (2018).

[31] R. Bajcsy, Y. Aloimonos, and J. K. Tsotsos, *Revisiting active perception,* Autonomous Robots **42**, 177 (2018).

[32] A. Loquercio, E. Kaufmann, R. Ranftl, A. Dosovitskiy, V. Koltun, and D. Scaramuzza, *Deep drone racing: From simulation to reality with domain randomization,* IEEE Transactions on Robotics **36**, 1 (2019).

[33] L. O. Rojas-Perez and J. Martinez-Carranza, *DeepPilot: A CNN for Autonomous Drone Racing,* Sensors **20**, 4524 (2020).

[34] E. Kaufmann, A. Loquercio, R. Ranftl, M. Müller, V. Koltun, and D. Scaramuzza, *Deep Drone Acrobatics,* in *RSS: Robotics, Science, and Systems* (Robotics: Science and Systems Foundation, Corvalis, Oregon, USA, 2020) pp. 1–10, arXiv:2006.05768 .

[35] E. N. Johnson and S. K. Kannan, *Adaptive Trajectory Control for Autonomous Helicopters,* Journal of Guidance, Control, and Dynamics **28**, 524 (2005).

9

[36] V. Murali, I. Spasojevic, W. Guerra, and S. Karaman, *Perception-aware trajectory generation for aggressive quadrotor flight using differential flatness,* in *2019 American Control Conference (ACC)* (IEEE, 2019) pp. 3936–3943.

[37] M. Bangura and R. Mahony, *Real-time Model Predictive Control for Quadrotors,* IFAC Proceedings Volumes **47**, 11773 (2014).

[38] O. Ronneberger, P. Fischer, and T. Brox, *U-net: Convolutional networks for biomedical image segmentation,* in *Lecture Notes in Computer Science (including subseries Lecture Notes in Artificial Intelligence and Lecture Notes in Bioinformatics)*, Vol. 9351 (Springer, 2015) pp. 234–241, arXiv:1505.04597 .

[39] R. S. Sutton and A. G. Barto, *Reinforcement Learning: An Introduction* (The MIT Press, 2018).

[40] S. Thrun, M. Montemerlo, H. Dahlkamp, D. Stavens, A. Aron, J. Diebel, P. Fong, J. Gale, M. Halpenny, G. Hoffmann, and Others, *Stanley: The robot that won the DARPA Grand Challenge,* Journal of field Robotics **23**, 661 (2006).

[41] T. Kohonen, *Self-organized formation of topologically correct feature maps,* Biological Cybernetics **43**, 59 (1982).

[42] K. J. Åström and B. Wittenmark, *Adaptive Control: Second Edition* (Dover Publications, 2013).

[43] N. J. Sanket, C. D. Singh, C. Fermüller, and Y. Aloimonos, *PRGFlow: Unified SWAP-aware deep global optical flow for aerial robot navigation,* Electronics Letters **57**, 614 (2021).

[44] G. Torrente, E. Kaufmann, P. Foehn, and D. Scaramuzza, *Data-driven MPC for quadrotors,* IEEE Robotics and Automation Letters **6**, 3769 (2021), 2102.05773 .

[45] S. Li, E. Öztürk, C. De Wagter, G. C. H. E. de Croon, and D. Izzo, *Aggressive online control of a quadrotor via deep network representations of optimality principles,* in *2020 IEEE International Conference on Robotics and Automation, ICRA 2020*, Proceedings - IEEE International Conference on Robotics and Automation (Institute of Electrical and Electronics Engineers (IEEE), United States, 2020) pp. 6282–6287.

[46] P. Foehn, A. Romero, and D. Scaramuzza, *Time-optimal planning for quadrotor waypoint flight,* Science Robotics **6**, eabh1221 (2021).

9

10

Conclusion

*Inspire the world to reduce the mass of flying robots
by proposing solutions to some of their biggest shortcomings.*

Mission at the TUDelft MAVLab

In this final chapter, the research questions and problem statement formulated in Chapter 1 are revisited and answered. Then the wider implications of the findings are discussed and finally, various directions for future work are explored.

10.1. Answers to Research Questions

Research Question 1

How light can minimum-mass flying robots be created that combine hover and fast flight for autonomous exploration missions?
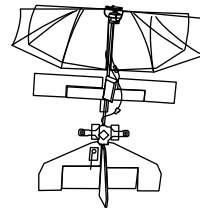
DelFly Explorer.

The first research question is addressed with the development of a passively stable 20 g indoor reconnaissance robot named DelFly Explorer, presented in Chapter 2. It uses flapping wings in a *tailed biplane concept* to minimize rocking of the fuselage and to obtain a stable observation platform that can combine fast flight and stable slow hovering flight. It became the lightest autonomous indoor exploration robot able to fly in unchanged rooms by using its custom 4 g stereo vision system. It obtains depth images using a simplified stereo vision algorithm, tailored towards small low-memory microprocessors. The appearance variation cue is added to overcome low-texture areas which are common in man-made indoor environments. This uses the principle that the variation in the appearance of many

different objects in view is larger than that of the detailed texture of one object alone. The navigation algorithm keeps the area in front of the robot—needed for timely avoidance—free of obstacles to enable automatic exploration of unchanged rooms while the 0.9 g autopilot stabilizes the direction of flight and altitude. Since testing and theoretical analysis showed that tailed ornithopters like de DelFly require a different center of gravity for passive longitudinal dynamic stability in slow hovering flight and fast flight, Chapter 3 finally proposes a mechanism to move the wings and combine both flight regimes.

> **Research Question 2**
>
> How can sensitivity to gusts be reduced and controllability increased in light flapping-wing robots?
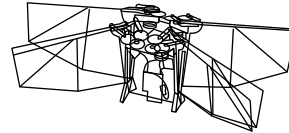

Quad-Thopter.

Chapter 4 identified that small actuators cannot be light, fast, and strong at the same time. To address the research question of agile flight, fast and strong actuation of the attitude of a tailless flapping-wing robot is sought. To minimize the weight penalty, a concept is proposed that reuses the main propulsion for attitude control. The so-called 'Quad-thopter' concept consists of 4 half pairs of independently driven flapping wings. These use simple cranked-rocker mechanisms that can control 4 thrust vectors not passing through the center of gravity to control attitude. The residual vibration is shown to be highly reduced by using pairs of synchronously flapping wings on each motor but it is still present in pitch and roll due to the frequency differences of different pairs of wings combined with the non-steady aerodynamic lift of the wing-pairs over the flapping cycle. The concept combines precise hovering flight up to fast forward flight with very rapid attitude control that allows the robot to make 3 m sideward steps in under one and a half seconds from hover to hover. This concept greatly enhances the amount of turbulence that small flapping-wing robots can handle while combining hover and fast flight without the need for reconfiguration.

> **Research Question 3**
>
> How can an efficient hover and an efficient forward flight be combined using a single rotor and high aspect ratio wings?
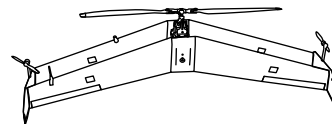

The DelftaCopter.

A helicopter-with-wings concept is introduced in Chapter 5 where the challenges in its control are explained. In particular, the inertia of the high aspect ratio wings is shown to interact with the helicopter rotor dynamics. In traditional fixed-wing aircraft, the gyroscopic effect of the propeller can typically be neglected as not more

than a small perturbation, and in pure helicopters, the fuselage does not fundamentally change the control effectiveness of the rotor. The DelftaCopter appears to be exactly in the cross-over regime. The phenomenon is reproduced in simulation and a rate controller is proposed that addresses the mixed dynamics. Chapter 6 describes how a low-sweep angle delta-wing biplane concept is used to reduce the lateral surface affected by turbulence and wind during hover for a given aspect ratio while adding structural rigidity, stability on the ground after landing, and improved stall behavior. While the swash-plate adds mechanical complexity and maintenance, it enables rapid changes in large control moments and the changes in collective pitch which are crucial to the efficiency of flight from hover to fast forward flight. The chapter shows how the flying robot is tested at the Medical Outback Challenge, where its flight efficiency is studied and a navigation and control strategy is proposed to maximize range and minimize risks. Chapter 7 proposes a more detailed dynamic model of the combination of a helicopter rotor and fixed wings in hover and forward flight. Overall the concept was shown to achieve very good efficiency combined with powerful attitude control at the cost of mechanical and control complexity (Chapter 6).

Research Question 4

How can electrically powered flying robots capable of hover and fast flight be designed to use pressurized hydrogen as their energy source?
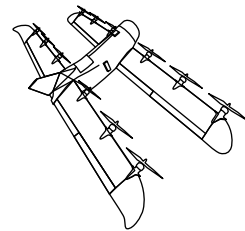

The Nederdrone.

A Polymer Electrolyte Membrane (PEM) fuel-cell is fed from a 300 bar hydrogen-filled type IV pressure cylinder power source for the Nederdrone concept presented in Chapter 8 to address research question 4. The average energy needed for fast forward flight and the peak power demands in hover are shown to impose the need for a hybrid power source which is found in a very light-weight passive combination of lithium polymer batteries and the fuel cell. The pressure cylinder is aligned with the flow for efficient fast flight and a tail-sitter concept is shown to minimize weight and complexity while maximally re-using the 12 motor propulsion for attitude control, hover, and forward propulsion. To achieve this, the robot pitches down 90° to transition from hover to forward flight. A double automotive CAN network and dual flight modes further minimize the number of single points of failure. Destructive pressure cylinder testing was performed to supplement the risk analysis of flying with pressurized hydrogen. The ground stability challenge in landing a hydrogen cylinder vertically is resolved by gently dropping the nose of the tail-sitter on its sprung landing gear. An angled take-off from this intermediate semi-tail-sitting attitude is developed and the entire concept is tested at sea departing from a moving ship in 5 Bf conditions during a test flight of over three hours. The priority-aware dual control bus, redundant power source, dual wiring, dozen propellers and motors,

10

dual flight modes, and model-less INDI based control make the Nederdrone particularly resilient to failures. Overall this chapter shows that practical and safe flying robots combining hover and fast flight can be created using pressurized hydrogen as fuel.

Research Question 5

How can very fast forward flight through gates be achieved in a GPS denied environment with minimal processing and training time?
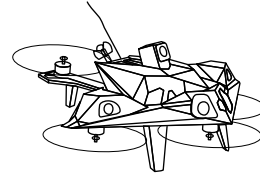
The AIRR Racer-AI.

The final research question originated from the real-world mission need to find light intelligent solutions to navigate at high speed close to obstacles and is addressed in Chapter 8. To allow flight at speeds beyond the capabilities of current visual-inertial navigation while not dramatically increasing the processing power, a light monocular navigation system was developed. The proposed solution starts by detecting known objects using a 4 layer U-Net-shaped segmentation Convolutional Neural Network (CNN) running on a GPU. A very light active vision algorithm called snake-gate then searches for characteristic points in the segmented image, which in this research were the corners of square gates. The accepted points after validation with the robot's prior expectations are subsequently fed into the navigation solution. A rough aerodynamic model is combined with inertial measurements to augment the visual observations and complement them in periods without visual measurements. A risk-aware control strategy found a compromise between maximizing speeds and increasing the chance of completing the track. The solution competed in the first Artificial Intelligence Robotic Racing (AIRR) season 2019 and was able to fly faster than the speeds reported by teams that used traditional approaches. Although the proposed solution was tested on heavy and powerful hardware provided by the organization, it used only a fraction of the available processing power while processing nearly all 60 frames per second and using excess computational resources for debugging purposes. Minimization of the required processing power and weight is a very important step in increasing the speed and agility of future flying robots.

Problem Statement

How can minimum-mass, mission-capable flying robots combine hover and fast flight?

The various chapters attempt to answer the problem statement from various perspectives by proposing novel solutions to combine hover and fast flight in flying robots, while always striving towards a minimum mass and maintaining mission capabilities.

Overall, this research proposes that the solution to this combination is highly dependent on the optimization criteria and leads to vastly different technologies. Optimizations were proposed around minimum mass, maximum agility at minimum mass, maximum efficiency, increased range, and increased environmental complexity. The optimization for minimum mass mainly became a sensory and processing power challenge. The optimization for agility in tiny robots was mainly an actuator challenge. The optimization for maximum efficiency started as aerodynamics, propulsion, and design challenges but revealed new insights in control. Optimization for range using hydrogen turned out to contain important safety challenges, required solutions to high power demands, and yielded novel take-off and landing maneuvers. Finally, optimization of GPS-denied fast flight near obstacles was first and foremost an Artificial Intelligence challenge.

10.2. Discussion of the future of UAV

In this research, the quest for mission-capable flying robots with combined hover and fast flight capabilities has led to vastly different challenges and corresponding solutions.

Applications of tiny flying robots

The desire to create very small flying robots has been fueled by the abundance of their many biological counterparts and has been the source of imagination in many science-fiction ideas like the *Black Mirror* robotic bees. But predicting what the true applications of lightweight flying robots will be is as difficult as predicting during the development of wireless communication technology several decades ago that social media apps would become the most popular applications on phones, and that phones would even be used to monitor personal health. In the case of small flying robots, the hobby market is an obvious potential candidate, but whether indoor aerial monitoring will go mainstream is uncertain given the alternatives offered by fixed cameras. Long-term goals like providing alternatives for natural pollinators still face many challenges, where recyclability is certainly not the least, as sowing lithium batteries from broken robots in orchards is not conducive to the long-term health of the crop. Recycling is an important topic if you consider how the frequent charging due to energy limitations and increased likelihood of mishap due to limitations of intelligence in a complex environment might reduce the lifespan of these ephemera. But the potential contribution in securing our food supply combined with inspiring visual properties largely offsets the uncertainties about their future use. And the solutions found in the fundamental research to address shortcomings of these tiny flying systems directly propagates to advantages in larger robots. Both make this a lively research field.

Challenges in miniaturization of robotic flight

To create very light robots, the reduction of component weight turns out to be the limiting factor. It is a lot easier to reduce the size than the weight as weight should scale down more than quadratically with size to keep the same wing surface in

10

more viscous air at comparable flight speeds. In particular, the weights of energy source, processing, and actuators become limiting factors. Battery technology is still off by an order of magnitude from the energy densities of sugar as used by insects [1], and bio-inspired energy harvesting could be lead to game-changing increases in operational capabilities. Furthermore, the dynamics of flying platforms become faster with reducing mass while the performance of sensors degrades with size. To make matters worse, the required processing power does not scale down at all with mass, while at the same time faster results are needed, often even in more complex environments. Small robots are thereby more interested in Koomey's law—the number of computations per joule of power dissipated [2]— than Moore's law about the number of transistors per unit of silicon surface. Smaller electric motors and actuators also have more losses and become relatively heavy for a given torque. Alternatives like piezo actuators need dangerously high voltages while shape memory alloys are slow. New technologies like using Microelectromechanical systems (MEMS) technology might bring new opportunities.

Flapping flight

Flapping wings cope relatively well with the viscous effects of scaling down to very small sizes and hereby offer interesting alternatives to quadrotors. Flappers in general also feature enhanced safety because of the absence of fast-rotating rotors. Their wings bounce off objects at low flight speeds as their wings reach zero velocity at the maximum deflection.

For attitude control, the variation in the flapping frequency of separate wings is shown to be a constructively simple and light yet effective solution, despite the a-priori reluctance caused by the obvious unbalanced flapping forces this entails. Moreover, re-using the main propulsion for attitude control maximizes the available control torques for a given system weight since no extra weight is needed for separate attitude control actuators. Although its design does not precisely correspond to any known biological counterpart, the proposed "quad-thopter" has several characteristics featured by natural fliers which even led to a flapping-wing robot design that helped discover a novel passive yawing torque in fruit flies [3]. The patent-protected [4, 5] inspiring huge insect resembling agile flapping-wing design even drove a spin-off company to investigate its use for show-business applications, in research, and hobby markets. Overall, smaller drones open new opportunities, either by bringing inherent safety properties, lower costs, higher-volume manufacturing, or simply by fitting in smaller spaces and this gives them the prospect of an interesting future.

10

Outdoor autonomous flight

Outdoors, the manually-flown quadrotor-dominated market is moving towards more robotization as the technology advances at a high pace. Remotely operated *drone-in-a-box* solutions are developed at high speed, automatic inspection of assets is growing, and the first fully automatic delivery drones have reached the operational testing stage in several cities where the robots must cleverly navigate the complex world on their own. While the inspection market seems to focus on multicopters

for their simplicity [6, 7], the drone delivery and cargo markets are showing more interest in combining hover and fast flight capabilities [8]. The prototype delivery drones of Google, Amazon, DHL [9] were all hybrid combinations of fixed-wing and rotorcraft flying robots trying to merge hover and fast flight capabilities. In this case, costs and safety are added to the list of optimization criteria.

The advantages of efficiency

The search for a theoretically efficient combination of hover and fast flight in this work led to the DelftaCopter concept, which was developed for a medical flying robot competition in the Australian outback. Its efficiency allowed the fully electrical DelftaCopter to be more than four times lighter than most other participants, including the petrol-powered concept winning the first prize. Reducing the total system mass has a very important effect on the potential consequences of a mishap. There are also indirect advantages of efficiency like the fact that the robot features very silent flight thanks to its large slow rotor and lack of gears. This property in itself can attract a new set of applications. The two main downsides of the concept are mechanical and control complexity. The latter is mainly a one-time cost during the development phase while the former is more important in the case of no-single-point-of-failure, manufacturing, or cost constraints. And although the total vehicle weight is low, the single large rotor has non-neglectable inertia and can still inflict injury upon contact with humans. Overall, the development of hybrid aircraft with precision landing and long-range capabilities opens a lot of new opportunities, as can be judged by the number of companies and spin-offs that optimize various hybrid unmanned aircraft concepts.

Robot-human collaboration

The DelftaCopter project also highlighted the benefits of human-robot collaboration in complex real-world tasks. For instance, in search tasks where little to no training data is available, the automatically flying robot collected probable points of interest and only sent back the most interesting thumbnails over the low-bandwidth datalink. Humans, who were aware of last-minute details that are hard to encode, could then make the best-informed decisions despite the fact that not all images could be transmitted. This remaining human superiority underlines the long road ahead, especially for weight-restricted flying robots, to reach general intelligence [10–12].

Hydrogen powered flying robots

On the topic of energy, hydrogen is seen as a promising future fuel for aviation thanks to its high energy density, zero carbon dioxide emissions, reduced air pollutants such as nitrogen oxide, reduced contrail formation in high altitude flight, and endless supply as water can be turned into hydrogen and back indefinitely. On the downside, storage and transportation of hydrogen remain challenging in a lot of ways. Hydrogen is not the safest source of energy and is thereby expensive while the cheapest way to produce hydrogen is currently based on methane. This shows that a lot of research is still needed to allow green hydrogen to go mainstream. Another challenge lies in the conversion of hydrogen to electricity through fuel cells

10

which is theoretically and practically inefficient. In the Nederdrone, half the hydrogen energy is converted to heat. Furthermore, while hydrogen can provide a lot of energy, the available power of fuel cells is limited, and this boosts the research on smart hybrid energy sources. Combining energy sources has implications for flight planning as, high power phases need to be altered with low power battery recharging phases, which poses new self-awareness challenges in the planning capabilities of flying robots.

Safely transporting hydrogen

A big efficiency loss in hydrogen-powered flight is that the onboard storage of pure hydrogen requires a pressure cylinder with a weight that is orders of magnitude heavier than the hydrogen it transports. The volumetrically large hydrogen storage also comes with shape constraints that have important aerodynamic consequences. The possible consequences of serious impacts of onboard hydrogen-filled pressure cylinders are also a topic of research. While cylinder manufacturers keep working on increasing the structural properties of cylinders, UAV designers can play a big role by creating safer flying platforms with redundant flight modes, redundant energy, redundant control, and protection of the cylinder—for instance with light energy-absorbing material around the cylinder to provide a combined aerodynamic shape and large crumple zone. While redundancy in the form of more motors, redundant wiring, etc., all increase the weight and thereby reduce the efficiency of the platform, in contrast, the redundant flight modes that originate from combining hover and fast flight play a more interesting role. When for instance aerodynamic actuators needed for forward flight would fail, then the platform can return and land in hovering mode. If on the other hand, many motor controllers would fail, then the platform can still be flown in forward flight by exploiting the efficiency of its fixed wings. This combined versatility and safety is expected to play an important role in the development of hydrogen-fueled flight. And safety improvements developed to enable hydrogen-based flight can propagate to differently powered vehicles as well.

Robotic intelligence

In the long run, once the main initial mechanical hurdles have been passed, more and more safety considerations will be pushed to software as the flying robots learn to deal with increasingly complex situations and cope with their hardware limitations and even malfunctions. Robotic intelligence is also the limiting factor in scaling up the use of unmanned aircraft in many applications as the costs of their human operators form a very large chunk of the total expenses. Combined with the fact that the speed-limiting factor when flying in complex, unknown, or densely cluttered environments is also a sensing and processing bottleneck, one can start to see the importance that artificial intelligence will play in the next decades in flying robots.

Power and weight-efficient intelligence

Flying adds severe weight and power limitations to the list of requirements of onboard processing, which is likely to lead to dedicated solutions advocating for power efficiency. This work proposed a light and quick-to-tune approach in the context

of drone racing that combines deep neural networks where needed with a classical approach where possible. It maximizes the benefits of the deep neural network in coping with varying conditions while the light engineer-understandable classical approach is power efficient and allows quick tuning cycles without the need for a lot of training data. Using the computationally heavy deep neural nets for image recognition makes a lot of sense since traditional computer vision does not nearly obtain the same quality of results, but for sensor fusion and control, the gain of using computationally expensive AI over light classical methods might not be sufficient to justify its use. This kind of computational trade-off is expected to be common practice in commercial drones to maximize flight time and payload, at least until Koomey's law or novel power-efficient spiking neural nets bring us technology where even heavy processing only uses a fraction of the power needed to fly.

10.3. Future Work

Although the proposed solutions offer new directions to approach the desire of combining hover and fast flight, many technological developments are still in their infancy and face very interesting challenges. Some extreme challenges like opening doors during indoor exploration with tiny flying robots [13] or reaching levels of general intelligence [11] guarantee a lot of future research opportunities.

Further miniaturization

For the miniaturization of flight, a deeper understanding of flapping-wing aerodynamics would still bring a lot of benefits. The structural deformations from fluid forces and resulting consequences of the newly formed structure shape on the motion of the fluid (structure-fluid/fluid-structure interaction) are particularly important for small bending wings in non-steady flows. Better and faster models could eventually enable Evolutionary Algorithm (EA) to optimize the structure. Furthermore, the quest for fast, light, and strong actuators continues. In the interest of weight, the small robots in this work have the minimum number of required actuators and cannot move their camera, their legs, etc. Even when only comparing the degrees of freedom that natural fliers have in the actuation of their wings, their robotic counterparts appear very rigid and non-controllable. So a lot of research is thus still needed to develop novel, high DOF wing actuation mechanisms, preferably using resonance to enhance their efficiency. An additional challenge occurs when using flapping-wing robots as observation platforms in that the residual vibration influences the camera images. While this vibration has the potential to enhance depth perception, from the point of view of the payload this is undesirable and the search for reduced vibration flapping-wing systems will benefit all applications where stable images are desired, especially in the case of a reduced number of wings. Overall, future work will try to bridge the gap between the bottom-up approaches which developed promising manufacturing techniques but faced energy and payload challenges, and the top-down approaches which faced weight reduction and constructive challenges.
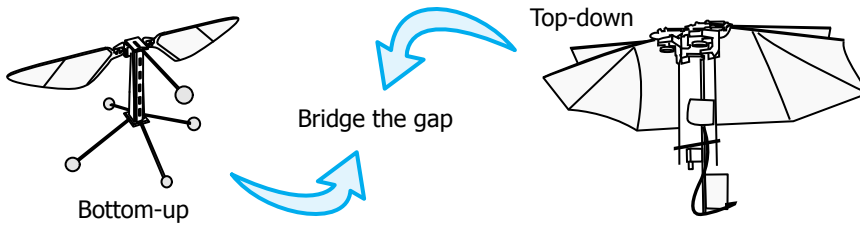
10

Figure 10.1: Bottom-up and top-down approaches meet in the middle.

Overcoming compromises

Future work in outdoor flying robots that combine hover and fast flight will need to keep working on minimizing the disadvantages of the combination. Forward flight can still be more efficient with a platform that is not able to hover, as this hovering capability costs weight, drag, or reduced propulsion efficiency. The best hovering platforms are the ones that cannot fly fast efficiently as the wing adds weight and increases sensitivity to turbulence. Future work on lighter wing structures, fully retractable propulsion, morphing propellors, retractable wings, inflatable wings, or wings that fold will further reduce these drawbacks and improve the overall concepts. In the end, every application will need to optimize the relative hover versus fast-flight efficiency to reflect the time operated in the respective regimes.

The DelftaCopter concept can still be enhanced by reducing the aerodynamic drag of the fuselage and rotor head. Also modeling the non-linearities in the rotor head and measuring the rotor blade deflections, the angle of attack of the wings, the sideslip of the vehicle, and even servo deflections in flight can still enhance the understanding of the dynamics and improve its control. This should complement the existing model to various airspeeds and rotor RPMs. The tip rotors furthermore cause drag and become dummy weights in forward flight. Single bladed props that align with the flow might reduce this drag until aerodynamics actuators can replace them to compensate the rotor torque entirely. All technologies that can increase the torque of motors without increasing their weight will lead to more efficient propulsion as well.

Tail-sitters, in general, contain a fundamental trade-off between aerodynamic efficiency in forward flight and static stability of the platform on the ground after landing which would benefit from further optimization. Also aerodynamically, airfoils with less abrupt stall behavior but very low drag during fast flight should be developed to accommodate the specific needs of tail-sitter UAVs that operate in and around the stall regime, for instance when hovering in non-zero wind.

Energy

A lot of work is still required to improve the weight efficiency of hydrogen storage. Obvious strategies include increasing the operational pressures from the 300 bar used in this work to 700 bar or more but this still requires a lot of work to keep the same level of safety. If it works out, the rewards would be game-changing not just for flying robots. Also, the production of green hydrogen is a topic of research

where a lot can be gained by addressing the efficiency and overcoming the need for special metals [14].

Getting inspiration from nature

Last but not least, although the state-of-the-art research is a few years ahead, commercial flying robots are only starting to show signs of intelligent behavior in large-scale real-world applications and still have a long road to go before bringing Automated External Defibrillator (AED)s at high speed in cities or performing automatic inspection of bridges without human supervision. When it comes to flying robots in general, nature still has a lot to teach as the endurance, intelligence, energy-harvesting capabilities, self-repair properties, and long-term sustainable properties—to name just a few—of natural flyers still have a big lead over our state-of-the-art robots. Aviation has always demanded extreme optimization of all its facets as the constant battle against gravity is particularly energy-demanding, and nowhere is this need for optimization more obvious than when it comes to optimizing robotic flight on other planets. But arguably the most important very-long-term optimization might be the life cycle optimization—maybe one day we can have sugar-battery-powered carbon-based electronics on biodegradable substrates [15, 16] and fully recyclable structures [17]—such that creating flying robots can be sustained for millions of years to come, a challenging but exciting future.

References

[1] Z. Zhu, T. K. Tam, F. Sun, C. You, and Y. H. P. Zhang, *A high-energy-density sugar biobattery based on a synthetic enzymatic pathway,* Nature Communications **5** (2014), 10.1038/ncomms4026.

[2] J. Koomey, S. Berard, M. Sanchez, and H. Wong, *Implications of historical trends in the electrical efficiency of computing,* IEEE Annals of the History of Computing **33**, 46 (2011).

[3] M. Karásek, F. Muijres, C. De Wagter, B. Remes, and G. de Croon, *A tailless aerial robotic flapper reveals that flies use torque coupling in rapid banked turns,* Science **361**, 1089 (2018).

[4] C. De Wagter, *Multiple pairs of flapping wings for attitude control,* (2017), patent NL2016130B1.

[5] M. Karasek, *Flapping wing aerial vehicle,* (2020), uS Patent US20200172240A1.

[6] M. Hassanalian and A. Abdelkefi, *Classifications, applications, and design challenges of drones: A review,* Progress in Aerospace Sciences **91**, 99 (2017).

[7] W. W. Greenwood, J. P. Lynch, and D. Zekkos, *Applications of UAVs in civil infrastructure,* Journal of Infrastructure Systems **25**, 04019002 (2019).

[8] A. S. Saeed, A. B. Younes, C. Cai, and G. Cai, *A survey of hybrid unmanned aerial vehicles,* Progress in Aerospace Sciences **98**, 91 (2018).

10

[9] M. Hochstenbach, C. Notteboom, B. Theys, and J. De Schutter, *Design and Control of an Unmanned Aerial Vehicle for Autonomous Parcel Delivery with Transition from Vertical Take-off to Forward Flight -VertiKUL, a Quadcopter Tailsitter,* International Journal of Micro Air Vehicles **7**, 395 (2015).

[10] R. Fjelland, *Why general artificial intelligence will not be realized,* Humanities and Social Sciences Communications **7** (2020), 10.1057/s41599-020-0494-4.

[11] F. M. Rocha, V. S. Costa, and L. P. Reis, *From reinforcement learning towards artificial general intelligence,* in *Trends and Innovations in Information Systems and Technologies* (Springer International Publishing, 2020) pp. 401–413.

[12] J. Hawkins, *A Thousand Brains* (Hachette Book Group USA, 2021).

[13] M. A. Estrada, S. Mintchev, D. L. Christensen, M. R. Cutkosky, and D. Floreano, *Forceful manipulation with micro air vehicles,* Science Robotics **3**, eaau6903 (2018).

[14] S. Javaid, X. Xu, W. Chen, J. Chen, H.-Y. Hsu, S. Wang, X. Yang, Y. Li, Z. Shao, F. Jones, and G. Jia, *Ni2+/co2+ doped au-fe7s8 nanoplatelets with exceptionally high oxygen evolution reaction activity,* Nano Energy **89**, 106463 (2021).

[15] S.-W. Hwang, H. Tao, D.-H. Kim, H. Cheng, J.-K. Song, E. Rill, M. A. Brenckle, B. Panilaitis, S. M. Won, Y.-S. Kim, Y. M. Song, K. J. Yu, A. Ameen, R. Li, Y. Su, M. Yang, D. L. Kaplan, M. R. Zakin, M. J. Slepian, Y. Huang, F. G. Omenetto, and J. A. Rogers, *A physically transient form of silicon electronics,* Science **337**, 1640 (2012).

[16] S.-K. Kang, R. K. J. Murphy, S.-W. Hwang, S. M. Lee, D. V. Harburg, N. A. Krueger, J. Shin, P. Gamble, H. Cheng, S. Yu, Z. Liu, J. G. McCall, M. Stephen, H. Ying, J. Kim, G. Park, R. C. Webb, C. H. Lee, S. Chung, D. S. Wie, A. D. Gujar, B. Vemulapalli, A. H. Kim, K.-M. Lee, J. Cheng, Y. Huang, S. H. Lee, P. V. Braun, W. Z. Ray, and J. A. Rogers, *Bioresorbable silicon electronic sensors for the brain,* Nature **530**, 71 (2016).

[17] K. Wong, C. Rudd, S. Pickering, and X. Liu, *Composites recycling solutions for the aviation industry,* Science China Technological Sciences **60**, 1291 (2017).

10

Acknowledgements

Nanos Gigantum Humeris Insidentes

Bernard of Chartres – Isaac Newton

Any achievement of the present is only made possible by building upon the insights and achievements of our predecessors. And the more complex the project, the more people are involved. Aerospace projects like creating flying robots are more often than not pretty complex and involve disciplines like aerodynamics, structures, propulsion, energy, electronics, programming, control, testing and piloting skills, regulatory skills, negotiating skills, and more. Large complex projects only succeed if all disciplines are sufficiently covered and thereby only become possible through the collaboration of very dedicated and skilled people.

I had the great chance to learn from and work with an overwhelming number of such people, each with their important contribution to shaping who I am today. The list of people is impressive and the more you think about it, the more people show up, making it hard to set a threshold on whom to include in an acknowledgment section. I would therefore like to highlight a subset of topics instead.

First off, I would like to thank everyone who played a role in my upbringing, education, and in sparking my curiosity. First and foremost there are my parents, family, siblings, grandparents, teachers, and classmates, but there were many more people who had a profound influence, not the least by for instance writing inspiring books or having interesting discussions and sharing experiences.

Special gratitude goes to my wife and kids who kindly and enthusiastically allowed and even stimulated the pursuit of accomplishing challenging ideas in this voyage of discovery. Most of this work would not have been possible without their flexibility, comprehension, support, motivation, and love.

On the topic of unmanned air vehicles, I was greatly inspired by family, good friends, fellow students, student projects, professors and their contacts, a great university, and an amazing internship opportunity. But what propelled most of the work presented here is also the culture of allowing initiative, a flat hierarchy that promotes critical thinking, and a stimulating environment with lots of facilities to realize ideas.

The MAVLab would not have grown to be what it is today if it wasn't for the work of a lot of people. The tremendous efforts of continuously attracting projects, arranging the required facilities & people, boosting the scientific level of the work, and arranging external support were critically important but would probably have been in vain without the hard work of staff, PhDs, MScs, interns, and anyone who helped realize the research and project ideas.

Most projects in this thesis were the result of not only teamwork but were also triggered by inspiring competitions and real-world challenges that prompted the search for innovative solutions. I therefore would like to express a special thanks to the organizers and sponsors of all the events we participated in, like the international micro air vehicle conference and competitions, the various outback challenges, indoor exploration challenges, the various autonomous drone race competitions, and maritime drone challenges. They all played a big role in boosting developments. The DelFly project started with a very motivated student team combined with skilled experts motivated by challenging competition requirements and was supported over the years by many contributors, materially and immaterially. It led to amazing opportunities for which I am exceptionally grateful. The DelftaCopter project involved a large team of particularly perseverant and resilient people over several years and owes its existence to generous sponsors, talented designers, unremitting builders, driven guidance, visionary ideas, and a fair amount of entrepreneurship. The Nederdrone project grew out of very challenging requirements, unique desires for new collaborations, substantial material support, and great collaboration in challenging conditions. Finally, I would like to thank the drone race team. It arose with the very first ADR competitions and brought many crucial contributions and insights over the years before forming the AIRR team, which was put to the test *in unique ways* but also led to great experiences, contacts, friendships, results, and subsequent new opportunities.

In general, I would like to thank everyone who participates in initiatives that stimulate the gathering of knowledge and rational thinking tools, the expression of creativity, the development of visionary ideas, the collaboration between people, and the stimulation of curiosity. I think these properties advance humanity.

Last but not least, I would like to particularly thank all my promotors and numerous co-authors during this unusual Ph.D. journey. While the intense desire to address challenges has not accelerated the doctorate journey, it will be with a lot of dedication that I will strive to grow in the "quality of judgment, integrity, transparency, and independent communication on results & social relevance" that the title represents.

10

Curriculum Vitæ

Christophe De Wagter

11-07-1979   Born in Eeklo, Belgium.

Education

1991–1998   Grammar School
Don Boscocollege, Zwijnaarde (Belgium)
Science and Mathematics

1998–2004   M.Sc. in Aerospace Engineering
Delft University of Technology, the Netherlands

2004   PhD. in Aerospace Engineering
Delft University of Technology, the Netherlands
Thesis: Hover and fast flight of minimum-mass mission-capable flying robots
Promotors: prof. dr. ir. J.M. Hoekstra and
prof. dr. G.C.H.E. de Croon

Experience

2000-2001   ASA Students Temporary Employment Agency

2002   Georgia Institute of Technology, Atlanta

2002-2003   Instructor for Delft Applied Mechanics Course, TUDelft

2004-2010   Aerospace Software and Technologies Institute

2007   TNO Defense, Security and Safety, Den Haag

2008-2020   De Wagter Consulting, Haarlem

2009-2015   AeroVinci v.o.f., Haarlem

2010-   TU Delft - Micro Air Vehicle Lab, Delft (NL) – Researcher

Selected awards

1998	School Record Award: Physics Olympiad Contest and Belgian Finalist Mathematics Olympiad Contest
2001	Winner of the TU Delft Design and Synthesis Symposium 1st prize
2003	Best Student Paper Award: D.A.S.C.
2005	Tutor of the winning TU Delft Design and Synthesis Symposium 1st prize
2008	Indoor Flight Dynamics - Best automatic MAV at the EMAV2008
2009	Guinness book of records: Smallest Camera Equipped Airplane in the World
2013	Triple 1st prize at the three IMAV2013 competitions
2016	Second Prize in IROS ADR and Outback UAV Challenge
2017	First Prize for the "Autonomous Race Drone" design
2019	World Champion Artificial Intelligent Drone Racing

(a) DSE   (b) Guiness Record   (c) IMAV 2008   (d) IMAV 2010

(e) IROS ADR 2016   (f) Outback Medical   (g) DSE   (h) AIRR

Figure 2: Selected awards.

List of Publications

The author has researched UAVs since 2002. For many years, his focus has been on completing projects that led to successful flying robots, while always pushing the boundaries of the state-of-the-art. He is not the first author in many papers but contributed fundamentally by proposing the concept, making key hardware, analyzing the data, writing, and guiding the main authors. He founded the MAVLab and chose the name to reflect the ambition to create mission-capable flying robots which are as small, smart, and safe as possible. He was part of the original DelFly team, and his work on the 4-gram stereo vision system enabled the first autonomous exploration robot DelFly Explorer in 2013. He also proposed and designed the first tail-less DelFly. The ideas behind this first tailless quad-thopter DelFly contributed to those behind the design of the DelFly nimble, which featured in Science and resulted in a spin-off company.

He helped to kick off the hybrid outdoor UAV research by working on the Quad-shot and worked on the ATMOS before they became another spin-off company. He drove the research to understand the particular dynamics of the DelftaCopter and develop a controller for it, and he helped to steer the design of the hydrogen Nederdrone towards a redundant versatile and safe mission-capable platform. He co-guided the drone race research and in particular, was the technical lead in the 2019 AIRR where his idea to not use traditional indoor navigation but lightweight AI-based perception combined with safety-aware control was a key factor in obtaining the title of 2019 world champion in AI drone racing. This results in over 100 peer-reviewed publications. Three particular publications are featured below: the DelFly book, and the Science and Nature Machine Intelligence articles where the research featured on the cover.
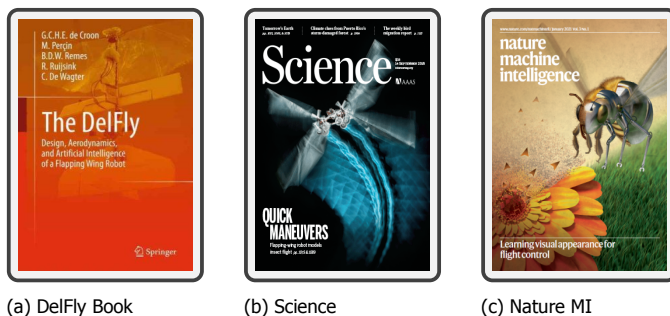

(a) DelFly Book   (b) Science   (c) Nature MI

Figure 3: Selected publications: The DelFly Book and journal papers in Science and Nature Machine Intelligence .

Journal Articles

[1] B. Rattanagraikanakorn, M. Schuurman, D. Gransden, R. Happee, **C. De Wagter**, A. Sharpanskykh, and H. Blom, *Variation in human injury and fatality from impacts by different uas types of similar weight,* Journal of Crashworthiness (submitted).

[2] S. Li, M. Coppola, **C. De Wagter**, and G. C. H. E. de Croon, *An autonomous swarm of micro flying robots with range-based relative localization,* Robotics and Autonomous Systems (submitted).

[3] **C. De Wagter**, F. Paredes-Vallés, N. Sheth, and G. C. H. E. de Croon, *The sensing, state-estimation, and control behind the winning entry to the 2019 artificial intelligence robotic racing competition,* Field Robotics **2** (2022), 10.55417/fr.2022042.

[4] J. Westenberger, **C. De Wagter**, and G. C. H. E. de Croon, *Efficient bang-bang model predictive control for quadcopters,* Unmanned Systems (2022), 10.1142/S2301385022410060.

[5] D. A. Olejnik, F. T. Muijres, M. Karásek, L. HonfiCamilo, **C. De Wagter**, and G. C. H. E. de Croon, *Flying into the wind: Insects and bio-inspired micro-air-vehicles with a wing-stroke dihedral steer passively into wind-gusts,* Frontiers Robotics and AI **9**, 1 (2022).

[6] S. Li, **C. De Wagter**, and G. C. H. E. de Croon, *Nonlinear model predictive control for improving range-based relative localization by maximizing observability,* Journal of Micro Air Vehicles (2022), 10.1177/17568293211073680.

[7] H. Karssies and **C. De Wagter**, *Extended incremental non-linear control allocation (xinca) for quadplanes,* Journal of Micro Air Vehicles **14**, 1 (2022).

[8] C. P. L. de Jong, B. D. W. Remes, S. Hwang, and **C. De Wagter**, *Never landing drone: Autonomous soaring of a unmanned aerial vehicle in front of a moving obstacle,* International Journal of Micro Air Vehicles **13**, 175682932110605 (2021).

[9] **C. De Wagter**, F. Paredes-Vallés, N. Sheth, and G. C. H. E. de Croon, *Learning fast in autonomous drone racing,* **Nature** Machine Intelligence **3** (2021), 10.1038/s42256-021-00405-z.

[10] S. Pfeiffer, **C. De Wagter**, and G. C. H. E. de Croon, *A computationally efficient moving horizon estimator for ultra-wideband localization on small quadrotors,* IEEE Robotics and Automation Letters **6**, 6725 (2021).

[11] **C. De Wagter**, B. D. W. Remes, E. Smeur, F. van Tienen, R. Ruijsink, K. van Hecke, and E. van der Horst, *The nederdrone: a hybrid lift, hybrid energy hydrogen uav,* International Journal of Hydrogen Energy **46**, 16003 (2021).

[12] D. Wijnker, T. van Dijk, M. Snellen, G. C. H. E. de Croon, and **C. De Wagter**, *Hear and avoid for uavs using convolutional neural networks,* International Journal of Micro Air Vehicles **13**, 1 (2021).

[13] G. C. H. E. de Croon, **C. De Wagter**, and T. Seidl, *Enhancing optical-flow-based control by learning visual appearance cues for flying robots,* **Nature** Machine Intelligence **3**, 33 (2021).

[14] M. Coppola, K. N. McGuire, **C. De Wagter**, and G. C. H. E. de Croon, *A survey on swarming with micro air vehicles: Fundamental challenges and constraints,* Frontiers in Robotics and AI **7**, 18 (2020).

[15] S. Li, M. Ozo, **C. De Wagter**, and G. C. H. E. de Croon, *Autonomous drone race: A computationally efficient vision-based navigation and control strategy,* Robotics and Autonomous Systems **133**, 103621 (2020).

[16] **C. De Wagter**, B. Remes, R. Ruijsink, F. van Tienen, and E. van der Horst, *Design and testing of a vertical take-off and landing UAV optimized for carrying a hydrogen fuel cell with a pressure tank,* Unmanned Systems **8**, 279 (2020).

[17] B. Rattanagraikanakorn, M. Schuurman, D. Gransden, R. Happee, **C. De Wagter**, A. Sharpanskykh, and H. Blom, *Modelling head injury due to unmanned aircraft systems collision: Crash dummy vs human body,* International Journal of Crashworthiness , 15 (2020).

[18] S. Li, E. van der Horst, P. Duernay, **C. De Wagter**, and G. C. H. E. de Croon, *Visual model-predictive localization for computationally efficient autonomous racing of a 72-gram drone,* Journal of Field Robotics **37**, 667 (2020).

[19] M. Karásek, M. Perçin, T. Cunis, B. W. Oudheusden, **C. De Wagter**, B. D. W. Remes, , and d. G. C. H. E., *Accurate position control of a flapping-wing robot enabling free-flight flow visualisation in a wind tunnel,* International Journal of Micro Air Vehicles **11**, 175682931983368 (2019).

[20] H. Moon, J. Martinez-Carranza, T. Cieslewski, M. Faessler, D. Falanga, A. Simovic, D. Scaramuzza, S. Li, M. Ozo, **C. De Wagter**, G. C. H. E. de Croon, S. Hwang, S. Jung, H. Shim, H. Kim, M. Park, T.-C. Au, and S. J. Kim, *Challenges and implemented technologies used in autonomous drone racing,* Intelligent Service Robotics **12**, 137 (2019).

[21] S. Li, **C. De Wagter**, C. C. de Visser, Q. P. Chu, and G. C. H. E. de Croon, *In-flight model parameter and state estimation using gradient descent for high-speed flight,* International Journal of Micro Air Vehicles **11**, 1 (2019).

[22] K. N. McGuire, **C. De Wagter**, K. Tuyls, H. J. Kappen, and G. C. H. E. de Croon, *Minimal navigation solution for a swarm of tiny flying robots to explore an unknown environment,* **Science** Robotics **4**, 1 (2019), eaaw9710.

[23] **C. De Wagter** and J. Meulenbeld, *Modeling the unstable DelftaCopter vertical take-off and landing tailsitter unmanned air vehicle in hover and forward flight from flight test data,* International Journal of Micro Air Vehicles **11**, 1 (2019).

[24] B. Rattanagraikanakorn, D. I. Gransden, M. Schuurman, **C. De Wagter**, R. Happee, A. Sharpanskykh, and H. A. P. Blom, *Multibody system modelling of unmanned aircraft system collisions with the human head,* International Journal of Crashworthiness **25**, 689 (2019).

[25] S. Li, **C. De Wagter**, and G. C. H. E. de Croon, *Unsupervised tuning of filter parameters without ground-truth applied to aerial robots,* IEEE Robotics and Automation Letters , 4102 (2019).

[26] **C. De Wagter**, M. Karásek, and G. C. H. E. de Croon, *Quad-thopter: Tailless flapping wing robot with 4 pairs of wings,* International Journal of Micro Air Vehicles **10**, 244 (2018).

[27] M. Karásek, F. Muijres, **C. De Wagter**, B. Remes, and G. de Croon, *A tailless aerial robotic flapper reveals that flies use torque coupling in rapid banked turns,* **Science 361**, 1089 (2018).

[28] S. Tijmons, **C. De Wagter**, B. Remes, and G. C. H. E. de Croon, *Autonomous door and corridor traversal with a 20-gram flapping wing mav by onboard stereo vision,* Aerospace – Open Access Aeronautics and Astronautics Journal **5** (2018), 10.3390/aerospace5030069.

[29] **C. De Wagter**, R. Ruijsink, E. Smeur, K. van Hecke, F. van Tienen, E. van der Horst, and B. Remes, *Design, control, and visual navigation of the delftacopter vtol tail-sitter uav,* Journal of Field Robotics **35**, 937 (2018).

[30] H. W. Ho, **C. De Wagter**, B. D. W. Remes, and G. C. H. E. de Croon, *Optical-flow based self-supervised learning of obstacle appearance applied to MAV landing,* Robotics and Autonomous Systems **100**, 78 (2018).

[31] J. P. R. Silva, **C. De Wagter**, and G. C. H. E. de Croon, *Quadrotor thrust vectoring control with time optimal trajectory planning in constant wind fields,* Unmanned Systems **6**, 1 (2017).

[32] K. McGuire, G. C. H. de Croon, **C. De Wagter**, K. Tuyls, and H. Kappen, *Efficient optical flow and stereo vision for velocity estimation and obstacle avoidance on an autonomous pocket drone,* IEEE Robotics and Automation Letters **2**, 1070 (2017).

[33] S. Tijmons, G. C. H. E. de Croon, B. D. W. Remes, **C. De Wagter**, and M. Mulder, *Obstacle avoidance strategy using onboard stereo vision on a flapping wing mav,* IEEE Transactions on Robotics **33**, 858 (2017).

[34] **C. De Wagter** and E. J. J. Smeur, *Control of a hybrid helicopter with wings,* International Journal of Micro Air Vehicles **9**, 209 (2017).

[35] J. A. Koopmans, S. Tijmons, **C. De Wagter**, and G. C. H. E. de Croon, *Passively stable flapping flight from hover to fast forward through shift in wing position,* International Journal of Micro Air Vehicles **7**, 407 (2015).

[36] J. V. Caetano, M. Perçin, B. W. van Oudheusden, B. Remes, **C. De Wagter**, G. C. H. E. de Croon, and C. C. de Visser, *Error analysis and assessment of unsteady forces acting on a flapping wing micro air vehicle: free flight versus wind-tunnel experimental methods,* Bioinspiration & Biomimetics **10**, 056004 (2015).

[37] J. V. Caetano, C. C. de Visser, G. C. H. E. de Croon, B. Remes, **C. De Wagter**, J. Verboom, and M. Mulder, *Linear aerodynamic model identification of a flapping wing mav based on flight test data,* International Journal of Micro Air Vehicles **5**, 273 (2013).

[38] G. C. H. E. de Croon, H. W. Ho, **C. De Wagter**, E. Van Kampen, B. Remes, and Q. P. Chu, *Optic-flow based slope estimation for autonomous landing,* International Journal of Micro Air Vehicles **5**, 287 (2013).

[39] G. C. H. E. de Croon, M. A. Groen, **C. De Wagter**, B. Remes, R. Ruijsink, and B. W. van Oudheusden, *Design, aerodynamics and autonomy of the delfly,* Bioinspiration & Biomimetics **7**, 1 (2012).

[40] G. C. H. E. de Croon, **C. De Wagter**, B. D. W. Remes, and R. Ruijsink, *Subsampling: Real-time vision for micro air vehicles,* Robotics and Autonomous Systems **60**, 167 (2012).

[41] G. C. H. E. de Croon, E. De Weerdt, **C. De Wagter**, B. D. W. Remes, and R. Ruijsink, *The appearance variation cue for obstacle avoidance,* IEEE Transactions on Robotics **28**, 529 (2012).

[42] G. C. H. E. de Croon, K. M. E. De Clercq, R. Ruijsink, B. Remes, and **C. De Wagter**, *Design, aerodynamics, and vision-based control of the delfly,* International Journal of Micro Air Vehicles **1**, 71 (2009).

[43] **C. De Wagter** and J. A. Mulder, *Vision-based guidance and awareness for autonomous uav,* Journal of Gyroscopy and Navigation **53**, 13 (2006).

[44] M. Mulder, T. M. Lam, **C. De Wagter**, M. M. van Paassen, and J. A. Mulder, *Increasing the safety of operating unmanned aerial vehicles,* Zeszyty Naukowe Politechniki Rzeszowskiej. Mechanika **0209-2689**, 13 (2004).

Book Chapters

[1] G. C. H. E. de Croon, M. Perçin, B. D. W. Remes, R. Ruijsink, and **C. De Wagter**, *Introduction to flapping wing design,* in *The DelFly* (Springer Netherlands, 2016) pp. 9–29.

[2] G. C. H. E. de Croon, M. Perçin, B. D. W. Remes, R. Ruijsink, and **C. De Wagter**, *Mechanical design and materials,* in *The DelFly* (Springer Netherlands, 2016) pp. 31–39.

[3] G. C. H. E. de Croon, M. Perçin, B. D. W. Remes, R. Ruijsink, and **C. De Wagter**, *Electronics,* in *The DelFly* (Springer Netherlands, 2016) pp. 41–54.

[4] G. C. H. E. de Croon, M. Perçin, B. D. W. Remes, R. Ruijsink, and **C. De Wagter**, *Introduction to fixed and flapping wing aerodynamics,* in *The DelFly* (Springer Netherlands, 2016) pp. 57–80.

[5] G. C. H. E. de Croon, M. Perçin, B. D. W. Remes, R. Ruijsink, and **C. De Wagter**, *Research on the delfly aerodynamics,* in *The DelFly* (Springer Netherlands, 2016) pp. 81–121.

[6] G. C. H. E. de Croon, M. Perçin, B. D. W. Remes, R. Ruijsink, and **C. De Wagter**, *Introduction to autonomous flight,* in *The DelFly* (Springer Netherlands, 2016) pp. 125–138.

[7] G. C. H. E. de Croon, M. Perçin, B. D. W. Remes, R. Ruijsink, and **C. De Wagter**, *Monocular obstacle detection,* in *The DelFly* (Springer Netherlands, 2016) pp. 139–165.

[8] G. C. H. E. de Croon, M. Perçin, B. D. W. Remes, R. Ruijsink, and **C. De Wagter**, *Optical flow based turning logic,* in *The DelFly* (Springer Netherlands, 2016) pp. 167–177.

[9] G. C. H. E. de Croon, M. Perçin, B. D. W. Remes, R. Ruijsink, and **C. De Wagter**, *Autonomous flight with onboard stereo vision,* in *The DelFly* (Springer Netherlands, 2016) pp. 179–196.

[10] G. C. H. E. de Croon, M. Perçin, B. D. W. Remes, R. Ruijsink, and **C. De Wagter**, *Conclusions and future research,* in *The DelFly* (Springer Netherlands, 2016) pp. 199–207.

[11] S. Tijmons, G. C. H. E. de Croon, B. Remes, **C. De Wagter**, R. Ruijsink, E.-J. van Kampen, and Q. Chu, *Stereo vision based obstacle avoidance on flapping wing mavs,* in *Advances in Aerospace Guidance, Navigation and Control* (Springer, Berlin, Heidelberg, Berlin, Heidelberg, 2013) pp. 463–482.

[12] **C. De Wagter**, A. Koopmans, G. C. H. E. de Croon, B. Remes, and R. Ruijsink, *Autonomous wind tunnel free-flight of a flapping wing mav,* in *Advances in Aerospace Guidance, Navigation and Control* (Springer, Berlin, Heidelberg, Berlin, Heidelberg, 2013) pp. 603–621.

Conference Proceedings

[1] S. Bahnam, **C. De Wagter**, and G. C. H. E. de Croon, *Improving the computational efficiency of rovio,* in *13th editionof the International Micro Air Vehicle Conference and Competition* (submitted).

[2] S. Wang, D. Olejnik, **C. De Wagter**, B. van Oudheusden, G. C. H. E. de Croon, and S. Hamaza, *Battle the wind: Improving flight stability of a flapping wing micro air vehicle under wind disturbance with onboard thermistor-based airflow sensing,* in *Intelligent Robots and Systems (IROS), 2022 IEEE/RSJ International Conference on* (submitted).

[3] S. Li, **C. De Wagter**, and G. C. H. E. de Croon, *Self-supervised monocular multi-robot relative localization with efficient deep neural networks,* in *2022 IEEE International Conference on Robotics and Automation (ICRA)* (IEEE, Philadelphia, USA, 2022) 2105.12797 .

[4] D. A. Olejnik, S. Wang, J. Dupeyroux, S. Stroobants, M. Karásek, **C. De Wagter**, and G. C. H. E. de Croon, *An experimental study of wind resistance and power consumption in mavs with a low-speed multi-fan wind system,* in *IEEE International Conference on Robotics and Automation* (2022) 2202.06723 .

[5] J. Karssies and **C. De Wagter**, *Extended incremental non-linear control allocation on the tu delft quadplane,* in *12th International Micro Air Vehicle Conference and Competition*, edited by J. Martinez-Carranza (IMAV, Puebla, México, 2021) pp. 74–84, iMAV2021-9.

[6] L. Dellemann and **C. De Wagter**, *Hybrid uav attitude control using indi and dynamic tilt-twist,* in *12th International Micro Air Vehicle Conference and Competition*, edited by J. Martinez-Carranza (IMAV, Puebla, México, 2021) pp. 131–136, iMAV2021-16.

[7] S. Li, **C. De Wagter**, and G. C. H. E. de Croon, *Nonlinear model predictive control for improving range-based relative localization by maximizing observability,* in *12th International Micro Air Vehicle Conference and Competition*, edited by J. Martinez-Carranza (IMAV, Puebla, México, 2021) pp. 28–34, iMAV2021-2.

[8] S. Li, E. Öztürk, **C. De Wagter**, G. C. H. E. de Croon, and D. Izzo, *Aggressive online control of a quadrotor via deep network representations of optimality principles,* in *2020 IEEE International Conference on Robotics and Automation, ICRA 2020*, Proceedings - IEEE International Conference on Robotics and Automation (Institute of Electrical and Electronics Engineers (IEEE), United States, 2020) pp. 6282–6287.

[9] B. Rattanagraikanakorn, H. Blom, A. Sharpanskykh, **C. De Wagter**, C. Jiang, M. Schuurman, D. Gransden, and R. Happee, *Modeling and simulating human fatality due to quadrotor uas impact,* in *AIAA Aviation 2020 Forum*, 2020-2902 (2020) pp. 1–18.

[10] F. Muijres, M. Karásek, **C. De Wagter**, B. Remes, and G. de Croon, *A bio-inspired free-flying robot reveals that flies use torque coupling in rapid banked turns,* in *SICB Annual Meeting 2019*, Vol. 59 Issue Supplement 1 (SICB 2019 Annual Meeting, The Society for Integrative and Comparative Biology, Florida, Tampa, United States, 2019) pp. E164–E164.

[11] D. Wijnker, T. van Dijk, M. Snellen, G. C. H. E. de Croon, and **C. De Wagter**, *Hear and avoid for uavs using convolutional neural networks,* in *11th International Micro Air Vehicle Competition and Conference*, edited by P. Campoy (IMAV, Madrid, Spain, 2019) pp. 144–156, iMAV2019-19.

[12] **C. De Wagter**, B. Remes, R. Ruisink, F. van Tienen, and E. van der Horst, *Design and testing of a vertical take-off and landing uav optimized for carrying a hydrogen fuel-cell with pressure tank,* in *11th International Micro Air Vehicle Competition and Conference*, edited by P. Campoy (IMAV, Madrid, Spain, 2019) pp. 49–54, iMAV2019-6.

[13] B. Rattanagraikanakorn, M. Schuurman, D. Gransden, R. Happee, **C. De Wagter**, A. Sharpanskykh, and H. Blom, *Modelling head injury due to unmanned aircraft systems collision: Crash dummy vs human body,* in *2019 AIAA Aviation and Aeronautics Forum and Exposition*, 2019-2835 (AIAA, 2019).

[14] G. C. H. E. de Croon and **C. De Wagter**, *Challenges of autonomous flight in indoor environments,* in *2018 IEEE/RSJ International Conference on Intelligent Robots and Systems (IROS)* (2018) pp. 1003–1009.

[15] K. Y. Scheper, M. Karásek, **C. De Wagter**, B. D. W. Remes, and G. C. H. E. de Croon, *First autonomous multi-room exploration with an insect-inspired flapping wing vehicle,* in *ICRA 2018: 2018 IEEE International Conference on Robotics and Automation* (IEEE, Brisbane, Australia, 2018) pp. 5546–5552.

[16] J. Meulenbeld, **C. De Wagter**, and B. Remes, *Modeling delftacopter from flight test data,* in *10th International Micro Air Vehicle Competition and Conference*, edited by S. Watkins (IMAV, Melbourne, Australia, 2018) pp. 18–29, iMAV2018-1.

[17] **C. De Wagter**, B. Remes, R. Ruijsink, E. van der Horst, F. van Tienen, D. van Wijngaarden, J. Meulenbeld, and K. van Hecke, *Delftacopter propulsion optimization from hover to fast forward flight using windtunnel measurements,* in *10th International Micro Air Vehicle Competition and Conference*, edited by S. Watkins (IMAV, Melbourne, Australia, 2018) pp. 30–38, iMAV2018-2.

[18] T. Braber, **C. De Wagter**, G. C. H. E. de Croon, and R. Babuska, *Optical-flow-based stabilization of micro air vehicles without scaling sensors,* in *10th International Micro Air Vehicle Competition and Conference*, edited by S. Watkins (IMAV, Melbourne, Australia, 2018) pp. 289–297.

[19] B. Rattanagraikanakorn, A. Sharpanskykh, M. Schuurman, D. Gransden, H. A. Blom, and **C. De Wagter**, *Characterizing uas collision consequences in future utm,* in *2018 Aviation Technology, Integration, and Operations Conference* (American Institute of Aeronautics and Astronautics (AIAA), Atlanta, Georgia, 2018) pp. 1–25.

[20] K. McGuire, M. Coppola, **C. De Wagter**, and G. C. H. E. de Croon, *Towards autonomous navigation of multiple pocket-drones in real-world environments,* in *Intelligent Robots and Systems (IROS), 2017 IEEE/RSJ International Conference on* (IEEE, Vancouver, BC, Canada, Canada, 2017) pp. 244–249.

[21] **C. De Wagter**, M. Karásek, and G. C. H. E. de Croon, *Quad-thopter: Tailless flapping wing robot with 4 pairs of wings,* in *International Micro Air Vehicle Conference and Flight Competition (IMAV) 2017*, edited by J.-M. Moschetta, G. Hattenberger, and H. de Plinval (IMAV, Toulouse, France, 2017) pp. 249–256.

[22] E. J. J. Smeur, D. C. Höppener, and **C. De Wagter**, *Prioritized control allocation for quadrotors subject to saturation,* in *International Micro Air Vehicle Conference and Flight Competition (IMAV) 2017*, edited by J.-M. Moschetta, G. Hattenberger, and H. de Plinval (IMAV, Toulouse, France, 2017) pp. 37–43.

[23] E. van der Sman, E. Smeur, B. Remes, **C. De Wagter**, and Q. Chu, *Incremental nonlinear dynamic inversion and multihole pressure probes for disturbance rejection control of fixed-wing micro air vehicles,* in *International Micro Air Vehicle Conference and Flight Competition (IMAV) 2017*, edited by J.-M. Moschetta, G. Hattenberger, and H. de Plinval (IMAV, Toulouse, France, 2017) pp. 111–120.

[24] **C. De Wagter** and E. Smeur, *Control of a hybrid helicopter with wings,* in *International Micro Air Vehicle Competition and Conference 2016*, edited by Z. PENG and D. F. LIN (IMAV, Beijing, PR of China, 2016) pp. 87–94.

[25] C. Nous, R. Meertens, **C. De Wagter**, and G. C. H. E. de Croon, *Performance evaluation in obstacle avoidance,* in *Intelligent Robots and Systems (IROS), 2016 IEEE/RSJ International Conference on* (IEEE, Daejeon, South Korea, 2016) pp. 3614–3619.

[26] L. N. C. Sikkel, G. C. H. E. de Croon, **C. De Wagter**, and Q. P. Chu, *A novel online model-based wind estimation approach for quadrotor micro air vehicles using low cost mems imus,* in *Intelligent Robots and Systems (IROS), 2016 IEEE/RSJ International Conference on* (IEEE, Daejeon, South Korea, 2016) pp. 2141–2146.

[27] K. Lamers, S. Tijmons, **C. De Wagter**, and G. C. H. E. de Croon, *Self-supervised monocular distance learning on a lightweight micro air vehicle,* in *Intelligent Robots and Systems (IROS), 2016 IEEE/RSJ International Conference on* (IEEE, Daejeon, South Korea, 2016) pp. 1779–1784.

[28] K. McGuire, G. C. H. E. de Croon, **C. De Wagter**, B. Remes, K. Tuyls, and H. Kappen, *Local histogram matching for efficient optical flow computation applied to velocity estimation on pocket drones,* in *Robotics and Automation (ICRA), 2016 IEEE International Conference on* (IEEE, Stockholm, Sweden, 2016) pp. 3255–3260.

[29] H. W. Ho, **C. De Wagter**, B. D. W. Remes, and G. C. H. E. de Croon, *Optical flow for self-supervised learning of obstacle appearance,* in *Intelligent Robots and Systems (IROS), 2015 IEEE/RSJ International Conference on*, IEEE (IEEE, Hamburg, Germany, 2015) pp. 3098–3104.

[30] J. L. Verboom, S. Tijmons, **C. De Wagter**, B. Remes, R. Babuska, and G. C. H. E. de Croon, *Attitude and altitude estimation and control on board a flapping wing micro air vehicle,* in *Robotics and Automation (ICRA), 2015 IEEE International Conference on*, IEEE (IEEE, Seattle, WA, USA, 2015) pp. 5846–5851.

[31] **C. De Wagter**, S. Tijmons, B. D. W. Remes, and G. C. H. E. de Croon, *Autonomous flight of a 20-gram flapping wing mav with a 4-gram onboard stereo vision system,* in *Robotics and Automation (ICRA), 2014 IEEE International Conference on* (IEEE, Hong Kong, China, 2014) pp. 4982–4987.

[32] J. V. Caetano, M. Perçin, C. C. de Visser, B. van Oudheusden, G. C. H. E. de Croon, **C. De Wagter**, B. Remes, and M. Mulder, *Tethered vs. free flight force determination of the delfly ii flapping wing micro air vehicle,* in *Unmanned Aircraft Systems (ICUAS), 2014 International Conference on* (IEEE, Orlando, FL, USA, 2014) pp. 942–948.

[33] J. V. Caetano, M. B. Weehuizen, C. C. de Visser, G. C. H. E. de Croon, **C. De Wagter**, B. Remes, and M. Mulder, *Rigid vs. flapping: The effects of kinematic formulations in force determination of a free flying flapping wing micro air vehicle,* in *Unmanned Aircraft Systems (ICUAS), 2014 International Conference on*, 14399756 (IEEE, Orlando, FL, USA, 2014) pp. 949–959.

[34] B. D. W. Remes, P. Esden-Tempski, F. van Tienen, E. Smeur, **C. De Wagter**, and G. C. H. E. de Croon, *Lisa-s 2.8 g autopilot for gps-based flight of mavs,* in *International Micro Air Vehicle Competition and Conference 2014*, edited by G. de Croon, E. J. van Kampen, **C. De Wagter**, and C. C. de Visser (IMAV, Delft, the Netherlands, 2014) pp. 280–285.

[35] E. J. J. Smeur, Q. P. Chu, G. C. H. E. de Croon, B. Remes, **C. De Wagter**, and E. van der Horst, *Modelling of a hybrid uav using test flight data,* in *International Micro Air Vehicle Competition and Conference 2014*, edited by G. de Croon, E. J. van Kampen, **C. De Wagter**, and C. C. de Visser (IMAV, Delft, the Netherlands, 2014) pp. 196–203.

[36] S. Tijmons, G. C. H. E. de Croon, B. D. W. Remes, **C. De Wagter**, R. Ruijsink, E. J. van Kampen, and Q. P. Chu, *Off-board processing of stereo vision images*

for obstacle avoidance on a flapping wing mav, in *Pegasus AIAA conference, Prague* (2013).

[37] S. Tijmons, G. C. H. E. de Croon, B. Remes, **C. De Wagter**, R. Ruijsink, E.-J. van Kampen, and Q. Chu, *Stereo vision based obstacle avoidance on flapping wing mavs,* in *Proceedings of the EuroGNC 2013, 2nd CEAS Specialist Conference*, edited by J. A. Mulder, D. Choukroun, E. J. van Kampen, C. C. de Visser, and G. J. Looye (Springer Verlag, Delft, the Netherlands, 2013) pp. 1225–1244.

[38] **C. De Wagter**, A. Koopmans, G. C. H. E. de Croon, B. Remes, and R. Ruijsink, *Autonomous wind tunnel free-flight of a flapping wing mav,* in *Proceedings of the EuroGNC 2013, 2nd CEAS Specialist Conference*, edited by J. A. Mulder, D. Choukroun, E. J. van Kampen, C. C. de Visser, and G. J. Looye (Springer Verlag, Delft, the Netherlands, 2013) pp. 17–35.

[39] **C. De Wagter**, D. Dokter, G. C. H. E. de Croon, and B. Remes, *Multi-lifting-device uav autonomous flight at any transition percentage,* in *Proceedings of the EuroGNC 2013, 2nd CEAS Specialist Conference*, edited by J. A. Mulder, D. Choukroun, E. J. van Kampen, C. C. de Visser, and G. J. Looye (Springer Verlag, Delft, the Netherlands, 2013) pp. 1190–1204.

[40] J. V. Caetano, C. C. de Visser, B. D. Remes, **C. De Wagter**, E.-J. van Kampen, and M. Mulder, *Controlled flight maneuvers of a flapping wing micro air vehicle: a step towards the delfly ii identification,* in *AIAA Atmospheric Flight Mechanics (AFM) Conference*, 2013-4843 (Boston, MA, 2013) p. 4843.

[41] J. V. Caetano, C. C. de Visser, B. Remes, **C. De Wagter**, and M. Mulder, *Modeling a flapping wing mav: Flight path reconstruction of the delfly ii,* in *AIAA Modeling and Simulation Technologies (MST) Conference*, 2013-4597 (Boston, MA, USA, 2013) pp. 1–12.

[42] B. Remes, D. Hensen, F. van Tienen, **C. De Wagter**, E. van der Horst, and G. C. H. E. de Croon, *Paparazzi: how to make a swarm of parrot ar drones fly autonomously based on gps,* in *Proceedings of the International Micro Air Vehicle Conference and Flight Competition IMAV 2013* (IMAV, Toulouse, France, 2013) pp. 307–313.

[43] J. V. Caetano, J. Verboom, C. C. de Visser, G. C. H. E. de Croon, B. D. W. Remes, **C. De Wagter**, and M. Mulder, *Near-hover flapping wing mav aerodynamic modelling - a linear model approach,* in *Proceedings of the International Micro Air Vehicle Conference and Flight Competition IMAV 2013* (IMAV, Toulouse, France, 2013) pp. 79–88.

[44] M. Perçin, H. E. Eisma, J. H. S. de Baar, B. W. van Oudheusden, B. Remes, R. Ruijsink, and **C. De Wagter**, *Wake reconstruction of flapping-wing mav 'delfly ii' in forward flight,* in *International Micro Air Vehicle Conference and Flight Competition IMAV 2012* (IMAV, Braunschweig, Germany, 2012).

[45] B. A. Hummelink, **C. De Wagter**, Q. P. Chu, and J. A. Mulder, *Ahrs for small fixed-wing uav with low-cost imu/gps using nonlinear complementary filtering,* in *AIAA Guidance, Navigation, and Control Conference*, 4461 (AIAA, Minneapolis, Minnesota, 2012) pp. 1–13.

[46] M. Perçin, H. Eisma, B. van Oudheusden, B. Remes, R. Ruijsink, and **C. De Wagter**, *Flow visualization in the wake of the flapping-wing mav 'delfly ii' in forward flight,* in *30th AIAA Applied Aerodynamics Conference*, 2664, AIAA (American Institute of Aeronautics and Astronautics (AIAA), New Orleans, Louisiana, USA, 2012) pp. 1–12.

[47] G. C. H. E. de Croon, **C. De Wagter**, B. D. W. Remes, and R. Ruijsink, *Sky segmentation approach to obstacle avoidance,* in *Aerospace Conference, 2011 IEEE* (IEEE, Big Sky, MT, USA, 2011) pp. 1–16.

[48] G. C. H. E. de Croon, B. W. van Oudheusden, B. D. W. Remes, **C. De Wagter**, and R. Ruijsink, *Aerodynamics and autonomy of the delfly,* in *International Workshop on BioInspired Robotics* (Nantes, France, 2011).

[49] G. C. H. E. de Croon, E. De Weerdt, **C. De Wagter**, B. D. W. Remes, and R. Ruijsink, *The appearance variation cue for obstacle avoidance,* in *Robotics and Biomimetics (ROBIO), 2010 IEEE International Conference on* (IEEE, Tianjin, China, 2010) pp. 1606–1611.

[50] E. Tijs, G. C. H. E. de Croon, J. Wind, B. Remes, **C. De Wagter**, H. E. de Bree, and R. Ruijsink, *Hear-and-avoid for micro air vehicles,* in *International Micro Air Vehicle Conference and Flight Competition 2010*, edited by D. G. für Ortung und Navigation e.V. (DGON) (IMAV, Braunschweig, Germany, 2010) pp. 88–93.

[51] G. C. H. E. de Croon, **C. De Wagter**, B. D. W. Remes, and R. Ruijsink, *Random sampling for indoor flight,* in *International Micro Air Vehicle Conference and Flight Competition 2010*, edited by D. G. für Ortung und Navigation e.V. (DGON) (IMAV, Braunschweig, Germany, 2010) pp. 94–102.

[52] M. J. Verveld, Q. P. Chu, **C. De Wagter**, and J. A. Mulder, *Optic flow based state estimation for an indoor micro air vehicle,* in *AIAA Guidance, Navigation, and Control Conference, Guidance, Navigation, and Control and Co-located Conferences*, edited by O. flow based state estimation for an indoor micro air vehicle, AIAA (American Institute of Aeronautics and Astronautics (AIAA), Toronto, Ontario, Canada, 2010) pp. 1–21.

[53] G. C. H. E. de Croon, **C. De Wagter**, B. D. W. Remes, and H. M. Ruijsink, *Local sampling for indoor flight,* in *BNAIC 2009: 21st Benelux Conference on Artificial Intelligence, Eindhoven, The Netherlands, 29-30 October 2009* (Eindhoven, The Netherlands, 2009).

[54] **C. De Wagter**, B. Bijnens, and J. A. Mulder, *Vision-only control of a flapping mav on mars,* in *AIAA Guidance, Navigation and Control Conference and Exhibit* (American Institute of Aeronautics and Astronautics (AIAA), Hilton Head, South Carolina, USA, 2007) pp. 1–7.

[55] **C. De Wagter** and M. Amelink, *Holiday50av technical paper,* in *3rd US-European Competetion and Workshop on Micro Air Vehicles & 7th European Micro Air Vehicle Conference and Flight Competetion (MAV07)* (Toulouse, France, 2007) pp. 1–18.

[56] **C. De Wagter**, *Development of inertial navigation, onboard vision and adaptive control for autonomous long-distance mav operations,* in *European Micro Air Vechile Competition 2006* (IMAV, Braunschweig, Germany, 2006) pp. 1–12.

[57] J. A. Mulder, *Development of "delfly" micro uav,* in *SAE Aerospace Control and Guidance Systems Committee, Nr 98* (Williamsburg, 2006).

[58] **C. De Wagter** and J. A. Mulder, *Vision-based guidance and awareness for autonomous uav,* in *Proceedings of the 12th Saint Petersburg International Conference on Intregrated Navigation Systems*, edited by V. G. Peshekhonov (State Research Center of Russia "Elektropribor", Saint Petersburg, Russia, 2005) pp. 1–10.

[59] **C. De Wagter** and J. A. Mulder, *Towards vision-based uav situation awareness,* in *AIAA Guidance, Navigation, and Control Conference and Exhibit* (American Institute of Aeronautics and Astronautics (AIAA), San Francisco, CA, USA, 2005) pp. 1–16.

[60] **C. De Wagter**, A. A. Proctor, and E. N. Johnson, *Vision-only aircraft flight control,* in *Digital Avionics Systems Conference, 2003. DASC '03. The 22nd*, Vol. 2 (IEEE, 2003) pp. 8.B.2–81–11.

(a) DASC2003   (b) IMAV2016   (c) IMAV2017   (d) IMAV2019   (e) IMAV2021

Figure 4: *Best paper awards* were received for [60], [57], [24], [21], and [7]. A *Special Award* for the significance and novelty of the work was received for [11] and a special mention for [5]

Misc

[1] **C. De Wagter**, *Multiple pairs of flapping wings for attitude control,* (2017), patent NL2016130B1.

[2] **C. De Wagter**, F. Paredes-Vallés, N. Sheth, and G. C. H. E. de Croon, *Logfiles of the Artificial Intelligence behind the winning entry to the 2019 AI Robotic Racing Competition,* (2021), DataverseNL, V1, 10.34894/CKL4TQ.

[3] S. Pfeiffer, **C. De Wagter**, and G. C. H. E. de Croon, *Data underlying the publication: "a computationally efficient moving horizon estimator for uwb localization on small quadrotors"",* (2021), 4TU.ResearchData, 10.4121/14827680.

[4] D. Wijnker, T. van Dijk, M. Snellen, G. C. H. E. de Croon, and **C. De Wagter**, *Hear-and-avoid: Acoustic detection of general aviation aircraft for uav,* (2020), DataverseNL, V1, 10.34894/ARULTD.

[5] M. Karásek, F. T. Muijres, **C. De Wagter**, B. D. Remes, and G. C. H. E. de Croon, *A tailless aerial robotic flapper reveals that flies use torque coupling in rapid banked turns (dataset),* (2018), DataverseNL, V1, 10.34894/JHNFNB.

[6] A. Narasimhan, C. C. de Visser, **C. De Wagter**, and M. Rischmueller, *Fault tolerant control of multirotor uav for piloted outdoor flights,* arXiv , 1 (2020), 2011.00481 .

[7] S. Li, M. Coppola, **C. De Wagter**, and G. C. H. E. de Croon, *An autonomous swarm of micro flying robots with range-based relative localization,* arXiv , 1 (2020), 2003.05853v1 .

[8] G. C. H. E. de Croon and **C. De Wagter**, *Learning what is above and what is below: horizon approach to monocular obstacle detection,* arXiv , 1 (2018), 1806.08007 .

[9] G. C. H. E. de Croon, E. J. van Kampen, and **C. De Wagter**, *Imav 2014: Proceedings of the international micro air vehicle conference and competition 2014,* International Micro Air Vehicle Conference and Competition 2014 (2014), 10.4233/uuid:ef248460-783a-4894-bc3b-668304715a60.

[10] S. Thomas, *Manoeuvres on the fly,* **Nature** Electronics **1**, 523 (2018).

[11] H. Moon, Y. Sun, J. Baltes, and S. J. Kim, *The IROS 2016 competitions [competitions],* IEEE Robotics & Automation Magazine **24**, 20 (2017).

[12] B. Mols, *Flapping micro plane watches where it goes,* Delft Outlook , 3 (2005), contributor: De Wagter, C. and Lentink, D.

[13] **C. De Wagter**, *Vision-based control for autonomous aerial vehicles,* Leonardo times **8**, 26 (2004), 8e Jaargang.
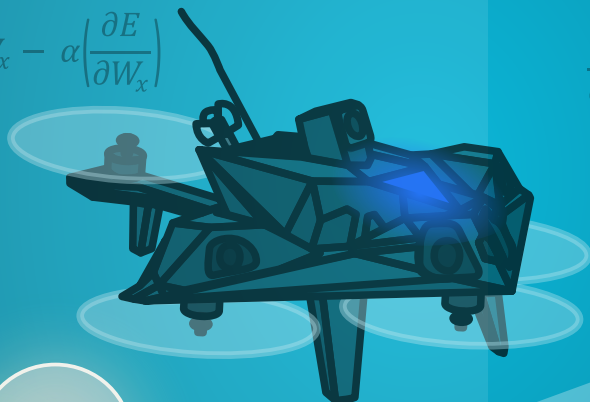
Index

$$\frac{\partial \mathbf{u}}{\partial t}+(\mathbf{u}\cdot\nabla)\mathbf{u}-\nu\nabla^2\mathbf{u}=-\nabla w+\mathbf{g}$$

$$\rho\left(\frac{\partial \boldsymbol{v}}{\partial t}+\boldsymbol{v}\cdot\nabla\boldsymbol{v}\right)=-\nabla p+\nabla\cdot\boldsymbol{T}+\boldsymbol{f}$$

$$W_x^*=W_x-\alpha\left(\frac{\partial E}{\partial W_x}\right)$$
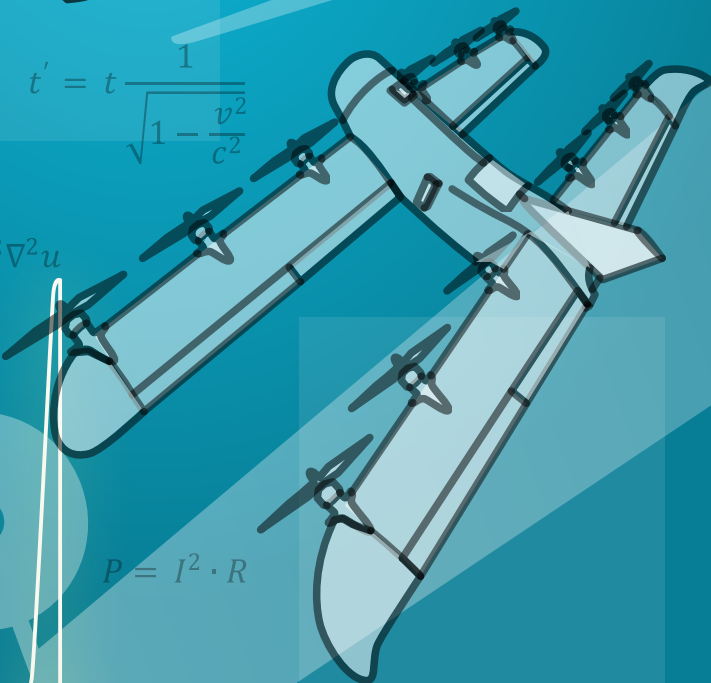
$$\frac{\partial I}{\partial x}V_x+\frac{\partial I}{\partial y}V_y+\frac{\partial I}{\partial t}=0$$

$$F=G\frac{m_1 m_2}{r^2}$$

$$t'=t\,\frac{1}{\sqrt{1-\dfrac{v^2}{c^2}}}$$

$$\frac{\partial^2 u}{\partial t^2}=v^2\nabla^2 u$$

$$P=I^2\cdot R$$

$$\frac{d}{dt}\left(\frac{\partial L}{\partial \dot{q}}\right)=\frac{\partial L}{\partial q}$$